UNIVERSITY OF LIVERPOOL

SCHOOL OF ENGINEERING

Quasi-static and dynamic behaviour of composite structures based on glass fibre reinforced PEKK

Thesis submitted in accordance with the requirement of the University of Liverpool for the degree of Doctor of Philosophy in Materials Engineering/Polymeric composite materials

By

Nassier A. Nassir

B.Sc. Materials Engineering

M.Sc. Materials Engineering

September 2018

DEDICATION

To the spirit of my father who dedicated his life to teach me;

To my mother whose love and blessing made my life happy;

To my wife Liqaa Al-Absi for her support and encouragement;

To my beloved children Mustafa, Noor and Jana;

To my brothers and sisters;

To all persons who helped me

I dedicate this work.

ACKNOLEDGMENTS

LIST OF PUBLICATIONS

Journal Papers:

N. Nassir, Z. W. Guan, R. S. Birch, and W. J. Cantwell, "Damage initiation in composite materials under off-centre impact loading," Polymer Testing, vol. 69, pp. 456–461, 2018.

Nassier. A. Nassir, R.S. Birch, W.J. Cantwell, Q.Y. Wang, Z.W. Guan (2018). The Perforation Resistance of Glass Fibre Reinforced PEKK composites. (Submitted to Composite Structures).

Conference Papers:

Nassier A. Nassir, R.S. Birch, Z.W. Guan (2017), Develop high temperature glass fibre/PEKK prepreg, 21st International Conference on Composite Materials, Xi'an, China (Published in Proceedings).

Nassier A. Nassir, R.S. Birch, D. Rico Sierra, S. P. Edwardson, G. Dearden, Z.W. Guan (2018), Surface modification of titanium alloy with laser treatment, World Academy of Science, Engineering and Technology, International Journal of Aerospace and Mechanical Engineering, 12(5), 580 - 583. (**Best presentation Award**).

Nassier A. Nassir, R.S. Birch, Z.W. Guan (2018), Manufacturing process of S-Glass fibre reinforced PEKK prepregs, 20th International Conference on Aerospace Composite Technology (ICACT 2018), Barcelona, Spain (Published in Proceedings).

R.T. Durai Prabhakaran, Nassier A. Nassir, Graham Ormondroyd and Guan Zhongwei (2017), Mechanical characterisation of green sandwich panels–Biomaterial skins and natural fibre cores, 2nd International Conference on Frontiers of Composite Materials (ICFCM2017), Melbourne, Australia (Published in Proceedings).

ABSTRACT

The aim of this thesis is to investigate the quasi-static and impact response of the newly developed composite material and the related fibre metal laminates (FMLs) that have potential to satisfy the requirements of the new generation of aircrafts such as the damage tolerance and high service temperatures.

Initially, this thesis presents the findings of a research study to develop high temperature thermoplastic composites. Here, woven S-glass fibre (GF) reinforced poly-ether-ketone-ketone (PEKK) thermoplastic prepreg materials are manufactured using a dry powder prepregging method. Prior to impact testing and modelling, the properties of the composites are evaluated by conducting a series of quasi-static tests, including tension, bending and in-plane shear, at room and elevated temperatures. Quasi-static mechanical testing has shown that the optimum weight fraction of PEKK, w_f, is approximately 0.4, with the properties remaining constant or dropping slightly at higher values of w_f in comparison to the optimum one. The high temperature tensile tests of GF/PEKK composites have shown that there is no obvious reduction of its tensile strength under heating up to 100 ºC. The perforation resistance of the target is also peaked at $w_f = 0.4$. As expected, the energy required to perforate the targets increases with indenter diameter. Subsequent tests show that panels impacted with partially flat indenter exhibit the highest perforation resistance among the other projectiles shapes investigated.

The perforation response of the titanium- and aluminium-based FMLs, with various stacking configurations, are also investigated under quasi-static and dynamic loading rates. Initial attention is focused on assessing the effect of the laser surface treatment on the residual strength of the titanium alloy and its bonding strength with the adhesive film. The tests show that the laser parameter of 4.54 J/cm^2 seems an optimum parameter which gives an excellent bonding strength between the titanium foils and the PEKK film. In contrast, these treatments do not show any significant drop in the residual tensile strength of the titanium alloy. However,

there is a reduction of around 35% in both tensile strength and yield strength of the aluminium alloy produced due to the processing temperature cycle.

A comparison of the quasi-static and dynamic perforation responses of the FMLs have demonstrated the rate-sensitivity of these laminates at which the perforation energy increases when the loading rates pass from the quasi-static to dynamic. After testing, the FMLs specimens are sectioned to highlight the failure modes under both test conditions. The cross-sections indicate that the impact energy on these FMLs is absorbed through (1) plastic deformation and tearing of the metals, (2) delamination between the composite plies and metal layers and (3) fibre fracture.

The finite element models using ABAQUS/Explicit have been developed to predict the response of the glass fibre reinforced PEKK composites to impact by projectiles based on different diameters and shapes. The outputs of these FE models are validated against the corresponding experimental force-displacement traces and failure modes. A good agreement between the predicted and measured results, in terms of the initial stiffness, maximum force and displacement and perforation mechanisms, is obtained.

The validated FE models are then used to predict the perforation resistance of the fibre metal laminates with various stacking configurations under low velocity impact loading. Here, prior to the onset of the damage, the fibre reinforced composites is modelled as an orthotropic elastic material with 2D Hashin's failure criteria. The titanium and aluminium alloys are modelled as isotropic elasto-plastic materials with strain hardening. Ductile and shear damage criteria are used to model the damage initiation of the metal layers. Again, the experimental results, including the load-displacement traces, perforation energies and failure modes are successfully predicted using the FE models developed. Furthermore, the validated models have been exploited to predict the perforation response of the FMLs under different loading conditions.

List of Abbreviations

Al   Aluminium

Al (2024-T3) An aluminium alloy consisted of 4.9% copper and 0.9% magnesium and
      tempered

ARALL   Aramid fibre reinforced aluminium

AS-4   Type of carbon fibre

ASM   American society for materials

ASTM   American standard test method

BMI   Bismaleimide

CAI   Compression after impact

CARALL   Carbon fibre reinforced aluminium

CCCs   Carbon-carbon composites

CF   Carbon fibre

CF/epoxy   Carbon fibre reinforced epoxy

CF/PEKK   Carbon fibre reinforced poly-ether-ketone-ketone

CFRPs   Carbon fibre reinforced plastics

CMCs   Ceramic matrix composites

CPU   Central processing unit

Cr   Chromium

DIF_{JC} Dynamic increase factor that included in Johnson-Cook model

DOC   Direct operating cost

El   Elongation

EN ISO   European standard

FAA   Federal Aviation Administration

FAR   Federal Airworthiness Regulations

FE   Finite element

FMLs	Fibre metal laminates
FRPs	Fibre reinforced plastics
GF	Glass fibre
GF/PEKK	Glass fibre reinforced poly-ether-ketone-ketone
GF/PEKK/Al	Aluminium-based fibre metal laminates
GF/PEKK/Ti	Titanium-based fibre metal laminates
GF/PP	Glass fibre reinforced polypropylene
GFRPs	Glass fibre reinforced plastics
GL	Gauge length
GLARE	Glass fibre reinforced aluminium
hcp	Hexagonal close-packed
HSC	High speed camera
HTHP	High temperature and high performance
ISO	International organization for standardization
K/E	Ketone/ether ratio
LDF	Trade name to carbon fibre reinforced poly-ether-ketone-ketone
MMCs	Metal matrix composites
NASA	National aeronautics and space admin
NF	Natural fibres
PAEK	Poly aryletherketone
PE	Polyethylene
PEEK	Poly-ether-ether-ketone
PEI	Poly-ether-imide
PEK	Poly-ether-ketone
PEKK	Poly-ether-ketone-ketone
PET	Polyethylene terephthalate
PI	Polyamides

PMCs	Polymer matrix composites
PP	Polypropylene
PPS	Polyphenylsulphone
PPS	Polyphenylene sulphone
RCBS	Rock chuck bullet swage dies
SEA	Specific energy absorption (Jm^2/kg)
SEM	Scanning electron microscopy
SLC	Structural laminates company
Sn	Tin
T/I	Terephthalic acid and isophthalic acid moieties ratio
Ti	Titanium
Ti-FMLs	Titanium-based fibre metal laminates
TP	Thermoplastic
TS	Thermosetting
UD	Unidirectional
UTS	Ultimate tensile strength
V	Vanadium
α	Alpha
β	Beta

List of Symbols

B, b	Width (mm)
C	Strain rate constant
D	Diameter of cylindrical supports (mm)
d	Damage variables
E	Modulus of elasticity (GPa)
E	Impact energy (J)
E_f^{secant}	Flexural secant modulus of elasticity (GPa)
F, P	Maximum load (N)
G	Slope of the secant of the force-deflection curve (N/mm)
G	Shear moduli (GPa)
G_{12}	In-plane shear modulus (GPa)
G_n	Work done by the traction- separation in the normal shear direction (J/m^2)
G_s	Work done by the traction- separation in the first shear direction (J/m^2)
G_t	Work done by the traction- separation in the second shear direction (J/m^2)
G_n^c	Failure fracture energy in the normal shear direction (J/m^2)
G_s^c	Failure fracture energy in the first shear direction (J/m^2)
G_t^c	Failure fracture energy in the second shear direction (J/m^2)
G_{ft}^F	Fracture energy for the fibre tension (J/m^2)
G_{fc}^F	Fracture energy for the fibre compression (J/m^2)
G_{mt}^F	Fracture energy for the matrix tension (J/m^2)
G_{mc}^F	Fracture energy for the matric compression (J/m^2)
p	Contact pressure (N/m^2)
S_T	Longitudinal shear strengths (N/m^2)
S_L	Transverse shear strengths (N/m^2)
T_g	Glass transition temperature (°C)

T_m	Melting temperature (°C)
T_R	Room temperature (°C)
T_c	Consolidation temperature (°C)
$t_n^0,$	Parameter of the interface strength in the normal shear direction (N/m²)
t_s^0	Parameter of the interface strength in the first shear direction (N/m²)
t_t^0	Parameter of the interface strength in the second shear direction (N/m²)
u^{pl}	Effective plastic displacement (m)
V_e	Impactor velocity (m/s)
W_f	Weight fraction
X_T	Tensile strengths in the longitudinal direction (N/m²)
X_C	Compressive strengths in the longitudinal direction (N/m²)
Y_T	Tensile strengths in the transverses direction (N/m²)
Y_C	Compressive strengths in the transverses direction (N/m²)
δ_{eq}^0	Initial equivalent displacement (m)
δ_{eq}^f	Displacement at which the material is damaged (m)
τ_{max}	Maximum shear stress (N/m²)
σ	Flexure strength (MPa)
σ_t	Ultimate tensile strength (MPa)
$\Delta\sigma$	Change in stress (MPa)
$\Delta\varepsilon$	Change in strain
τ_{12}	In-plane shear stress (MPa)
τ_{12}'	Shear stress at a shear strain of γ_{12}'=0.001(MPa)
τ_{12}''	Shear stress at a shear strain γ_{12}'' =0.005 (MPa)
v	Poisson's ratio
δ_i	Relative displacements (m)
$\dot{\varepsilon}^*$	Strain rate ratio

$\dot{\varepsilon}_0$	Reference quasi static strain rate (s^{-1})
$\overline{\varepsilon}^{pl}$	Equivalent plastic strain associated with the initiation of damage
$\dot{\overline{\varepsilon}}^{pl}$	Equivalent plastic strain rate (s^{-1})
ε_{eng}	Engineering strain
ε_{true}	True strain
η	Stress triaxiality
θ_s	Shear stress ratio
μ	Coefficient of friction
σ_y	Yield stress (N/m^2)
σ_{true}	True stress (N/m^2)
σ_{eng}	Engineering stress (N/m^2)
τ_{eq}	Equivalent frictional stress (N/m^2)
$\langle . \rangle$	Macaulay bracket

Table of Contents

List of Figures

XV

List of tables

1 Chapter 1: Introduction

1.1 Overview

This chapter gives an overview of the fibre reinforced composites along with their applications in aerospace. The reasons behind the need for developing a higher performance composite structures are presented, followed by the impact behaviour of the related composite structures. After that, the motivation, objectives and the scope of the thesis are discussed.

1.2 Applications of composite structures in aerospace

The aerospace industry was the first sector that realised the advantages of the composite materials. The field of commercial and military aircrafts has the main structural applications for fibre reinforced composites in which the weight reduction is critical for increased payloads and high speeds. Fibre reinforced polymers (FRPs) have found their extensive applications in civil aerospace and military aircraft since December, 1903, in North Carolina. The discovery of glass fibre (GF) in 1940's initially supported the growth of composites. However, adoption of composite materials as a major contribution to manufacture aircraft components was followed by the discovery of carbon fibre at the Royal Aircraft Establishment at Farnborough, UK, in 1964, which then later became the backbone of the aerospace industry [1].

This section presents a short overview to the applications of composite materials in aerospace industry including the commercial and military aircrafts.

1.2.1 Commercial aircrafts

Compared to conventional materials, fibre reinforced plastic (FRP) composites have been extensively used in aerospace sector due to their unique properties such as lightweight, noncorrosive, high specific stiffness and high strength. Also, FRP composites can tailor their structure to produce more aerodynamically efficient structural configurations [2, 3]. In the past decades, the FRP composites in airplanes were enlarged to manufacture secondary structures such as wing edges and control surface. In 1987, Airbus was the first commercial aircraft manufacturer to use composites in their aircraft (A310) in which the total weight of the

composites was about 10% of the aircraft weight [4]. Then, Airbus (A320), produced in 1988, was the first commercial aircraft in which all tail parts, such as tail cone, horizontal and vertical stabilisers were made only from composite materials. Another airplane (Boing 777) was introduced by Boing Company in 1995 in which the airplane tail was also manufactured from composite materials. About 10% of carbon or glass fibre reinforced composites were used for these airplanes. Recently, the fuselage and wings of the airplane were manufactured using fibre reinforced composite [4]. This can be seen in Airbus A380, introduced in 2006, which about 25 % of its total weight was made from composite materials, as shown in Figure 1-1.
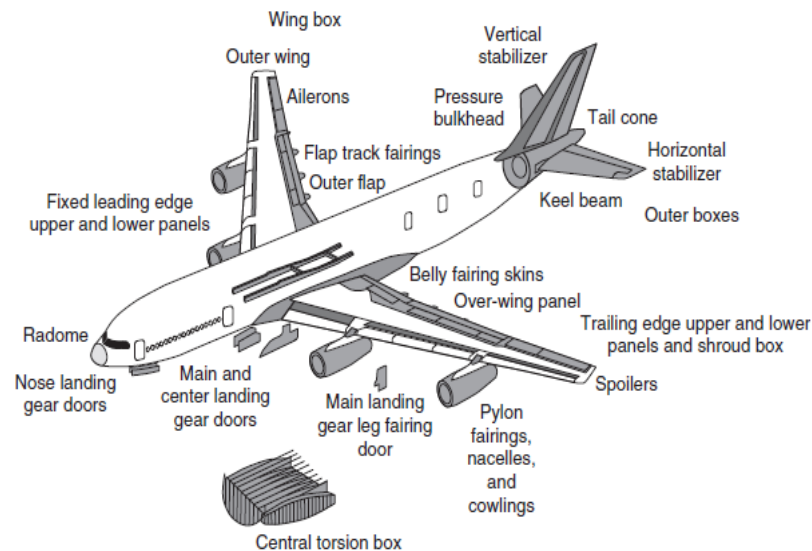
Figure 1-1. The use of composite materials in Airbus 380 [4].

In the new generation of aircrafts, such as Airbus A350XWB and Boeing 787, more than 50% of the total weight of airplanes was made with advanced composite components [5, 6], as shown in Figure 1-2.
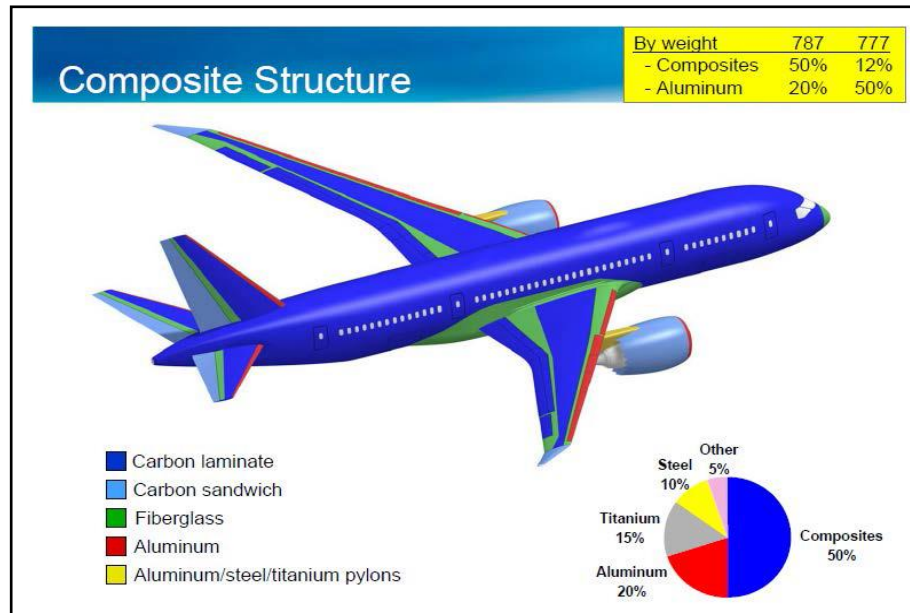
Figure 1-2. Distribution of composite material on Boing [6].

1.2.2 Military aircrafts

The materials used in military industry require to be very trustworthy, safe and strong in order to reach a satisfactory level of reliability. Due to its durability and structural integrity, fibre reinforced composites were extensively used in military applications. In F-11, F-14, F-15 and F-16 aircrafts, composite materials are used in various structural components such as vertical and horizontal stabilisers, fin boxes, flaps and wing skin. The total weight of aircraft can be reduced by around 20-35 %, if FRP composites are used as shown in Figure 1-3. The air frame of AV-8B V/STOL strike aircraft being introduced in 1982, F-22 aircraft fighter and B-2 Spirit contain about 25% by weight of composite materials. The stealth aircraft, F-35 Joint Strike Fighter, contains nearly 40 % by weight of composite structures, which uses the highest weight percentage of composites among any aircraft up to date [7].
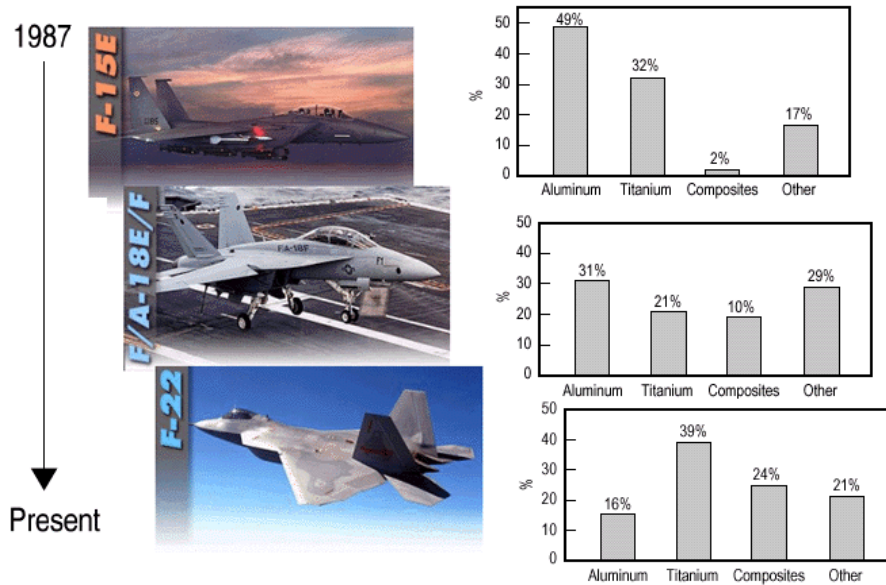
Figure 1-3. Composites used in military aircrafts [7].

1.3 High performance thermoplastic composites

The introduction of high-performance thermoplastic composites has resulted in increasing interest from the aerospace, automotive and marine industries. This can be attributed to their extraordinary merits such as light-weight characteristics, ability for integral design, fire/smoke resistance, recyclability, unlimited shelf life and superior impact properties [5, 8–11]. Moreover, thermoplastic matrices are suitable for high speed production processes such as thermoforming and allowable for the applications of novel joining techniques such as ultrasonic and induction welding. This is due to their ability to be welded in high-temperature [12]. Correspondingly, thermosetting (TS) prepregs, such as epoxy prepregs, are also used widely in automotive, construction and aerospace industries, but with a limited shelf life. Besides, they need to be stored in a freezer, typically at -18 °C [13–16] to prevent polymerisation of the resin.

In the aerospace applications, fibre metal laminates (FMLs) are used in fuselage, wing and leading edge tail structures, most of which are based on thermosetting epoxy based prepregs. Low viscosity, low fabrication temperature and good resin/fibre wettability are the major

reasons behind using epoxy-based composites. However, these kinds of prepreg do exhibit a relatively poorer hot/wet stability, higher cost of manufacturing, higher combustibility if compared with high performance thermoplastic-based composites [17–21]. Thermoplastic matrices are good alternative for advanced structural composite systems due to their substantial advantages over thermoset matrices, such as improved fracture toughness, recyclability and rapid processing due to shortened curing cycles. Thermoplastic prepregs can be stored in an ambient environment resulting in an infinite shelf-life unless they contain solvent, which may limit their shelf life [10]. Despite the advantages offered by the traditional thermoplastic matrices, their usage has been limited due to their low moduli values, poor chemical resistance, low glass transition temperature and poor thermal stability at elevated temperatures. Therefore, the development of multi-functional thermoplastic matrices based on an aromatic polymer such as PEKK has potential to address all the aforementioned limitations. High-performance thermoplastics have demonstrated exceptional impact resistance, vibration damping and thermal properties at high temperatures, especially when reinforced with high performance fibres [22, 23].

Previous work has shown that there are different procedures to combine a thermoplastic matrix with fibres to make prepregs, such as solution dip prepregging, hot melt prepregging, film calendaring, dry powders and aqueous suspension techniques. These techniques will be more detailed in Chapter 2. Differences between these methods relate to the way in which the matrix is deposited on fibres and the bonding force between the matrix and the fibre, which is responsible for adhesion at the microstructural level [24]. There are a number of advantages associated with dry powder prepregging, including a wide range of melt viscosities without the need for a solvent or hot melt problems, thus widening the potential range of available polymers [25].

1.4 Composite materials (structures) under impact loadings

As a result of their excellent specific mechanical properties, composite structures have been extensively used in aerospace applications. However, these materials are highly sensitive to localised impact loadings, particularly at low incident energies such as impact imparted by a dropping tool during maintenance and small stones thrown up from the runway. For the metallic structures, due to their ductility, a large amount of impact energy can be absorbed by plastic deformation. Here, minor cracks (dents), that caused by minor impacts, can be easily detected and it can be safely ignored. For the major cracks under higher impact levels, it can be perfectly detected by the naked eye and the repair or replacement of the damaged parts can be easily made [26].

In contrast, fibre reinforced plastics (FRPs) are brittle with a little ability to deform plastically. In FRPs, the impact energy can be absorbed in various fracture processes, which are normally matrix cracking, delamination between the plies, fibre fracture and matrix/fibre debonding [26]. Damage process of the laminated composites is very complex. The reason can be attributed to the anisotropy of the composite laminates and the random stress distribution during the impact event [27]. Depending on its severity, impact damage may lead to a loss in the compressive strength of the composite structure which may lead to a catastrophic failure. Damage of this type causes several design problems because it forms as an internal damage with no visible mark on the impacted surface [28].

Even though the dynamic response of composite laminates has been intensively investigated (as will be discussed in Chapter 2), the majority of the work is focused on epoxy-based composite structures under low incident energies.

1.5 Motivation of the research work

It is expected that the high performance composites based on PEKK as matrix material offer a great potential in aerospace and automotive applications either being used alone or integrated with alloys for FMLs. To date, little work has been undertaken to investigate the mechanical

properties of such composites under various loading conditions, as will be discussed in Chapter 2. Therefore, the aim of the current work is to develop a new material that can satisfy the requirements of the new generation of aircrafts such as damage tolerance and high service temperatures. Here, experimental investigations and finite element modelling are undertaken to characterise the response of these novel composites and the related fibre metal laminates subjected to low velocity impact loadings.

1.6 Research objectives

This research is focused in the following objectives

- To develop multi-functional high-performance thermoplastic composites based on S-glass fibre as a reinforcing material and PEKK polymer as a matrix material.

- To compare the response of these high performance composites developed with that of thermosets based epoxy laminates under quasi-static perforation tests.

- To experimentally investigate both quasi-static and impact performance of the GF/PEKK composites.

- To experimentally investigate both quasi-static and impact performance of the GF/PEKK/Ti and GF/PEKK/Al fibre metal laminates.

- To compare the response of titanium-based and aluminium-based PEKK laminates under both quasi-static and dynamic loading rates.

- To develop finite element models to assist predicting the low velocity impact response of laminates investigated, as well as to validate the FE models developed against the corresponding experimental results.

- To use the validated finite element models for further parametric studies to cover the cases which are expensive and difficult to conduct experimentally.

1.7 Scope of the thesis

The scope of this thesis is to evaluate newly developed GF/PEKK thermoplastic composites under various loading conditions. Also, it includes investigation of the perforation resistance of the GF/PEKK composites and the related fibre metal laminates experimentally and numerically. Therefore, the thesis is divided into six chapters. Each chapter is described briefly as follows:

Chapter 1 gives a general overview on the composite structures and their applications in aerospace industry. An overview of the high performance thermoplastic and the impact response of composite structures are provided. Also, it presents the major contribution and scope of this thesis.

In chapter 2, the review of previous studies related to the high performance thermoplastic composites and the related fibre metal laminates is presented. Attention is focused on the perforation response of the composite investigated under quasi-static and dynamic loading rates. The manufacturing process of high temperature GF/PEKK composites is also reviewed in this chapter.

The experimental work procedures including the material fabrication, test setup and the instrumentation used for both quasi-static and dynamic perforation tests as well as material testing, in addition to those used for high temperature tests is presented in chapter 3.

The experimental results obtained under the aforementioned loading regimes are then presented and discussed in Chapter 4. This includes the influence of fibre coating and PEKK resin proportions on the mechanical properties, the effect of the target thickness on the static

and dynamic response of the GF/PEKK composites and fibre metal laminates. Also, it includes investigating the influence of projectile configurations on the GF/PEKK laminates.

Chapter 5 presents the developed finite element (FE) models of the composite materials investigated, including implementation of material properties, specimen geometry, boundary and loading conditions, contact properties, constitutive models and damage criteria. Mesh sensitivity study is also carried out. The FE models are then rigorously validated against the experiments. After that, the parametric studies are presented based on the validated FE models to investigate the effect of the selected parameters.

Chapter 6 presents conclusions drawn from the experimental and FE results in addition to the recommendations for future works.

2 Chapter 2: Literature Review

2.1 Introduction

An overview of the early and recent publications in the relevant research development on composite laminates, focused on the plain composites and fibre metal laminates (FMLs) is presented in this chapter. Firstly, the definition and historical background of composite structures related to the project (i.e. plain composite and FMLs) are reviewed. Subsequently, a review of manufacturing processes of thermoplastic composites used in aerospace applications is given. The constituent materials used to manufacture the fibre metal laminates are given. Finally, experimental and numerical work on dynamic response and perforation resistance on those composite structures under low velocity impact loading are reviewed.

2.2 Composite materials

2.2.1 Overview

In engineering applications, various metals, ceramics and polymers have been successfully combined by scientists and engineers to develop a new generation of materials with excellent mechanical properties, which are called composite materials. Wood is an example of natural composite materials in which fibres of cellulose are embedded in a matrix of natural glue, called lignin. Moreover, ancient people (in India, Greece and other countries) used a mixture of clay with husks or straws to build their houses for several hundred years [29].

Recently, there is a rapid growth in the development of composite materials, including novel manufacturing processes and new designs. Composite materials offer a unique set of properties which can be tailored to fulfil the application requirements. Composite materials can be easily combined with other materials with good adaptability under various specific conditions. Therefore, these materials are one of the most widely used materials in the modern engineering applications. Many conventional materials such as metals, ceramics, polymers and woods have been replaced by composite materials due to their advantages, i.e. specific strength (strength-to-weight ratio), specific stiffness (stiffness-to-weight ratio), long fatigue life, excellent

corrosion resistance, wear resistance, good thermal and electrical insulator and environmental stability. Nowadays, the applications of composite materials have become very common in our lives not only in the aerospace industry, but also in construction, transportation, sport and marine industries [29].

2.2.2 Definition and classification of composite materials

Composite materials are a combination of two or more constituents at a macroscopic level to form a new generation of materials with better combined material properties from its individual constituents. The constituents retain their properties and do not dissolve or merge completely into each other. During processing, the relative arrangement of the phase relative to each other can be controlled so that it can be tailored to the desired properties.

Composite materials consist of two phases, i.e. the reinforcing phase which is known for high strength and stiffness properties, and matrix phase in which the reinforcing phase is embedded into, as shown in Figure 2-1. The roles of the matrix phase are to transfer the applied load on the composites to the reinforcement uniformly and to protect it from harsh environmental conditions. The matrix materials are generally continuous, whilst the reinforcing phase could be in the form of particles, flakes or fibres. Bone is an excellent example of a natural composite material in which calcium and phosphate ions reinforce the soft collagen [29].

In many technologies that are related to aerospace, underwater and transportation applications, conventional engineering materials such as metals, polymers and ceramics cannot meet the requirements for these applications. However, the properties of composite materials can be tailored for different properties by choosing suitable constituents, percentages, structure, distribution, composition and the interface between the constituents. Composite materials can be named based on the reinforcing and matrix materials. According to the type of the reinforcement, there are particle reinforced composite, fibre reinforced composites and structural reinforced composites. Based on the matrix materials, composite materials can be grouped as metal matrix composites (MMCs), ceramic matrix composites (CMCs), polymer

matrix composites (PMCs) and carbon-carbon composites (CCCs). The types of composite

materials are shown in Figure 2-2 [30–33].
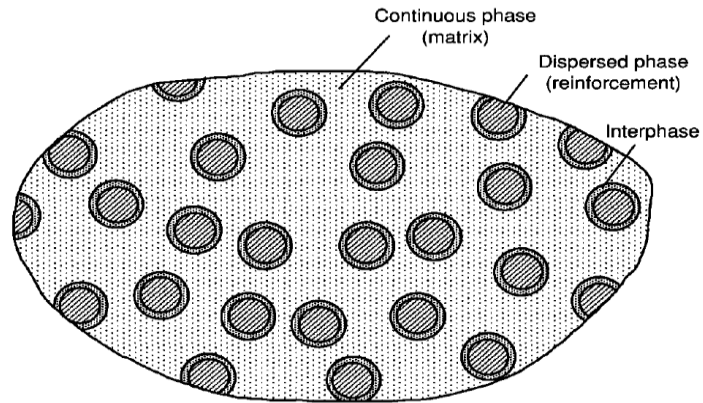
Figure 2-1. Composite material phases [29].
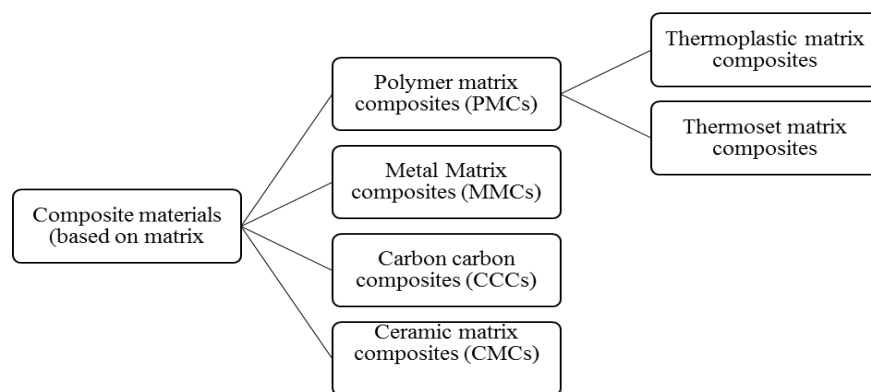
(a)
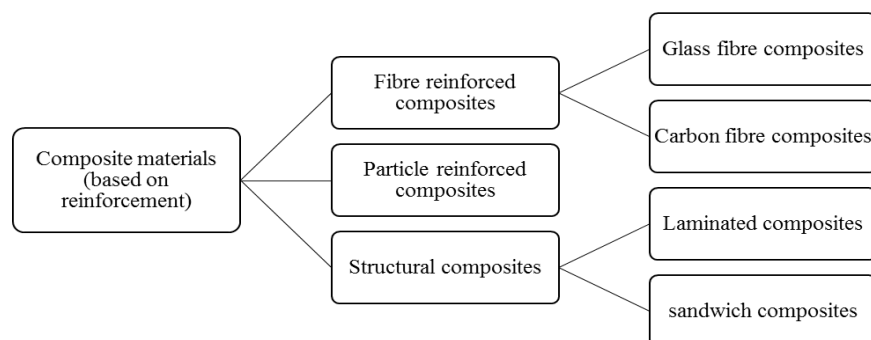
(b)

Figure 2-2. Composite types: (a) based on their matrix (b) based on their

reinforcement.

14

PMCs are the most well developed composites in which polymers are reinforced with thin fibres, i.e. glass, carbon, aramids and boron. Among composite materials, PMCs have found their applications in the construction of different engineering structures due to their low cost, high strength and ease of manufacturing. Glass fibre reinforced plastics (GFRPs) and carbon fibre reinforced plastics (CFRPs) are considered as primary fibre reinforced composites which are used extensively in industrial applications. However, low service temperature, poor moisture resistance, and high coefficients of thermal expansion are the main disadvantages of these composites [34].

In MMCs, the reinforcing fibres, i.e. silicon carbides are embedded in a metal matrix such as aluminium. MMCs are widely used in automotive industries. The advantages of MMCs over PMCs are high service temperature up to 1200 °C, high resistance to fluid degradation, and resistance to fire. However, the manufacturing processes of MMCs are more difficult and more expensive compared to those of PMCs, resulting in their limited use for industrial applications.

CMCs consist of fibres such as boron nitride and ceramic material as a matrix. CMCs are very expensive materials due to the requirements for their manufacture, such as very high fabrication temperature and special fabrication techniques [35].

Carbon Carbon Composites (CCCs) are the most promising and advanced materials in which the matrix and reinforcement phases are carbon. These composites can be used successfully for high-temperature applications due to their high tensile moduli and high tensile strength at temperatures in excess of 2000 °C. Moreover, these composites offer a good creep resistance associated with good fracture toughness. However, these composites are relatively new and very expensive with limited utilisation in industry [30, 36, 37].

2.2.3 Advantages and disadvantages of PMCs

The constituents of the composite materials give many functions to achieve useful advantages as shown below [38]:

- Excellent performance for a given weight, leading to substantial fuel savings.

- Good impact and fatigue resistance.

- It shows good strength/stiffness to weight ratio (specific strength/modulus).

- It can be tailored to fulfil the required properties in various applications.

- It is easy to manufacture. Also, complex parts with good and smooth finish can be obtained in the fabrication process.

- The production cost is relatively low as well as the maintenance cost.

- Composite materials have shown excellent resistance to corrosion, chemical attack, and harsh environmental conditions.

Although there are outstanding features offered by using PMCs, several drawbacks can be identified, e.g.

- Special equipment is required for hot curing.

- Fabrication defects such as voids and inclusions.

- Toxic fumes and smoke generation at high temperature, especially for epoxy-based composites.

- Materials such as thermoset composites require refrigerated storage with limited shelf life.

2.3 Fibre reinforced plastics (FRPs)

Fibre reinforced plastics are made by embedding or bonding high strength and high modulus fibres into a matrix resin with distinct boundaries (interface) between them. Although the two phases are combined together to produce a combination of properties which cannot be met by

their individual constituents, both phases retain their physical and chemical properties. In FRPs, the high modulus fibres are the principal load-carrying phase, whereas the surrounding phase (matrix) works to hold the fibres in their desired orientation and locations and protects them against the environmental changes, i.e. humidity and elevated temperatures. Furthermore, the matrix materials work as a medium to transfer the applied load to the fibres.

Commercially, glass, carbon and kevlar are the principal fibres used in FRPs, while other fibres such as aluminium oxide, boron and silicon carbide have found limited applications. Here, the fibres can be mixed with matrix either in short lengths (discontinuous) or long lengths (continuous). The manufacturing of fibre reinforced composites starts with the form of lamina which is made by the incorporation of a larger number of fibres into a thin layer of matrix. The thickness of the lamina is usually between 0.1 to 1 mm. If long fibres are used to make the lamina, they can be arranged in unidirectional, bi-directional or multidirectional orientations, as shown in Figure 2-3. A wide range of physical and mechanical properties of the composite laminates can be generated by controlling the fibre orientation of the layers and the staking sequences of various layers [29]. FRPs offer a unique combination of strength and modulus when compared with traditional metallic materials. FRPs are superior to the metallic components due to their low density and specific properties, i.e. strength to weight ratio and modulus to weight ratio.

(a) Unidirectional continuous fibers

(b) Bidirectional continuous fibers

(c) Multidirectional continuous fibers

(d) Unidirectional discontinuous fibers

(e) Random discontinuous fibers

Laminate
(consolidated stack of many layers)
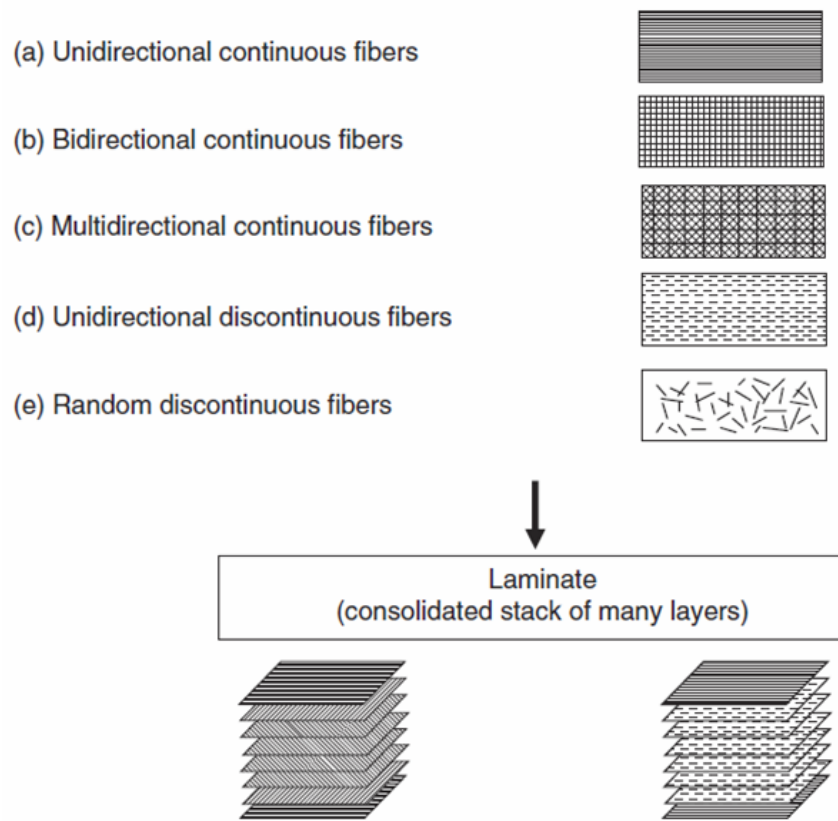
Figure 2-3. Basic stacking configurations in the fibre reinforced composites [4].

2.3.1 Thermoplastic and thermoset composites

The used of high performance composites made with thermoplastics (TP) as matrix materials in conjunction with glass fibre (GF), carbon fibre (CF) and natural fibres (NF) have increasingly found their uses in the aerospace, automotive and marine applications due to their properties such as light-weight construction potential, integral design, fire/smoke resistance, recyclability, unlimited shelf life and good impact properties [5, 8–11]. Moreover, thermoplastic matrices have a good ability to be welded at high temperatures thus, making them suitable for high-speed production such as thermoform [12].

These advanced materials were introduced in the form of prepregs (pre-impregnated fibre or fabric in a flat form). Prepregs have been used extensively due to their low cost, ease of processing, consistent quality and high volume capability. Carbon fibre, glass fibre and aramid fibre are the main reinforcement for prepregs, and these fibres are produced in the form of

bundle of individual fibre filaments. If the reinforcement is carbon, tow term can be used instead of bundles, and strands, roving or yarn are referred to glass and aramid fibres [13]. In late 1960s, the first prepreg machine was developed to support the production of carbon fibre tape for manufacturing the composite structures on a U.S. National Aeronautics and Space Admin (NASA) Lunar Lander to address the under developed and un-reliable composite processing techniques [39].

The mechanical properties of prepregs over a wide range of temperatures are better than those from wet layups, as the resin is applied in uniform and exact quantities and an optimum fibre/resin ratio is attained. In addition, prepregs reduce the health and safety risk associated with handling resin [14]. Based on the resin type, prepregs can be grouped into two main categories; thermosetting (TS) and thermoplastic (TP) prepregs. The significant difference between the thermoplastic and thermosetting matrices is their discrete chemical character.

Thermosetting (TS) are cross-linking polymers which are used in a wide variety of applications such as automotive, construction and aerospace industries due to their superior tensile, shear and compressive strengths. Also, due to the convenience of manufacturing processes (i.e. by hand lay-up technique) of the epoxy resin, thermosetting composites became established as excellent prototyping materials and therefore translated into full-scale production. However, three problems existed in the epoxy-based composites structures: sensitivity to water, brittleness and slow manufacturing process. Although attempts to improve the toughness and the water resistance were introduced to such thermosetting composites, it showed that an improvement in one property usually led to reduction of other properties Thermosetting (TS) prepregs need curing to consolidate and it has a limited shelf life due to their cross-linking degree in B-stage. These materials have to be kept in freezers at around -18 °C to prevent the cross-linking polymerisation reaction from taking place at ambient temperatures, and it cannot be re-moulded. Epoxies are the most commonly thermosetting polymers used for manufacturing high-performance composites due to their strength, durability and relatively low cost however; other thermosetting resins are also made into

prepregs depending on the application including bismaleimide (BMI) and phenolic resins [13, 15, 16, 40].

Thermoplastics are characterised by linear polymer chains thus, difficult to process due to their high viscosity, essentially need solvents, no curing, and can be stored at room temperature with infinite shelf life, however, the presence of a solvent in the prepregs may have adverse effects on the shelf life. More importantly, thermoplastics have a short processing cycle and can be re-moulded, and thus create a possibility for repair. The most commonly used thermoplastic resins include polypropylene (PP), Polyethylene terephthalate (PET), polyethylene (PE), polyphenylsulphone (PPS) and poly-ether-ether-ketone (PEEK) [41, 42]. Thermoplastics matrix can be combined with fibres to manufacture prepregs through a variety of processes. These processes can be divided into hot melts, film stacking, dry powders and solutions techniques. Each process has its requirements and process variables which affect the quality of the finished product.

2.3.2 Classification of thermoplastic polymers

According to their morphology, thermoplastic polymers can be grouped into two categories, i.e. amorphous and semi-crystalline. The amorphous polymers were considered as the first matrices for the structural composites, i.e. amorphous polysulphone family. The chains of the amorphous polymers are distributed randomly without any high degree of local order, as shown in Figure 2-4a. Due to their random structures, these polymers can be dissolved easily in a range of industrial solvents. Thus, it can be manufactured by conventional process techniques such as hot solutions technique. However, these composites are very sensitive to such solvents in service. Moreover, removing the solvent after prepregging is too difficult which has an effect on the residual strength of the composite structures such as reducing the glass transition temperature (T_g) of the polymer, defects in the composite moulding and environmental concerns. Although the drawbacks mentioned can be eliminated by melting the resins, these manufacturing techniques are difficult to operate [40].

The crystalline term of polymers always involves partially crystalline, and in some cases, the crystallinity degree may vary between 65 – 90 %. Semi-crystalline thermoplastics consist of crystalline and amorphous morphologies in their volume in which polymeric chains can order themselves (Figure 2.4b). The proportional percentages of these morphologies depend on the polymer type. Some of the polymeric chains of the semi-crystalline thermoplastics show a good ability to form three-dimensionally ordered arrays, creating a physical linkage with the neighbouring chains to form a crystalline structure. In contrast, the molecules of the amorphous polymers are unable to pack and form an ordered crystalline structures. The advantages of these kinds of polymers are that it can be formed into various shapes, i.e. powders, films and filaments which can be combined with reinforcing fibres to form unidirectional tapes, towpregs and woven prepregs. Examples of the semi-crystalline thermoplastic polymers are ploy-ether-ether-ketone (PEEK), poly-ether-ketone-ketone (PEKK), poly-ether-ketone (PEK), polyamides (PI) and polyphenylene sulphide [10, 43].

a   b
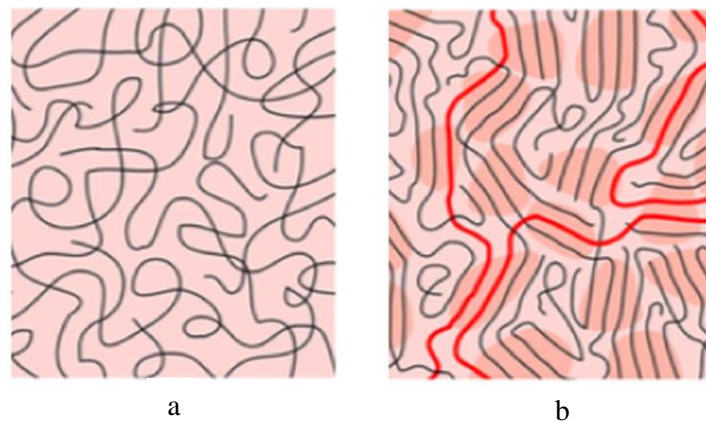
Figure 2-4. Chemical structures of amorphous (a) and semi-crystalline (b) thermoplastics [44].

2.3.3 Glass transition temperature (T_g)

At high-temperatures, the performance of high-performance thermoplastic composites depends on the Tg and thermal properties of the resin matrices. Tg is a temperature at which amorphous polymer or amorphous part of semi-crystalline polymer change from rigid to rubbery states. Figure 2-5 shows the elastic modulus values as a function of the temperature

of the amorphous, semi-crystalline and thermosets polymers. It can be seen that the Young's modulus values for various polymeric materials decrease with an increase in temperature. The chains of the amorphous polymers are arranged randomly below the glass transition temperature (T_g). Here, Young's modulus values change slowly with temperature (region one). Once the applied temperature reaches to the T_g values, a sharp decrease in the modulus values are obtained (region two). Thereafter, these polymeric materials show a more substantial plastic deformation until the melting point (T_m) is reached. There is no obvious melting point for the amorphous thermoplastics as melting is associated with the crystal structure. With respect to the cross-linked thermosets, there is also a significant reduction in the modulus values at T_g point. However, due to the cross-linked network in the rubbery stage, there is a plateau in the modulus values. In the case of semi-crystalline polymers (dashed line), semi-crystalline resins exhibit both glass transition (T_g) and melting point (T_m) temperatures. In semi-crystalline polymers, the melting point is attributed to the melting of the crystalline domain, whereas the glass transition is caused by the change in the modulus values in the amorphous region. The reduction in modulus values between region one and region two depends on the degree of crystallinity, i.e. higher crystallinity leads to higher plateau modulus which is caused by the higher crystalline domain contribution. Between the temperatures of T_g and T_m, these polymers involve a rigid crystalline domain embedded in a soft amorphous matrix, which results flexible polymers. When full crystallinity is obtained, the polymers will only have melting point and the effect of T_g can be eliminated. However, the extensive crystallization leads to a reduction in the ductility of the polymers. Although, the mechanical properties of the semi-crystalline polymers are significantly decreased, they retain a portion of their load-bearing properties [10, 45, 46].
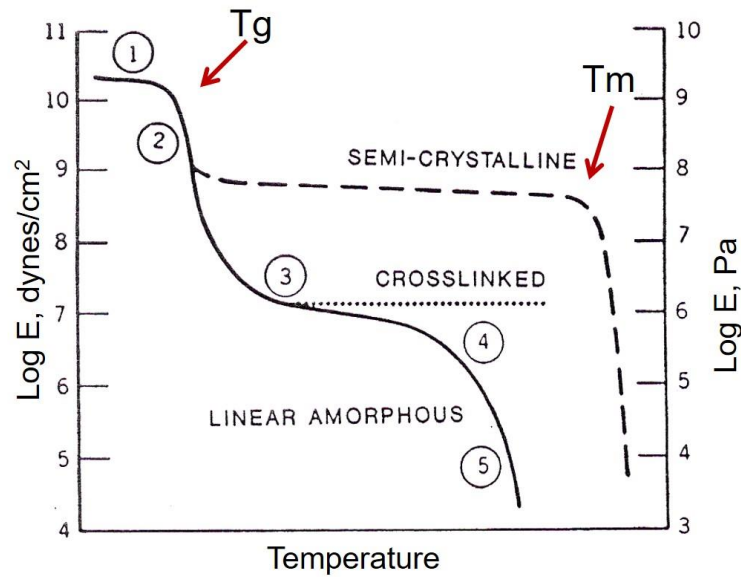
Figure 2-5. Variation of the modulus values with temperature for various morphologies [46].

2.4 High-temperature thermoplastic polymers

Thermoplastic matrices present a promising opportunity for the automotive sector and have a potential to bridge between the lightweight and re-processable high strength composite materials in mass production [47]. However, many challenges still remain in these materials that need to be solved to utilise their potential. Compared to metallic materials, traditional thermoplastic polymers show high sensitivity to temperature with very low softening due to the intrinsic flexibility of their molecular chains. For example, the softening point of many polymers, i.e. poly (vinyl chloride), polystyrene and polyethylene, is about 100 ℃. Thus, due to their low thermal resistance, these polymers are greatly restricted from some of their potential applications, i.e. electrical and transport sectors. Although the specific properties (i.e. strength and stiffness) of fibre reinforced polymers such as strength due to their low density has encouraged the use of these polymers in transport applications, high-temperature resistance is in demand, especially in the aerospace industry [48]. Despite the several advantages offered by the traditional thermoplastic matrices, their usage has also been limited due to their low moduli, poor chemical resistance, low glass transition temperature and low thermal stability at elevated temperatures [22]. Thus, the rigidity of these polymers can be

obtained by restricting the movement of the aliphatic carbon–carbon backbone by introducing side groups or crystallinity.

The development of multi-functional thermoplastic composites based on aromatic polymers such as poly (aryletherketone) (PAEK) can address these aforementioned limitations. PAEK is a family of high-performance thermoplastic copolymers in which the resulting polymers differ according to the ratio of ketone-ether linkages within the structure. In the past two decades, these polymers have received considerable attention as high-performance thermoplastic materials [49]. PAEK polymers are usually semi-crystalline and have found many applications in aerospace due to their unique properties, i.e. high glass transitions, stiffness, strength, toughness, flame retardancy, infinite shelf life, recyclability, weldability, good properties at high temperature, good impact properties, high oxidation and chemical resistance [49, 50]. As the ketone/ether (K/E) ratio increased, the glass transition temperature (T_g) and the melting point (T_m) increase.

As high-temperature and high-performance thermoplastics, PEEK and PEKK [51, 52], are considered to be the most favourable matrices in the aerospace industry to satisfy the need of light-weight, low-cost primary load bearing structures and high-temperature FMLs [43, 53, 54]. PEEK and PEKK polymers have also demonstrated exceptional impact resistance, vibration damping and thermal properties at high temperatures, especially when reinforced with high-performance fibres [23].

Although PEEKs are the most recent polymers investigated in the last decades [55–58] due to their high-temperature performance and excellent resistance against oxidation and chemicals, they have a high melting temperature which makes their manufacturing processes difficult [59]. PEKK is the latest product of PAEK family, and it receives a great interest as an alternative polymer to PEEK [60]. PEKK has a semi-crystalline aromatic structure and exhibits a low melt viscosity, excellent thermal stability, low moisture absorption, high toughness, high tensile modulus, good chemical resistance and good flammability resistance.

PEKK offers a wide range of processing techniques and thermo-mechanical properties which significantly increases the applications for these high-performance polymers. PEKK is expected to become a competitive option for aerospace applications because it is cheaper than PEEK by more than 60% with a higher glass transition temperature (T_g) of 165 ℃ compared to 145 ℃ for PEEK [10]. Table 2-1 shows the mechanical and physical properties of PEKK and other advanced thermoplastic polymers. Moreover, the processing temperature of PEKK is lower than PEEK which facilitates good handling during the manufacturing. In industrial applications, lowering the processing temperature is an important point not only to facilitate the composites manufacturing but also to avoid materials degradation [60].

The higher values of T_g and T_m of PEKK is due to the high content of ketone linkages which are more rigid than ether groups. PEKK copolymer is prepared in different formulations with individually unique properties. These formulations can be represented by the ratio of terephthalic acid (T) and isophthalic acid (I) moieties used during the synthesis of this copolymer. One of the principal advantages of PEKK over PEEK is that the polymer properties, glass transition temperature (T_g), melting point (T_m) and the crystallization kinetics can be modulated by changing the T/I ratio. For example, the melting point of the PEKK can be lowered by incorporation I moiety into its crystals as well as the crystallization kinetics can be significantly changed without a reduction in the T_g point and the end use temperature [61].

Table 2-1. The properties of PEKK and other high-performance thermoplastic resins [10].

Property	unit	PEI	PPS	PEEK	PEKK
Density	kg/m^3	1270	1330	1320	1290
Tensile strength	MPa	105	90	100	90
Tensile Modulus	GPa	3.0	3.8	3.5	3.4
Elongation at Failure	%	60	3	60	80
Flexural Modulus	GPa	3.3	3.8	4.0	3.3
Flexural Strength	MPa	152	96	170	138
Notched Izod Impact Strength	J/m	53	16	60	48

2.5 Fibres

There are two types of fibre forms mainly employed in the aerospace applications, they are fabrics and unidirectional tapes (UD). In UD tapes, untwisted filament rovings are laid parallel to each other before prepregging with the polymers [43]. UD tapes offer an optimum reinforcement efficiency in the direction of the fibre arrangement. Thus, these UD tapes are mostly used when highly loaded structures are required. With respect to the woven fabrics, there are two forms of fabrics, i.e. woven and non-woven. The woven fabrics are two-dimensional products which are usually provided as 0° and 90° constructions, as shown in Figure 2-6. Woven fabrics are made from traditional textile weaving process in which the warp yarns and the weft can be interlaced in a variety of weave patterns to form a stable fabric [43]. These types of fabrics are not only characterised by the weaving patterns but also with the weaving density (i.e. the number of yarns per unit length). Although the yarn arrangement in a woven fabric is never perfectly straight, they have good handling characteristics due to the locking of the roving at the cross-overs [43].

For a given impact energy, woven based composites exhibit high impact properties than those manufactured with unidirectional fibres [62]. This is because the weave prohibits the propagation of the damage between the layers. Moreover, woven based composites offer good handling and high fracture toughness compared to those offered by unidirectional fibres. The fibre packing density and structural integrity of the woven composites depend on the architecture and orientation of fibres in the composites [62]. Glass fibres are the most common fibres used to reinforce polymer matrix composites. The glass fibre reinforced composite structures have found their use in the aerospace industry due to their low cost, high impact properties, heat resistance, high tensile strength, insensitivity to moisture and good resistance to chemicals. Table 2-2 shows the types of glass fibres used for structural reinforcements such as A-, C-, E-, D-, R- and S- glass fibres [4].
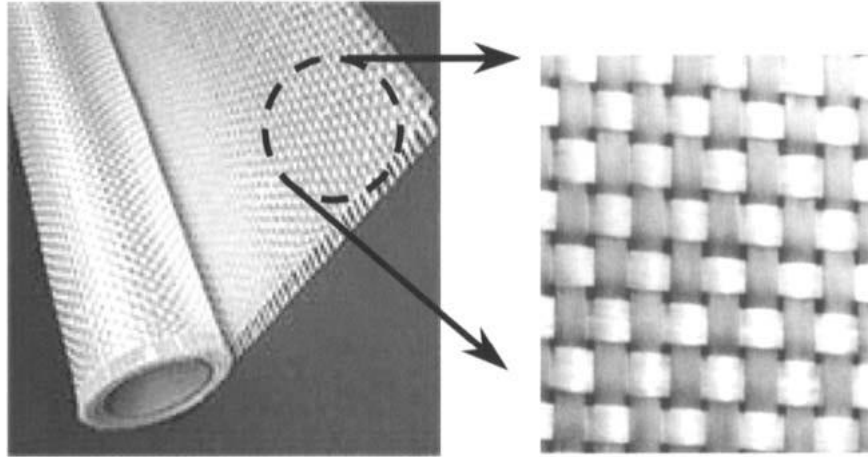
Figure 2-6.Typical woven glass cloth [63].

Table 2-2. Properties of glass fibres [4].

Fibre type	Properties
S-glass	High strength, high modulus, stability at high temperature and in corrosive environments.
E-glass	Good strength and high electrical resistivity
R glass	Good strength and high chemical corrosion resistance
D glass	Low dielectric constant
C-glass	High corrosion resistance
A glass	High strength and electrical resistivity properties

Glass fibres types S and E are the most common glass fibres employed in industry. The differences between these two glass fibres in terms of chemical compositions are shown in Table 2-3. E-glass is the most common fibres that are used extensively in commercial composite products when the high strength for the filament is not required. In contrast, S-glass fibres were developed to be used when the high strength properties are required (i.e. aerospace industry). Although S-glass fibres are more expensive than E-glass, they have a 40% tensile strength higher than that of E-glass fibre [64]. The performance level of the S-glass fibres lies between those of E-glass and carbon fibres, as shown in Figure 2-7.

Table 2-3. Chemical compositions of E-glass and S-glass fibres [64].

	Weight %	
Materials	E-Glass	S-glass
Silicon oxide	54.3	64.20
Aluminium oxide	15.2	24.80
Ferrous oxide	-	0.21
Calcium oxide	17.2	0.01
Magnesium oxide	4.7	10.27
Sodium oxide	0.6	0.27
Boron oxide	8.0	0.01
Barium oxide	-	0.20
Miscellaneous	-	0.03
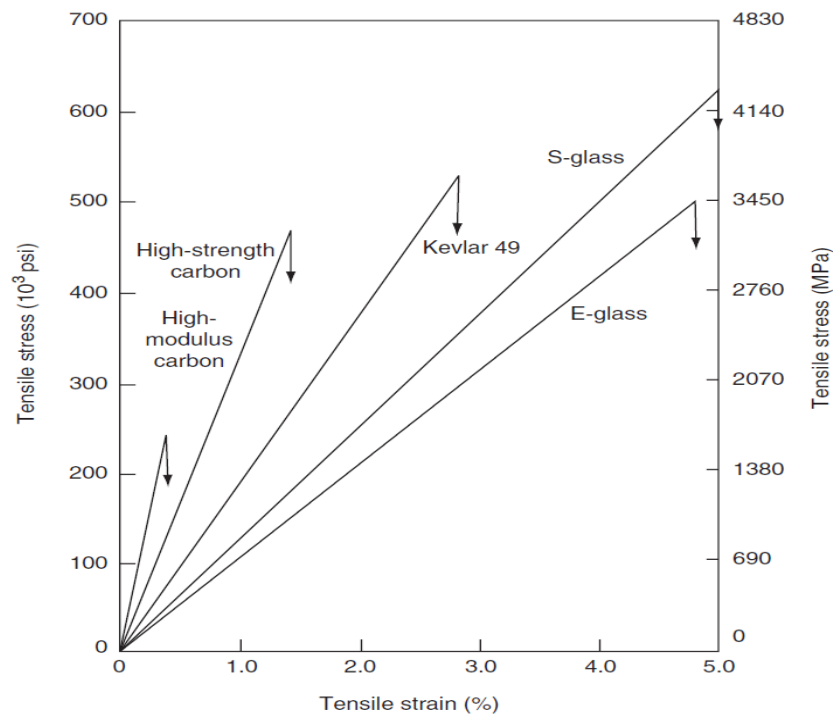
Figure 2-7. Schematic of tensile stress-strain curves for different reinforcing fibres [4].

2.6 Manufacturing processes of advanced thermoplastic composites

The manufacturing processes of thermoplastic composite materials are based on the incorporation of fibres into thin layers of resin to make prepregs (ply). The thickness of these prepregs ranges between 0.1 to 1 mm thick. As a result of their high melt viscosity and processing temperature, the impregnation of the thermoplastic matrices is crucial, as this can result in poor mechanical properties of the composite. Thermoplastic matrices can be combined with fibres to manufacture prepregs through a variety of processes, which can be broadly divided as pre-impregnation and post-impregnation methods. The fibres are wetted and impregnated in one step in the pre-impregnation stage. Melt or solution impregnation processes are then used to make the prepregs. Subsequently, the prepreg layers are stacked together and consolidated under the application of heat and pressure at the same time. In the post-impregnation technique, the resins are in the form of films, filaments and powder in which the impregnation occurs during the part manufacturing. Figure 2-8 shows the various ways used to wet the fibres with the thermoplastic resins [24].
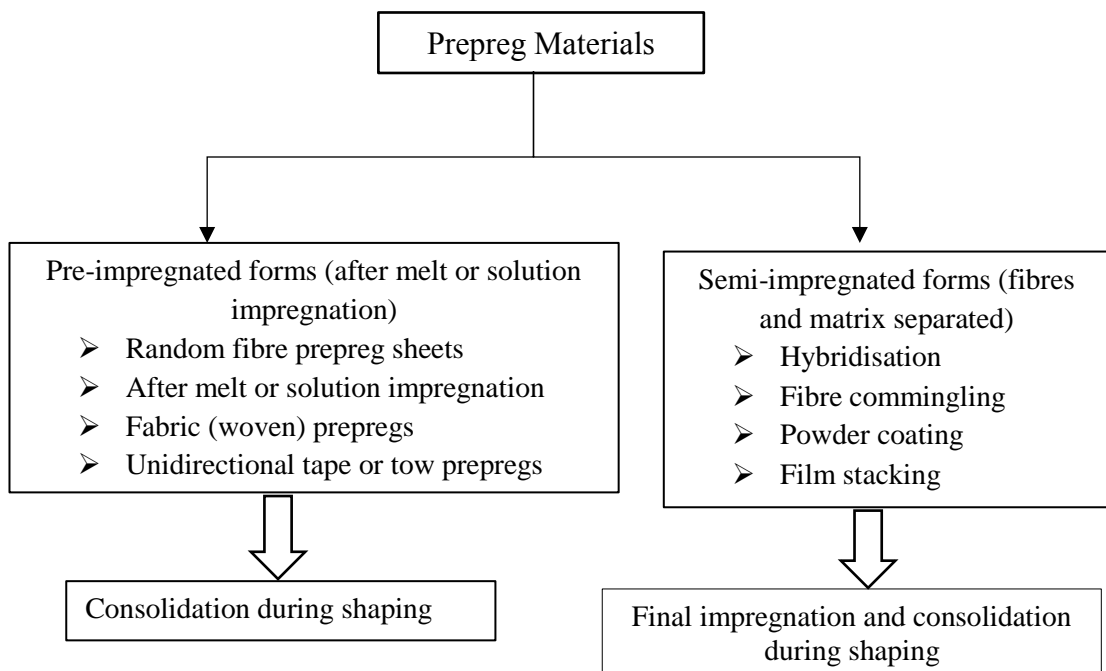
Figure 2-8. Typical impregnation methods of thermoplastic composites [24].

 The common processes used to combine the resins with reinforcing fibres can be categorised as (1) solution dip prepregging [65], (2) hot melt prepregging [66, 67], (3) film stacking [67] and (4) dry powders prepregging [68, 69]. Each process has its requirements and process variables that affect the quality of the finished product.

In the solution dip prepregging [65], which is mainly used with amorphous thermoplastic polymers, polymers in solution form are used to reduce the viscosity enough to allow the impregnation of these resins and thus improve the wettability of the fibres. Here, the solution is obtained by dissolving thermoplastic resin with organic solvents which are toxic with high boiling points. In this process, the fibres pass through a bath of a polymer solution. The bath contains a set of nip rollers which control the degree of solution uptake. After passing the resin bath, the reinforcement with the attached resin passes through a unit of solvent evaporation to remove the solvents from the resin, as shown in Figure 2-9. Although high-pressure facilities are not required in this technique, it is proved too difficult to remove the residual solvents used to dissolve the polymers, and their retention has a significant effect of the residual strength of such materials, particularly at a high temperature [65, 68].
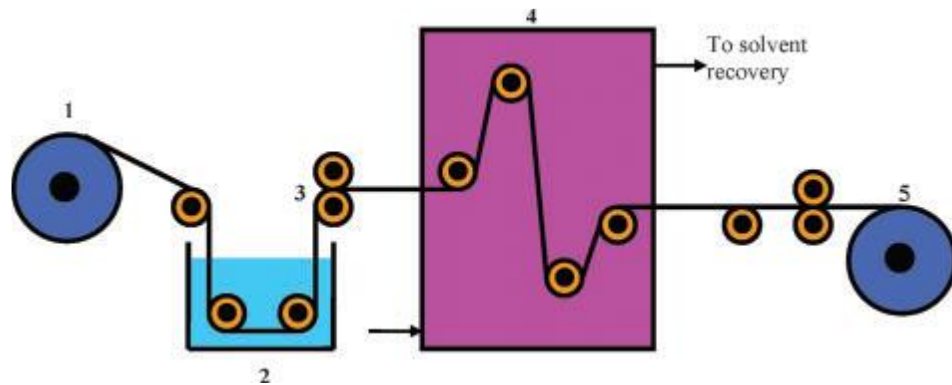
Figure 2-9. Schematic of solution impregnation process: fibre supply (1); resin bath (2); calendaring rollers (3); evaporation unit (4) and batch collection (5) [24].

In the hot melt methods, the fibre bundles usually referred to as roving are impregnated with molten polymer. Two different methods have been used, i.e. bath of molten resin fitted with impregnation pins and a cross heat extruder in combination with a die of a suitable cross-section. Once a molten thermoplastic polymer is provided to a melt pool by the extruder, the

30

fibre bundle is pulled into the molten over a set of spreader pins [66]. High melt viscosities are the main problem of the hot melt impregnation which leads to fibre distortion and breakage [68]. High-performance thermoplastics with high glass transition temperature have a possibility of thermal degradation and therefore may not be easy to process.

The film stacking is a standard technique for producing thermoplastic laminates, in which different plies of fibres are stacked between films of thermoplastic polymer under heat and pressure [67]. The pressure needs to be sufficient to force the polymeric melt to flow into the fibres. Although the difficulty of forcing a highly viscous resin through the gaps between fibres that are normally in micron is overcome by applying pressure, this also forces the fibres together, packing them in such a way as to make infiltration by the resin more difficult [40, 67]. The difference between these above approaches is the matrix particle deposition on the fibres and the bonding force between particle and fibre, which are responsible for their adhesion [24]. Several advantages can be obtained using the dry powder prepregging including a wide range of high melt viscosities used with the elimination of the solvent removal or hot melt problems, thus providing an increase in polymer selection [25]. The dry powder prepregging process involves the impregnation of the reinforcing fibres with microparticles of the thermoplastic polymers, as shown in Figure 2-10.
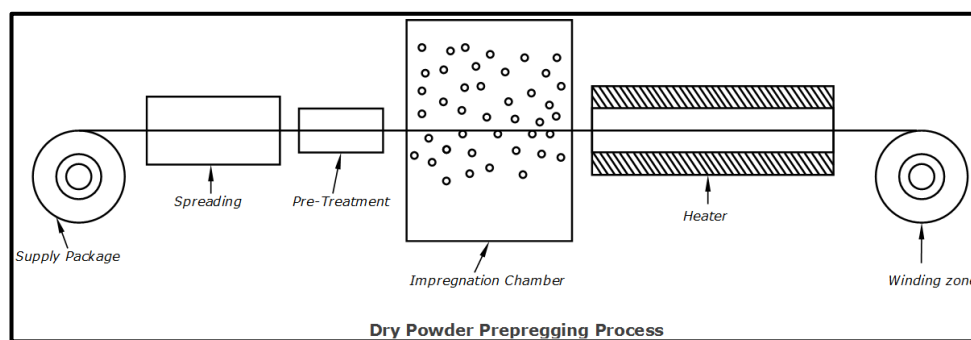
Figure 2-10. Schematic of dry powder prepregging process [70].

Price [71] carried out some pioneer work on the incorporation of thermoplastic powder into fibre tow. The fibres were separated to its individual filament before passing through a bed of powdered thermoplastic materials. Here, the resin powders got attached to the roving due to

electrostatic charges. Subsequently, fibres tow with attached powder was heated to sinter the dry powder prior to consolidation unit. A similar approach was used by Chand et al. [72] and Muzzy et al. [73]. The authors found that the impregnation quality can be improved by the reprocessing without losing residual properties. Edie et al. [74] conducted the same approach, but they used rapid heating to fuse the powders onto the fibres. In previous research reported, the optimum particle size of resin powder was found to be greater than 20 microns. Ogden et al. [75] discussed a different process towards the dry powdered impregnation, in which the reinforcing fibres are pre-wetted with a fine water mist using an ultrasonic humidifier before deposing into a dry powder.

A review of the literature indicates that there is a number of advantages associated with dry powder prepregging, including a wide range of melt viscosities without the need for solvent or hot melt problems, thus widening the potential range of available polymers. High-temperature thermoplastics, such as PEEK and PEKK [51, 52], are considered to be amongst the most suitable matrix systems for use in the aerospace industry, satisfying the need for light-weight, low-cost primary load-bearing structures and high-temperature FMLs [43, 53, 54]. Extensive work has been carried out on PEEK-based composites [55, 57, 58, 76, 77]. However, as mentioned before, PEKK is 60% cheaper than PEEK, with a higher glass transition temperature (T_g) of 165 °C compared to 145 °C for PEEK. Moreover, the processing temperature of PEKK is lower than that of PEEK, thereby simplifying the manufacturing process.

Based on the literature review, up to date few researchers have studied the behaviour of PEKK-based composites under various loading conditions [78–80]. The influence of accelerated ageing on the compression strength and interlaminar shear strength of carbon fibre reinforced PEKK composites has been investigated by Mazur et al. [77]. In this study, laminates were manufactured using hand lay-up and hot compression moulding techniques. The authors showed that hot compression is a suitable technique for producing thermoplastic composites. Bucher and Hinkley [81] also studied the flexural strength of PEKK reinforced composites

based on different types of unidirectional carbon fibres (examples include AS-4, IM-7 and G30-500). The unidirectional towpreg was manufactured using a dry powder prepregging technique using a continuous powder prepregging line. The results showed that composites based on carbon fibre reinforced PEKK prepregs behave differently with different carbon fibre types. Sun et al. [82] investigated the elasto-plastic behaviour of PEKK reinforced composites with discontinuous (LDF) and continuous carbon fibres (AS-4).

It can be seen from the previous work that some studies were conducted to develop CF/PEKK, because carbon fibre reinforced plastic (CFRP) was considered as a potential composite for aerospace applications due to their high strength and specific stiffness compared to glass fibre and aramid fibre reinforced plastics. However, the significant difference and the mismatch of the thermal expansion coefficient between carbon fibre and aluminium alloys are the major issues for FMLs. These problems may severely reduce the strength of aluminium during their service life [83] due to galvanic corrosion. Therefore, high strength glass fibres such as S-glass fibre could be good alternatives to carbon fibres in aerospace applications.

2.7 Fibre metal laminates (FMLs)

2.7.1 Background and classification of FMLs

For an optimal structural design, there has been attention to replace conventional aluminium alloys in aerospace structures with new low density materials which offer high elasticity, high strength, good corrosion resistance, improved fracture toughness and fatigue properties. Traditional fibre reinforced composites are good options because they almost cover all these requirements, except the fracture toughness properties [84]. In 1974, the United States Air Force officially introduced the philosophy of the damage tolerance design. In 1978, the Federal Aviation Administration (FAA) published a new Federal Airworthiness Regulations (FAR) involving the required certification of the fatigue evaluation and damage tolerance of transport category aircraft structures [84].

The maintenance costs for the airliners are about 20% of the direct operating cost (DOC). This means that durable structural materials with more damage tolerance are required to reduce the maintenance cost and the structural weight of the aircraft [85]. A research was carried out on the fuselage repairs of Boeing 747 aircraft with an average flying life of 29 500 hours. The results showed that the highest repairs percentage of 57.6 % was for the fatigue cracks compared to 29.4% and 13.0% for the corrosion and impact damage repairs, respectively [85]. Therefore, there is a definite need for materials with damage tolerance and excellent fatigue properties for aerospace applications. Even though the cost-effectiveness of the aircraft structure can be increased by using advanced materials such as aluminium alloys and fibre reinforced composites, they still have their drawbacks, like poor impact properties of the fibre reinforced composite and poor fatigue resistance of aluminium alloy [84, 85].

During the past decades, the demand for high-performance composites in the aircraft industry has led to the development of a new type of composites, named as fibre metal laminates (FMLs). FMLs are hybrid composite structures in which a number of thin sheets of metal alloys and plies of composites (prepregs) are stacked together, as shown in Figure 2-11. FMLs combine the high toughness and impact energy offered by metals and the high specific properties associated with the fibre reinforced composites. It has been demonstrated that FMLs have superior in-plane tensile strength and tension fatigue properties compared to those for aluminium alloys [86].
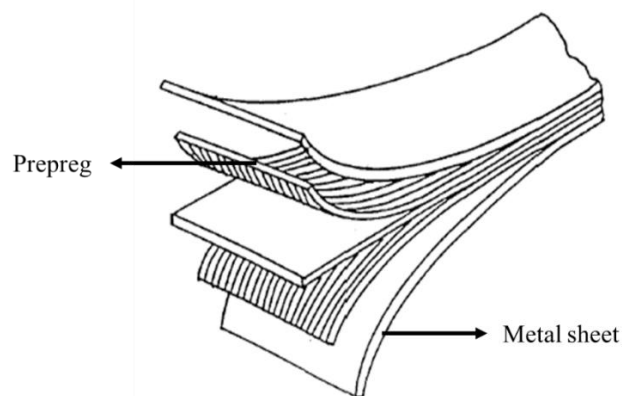
Figure 2-11. Fibre metal laminate configuration [84].

34

FMLs have been extensively used as structural materials due to their advantages over the conventional fibre reinforced composites, i.e. high fatigue resistance, excellent corrosion and impact resistance, high damage tolerance and low density. In the FMLs, the rates of the failure crack growth are reported to be lower than those offered by aluminium due to the bridging of the crack in the metallic layers by the fibres [85, 87–89]. FMLs can be classified based on the plain composites and metal types, as shown in Figure 2-12. ARALL (aramid fibre reinforced aluminium), CARALL (carbon fibre reinforced aluminium) and GLARE (glass fibre reinforced aluminium) are the most commercially available fibre metal laminates [21].

The fatigue properties of GLARE laminates were investigated by Vogelesang and Vlot [85], and they showed that the fatigue resistance of the FMLs is between 10 to 100 times higher than that offered by monolithic aluminium alloy. Other advantages of FMLs such as an excellent corrosion resistance, impact properties, fire containment capacity are also highlighted.

Cortes and Cantwell [90] conducted tensile tests on novel FMLs based on carbon fibre reinforced PEEK and titanium alloy to assess their tensile and fatigue properties. They concluded that the fatigue life of the notched unidirectional FMLs is up to 50 times higher than those achieved by notched titanium alloys. The authors also showed that the delamination area in FMLs based on thick composite plies is higher than that resulted in FMLs with thin composite plies.
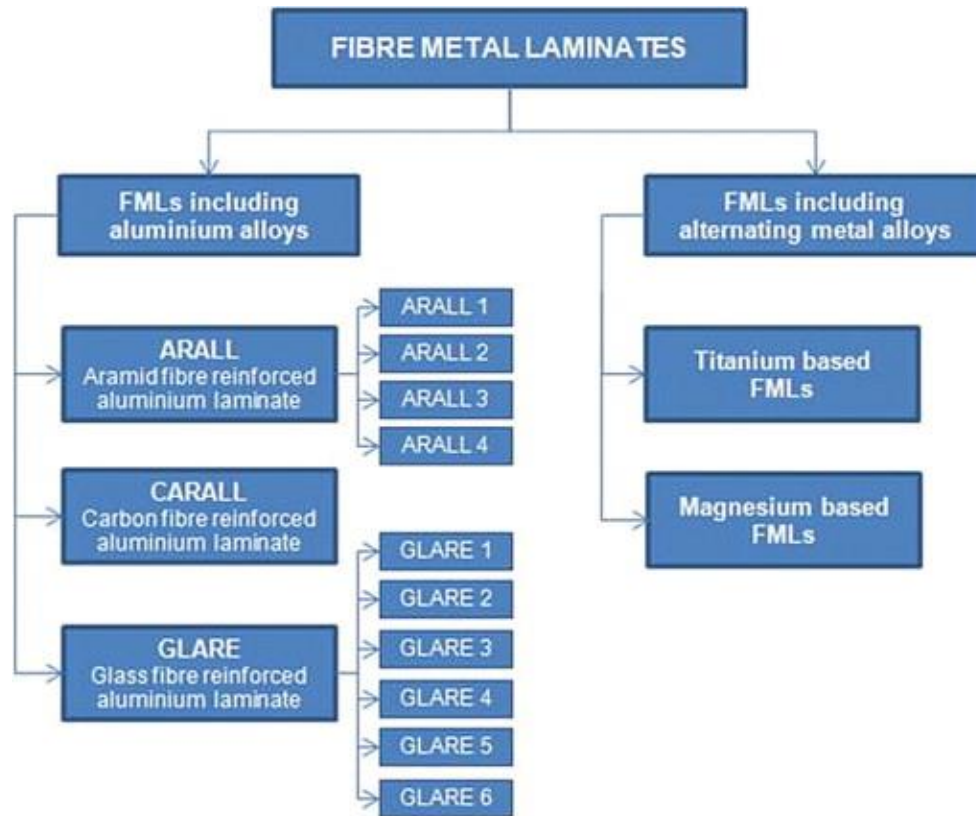
Figure 2-12. Classification of the fibre metal laminates [53].

2.7.2 Historical development of FMLs

In 1978, researches were undertaken to improve the fatigue behaviour of the aluminium alloys at Delft University of Technology (National Aerospace Laboratory) in the Netherlands. A fundamental improvement in the fatigue properties of these laminates was achieved by bonding these alloy sheets with a high strength aramid fibre composites using adhesive layers. Aramid reinforced aluminium laminates (ARALL) was the first fibre metal laminates introduced at the Faculty of Aerospace Engineering [84, 86, 91].

In 1984, four different types of standardised ARALL were produced by the Alcoa Company. One of these newly developed fibre metal laminates was used to design the full scale of lower wing panel for the Fokker-27 aircraft with benefits of 33% weight saving [84]. These laminates consisted of a thin 0.2 ± 0.4 mm high strength aluminium alloy sheet (i.e. 2024 or 7475) bonded with uniaxial or biaxial aramid fibre prepreg. However, these FMLs showed disadvantages of low blunt notch strengths and doublers should be used to avoid the premature

fatigue cracking. Moreover, ARALL laminates can only save 8% of the fuselage weight, making it unsuitable for fuselages. The interface strength between the aramid fibres and the adhesive is poor, causing fibre pulling out, and fibres can be damaged easily when the composite structures are subjected to compressive loads [92].

The first application of ARALL 3, which is made by using layers of aluminium alloy 7475, was to manufacture the cargo doors of the military transport airplane (C-17), resulting in a weight saving of 26%. However, the manufacturing processes cost of these laminates were 8 to 10 times higher than those for monolithic aluminium alloys. Following that, much stiffer FMLs were developed; namely, CARALL (Carbon Reinforced Aluminium Laminates), which is based on aluminium alloy bonded with carbon fibre reinforced composites. These FMLs type have limited applications due to the dissimilarity in the thermal expansion coefficients of the aluminium alloy and the carbon fibre reinforced composites, resulting in residual thermal stresses, and also, galvanic corrosion can be experienced between the aluminium and carbon layers, which may cause a reduction in the materials strength [83].

GLARE, as fibre metal laminates family member, consists of aluminium layers bonded with glass reinforced epoxy prepregs. In 1990, GLARE laminates were introduced as an improvement of ARALL for aeronautical applications at the Technical University of Delft in the Netherlands. Following this, AKZO and ALCOA operated a collaboration to produce and commercialise GLARE in 1991[53]. In 1992, the new concept of the FMLs (i.e. ARALL and GLARE) was launched by the Structural Laminates Company (SLC) in Delft [84]. The advantages and drawbacks of the various fibres used in FMLS are shown in Table 2-4.

In the fibre direction, GLARE laminates exhibit higher specific strength and specific stiffness offered by high strength aluminium alloys, resulting in weight saving in the designs of tension-dominated structural components. As mentioned before, under fatigue loading, crack growth and propagation in the layers of the aluminium alloys are impeded by fibre bridging mechanism [53, 93].

Compared to ARALL, GLARE laminates have better adhesion properties between the glass fibres and more resistance under compression loadings. Also, GLARE laminates show more advantages over ARALL in terms of tensile strengths, impact properties and residual strength. Due to the good glass fibre-resin adhesion, multidirectional prepregs can be easily involved in GLARE laminates, making it more suitable for some structures where biaxial stresses occur. Due to the aforementioned advantages, GLARE laminates have found a wide range of potential applications with a lot of attention from the manufacturers [53]. As shown in Figure 2-12, there are six commercial standard grades of GLARE; they are GLARE 1 to GLARE 6. They are based on glass fibre reinforced epoxy prepregs stacked with aluminium alloys type 7475-T761 for GLARE 1 and 2024-T3 for other GLARE grades [84]. Currently, GLARE structures are used in the new and high capacity Airbus (A380) for making the main fuselage skin and leading edges of the vertical and horizontal tail planes [53, 84].

Table 2-4. Advantages and disadvantages of FMLs with various fibres [53].

Fibre	Advantage	Disadvantage	Conventional FML
Aramid	• Outstanding toughness • Excellent fatigue resistance in both- tensile and flexural fatigue loading • High Young's modulus • Low density	• Weak in bending, buckling, compression loading and transverse tension • Absorb moisture • Do not form strong bonds with other materials such as composite matrices	ARALL
Glass	• High tensile strength • High failure strain • Do not absorb moisture	• High density • Low stiffness	GLARE

2.8 Titanium alloys

Titanium alloys are used in aerospace industries due to their superior mechanical, physical and chemical properties, i.e. excellent strength to weight ratio, good corrosion resistance and high melting point [94]. The modulus of elasticity of these alloys is about 110 GPa which is between those of steel and aluminium alloys. The service temperatures of titanium alloys range between 425 to 580 °C. The high corrosion resistance of these materials is attributed to the formation of the passive layer of TiO_2 on the titanium surface [94]. The large volume application for titanium alloys are represented in the airframes, and the usage increased steadily through the latter decades of the twentieth century [95]. Figure 2-13 shows the utilisation of the titanium alloy in Boeing aircrafts. The areas of titanium usage in the airframe of the advanced fighter (F-22 Raptor) is about 42% of all of its structural weight, and about two-thirds by weight of the aft fuselage, as shown in Figure 2-14 [95].
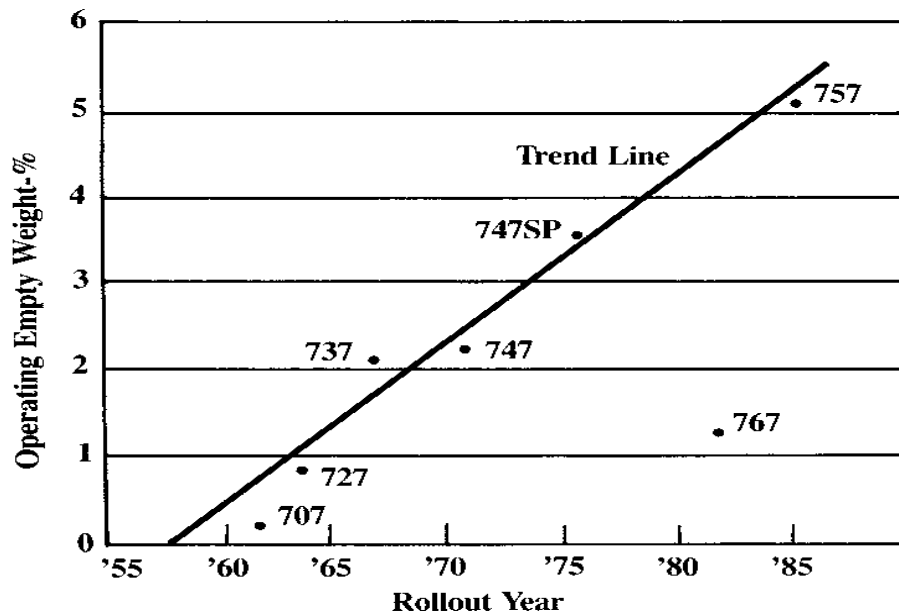
Figure 2-13. The usage of titanium in Boing aircrafts [95].

Wings
• Side of body fitting: titanium HIP casting
• Spars:
Front, titanium intermediate, resin transfer molded
composite and titanium
 Rear, composite and titanium

Aft fuselage
• Forward boom: titanium
welded
• Bulkheads/Frame: titanium
• Upper skins: titanium and
composite
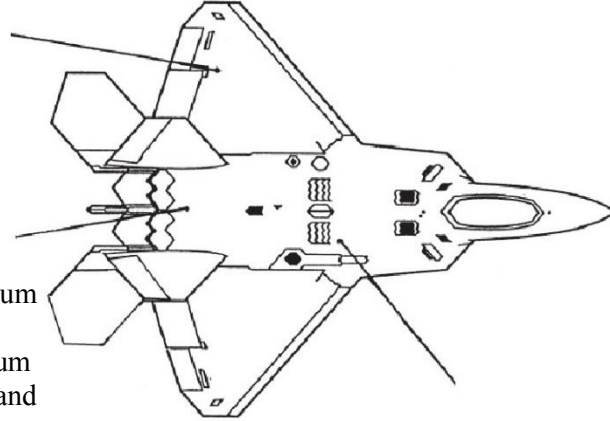
Mid fuselage
• Skins: composite and titanium
• Bulkheads and frames: titanium,
aluminium, composite

Figure 2-14. Usage of titanium alloy in the advanced fighter aircraft (F-22 Raptor)
[95].

2.8.1 Titanium structures

Titanium alloys exist in various structures, i.e. alpha (α)-, alpha-beta (α-β) - and beta (β)-

titanium alloys. The pure titanium, with a transition point of 883 °C, can be altered to give a

wide range of alloys with different mechanical properties either by employing alloying

elements or applying thermo-mechanical treatments. The structure of the α-titanium alloys is

hexagonal close-packed (hcp), and it is formed by adding α-stabilising alloying elements, i.e.

aluminium and tin to the pure titanium. The resulted alloys show higher creep resistance than

that offered by β-titanium alloys. The α-β-alloys contain a combination of alpha and beta

structures, and their properties can be manipulated by the heat treatment processes by changing

the type and amount of β phase. Finally, metastable β-alloys consist of β-stabilised elements

such as vanadium or niobium, which decrease the transition temperature from α to β. These

latter alloys have shown better hardenability and deformability compared to those of α-alloys.

Ti 15-3-3-3-titanium alloy, as commercial β-titanium alloy, with a nominal composition of 15% V, 3% Al, 3% Cr, and 3% Sn is utilised in this research. These alloys can be provided into different forms, i.e. sheets, strips and plates and it can be produced either as wrought or cast alloys. Titanium (β) is a heat treatable alloy with a tensile strength of 1310 MPa, and it can be cold worked at room temperature; thus, it can be produced as thin sheets to be stacked with composites to manufacture fibre metal laminates panels. Due to the aforementioned properties, metastable β-alloys have mainly used in the components of aerospace and high strength aircraft such as supersonic aircraft. Table 2-5 shows the physical and mechanical properties of the titanium alloy type Ti 15-3-3-3 according to ASM handbook [94–96].

Table 2-5. Physical and mechanical properties of titanium alloy (Ti 15 -3-3-3) [94].

Property	unit	value
Electrical resistivity	$\mu\Omega$.m	1.47
Thermal conductivity	W/m.K	8.08
Density	g/cm^3	4.71
Coefficient of linear thermal expansion (at 20-100 ºC)	µm/m	8.5
Tensile strength	MPa	773
Ultimate tensile strength (UTS)	MPa	785
Elongation (El)	%	22

2.9 Aluminium alloys

Aluminium alloys have been used as airframe materials in the late of 1920s as a good replacement to wood. Aluminium alloys have been employed extensively in aerospace applications due to their excellent mechanical properties, i.e. high specific strength, high fracture toughness, high fatigue resistance, high formability, super-plasticity that fulfil the requirements of low structural weight, good damage tolerance and high durability. However, these alloys exhibit a low modulus of elasticity comparing to steel, low-temperature capability,

and susceptible to corrosion in high-strength alloys [97–99]. The utilisation of aluminium alloys in several types of Boeing programs is presented in Figure 2-15.

Even though the role of aluminium alloys in future aircraft (i.e. Boeing 787) will be somewhat diminished by the increasing usage of the high-performance composites, high strength aluminium alloys are still the most used materials in the current operation Boeing aircrafts, i.e. 747, 757, 767 and 777, and it will remain the essential airframe material [100, 101].

Aluminium alloys are usually classified as wrought and cast alloys. Depending on whether they respond to precipitation hardening or not, each of these alloys can be further categorised as heat treatable and non-heat treatable alloys. Currently, the American nomenclature (Aluminium Association) creates a classification, in which wrought aluminium and aluminium alloys are classified according to a numerical designation. This designation system is also used in European countries. This type on designation is based on four figures, in which the first figure of the "1 series" represents alloys with a higher percentage of aluminium (i.e. higher than 99%). In contrast, the first figure of the 2 to 8 series denotes the main alloying element as shown below:

1xxx-pure aluminium (higher than 99%) in which the last two figures represent the aluminium percentage. The second figure indicates the impurities level which is equal to zero if the impurities are uncontrolled, and it can vary between 1 and 9 depending upon the level when the content of impurity is not exceeded. Aluminium alloy grouped by main alloying elements; 2xxx-copper; 3xxx-manganese; 4xxx-silicon; 5xxx-magnesium; 6xxx-silicon and magnesium; 7xxx-zinc; 8xxx-other elements and 9xxx-unused series. Here, the last two figures identify the specific alloy in each group. For the main alloys, the second figure is equal to zero, and it varies between 1 and 9 for its modifications [101]. The alloy designations followed by the temper designation system, are based on the sequences of the thermal and mechanical treatments used, as shown in Table 2-6. Table 2-7 shows a review of the applications of the aluminium alloys, i.e. 2XXX series in the aerospace structures.
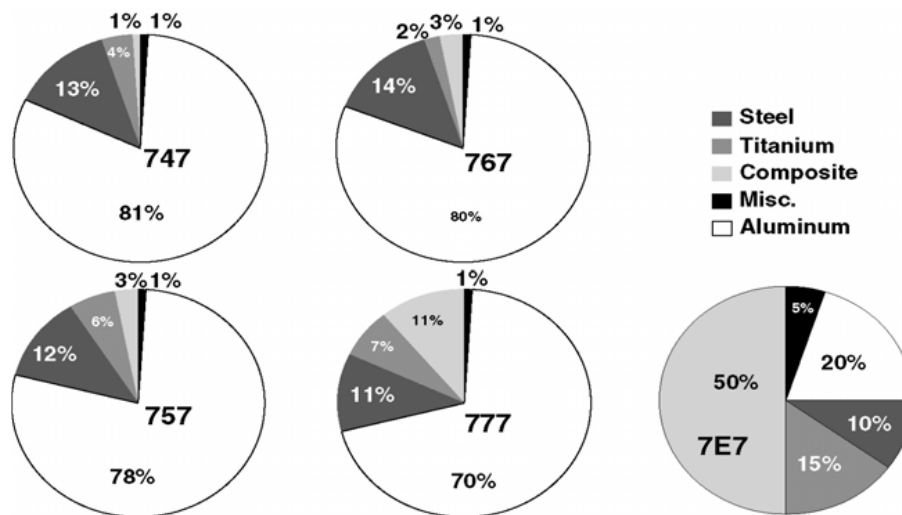
Figure 2-15.The approximate usage by weight of the primary structure materials on several Boeing aircraft [95].

Table 2-6. Thermal and mechanical treatment of aluminium alloys [101].

Temper designation	Mechanical and thermal treatments
T	Heat treated to produce stable tempers cooled
T1	Cooled from high temperature and natural ageing
T2	Cooled from high temperature, cold working and natural ageing
T3	Solution heat treatment, cold working and natural ageing
T4	Solution heat treatment and natural ageing
T5	Cooled from high temperature and artificial ageing
T7	Solution heat and over ageing treatments
F	As fabricated
O	Annealed state, the lowest strength, highest ductility
H	Work-hardened state
W	Solution heat treated only

Table 2-7.The applications of aluminium alloys (2xxx) in airframe structures [101].

Product	Strength levels	Alloy/temper	Applications
Sheets	Damage tolerant	2024-T3, 2524-T3/351	Fuselage/pressure cabin skins
Plates	Damage tolerant	2324-T39, 2024-T351, 2624-T351, 2624-T39	Lower wing covers
	Medium strength	2024-T62,	Aircraft fuselage panels
Extrusions	Damage tolerant	2026-T3511, 2026-T3511, 2024-T4312, 6110-T6511	Lower wing stringers Fuselage/pressure cabin stringers

2.10 Impact response of composite structures

The main advantage of using fibre reinforced composites is their superior strength to weight ratio compared to metal alloys. Therefore, composite laminates have been extensively used in aerospace applications for designing primary and secondary load bearing components [102, 103]. However, composites are very susceptible to transverse impact which leads to a reduction in the residual strengths of structures as well as catastrophic failures. Damage in composite structures is very complex, and it can be formed through a matrix crack, ply delamination, fibre-matrix de-bonding as well as fibre breaking and buckling. Manufacturing defects such as voids and stress concentration are the main reasons for these kinds of damage.

In aerospace applications, composite materials may be exposed to impact loadings by foreign bodies in the external environment, such as dropping of tools during maintenance, hail ice, bird and runway debris. The impact loadings can be grouped as; high-velocity impact and low velocity impact. In high-velocity impact, composite materials are subjected to low mass-

projectiles with high velocity such as gun bullets, whereas in low velocity impact loadings, composite materials may be exposed to loading such as dropping tools during maintenance. Low velocity impact damage results in multiple in-plane cracks on the surface of the composite material. These cracks are not easily visible to the naked eye and lead to catastrophic failure of components [102–107]. When composite structures are subjected to low velocity impact, the majority of energy can be absorbed in very complex mechanisms of distortion and fracture. Impact damage can be divided into: intralayer damage including matrix cracking and fibre breakage, and interlayer damage (delamination) which occurs between the adjusting layers with different orientations. Delamination and matrix cracks are the main damage events which strongly affect the integrity of the composite structures. Even though complete structural failure may not happen with low velocity impact, critical damage in the panel may lead to a replacement of the component rather than a repair [108, 109].

2.10.1 Plain composite structures

A large number of experimental and numerical studies has been undertaken to understand and characterise the low velocity impact response of composite structures comprised of epoxy resin [108, 110–118] with particular attention focusing on damage development in these materials during the dynamic loading. Cantwell and Morton [110] conducted a series of low velocity impact tests to assess the initiation and development of the damage on CFRP laminates. The authors observed that the damage type of the impacted panels showed a dependency of the laminate thickness, in which the thin panels fail in the bottom layers, whereas, the damage on thick panels initiate in the upper layers before propagation through the laminate thickness. Wang et al. [106] investigated the influence of the low velocity impact on the residual strength of carbon fibre reinforced epoxy experimentally and numerically using ABAQUS/Explicit software. The results showed that the impact force and residual strength could be reasonably predicted by using finite element analysis. The authors have also showed that the residual strength of the laminates investigated depend on its stacking configurations

at which angle-ply stacking configurations offer higher residual strength than those offered by cross-ply stacking configuration laminates.

The influence of the target geometry, projectile diameter and testing temperature on the damage initiation threshold on a glass fibre reinforced epoxy is investigated by Yang and Cantwell [119]. The results showed that the critical load at which damage initiates shows high dependency on the projectile diameter. It was also observed that the damage threshold, for the range of target thicknesses investigated, did not show a significant change with the plate diameter.

Mitrevski et al. [120] investigated the influence of different projectile shapes, i.e. hemispherical, ogival and conical on the damage initiation in a carbon fibre reinforced epoxy. They showed that panel impacted with a hemispherical projectile exhibited the shortest contact duration and highest impact force among the other projectile shapes. Indentation and perforations damage were observed following loading by ogival and conical projectile and barely visible impact damage was observed for those impacted with a hemispherical projectile.

Choi and Chang [121] investigated the influence of the low velocity impact loading on the initiation and development mechanisms of damage for carbon fibre reinforced epoxy. The results showed that the damage occurred when the impact velocity passed the critical value (i.e. impact velocity threshold) and there was no delamination below the threshold value. They also observed that the matrix cracking is the initial failure mode. Subsequently, these cracks led to delamination at the neighbouring interfaces.

Kumar et al. [122] investigated the effect of impactor materials (i.e. steel and aluminium) on the impact response of CF/epoxy composites. They showed that, for a given energy, the steel projectile generates impact damage of 30-50 % higher that of aluminium projectile. Moreover, the steel projectile produced greater delamination and higher contact stresses than those obtained by using aluminium impactor.

Lopez-Puente et al. [123] conducted a series of high velocity impact tests on carbon fibre reinforced laminates made with tape or/and woven plies. They found that the impact properties of woven based-CFRP laminates were higher than those offered by tape-based laminates.

The perforation resistance of glass fibre reinforced epoxy subjected to low velocity impact was investigated experimentally and numerically by Fan et al. [124]. The authors observed that the perforation energy increased rapidly with the target thickness. The FE results from the numerical modelling by the use of ABAQUS software showed a good agreement with the experimental data. The results also showed that increasing the projectile diameter resulted in a noticeable increase in the energy absorbed by the targets.

As mentioned before, the impact-induced damage in the composite structures is particularly critical due to its effects on the residual mechanical properties. Some researchers have compared the impact response of thermoplastic and thermoset composites in terms of residual strength and damage tolerance [76, 125–130].

Vielle et al. [76] conducted a series of low velocity impact tests on woven-CFRP based on different resin matrices (Epoxy, PPS and PEEK) to assess their damage tolerance after impact. The results showed that the impact loading leads to cross-shaped damages resulting from different failure modes, i.e. fibre breakage, inter-laminar and intra-ply damage and delamination. The results also showed that CF/PEEK composites displayed the highest impact properties, whereas the lowest performance belonged to CF/epoxy composites which showed larger delamination area. The results suggested that the better impact performance of the thermoplastic composite structures is mainly due to the tough matrices used.

The impact damage response of PEEK reinforced with intermediate strain carbon fibre (AS4) and toughened epoxy reinforced with high strain carbon fibre after impact tests was investigated by Morton and Godwin [131]. They showed that damage tolerance of the CF/PEEK laminates is superior to that of CF/epoxy laminates.

Nejhad et al. [57] investigated the damage tolerance and impact performance of woven-CF/PEEK and carbon fibre reinforced polyphenylene sulphide (CF/PPS) under low velocity impact and compression after impact (CAI) tests. They showed that the perforation energy of the CF/PPS system was higher than that of CF/PEEK composites. However, the ability of the CF/PEEK composites to absorb energy without extensive delamination led to a relatively smaller reduction in the residual strength compared to CF/PPS.

2.10.2 Fibre metal laminates

FMLs have received significant attention in aerospace applications and it has been used extensively in the design of specific aircraft such as the upper fuselage of the Airbus A380 due to their outstanding fatigue properties [85, 90]. FMLs also offer attractive properties under dynamic loadings, i.e. localised impact tests [132]. The superior properties of FMLs are related to their constituents. The static and dynamic responses of ARALL, CARE (epoxy based carbon fibre /aluminium) and GLARE laminates were investigated by Vlot [21]. The results showed that FMLs exhibited a smaller post-impact damage zone than fibre reinforced composites. Extensive work have been undertaken to investigate the impact properties of epoxy-based fibre –metal laminates [21, 133–137].

Caprino et al. [138] investigated the impact response of FMLs manufactured by stacking sheets of aluminium 2024-T3 and prepregs of S2-glass reinforced epoxy under various low velocity impact parameters, i.e. impactor velocity, impactor mass and impact energy. Similar test conditions were carried out on sheets of monolithic 2024-T3. The authors found that the response of the laminates investigated in terms of load-displacement depends on the impact energy rather than on the impactor's velocity and mass separately. They also observed that the penetration energy of the monolithic aluminium is higher than that of glass fibre-aluminium FMLs and the performance of these FMLs (i.e. based on glass fibre and aluminium) is higher than that offered by glass fibre reinforced composites in terms of damage resistance and penetration energy.

The damage propagation mechanisms of GLARE 4 and GLARE 5 laminates based on cross-ply glass prepreg layers under low velocity impact tests were investigated by Wu et al. [139]. The authors observed that the specific energy absorbed by the first crack on the FMLs based on 2/1 stacking configuration was 10 % higher than that obtained by using aluminium alloy (2024-T3). They concluded that the two GLARE systems exhibited higher impact properties with longer service life than that associated with a 2024-T3 monolithic aluminium alloy.

Fan et al. [140] investigated the impact response of GLARE laminates by conducting a series of low velocity impact tests on FMLs made of epoxy prepregs and Aluminium 2024-T3. The effect of the various impact factors, i.e. plate and projectile geometries, on the perforation resistance of the FMLs investigated were also highlighted and compared to those offered by plain composite targets. The results showed that the FMLs can absorb the energy in different mechanisms, i.e. plastic deformation, tearing in the metals layers and fibre fracture. They also observed that FMLs exhibit superior properties compared to the plain composite which was used to manufacture the FMLs.

Zhou et al. [132] conducted split Hopkinson bar, quasi-static perforation and low velocity impact tests on a range of epoxy-based GLARE laminates to investigate their rate sensitivity. The authors observed that GLARE-based FMLs showed a low degree of rate sensitivity. The perforation energies and peak loads are only 10 to 15 % higher than those obtained quasi-statically. They also showed that the failure processes of the failed specimens, i.e. plastic deformation, fibre fracture and delamination are similar under both quasi-static and dynamic loading rates.

Long processing cycles, lower interlaminar fracture toughness and repair difficulties are the key limitations of these first generations of thermosetting based- FMLs (i.e. epoxy), as mentioned before. Therefore, FMLs based on thermoplastic composites were developed and tested to overcome the limitations of the epoxy-based FMLs [141–143]. The quasi-static and impact properties of FMLs based on glass fibre reinforced polypropylene prepregs and

aluminium layers (2024-T0) were studied by Reyes and Cantwell [144]. They observed that the surface treatment of aluminium alloy and using adhesive layers at the interface between the aluminium sheets and composite plies increased the adhesion between the FMLs constituents. The results also showed that these FMLs offered an excellent resistance to dynamic loading.

There is a huge potential for high temperature and high performance (HTHP) thermoplastic composites for aerospace applications to satisfy the design requirements of the next generation of a fuselage, especially the large size supersonic aircraft where the material has to withstand high temperatures. Here, FMLs based on high-temperature composites such as PEEK, poly-ether-imide (PEI) and PEKK represent ideal options for satisfying the requirements associated with these potentially aggressive loading environments [145]. To the authors' knowledge, there is very limited work that investigated the impact response of fibre metal laminates based on PEKK or PEEK under various loading rates.

Cortes and Cantwell [146] investigated the impact response of titanium alloy fibre metal laminates based on glass fibre reinforced PEI (GF/PEI) and carbon fibre reinforced PEEK (CF/PEEK) under low and high velocity impact tests. They showed that, the specific perforation energy of the FMLs based on CF/PEEK composites following low velocity impact loading is similar to those offered by the plain composites of CF/PEEK, whereas FMLs based on GF/PEI exhibit lower specific perforation energy than that of plain GF/PEI. The failure processes of the laminates investigated under high impact velocity were similar to those observed following low velocity impact tests.

2.11 Finite element modelling

The numerical response of FMLs under impact loading has been developed using finite element models. Lee et al. [147] used explicit finite element code, LS-DYNA3D, to model the penetration and perforation responses of aluminium (6061-T6) and carbon fibre reinforced 6061-T6 (MMC) plates under impact loading. Hughes-Liu shell elements were used to model

carbon fibre reinforced composites, whereas the projectile, aluminium plate and aluminium matrix of the composite were modelled using 8-node hexahedron elements. Perforation damage of the plate was found to occur under all the impact conditions investigated. The deformation behaviour of the projectile, plate, projectile post-perforation velocity and projectile's deceleration were significantly dependent on the properties of the plate and impact velocity.

Guan et al. [148] investigated the impact resistance of the FMLs manufactured by stacking woven self-reinforced polypropylene plies with two aluminium types, these being 2024-O and 2024-T3. The plain composite was modelled as an isotropic material with a specific tensile cut-off stress. The failure of the aluminium layers was modelled using shear and tensile failure criteria. Both predicted maximum permanent displacement and failure modes were correlated well with the corresponding experimental results as shown in Figure 2-16. The FE models showed that, at perforation threshold, the passage of the projectile through target introduces a significant plastic deformation immediately under the impact location. The failure in the lower plies of the thick panels, (i.e. 5/4 FMLs), is significantly delayed at which the projectile should perforate the upper layers before completely passing the laminates.

2024-O (2/1 FML)   2024-T3 (2/1 FML)

2024-O (5/4 FML)   2024-T3 (5/4 FML)

(a)

51

(b)
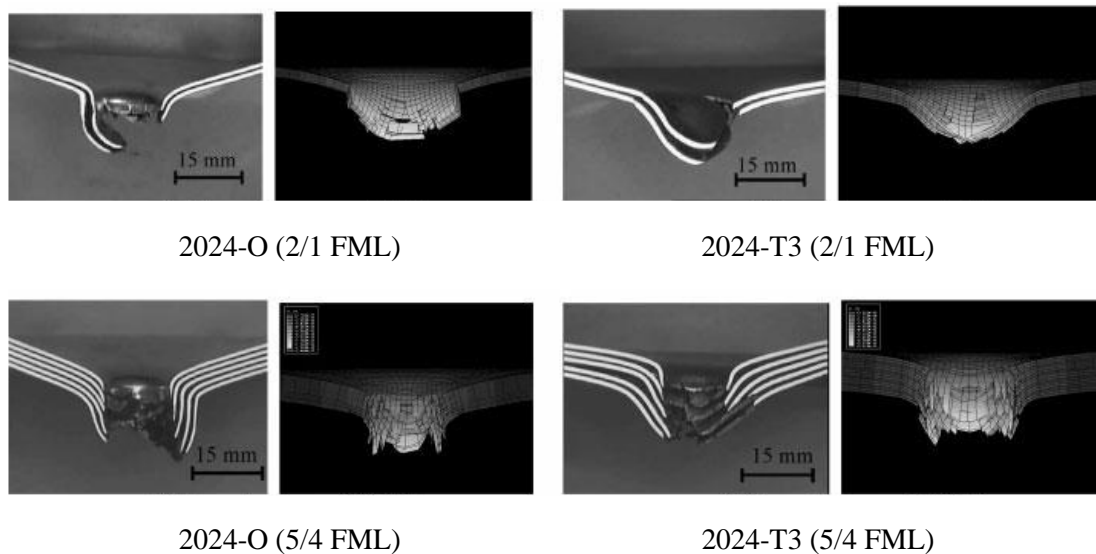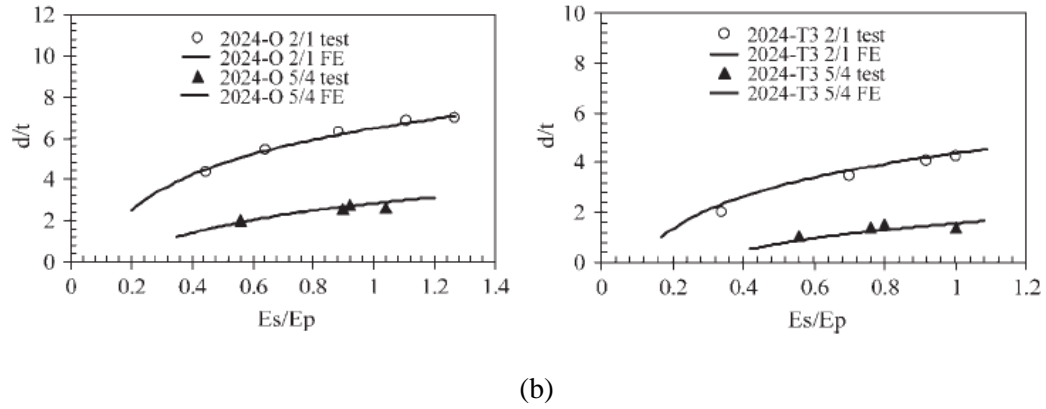
Figure 2-16. Predicted and experimental (a) failure modes and central cross-sections
(b) maximum permanent displacement of the 2/1 and 5/4 FMLs [148].

FE models were developed by Payeganeh et al. [149] to investigate the impact response of GLARE laminates in terms of contact force history, deflection, in-plane strains and stresses. The results showed that the parameters such as target stacking configurations, the masses and velocities of the impactor are important in determining the impact response of the FMLs.

Fan et al. [150] modelled the perforation response of GLARE laminates which includes woven glass fibre reinforced composite and 2024-O aluminium alloy sheets with various stacking configurations, i.e. 2/1, 3/2 and 4/3 subjected to a low velocity impact loading. The aluminium alloy was modelled as an elasto-plastic material with rate dependent behaviour. The failure behaviour of the aluminium plies was modelled using both shear failure and tensile failure. The woven plain composite was modelled as an orthotropic elastic material prior to the initiation of the damage. Hashin's damage criterion was then employed to model the damage initiation of these plain composites. General contact interaction was defined between the adjusting layers to model the interaction between the layers in the FMLs. The contact between the projectile surface and node set at the target centre of each layer was defined using surface-to-surface contact interactions. The aluminium sheets were meshed using eight-node linear brick elements with reduced integration and hourglass control (C3D8R), whereas the composite plates and projectile were meshed using continuum shell elements (SC8R) and four-node bilinear quadrilateral elements (R3D4), respectively. The output results of the numerical

simulations, in terms of failure modes, correlated well with the experimental results as shown in Figure 2-17. The rear surface plies of the perforated panels exhibited petalling around the perforation area. The cross-section of the failed panels shows significant delamination between the aluminium layers and composite plies, plastic deformation in the metal layers and fibre fracture in the composites. The perforation region of these panels was successfully predicted using the FE analyses. The authors also showed that the FE models are capable of predicting the perforation energy of the FMLs under impact with various projectile diameters, as shown in Figure 2-18. The FE models suggest that the perforation energy increases rapidly with the projectile diameter in a non-linear pattern.

(a) Photo of the perforated sample

(b) FE simulation

(c) Cross-section of the perforated sample

(d) the predicted cross-section
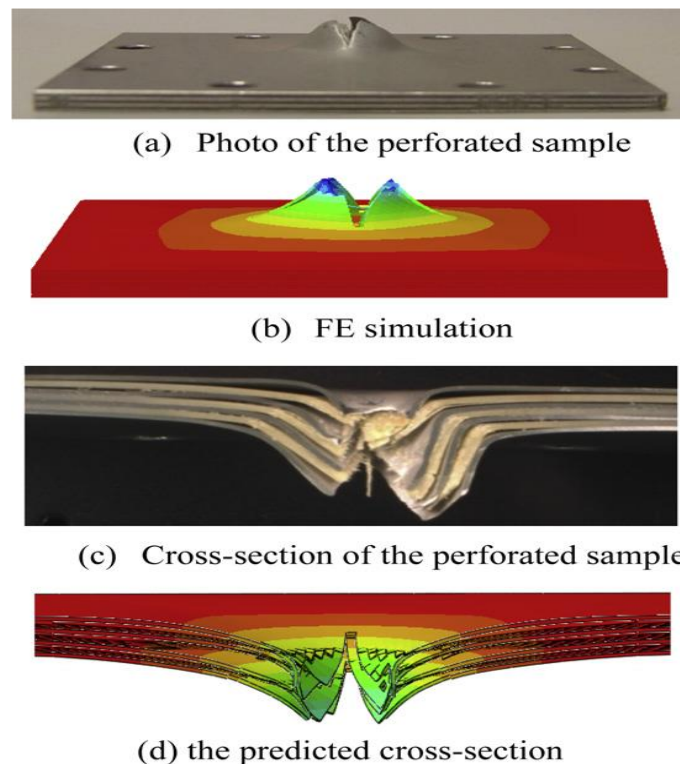
Figure 2-17. The failure mode and central cross-sections of the failed 4/3 FML plate made with 8-ply composite cores subjected to low velocity impact [150].
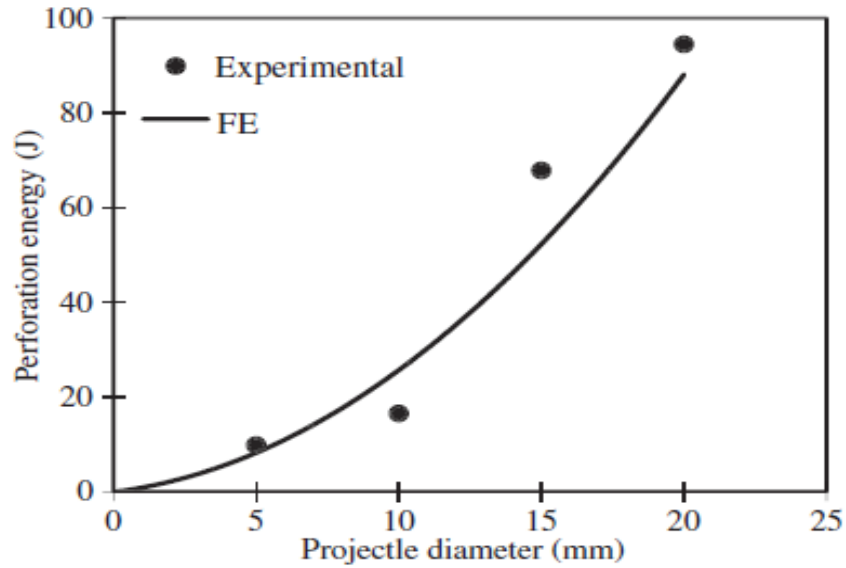
Figure 2-18. The measured and predicted perforation energy of 3/2 FMLs impacted by projectiles with diameters of 5, 10, 15 and 20 mm [150].

Nakatani et al. [151] investigated the impact-induced damage in GLARE laminates based on titanium alloy sheets (Ti–6Al–4V, 140 µm thickness) and GF/epoxy prepregs under low velocity impact tests. Table 2-8 shows the element types used for each part in the FE analysis.

Table 2-8. Element types for each part in the FE models.

Part name	Element type	Element properties
Impactor	Rigid element	4-node, quadrilateral, linear
Ti alloy layer	Solid element	8-node, brick, linear
Adhesive layer		
GFRP ply layer	Continuum shell element	8-node, quadrilateral, linear
Interface layer	Cohesive element	8-node, brick, linear

Many researchers suggested a full three-dimensional composite failure criterion to model the response of the composite material under impact loading [152–156]. However, it is worth mentioning that other researchers concluded that continuum shell elements available in ABAQUS/explicit can be used to successfully model the response of the composite laminates [150, 151, 155–157] under impact loading with good agreement between the numerical and

54

experimental results. Seo et al. [156] developed FE models to predict the dynamic response of GLARE laminates. 2D and 3D failure criterion were used to simulate stiffness degradation in the glass fibre reinforced composites. The FE models were validated against the experimental results reported by Wu et al. [139]. The agreement between the measured and predicted peak loads of the laminates investigated is presented in Figure 2-19. They observed that the results of both 2D and 3D models are correlated well with the experimental data.
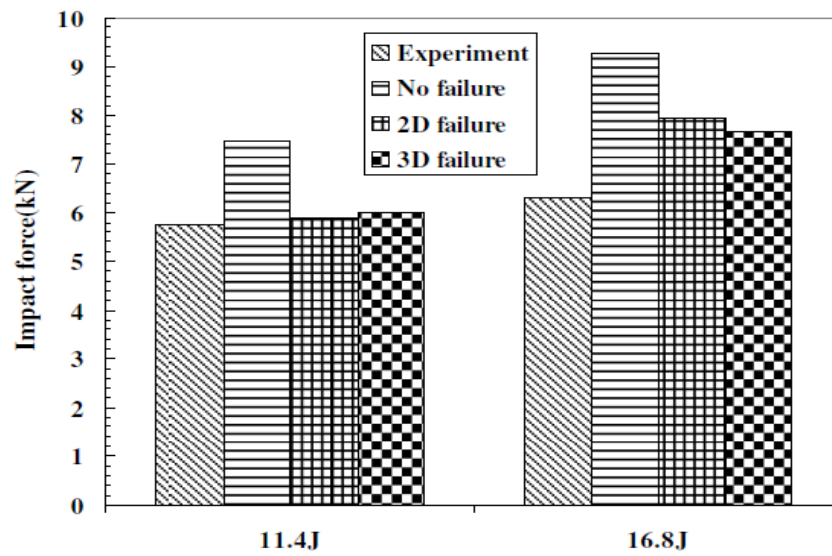
(a) GLARE 4-3/2
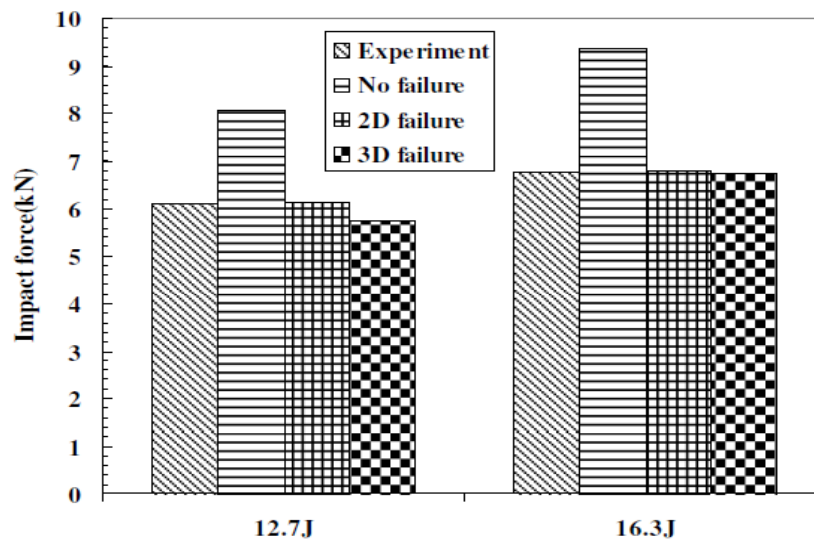
(b) GLARE 5-2/1

Figure 2-19. Predicted and measured peak loads of FMLs [156].

2.12 Summary

The previous and current research studies relevant to this thesis are reviewed and discussed in this chapter. A brief overview is given on the classification of composite materials and their applications in the aerospace sector, followed by the background of high performance thermoplastic composites and their manufacturing process. Four main manufacturing techniques, i.e. solution dip prepregging, hot melt prepregging, film stacking and dry powders prepregging have been reviewed. It can be seen from the review that the dry powder prepregging process offers several advantages over other impregnation techniques.

The background and classification of fibre metal laminates have also been presented. It has shown that the FMLs used in aerospace applications extensively due to their superior properties (such as excellent fatigue properties, high specific strength and stiffness), which are usually related to thermoset epoxy prepregs. However, these kinds of prepregs are costly and have poor properties at high temperatures. These limitations can be eliminated using composite structures based on high performance thermoplastic polymers such as PEKK.

Finally, this chapter has presented a review on the modelling procedures using commercially-available FE codes to predict the response of the composites structures (i.e. plain composite and FMLs) under both quasi-static and impact loading. It has concluded that the failure mechanisms and energy absorption of the laminated composite structures can be effectively predicted using the finite element analysis. ABAQUS/Explicit is well suited to model the dynamic response of composite structures.

Recently, a lot of work including experiments, numerical modelling and theoretical analysis has been undertaken to investigate and optimise the properties and the design procedures for fibre metal laminates. However, the damage behaviour of the laminates based on high-performance thermoplastic polymers under quasi-static and dynamic loading rates remains a subject area of great concerns for those interested in employing these new generations of fibre metal laminates in advanced engineering structures.

3 Chapter 3: Materials and Experimental Procedure

3.1 Introduction

The details of the experimental procedures undertaken in this project are presented in this chapter. The fabrication processes of the S-glass fibre reinforced PEKK (GF/PEKK) composites, β-titanium-based FMLs and aluminium-based FMLs are given here. This chapter also describes the sample geometries, sample stacking configurations as well as the experimental methodology on the laminates investigated. Initially, a series of mechanical tests were carried out on the plain GF/PEKK composites to investigate their mechanical properties and these being tensile, flexural, shear, quasi-static perforation and low velocity impact tests. Quasi-static and low velocity impact perforation tests were also conducted subsequently on the fibre metal laminates to study their behaviour under both loading rates.

3.2 Manufacturing procedure of woven S- glass fibre reinforced PEKK (GF/PEKK)

The composite material investigated in this research project was based on plain woven S-glass fibre fabric from East Coast (UK) as reinforcing phase and poly-ether-ketone-ketone (PEKK) resin (KEPSTAN 6003PL) from ARKEMA (France) as matrix phase. The manufacturing process of S-glass fibre reinforced PEKK (GF/PEKK) can be divide into two parts. Firstly, prepregs were manufactured, then they were stacked together to manufacture the composite laminates with various stacking configurations.

3.2.1 Prepregs manufacturing process

A dry powder prepregging technique was used to manufacture prepregs of PEKK and woven S-glass fabric, in which PEKK resin in the form of a dry powder with particle size of 50 µm, was deposited onto the fibres as shown in Figure 3-1. The GF/PEKK prepreg was manufactured following the procedures below:

1.   The woven S-glass fibre fabric was cut into square cloths (250 mm x 250 mm) and weighed using a Rock Chuck Bullet Swage dies (RCBS) balance (precision 0.006 g).

2.   An adhesive (3M Multipurpose Spray) was sprayed evenly on the fabric which was re-weighed. The adhesive serves as a temporary binder to hold the resin powder in place on the glass fibre fabric.

3.   The fabric was then repeatedly dipped into a powder tank, and weighed until the target weight fraction of resin was obtained.

4.   The glass fibre fabric with the desired amount of powder was placed in a mold with dimensions of (300 mm x 300 mm) and heated to 330 $^{\circ}$C in a hot press. A high temperature release agent (Frekote) was applied to the mould to facilitate removal after consolidation. The processing cycle involved a holding time of 10 minutes and a pressure of 6 bar, respectively.
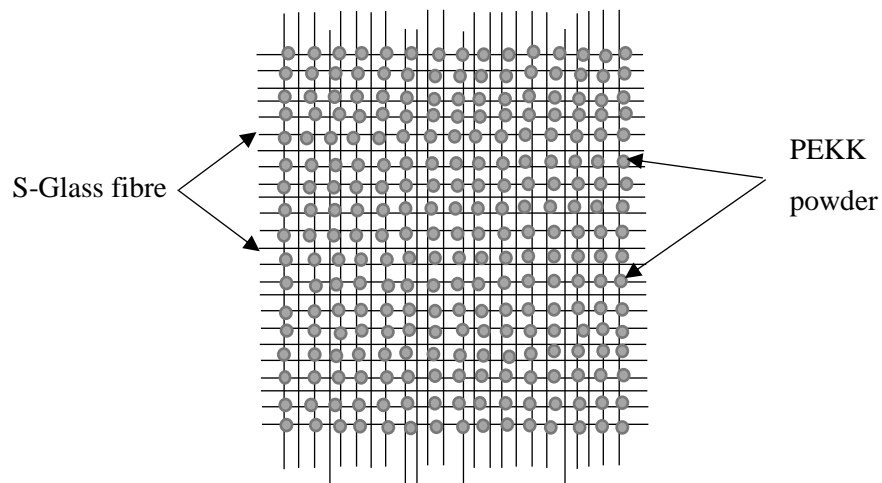
Figure 3-1. Schematic diagram showing the deposition of the thermoplastic resin (PEKK) on the plain weave S-Glass fibre.

3.2.2 Preparation of plain composite laminates

The composite laminates were manufactured by stacking the prepreg plies (0.12 ± 0.005 mm thick) in a mould with dimensions of 300 mm x 300 mm. Here, 4, 8, 12 and 16 sheets of S-glass fibre reinforced PEKK prepreg are used to make the corresponding number ply woven glass fibre reinforced laminates. Once these stacking arrangement placed in the lower mould, a digital thermocouple was inserted between the plies which measures the temperature during the cure circle. Then, the upper mould was positioned on the top of the prepregs. The resulting stack was then heated to a temperature of 330 $^{\circ}$C at a heating rate of 5 $^{\circ}$C/minute inside the Meyer press. The stacking arrangement for a 4- ply of woven S-glass fibre reinforced PEKK prepreg inside the hot press is shown in Figure 3-2**.**
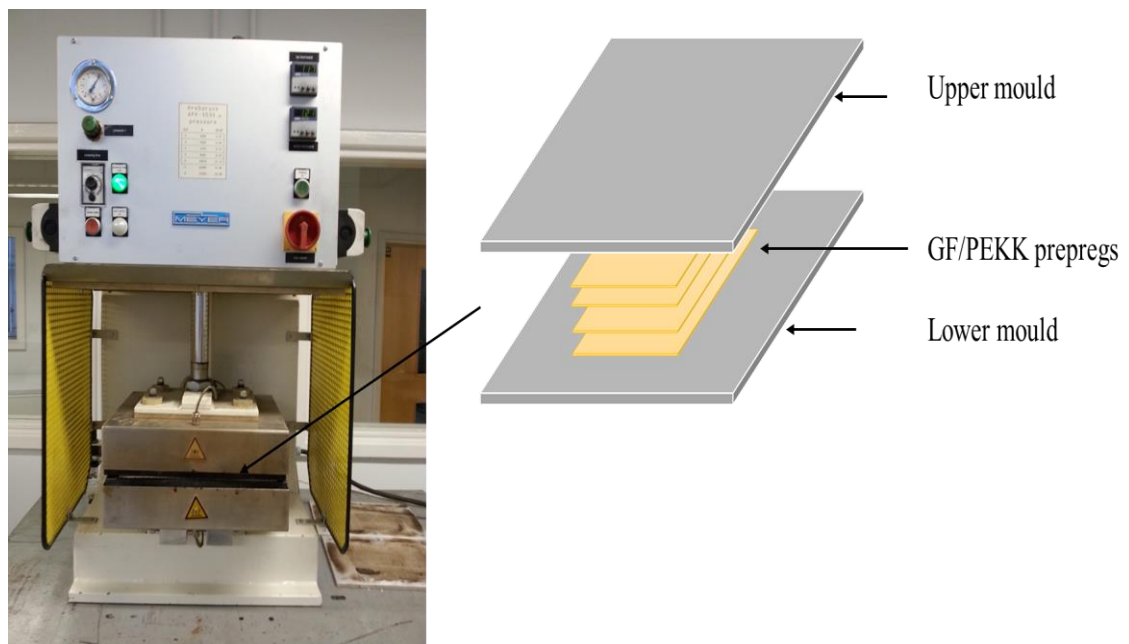
Figure 3-2. Hot press setup.

Laminates, with dimensions (125 x 125 mm) and (250 x 62.5 mm), were consolidated under a pressure of 3 bar for 30 minutes prior to cooling at a rate of 2 $^{\circ}$C/minute. The processing cycle is shown in Figure 3-3. After cooling, the pressure was released and the laminates were removed from the mould and visually inspected for defects. The composite laminates were

produced based on different weight percentages of PEKK. Prior to the mechanical testing, the specimens were sectioned, polished and examined under an optical microscope and scanning electron microscopy (SEM) to study their microstructure and the distribution of the fibres within the laminated panels. Table 3-1 gives details of the panels investigated in this study. Four thicknesses of plain GF/PEKK laminates were tested, these being 0.47, 0.96, 1.4 and 1.8 mm.
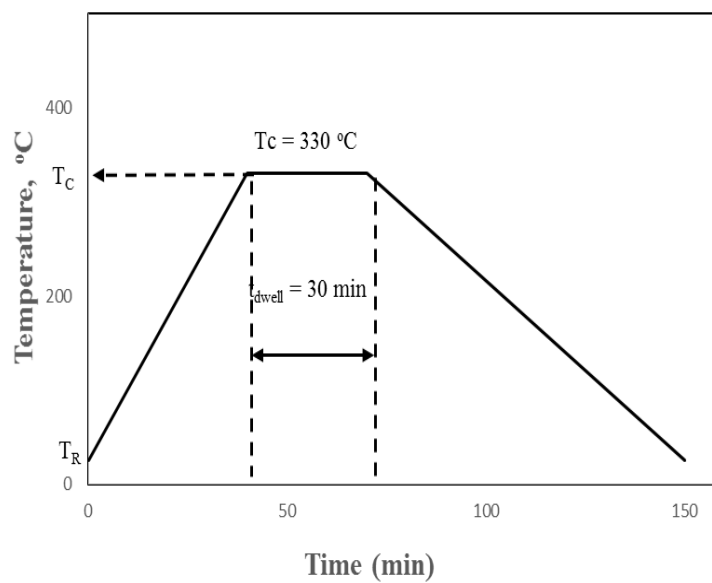
Figure 3-3. The processing cycle for the plain composites.

Table 3-1. Summary of the laminates investigated in this study.

No. of plies	Thickness (mm)	Fibre weight fraction (wt. %)	Areal density (kg/m^2)
4	0.47	60	0.77
8	0.96	60	1.58
12	1.4	60	2.31
16	1.8	60	2.97

3.3 Testing on mechanical properties of plain composite materials

3.3.1 Flexural testing

Three-point bending tests were performed on a 16-ply GF/PEKK composite using an Instron 4024 mechanical test machine at a crosshead displacement rate of 1 mm/minute. The GF/PEKK panel was cut into samples with length (L_t), width (b) and thickness (h) dimensions of 80, 13 and 2 mm, respectively. Test specimens were mounted on the fixture of the flexural testing as shown in Figure 3-4.
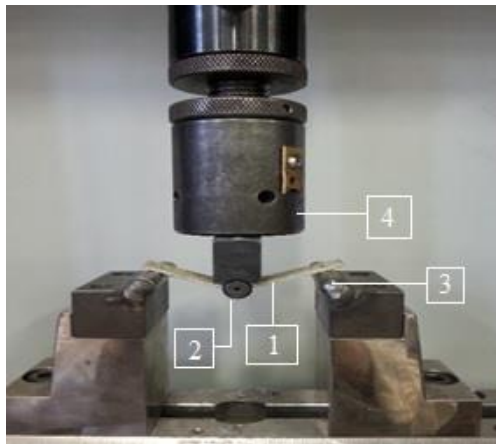
Figure 3-4. Flexural test using setup: (1) Specimen (2) Cylindrical bar   (3) Cylindrical support (4) Loading ram.

The samples were simply supported on two fixed cylindrical supports placed 66 mm apart (L) and loaded to failure by a 10 mm diameter cylindrical bar (D) at the mid-span. The tests were undertaken in accordance with ASTM D7264 / D7264M -15 [158]. The schematic geometry of the three-point bending test setup is illustrated in Figure 3-5.

Load (P)
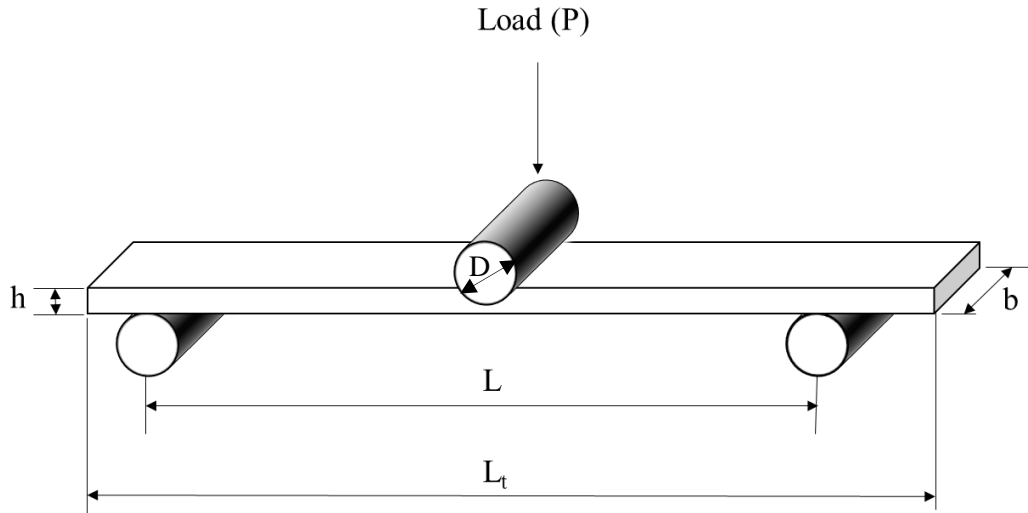
Figure 3-5. Schematic of the three-point bending test.

From the load-displacement curve, the flexure strength and flexural secant modulus of elasticity were calculated using Equations (3.1) and (3.2) below.

$$\sigma = \frac{3PL}{2bh^2} \tag{3.1}$$

$$E_f^{secant} = \frac{L^3 G}{4bh^3} \tag{3.2}$$

where P is the maximum load, L is the support span, G is the slope of the secant of the force-displacement curve, b and h are the width and thickness of the sample, respectively.

3.3.2 Tensile testing

In order to determine the tensile properties of the plain weave GF/PEKK laminates, coupons were cut from the plates according to ASTM D3039/D3039M–14 [159]. Quasi-static tensile tests were conducted using an Instron 3369 testing machine, as shown in Figure 3-6. An extensometer, with a gauge length (GL) of 25 mm, was attached to the middle section of the specimen to measure extension. Three repeat tests were undertaken at a constant crosshead speed of 0.5 mm/minute. The data of load-displacement were recorded by a computer connected to the Intron machine. Here, from the load-displacement data, the ultimate tensile strength σ_t can be calculated using the following equation:

$$\sigma_t = \frac{P}{Bh} \qquad\qquad (3.3)$$

where P is the maximum force, B and h are the specimen's width and thickness, respectively. The following equation was used to calculate the modulus of elasticity (E) values for the constituent materials:

$$E = \frac{\Delta\sigma}{\Delta\varepsilon} \qquad\qquad (3.4)$$

where $\Delta\sigma$ and $\Delta\varepsilon$ are the change in stress and strain, respectively.
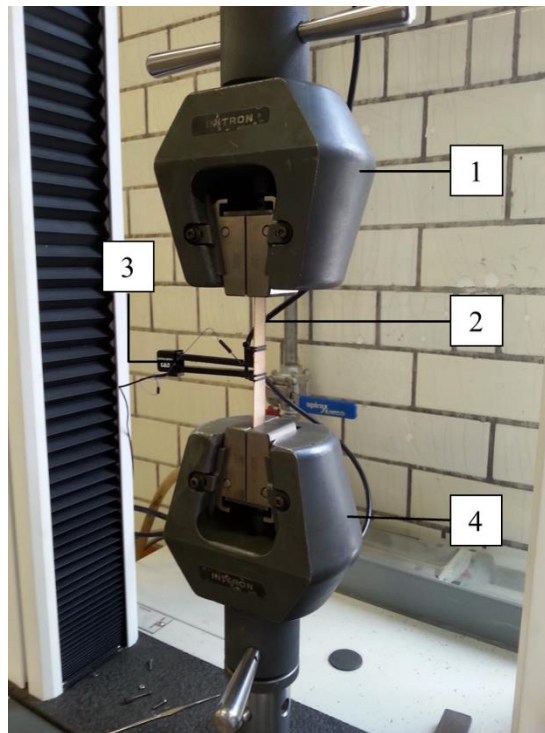
Figure 3-6. Tensile test setup: (1) Upper grip (2) Specimen (3) Extensometer (4) Lower grip.

3.3.3 Shear testing

In order to obtain the shear strength and shear modulus of the composites, a series of in-plane shear tests were undertaken on the GF/PEKK samples according to EN ISO 14129 [160]. Shear test specimens with dimensions of 130 mm (L), 10 mm (B) and 2 mm (h) were cut from the laminated panels and tested at a crosshead displacement rate of 1 mm/min. The tests were

conducted using a screw-driven Instron 3369 universal testing machine. The specimens were prepared by stacking 16 plies at angles of ±45° to the loading axis. The in-plane shear stress (τ_{12}) and in-plane shear modulus (G_{12}) were obtained using the following equations:

$$\tau_{12} = \frac{F}{2bh}$$

$$(3.5)$$

$$G_{12} = \frac{\tau_{12}{}'' - \tau_{12}{}'}{\gamma_{12}{}'' - \gamma_{12}{}'}$$

$$(3.6)$$

where τ_{12} is in-plane shear stress (MPa), F is the maximum load (N), b is the specimen width (mm), h is the sample thickness (mm), G_{12} is the in-plane shear modulus (MPa), $\tau_{12'}$ is the shear stress at a shear strain of $\gamma_{12}{}'$=0.001, $\tau_{12}{}''$ is the shear stress at a shear strain $\gamma_{12}{}''$=0.005.

3.3.4 High temperature tensile testing

The influence of temperature on the tensile strength of GF/PEKK laminates was investigated by conducting tensile tests on an Instron 3369 testing machine, as shown in Figure 3-7. Here, GF/PEKK samples were tested at temperatures of 25, 50, 100, 150, 200 and 250 °C. In order to control the heat as well as the specimen temperature, temperature control system was designed in this study. Here tensile specimens were placed inside a small chamber made of aluminium alloy. Figure 3-8 shows the engineering drawing of the temperature controlled chamber used in this study. The aluminium chamber was surrounding with an insulation material of glass fibre to reduce the heat loss. Here, two thermocouples were attached to the sample at edge and centre locations to monitor the temperature differentiation of the specimens throughout the test. The variation of the temperature inside the chamber was approximately within ± 0.5 % of the desired values.
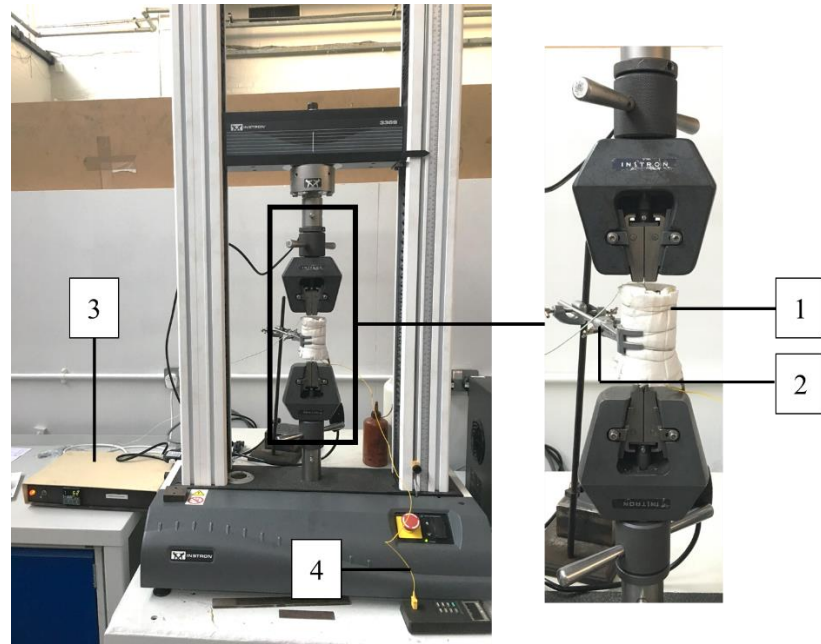
Figure 3-7. Test arrangement for the tensile tests at elevated temperatures: (1) Heating chamber (2) Clamp (3) Temperature controller (4) Thermocouple.
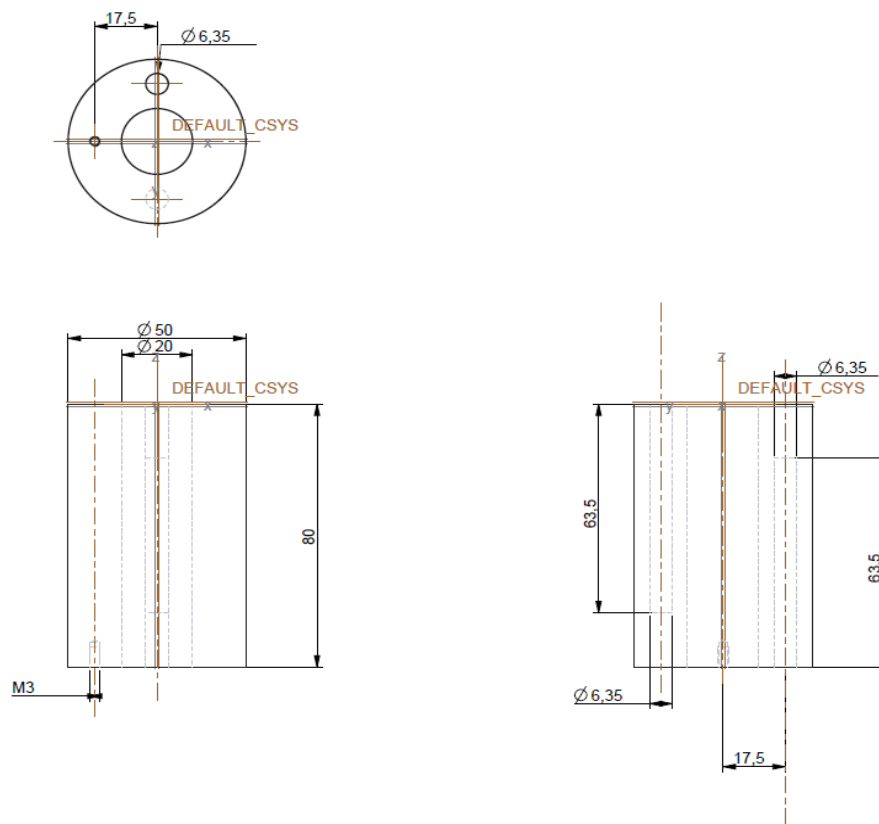
Figure 3-8. Engineering drawing of the temperature controlled chamber.

3.3.5 Quasi-static perforation testing

A series of quasi-static perforation tests were also carried out on the plain GF/PEKK composites. Specimens with dimensions of 100 x 100 mm were clamped in a square steel frame with a 72 mm x 72 mm opening. Figure 3-9 shows a schematic of the square support used in this investigation. A hemispherical indenter, with a diameter of 10 mm, was used to perforate the specimens centrally. The specimens were tested on an Instron 3369 universal testing machine with a maximum loading capacity of 50 kN, as shown in Figure 3-10. A crosshead displacement rate of 1 mm/minute was selected and the load-displacement curve was recorded during each test from which the absorbed energy can be calculated. Optical microscope was then used to highlight the failure modes of the specimen after testing.
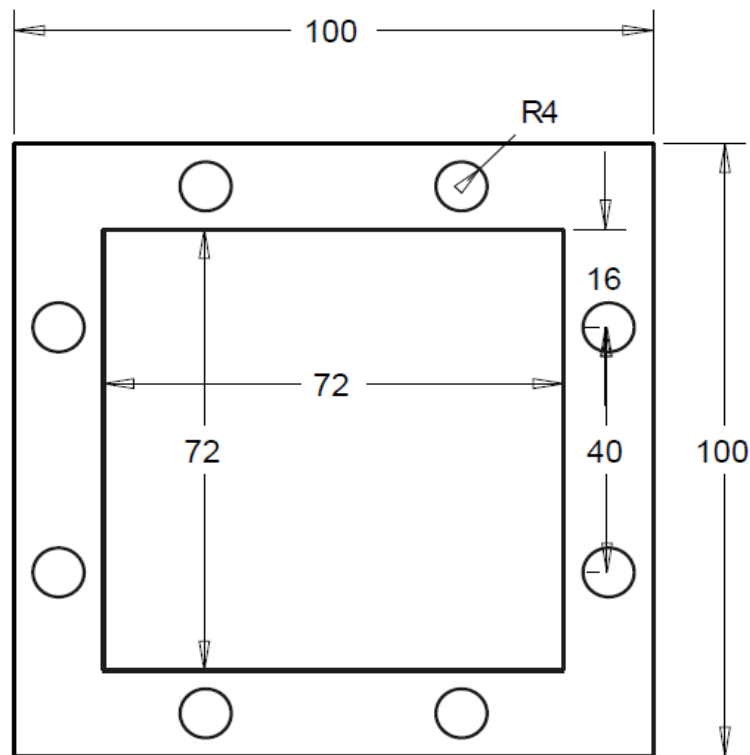
Figure 3-9. The square fixture used to clamp samples.
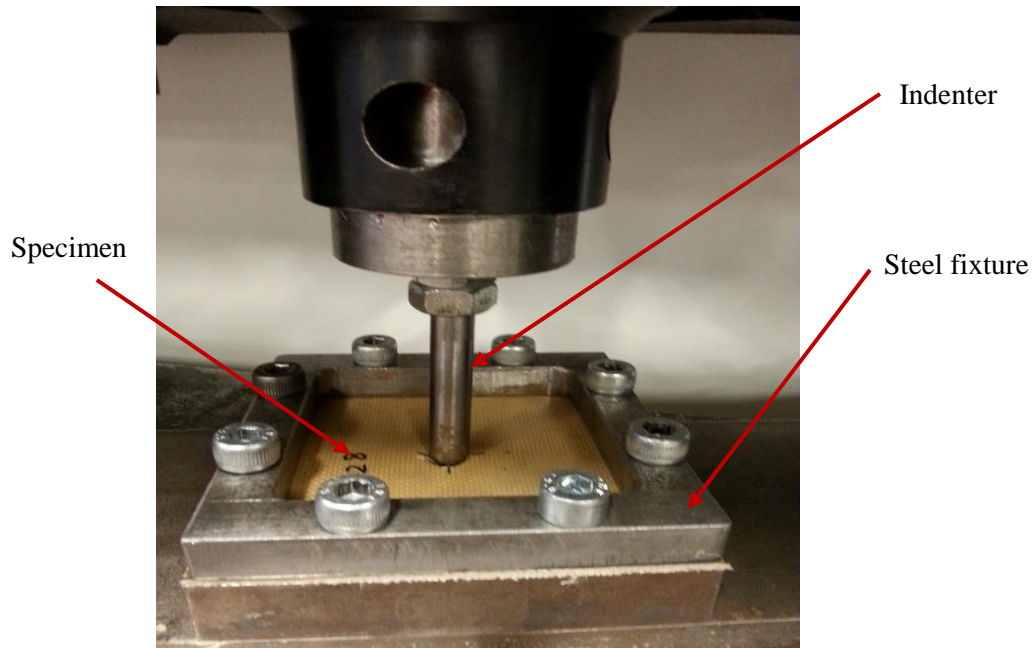
Figure 3-10. Quasi-static perforation test set-up.

3.3.6 Low velocity impact testing

3.3.6.1 Impact perforation testing

Low velocity impact tests were conducted on 4-, 8-, 12- and 16- ply plain weave S-glass fibre reinforced PEKK laminates using a drop-weight tower, a schematic of the impact setup is shown in Figure 3-11. Here, a steel mass was attached to a carriage with a 10 mm diameter hemispherical steel indenter to impact the panels, with size of 100 mm x 100 mm, centrally. The mass of the impactor was 1.37 kg and the release height of the carriage was varied between 0.29 and 1.09 meters. The measured perforation energies for these composites under quasi-static perforation tests (described in section 3.3.5) were initially used as a reference to select the required energies to perforate the specimens under dynamic loading. However, these absorbed energy values were not enough to give a full perforation to the investigated specimens. Therefore, the impact energy for each system was increased slightly up to perforation. The perforation energies for the 4-, 8-, 12- and 16-ply laminates were set to 4, 8, 11 and 15 Joule, respectively.

The composite plates were clamped on the same fixture frame used for quasi-static perforation test. The impact force during testing was measured using a piezo-electric load cell located immediately above the indenter. During the test, the traces of force-time were obtained by converting the voltage history using a 10 kN load cell (Kistler 9321A piezo-electric). The maximum displacement of the targets was captured by using a high speed camera (HSC, MotionPro X4, Model No. X4CU-U-4) with resolution of 10000 frames per second placed in the front of the impact tower, as shown in Figure 3-12. Here, the target was attached to the projectile and the HSC was placed in the same level when the projectile starts to hit the targets. In order to increase clarity, two high voltage lights were directed towards the samples. Once the impactor mass was released, the high speed camera begins to record the video frames of impact event which takes not more than 10 ms. The recorded displacement by the HSC was then converted to displacement–time history using a Pro-analyst software. More details about the motion analysis software Pro-analyst is presented in Table 3-2. Table 3-3 shows the details of the specimens investigated following the impact tests. The specific perforation energy of the panels can be calculated by normalising the absorbed energy during perforation by the areal density of the target.
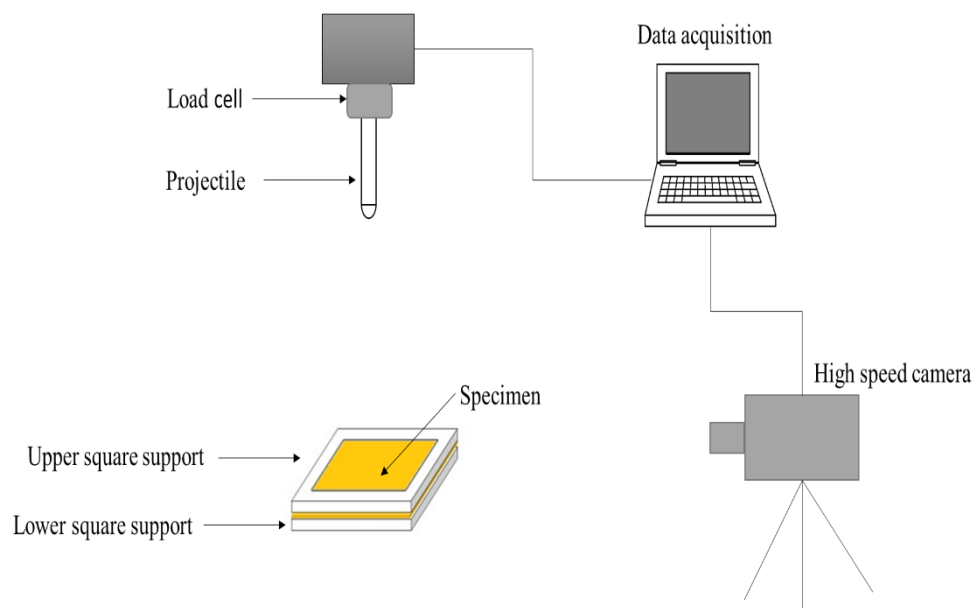
Figure 3-11. Schematic of impact test.
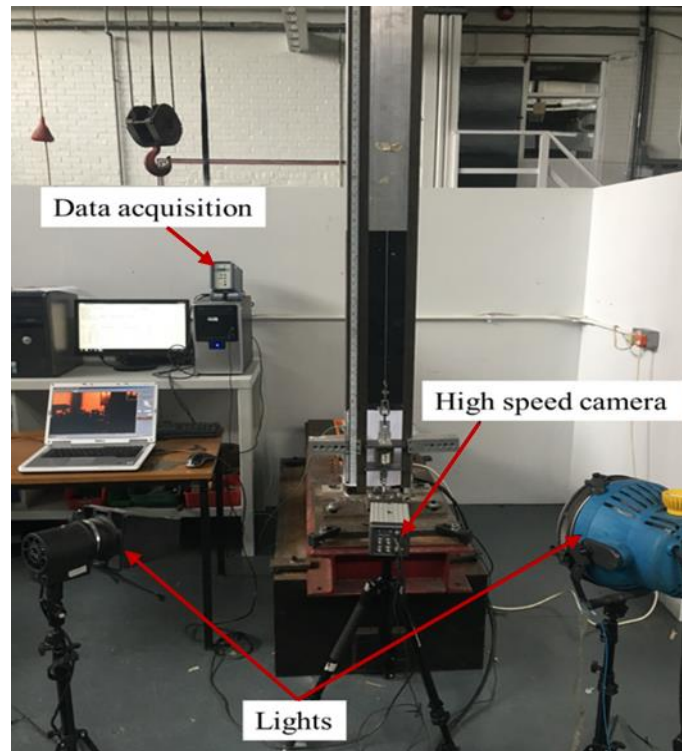
Figure 3-12. Low velocity impact set-up.

Table 3-2. Details of the motion analysis software Pro-analyst.

Make	Xcitex
Version	Workstation
Edition	Professional
Registration code	13146-7689-930
Serial number	726261

Table 3-3. Summary of the GF/PEKK laminates subjected to low velocity impact test with a 10 mm diameter hemispherical steel indenter.

GF/PEKK laminates	Impactor mass (kg)	Initial velocity (m/s)	Energy (J)
4-ply	1.37	2.42	4
8-ply	1.37	3.42	8
12-ply	1.37	4.01	11
16-ply	1.37	4.68	15

3.3.6.2 Additional impact testing

Further impact tests were undertaken to investigate the influence of the project shapes and diameters on the impact response of 8-ply GF/PEKK panels. Here, a steel fixture which is described previously was used to clamp 100 x 100 mm samples. Three indenter shapes were used in this investigation, and these being hemispherical, partially flat and conical projectiles, as shown in Figure 3-13.

For the hemispherical projectiles, four diameters were used to impact the specimens, and these being 5, 10, 15 and 20 mm, as shown in Figure 3-14. Here, 8-ply laminates were undertaken in this investigation. Details on these tests are shown in Table 3-4. Low magnification micrographs with a magnification factor of 3.6 were then taken to the cross-section for the failed specimens to highlight the failure modes.

(a)
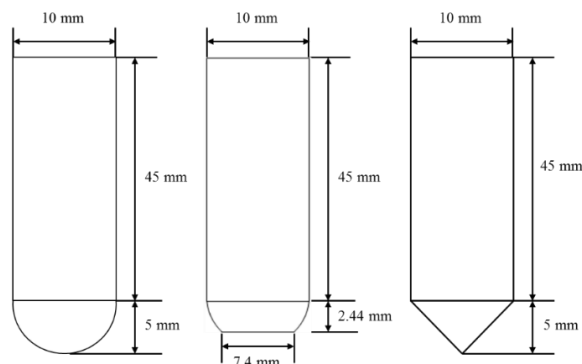
(b)

Figure 3-13. Photograph (a) and schematic cross-sections (b) of the hemi-spherical, partial-flat and conical indenter (10 mm diameter).

Figure 3-14. Hemi-spherical projectiles with diameters of 5, 10, 15 and 20 mm.

Table 3-4. Summary of laminates under low velocity impact.

Indenter shape	Indenter diameter	Impactor mass (kg)
Hemispherical	5	3.02
Hemispherical	10	3.02
Hemispherical	15	3.19
Hemispherical	20	3.22
Partial flat	10	3.02
conical	10	3.02

3.4 Manufacturing FMLs and perforation testing

3.4.1 Manufacturing processes

3.4.1.1 Titanium-based fibre metal laminates (FMLs)

The fibre metal laminates (FMLs) examined in this investigation were based on 0.14 mm thick layers of β-titanium alloy (15% V, 3% Al, 3% Cr, and 3% Sn) foil from TICOMP (California, USA) and woven S-glass fibre reinforced PEKK (GF/PEKK) prepregs (details of the manufacturing procedure are mentioned in Section 3.2.1). The FMLs were manufactured by stacking an appropriate number of metal and composites plies in a picture frame with dimensions of 100 x 100 mm, as shown in Figure 3-15.
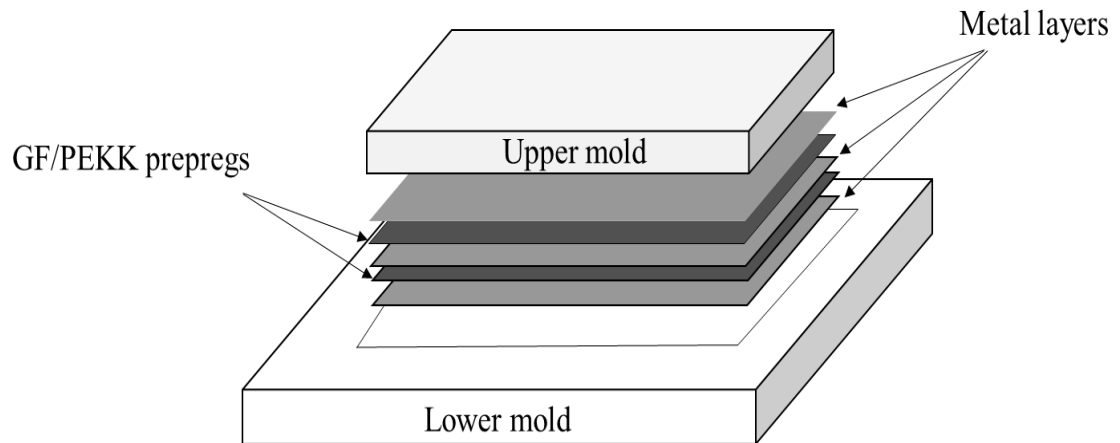
Figure 3-15: Stacking arrangement of the fibre metal laminates.

A 50 µm film of PEKK (ARKEMA, France) was placed between the titanium and GF/PEKK prepregs to ensure good bonding between the constituent materials. Prior to manufacturing, the titanium sheets were subjected to laser treatment to increase the surface roughness as well as the interface bonding strength. The FMLs specimens were manufactured by stacking the titanium alloy foils and plies of GF/PEKK prepregs in a picture frame mould with 100 x 100 mm dimensions. The mold was then heated in a Meyer hydraulic hot press to 330 ºC at a heating rate of about 3 ºC/min, maintained at this temperature for 30 minutes before cooling to room temperature. A pressure of 0.5 MPa was applied to the laminates during the processing cycles.

Details of the composite laminates investigated in this study are given in Table 3-5. A range of stacking configurations (i.e. the number of the metal and composite laminates) were considered in this study. Initial attention was focused on the 2/1 FMLs with various composite cores, and these being 2, 4, 8, 12 and 16 plies of GF/PEKK laminates. More tests were undertaken subsequently on the 3/2, 4/3 and 5/4 FMLs with composite core based on 2 plies of GF/PEKK composite.

Table 3-5: Stacking configurations of titanium-based FMLs investigated.

Laminate	Configuration		Nominal thickness (mm)
FMLs (2/1)	2 Titanium layers+1 composite layer	(2-ply)	0.51
FMLs (3/2)	3 Titanium layers+2 composites layers	(2- ply)	0.92
FMLs (4/3)	4 Titanium layers+3 composites layers	(2- ply)	1.29
FMLs (5/4)	5 Titanium layers+4 composites layers	(2- ply)	1.64
FMLs (2/1)	2 Titanium layers+1 composites layers	(4- ply)	0.75
FMLs (2/1)	2 Titanium layers+1 composites layers	(8- ply)	1.15
FMLs (2/1)	2 Titanium layers+1 composites layers	(12- ply)	1.6
FMLs (2/1)	2 Titanium layers+1 composites layers	(16- ply)	2

3.4.1.1.1 Laser surface treatment of titanium alloys

Laser pre-treatment of titanium surface was carried out using different power parameters of laser to investigate the influence of these parameters on the surface roughness, residual tensile strength of titanium alloy and metal-resin bonding strength. Firstly, titanium alloys were cut to required sizes and cleaned with acetone prior to the laser treatment. A nanosecond pulsed laser (SPI 20W G4 HS L Type) was used to modify the surface microstructure of the material. The laser pulsed system works with 1064 nm wavelength, a variable pulse width of 9 - 200 ns, 20 W of maximum output power and a pulse repetition rate of 25-500 kHz. The spot size of the focused beam is 45 μm. A line pattern microstructure was created; the space between the lines was set as 29 μm. The processing area was treated with the parameters on Table 3-6. The parameters were used in order to create overlap between the laser pulses modifying the roughness of the surface, with an example of the scanning technique being showed in the Figure 3-16. After that, surface was characterised by an optical profiling system (Wyko NT1100) to measure the mean surface roughness. The three dimension (3D) profile of titanium foils treated under different laser power parameters is shown in Figure 3-17 . The resultant morphologies of the different laser treatment powers were then characterised by scanning

electron microscope (SEM) using a JEOL JSM 6610 SEM (imaging centre at University of

Liverpool).

Table 3-6: Laser treatment parameters used for titanium alloy.

Laser fluence	4.09, 4.54, 5 and 5.45 J/cm^2
Repetition Rate	70 kHz
Pulse Length	200 ns
Scan Speed	2.380 mm/s
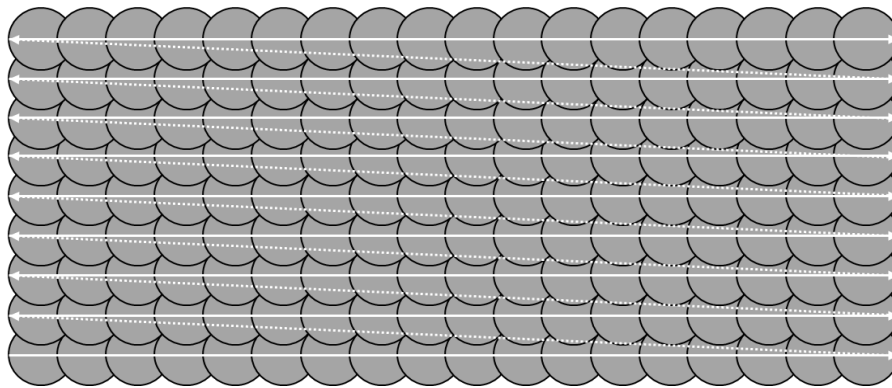
Figure 3-16: Scanning path of the laser, horizontal distance between pulses of
34 μm, and a vertical distance between lines of 29 μm.

(a)   (b)
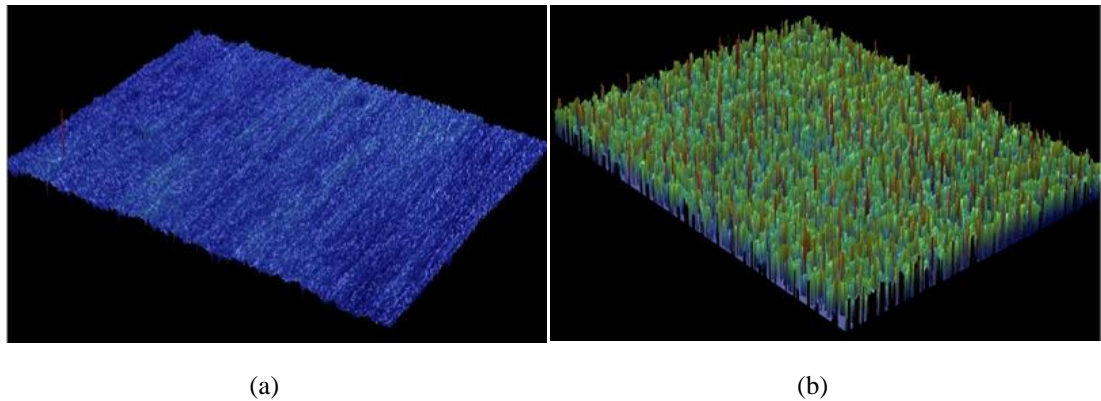
Figure 3-17. 3D profile of a titanium surface under different power parameters, (a)
as received surface, (b) surface treated with laser fluence of 4.54 J/cm^2.

3.4.1.2 Aluminium-based fibre metal laminates (FMLs)

Aluminium-based FMLs used in this investigation were manufactured by bonding layers of

GF/PEKK composites with 0.5 mm thick 2024-T3 aluminium alloy sheets, supplied by

Aircraft Materials Ltd. The stacking configuration was ranging from 2/1 lay-up to 5/4 laminates. Table 3-7 summarises the stacking configurations of the aluminium-based FMLs investigated in this study.

A 50 µm film of PEKK (ARKEMA, France) was placed between the aluminium alloy and GF/PEKK to ensure good bonding between the constituent materials. Prior to manufacturing, the aluminium sheets were subjected to surface treatment by using sand blasting technique to increase the surface roughness as well as the adhesion between the composite and metal layer. The FMLs were manufactured by stacking an appropriate number of metal and composites plies in a picture frame with dimensions of 100 x 100 mm using Meyer hydraulic hot press.

Table 3-7. Stacking configurations of aluminium-based FMLs investigated in this study.

Laminate	Configuration	Nominal thickness (mm)
FMLs (2/1)	2 Aluminium layers+1 composite layer (4- ply)	1.51
FMLs (3/2)	3 Aluminium layers+2 composites layers (4-ply)	2.48
FMLs (4/3)	4 Aluminium layers+3 composites layers (4-ply)	3.61
FMLs (5/4)	5 Aluminium layers+4 composites layers (4-ply)	4.37

3.4.1.2.1 Surface pre-treatment of aluminium alloy

The surfaces of aluminium alloy specimens were pre-treated using sand blasting technique to enhance the surface properties as well as the resin-metal adhesion properties. Here, a blasting powder of glass beads with average diameter of 200-300 µm was used in this study. All the sandblasting treatments were conducted using Guyson Bead Blaster (Formula F1200 system). A pen type hand piece blaster was used to power the sandblasting with air pressure of 65 Psi. During the sandblasting process, the nozzle of the sandblasting was always kept perpendicular to the aluminium surface. The distance of about 30 mm was kept constant between the nozzle and the work piece and the time of sandblasting treatment for all specimens was kept constant of 15 seconds.

3.4.2 Mechanical testing

3.4.2.1 Tensile testing

Tensile tests were undertaken on aluminium alloy and titanium alloy to determine the tensile properties of the constituent materials. Here, coupons of aluminium alloy (2024-T3) and titanium alloy (15-3-3-3-β) were cut from the plates with different geometries according to ASTM recommendations, as shown in Figure 3-18. For the aluminium alloys specimens were prepared according to ASTM E8/E8M-16a [161], whereas the tensile test of titanium alloy were conducted according to previous work [162]. An extensometer, with a gauge length (GL) of 50 mm was used to measure the extension for the aluminium and titanium alloys. The tensile tests were undertaken at a constant crosshead speed of 0.5 mm/minute using a screw-driven Instron 3369 universal testing machine, as shown in Figure 3-19.

a

b
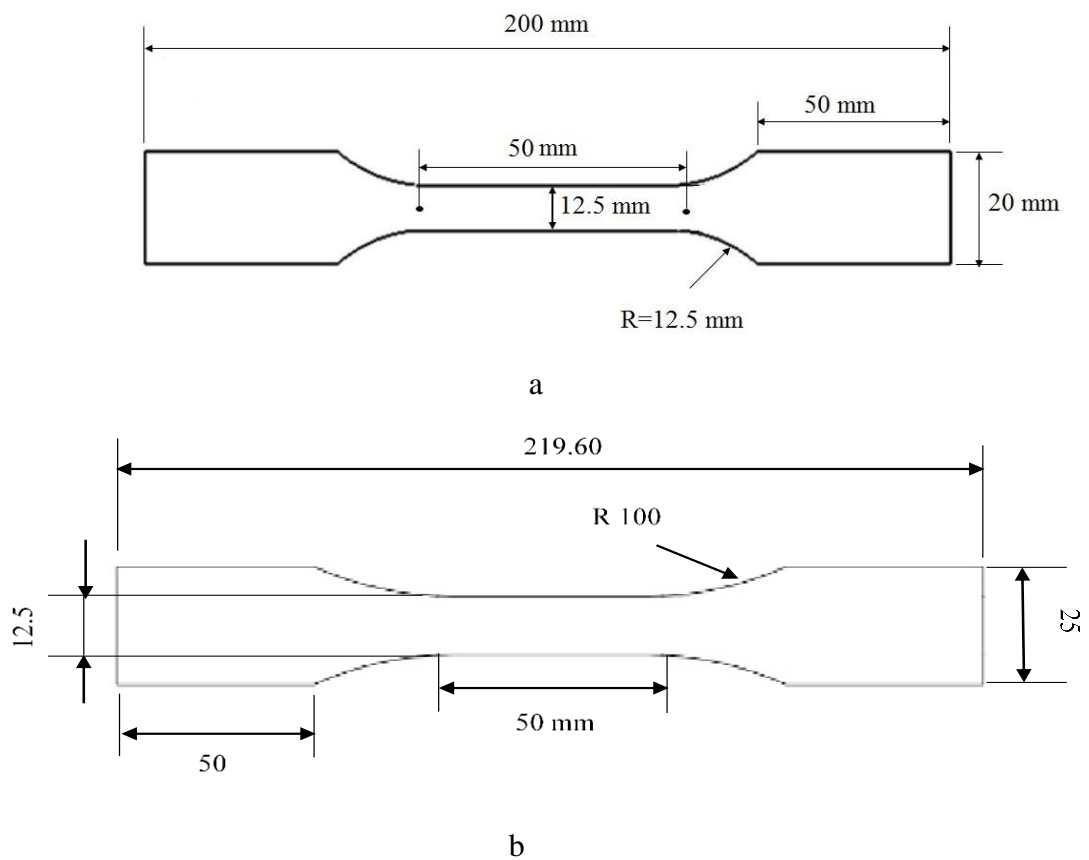
Figure 3-18. Specimen geometries for investigated materials; (a) aluminium alloy, (b) titanium alloy.
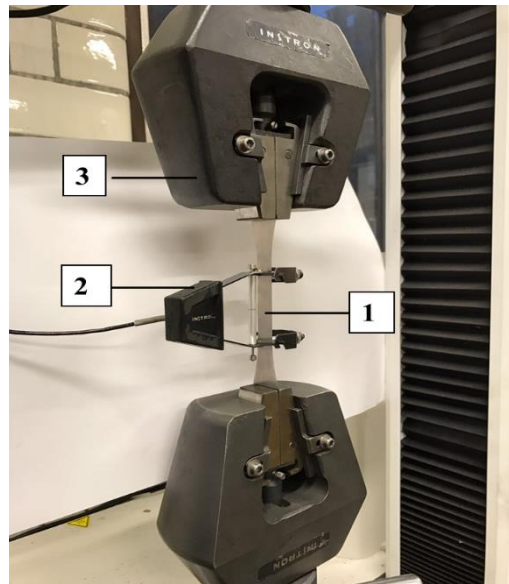
Figure 3-19.Tensile test setup: (1) Specimen (2) Extensometer (3) Holding grips.

3.4.2.2 Single-lap shear testing

The single shear lap test was performed to examine the shear strength between PEKK film and modified surface titanium, Here, single-lap shear tests were conducted on pairs of the laser treated titanium stripes. An overlapping area of 23x 4 mm^2 using PEKK film (0.1 mm thick) was used to bond these titanium strips as shown in Figure 3-20. The dimensions of the lap shear specimens were prepared according to German standard DIN EN 1465 which suitable for testing adhesive bonds with thermosetting glue. The bonding strength of the thermoplastic-based adhesive was expected to be higher than those obtained by thermosetting adhesive. Therefore, higher load and stress would be needed to fail the specimens, resulting in high stress concentration and plastic deformation which leads to fail the titanium strips instead of the joint [163]. To avoid this, the overlap (joint) area between the stripes was reduced to be 23x 4 mm^2. The maximum shear (bonding) was measured using an Instron model 3369 universal testing machine equipped with a load cell with a capacity of 50 kN, as shown in Figure 3-21. The tests were carried out at a slow extension rate of 1 mm/min which corresponds to quasi-static conditions. Three samples were tested for each laser parameter and the average values with standard deviation were given.

Width: 23   Titanium strip   4   72.5

Thickness: 0.14

PEKK film   140
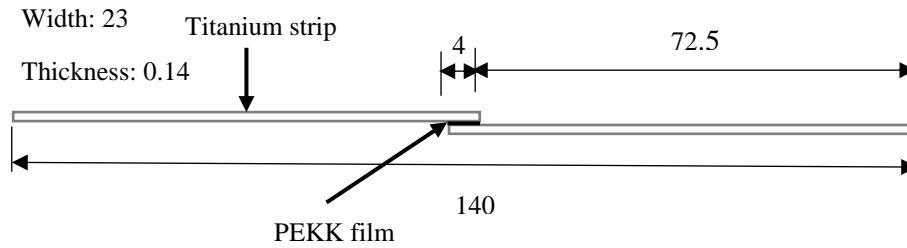
Figure 3-20. Single-lap shear specimen (dimensions in mm).
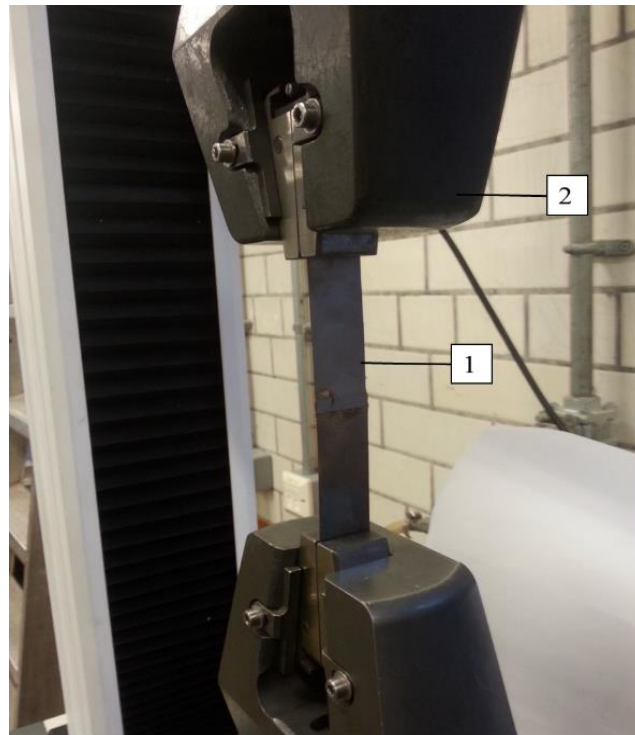
Figure 3-21. Single-lab shear test setup: (1) Specimen (2) Holding grips.

3.4.2.3 Quasi-static perforation testing

Quasi-static perforation tests were conducted on 2/1, 3/2, 4/3 and 5/4 titanium- and aluminium-based FMLs. The composite cores were 2- and 4-ply for titanium- and aluminium-based FMLs, respectively. The targets were fixed in a 100 mm x 100 mm square frame with internal dimensions of 72 mm x 72 mm same as before. The perforation tests were carried out using a hemispherical indenter with diameter of 10 mm (Figure 3-13). The tests were undertaken also using the Instron 3369 universal testing machine with a maximum loading capacity of 50 kN, as shown in Figure 3-22.
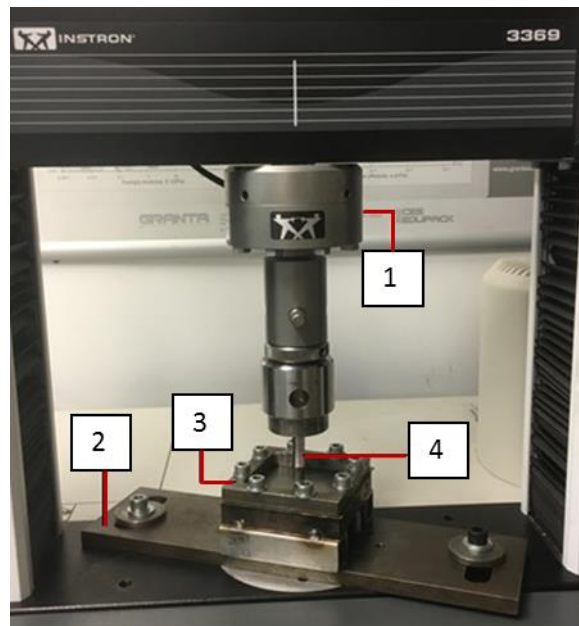
Figure 3-22. Quasi-static perforation setup for FMLs: (1) Load-cell (2) Fixture (3) specimen support (4) indenter.

3.4.2.4 Low velocity impact testing

Low velocity impact perforation tests were conducted on the titanium- and aluminium-based fibre metal laminates using the drop-weight tower, as shown in Figure 3-23 . A steel mass was attached to a carriage with hemispherical steel indenter (10 mm diameter) to impact the panels with size of 100 mm x 100 mm, centrally. The specimens were clamped using the same frame used for the quasi-static perforation tests. Details of the specimens stacking configuration, project mass and the initials velocity for both FMLs systems are summarised in Table 3-8 and Table 3-9, respectively.
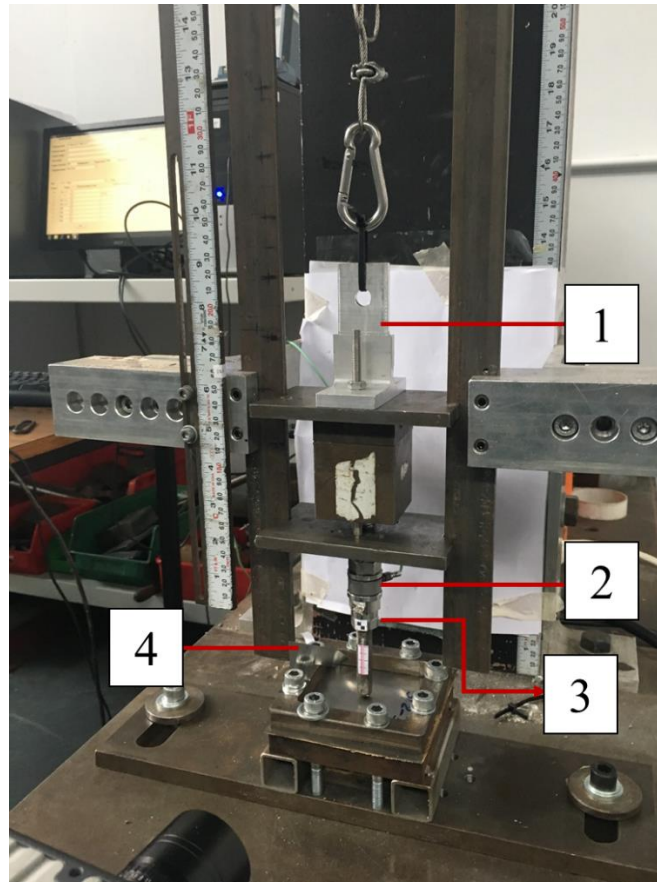
Figure 3-23. Impact test for FMLs: (1) impactor mass (2) Load cell (3) Target (4) Guide.

Table 3-8: Summary of the titanium-based FMLs subjected to low velocity impact. test.

FMLs	Impactor mass (kg)	Initial velocity (m/s)
2/1 (2-ply)	1.48	4
3/2 (2-ply)	2.67	3.6
4/3 (2-ply)	3.84	3.6
5/4 (2-ply)	4.97	3.6
2/1 (0-ply)	1.43	3.6
2/1 (4-ply)	1.43	4
2/1 (8-ply)	1.43	4.4
2/1 (12-ply)	1.43	4.7
2/1 (16-ply)	1.43	5.1

Table 3-9: Summarise the details of aluminium based FMLs subjected to low velocity impact.

FMLs	Impactor mass (kg)	Initial velocity (m/s)
2/1 (4-ply)	3.56	4
3/2 (4-ply)	5.57	4
4/3 (4-ply)	8.34	4
5/4 (4-ply)	9.80	4

3.5 Imaging for damage characterization

3.5.1 Optical and scanning microscopies

Low magnification images (3.6x) were obtained by using an optical microscope camera (Infinity 2, Lumenera Corporation) with low magnification microscopy to elucidate the failure mechanism of damaged zone for the plain composites and fibre metal laminates tested. After testing, samples were sectioned and polished using various grades of silicon carbide papers. For the high magnification resolution, a microscopy type A Leitz Wetzlar Metalloplan was utilised to highlight the distribution of the fibres and resin powders.

3.5.2 Scanning electron microscopy (SEM)

Scanning electron microscope (SEM) Type JEOL JSM 6610 SEM (Imaging Centre at University of Liverpool) was used to highlight the resin-fibre distribution of the GF/PEKK and the surface morphology of the titanium alloy surfaces before and after laser treatment. For the plain composite laminates, the specimen surface was coated with a thin layer of silver to make it more conductive.

3.6 Summary

Chapter 3 presents the details of the experimental work in terms of specimen manufacturing process, experimental procedures and testing of the material properties under quasi-static and dynamic loading rates. Here, plain composite laminates of S-glass fibre reinforce PEKK, aluminium-based FMLs and titanium-based FMLs are included in this investigation. Firstly, the GF/PEKK composites were subjected to a series of tensile and quasi-static perforation tests to optimise the PEKK percentages. The material properties of these specimens were then characterised throughout tensile, shear, flexural tests on the plain GF/PEKK composites, and tensile tests on titanium and aluminium alloys. Low velocity impact tests were conducted on the plain composite laminates and the both FML systems. Then, the cross-sections of the tested specimens have been highlighted to clarify the failure mechanisms. Details of the test results will be presented and discussed in Chapter 4.

4 Chapter 4: Experimental Results and Discussion

4.1 Introduction

The experimental results obtained in chapter 3 are presented in this chapter. Initially, the influence of the binder between S-glass fibre and the resin powder (PEKK) on the mechanical properties of the GF/PEKK laminates is presented. The results of quasi-static and tensile tests of the composites are then evaluated to obtain the optimised weight fractions of the fibre and the resin within the composites. Subsequently, the results of flexural, shear and tensile tests conducted on woven s-glass fibre reinforced PEKK (GF/PEKK) laminates are given, together with a discussion. The results of the 4-, 8-, 12- and 16-ply GF/PEKK laminates subjected to quasi-static perforation and low velocity impact are also presented and outlined. In addition, the impact response of 8-ply GF/PEKK laminates impacted by various projectile shapes and diameters are outlined and discussed.

For the work on fibre metal laminates, the material properties of titanium and aluminium alloys following tensile tests are initially presented. This is followed by the results following tests investigated by the quasi-static perforation and impact perforation response of the 2/1, 3/2, 4/3 and 5/4 FMLs based on titanium and aluminium alloys. Finally, the results of titanium-based FMLs (2/1) with various core thicknesses, i.e. 2-, 4-, 8-, 12- and 16-ply GF/PEKK composites are also shown and discussed.

4.2 Mechanical characterization of the plain composite

4.2.1 Optimization study on the composite materials

Experimental testing initially focused on investigating the effect of a binder between the thermoplastic powder and the fibres on the mechanical properties of the GF/PEKK laminates. This work was based on manufacturing (100 x 100) mm^2 composite panels (4-ply) with and without binder. The first group of panels was manufactured without using an adhesive (binder) between the fibres and the matrix. In contrast, the other panels were made with using an

adhesive between resin and the fibres. The response of these panels under tensile and quasi-static perforation tests was then evaluated

4.2.1.1 The effect of the adhesive on the perforation resistance of the laminated composites

Figure 4-1 shows the average load-displacement traces following quasi-static perforation tests on panels manufactured with and without the use of an adhesive. An examination of the figure indicates that both traces exhibit similar initial stiffness characteristics. However, the maximum force for the modified laminate is roughly double that of its untreated counterpart. Clearly, the higher maximum forces value for the treated panels are associated with the enhanced level of adhesion between the thermoplastic polymer and the glass fibres.
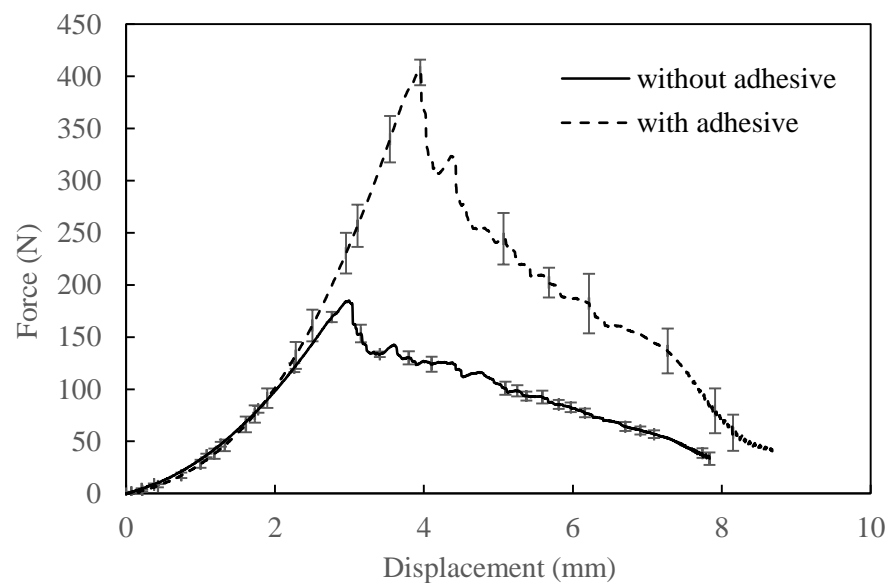
Figure 4-1. Load-displacement traces following quasi-static perforation tests on the 4- ply GF/PEKK composites. The loading head is hemi-sphere with a 10 mm diameter.

4.2.1.2 The effect of adhesive on the tensile properties of the laminated composites

The influence of fibre treatment on the tensile strength of the GF/PEKK samples was also studied. Here, tensile tests were conducted on 4-ply laminates with a thickness of 0.47 mm and the engineering stress-strain traces are shown in Figure 4-2. As noted previously, the adhesive-treated laminates offer strength properties that are more than double those associated with the untreated laminates. This is attributed to the adhesive which makes a uniform distribution of PEKK powder on the glass woven.
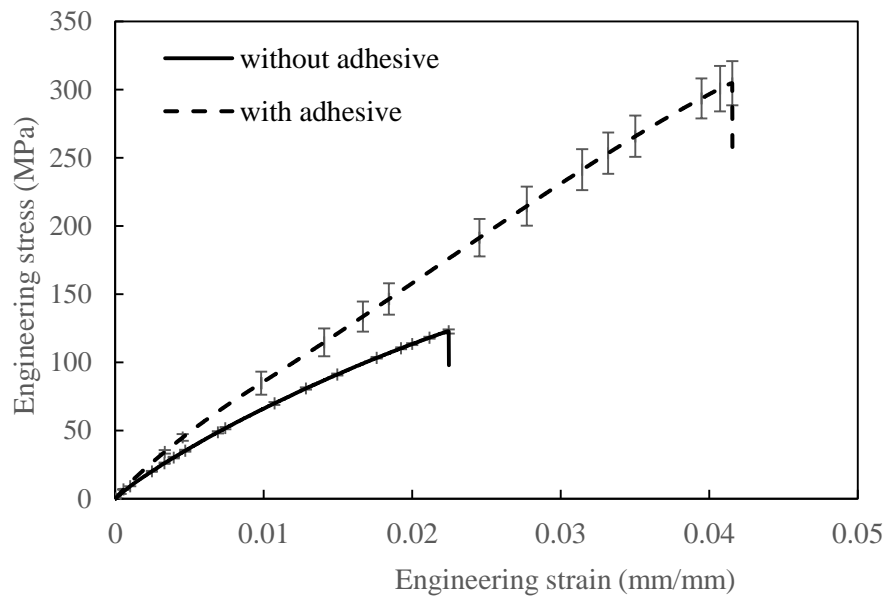
Figure 4-2. Engineering stress-strain curves for the 4-ply PEKK/GF composites
(with and without fibre adhesive treatment).

4.2.1.3 The effect of the weight fraction of PEKK on the tensile properties of the PEKK laminates

Further investigations have been undertaken on GF/PEKK panels to evaluate the influence of the weight fraction of PEKK on the tensile strength of the laminates. Figure 4-3 shows the typical engineering stress-strain traces of GF/PEKK with different PEKK weight percentages (30, 35, 40, 45 and 50 wt. %). It can be noted from the figure that all samples show a similar

behaviour under tension in which the stress increases to a peak value which represents the tensile strength of the laminates before failure. Clearly, a 40 % weight fraction of PEKK powder gives the best performance in terms of the peak stress and the corresponding strain.
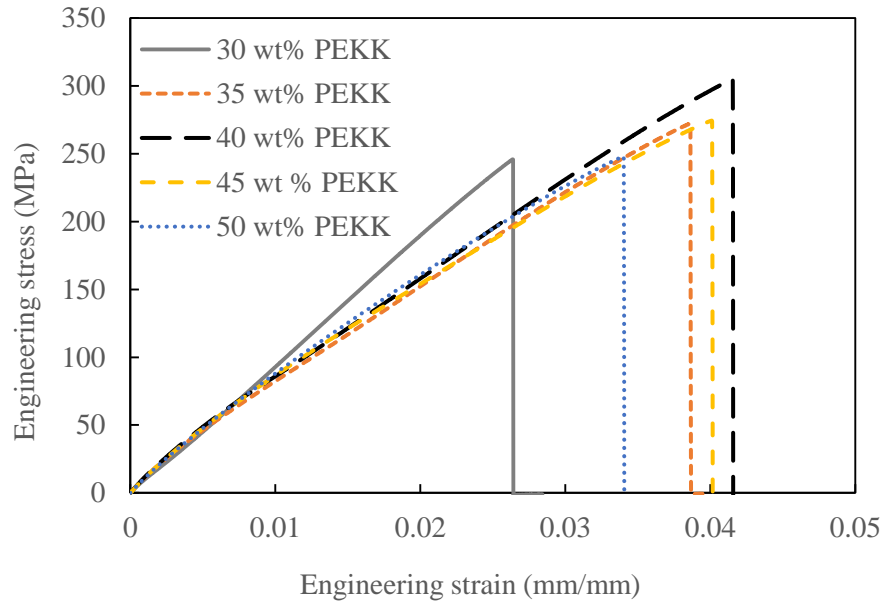
Figure 4-3. Engineering stress-strain traces of GF/PEKK with different PEKK weight percent.

The influence weight percentage of PEKK on the tensile strength of the GF/PEKK composites is illustrated in Figure 4-4. Clearly, the tensile strength increases with PEKK wt. %, reaching the maximum of 304 MPa, corresponding to a PEKK weight fraction of 0.4. At higher weight fractions, a noticeable drop in the tensile strength occurs, probably due to the presence of fibre-poor regions within the matrix. The above results suggest that, in terms of mechanical properties, the optimum weight fraction of PEKK is close to 0.4.
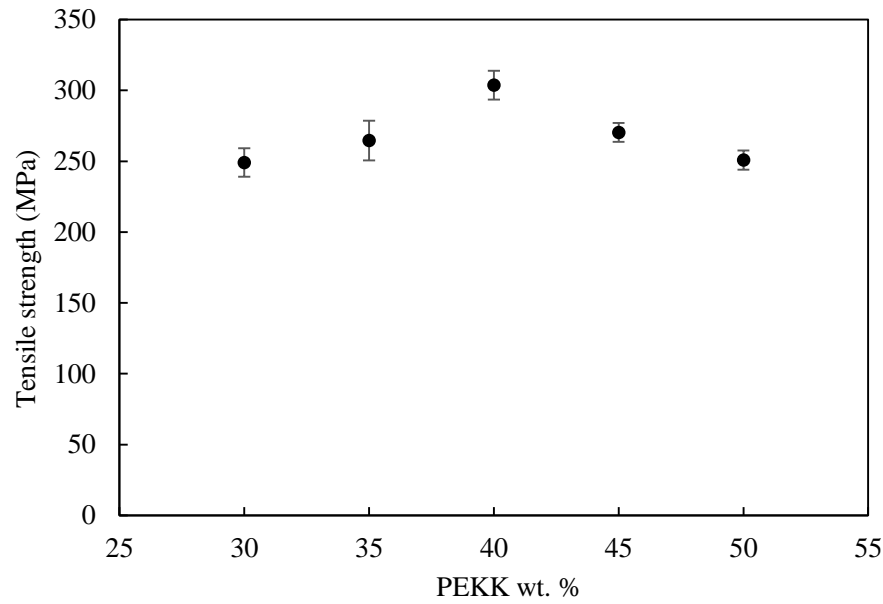
Figure 4-4. Tensile strength versus weight percentage of PEKK.

4.2.1.4 The effect of the weight fraction of PEKK on the quasi-static perforation properties of the PEKK laminates.

The next part of this investigation considers optimising the proportion of PEKK resin (wt. %) in the prepregs. In this study, quasi-static perforation tests were performed on 4-ply GF/PEKK panels placed on a steel support with an open internal rectangular area of 72 mm x 72 mm. Different PEKK powder concentrations (30, 35, 40, 45 and 50 wt. %) were investigated. Figure 4-5 presents load-displacement traces following quasi-static perforation tests on laminates with the weight fractions of PEKK being investigated. It can be seen that all of the traces exhibit similar trends during the perforation process, with the force initially increasing in a non-linear fashion to the maximum value at a displacement of approximately 4 mm, followed by a progressive decrease as the indenter perforates the plate. Clearly, the maximum force increases with PEKK weight fraction, reaching the highest value at 0.4. The area under the force-displacement curve was then used to determine the perforation threshold of each laminate. Figure 4-6 shows the variation of energy absorption with PEKK weight percentage following quasi-static perforation tests. It can be seen that the perforation energy of these laminates increases with increasing PEKK percentage, reaching a plateau value at 0.4 again.
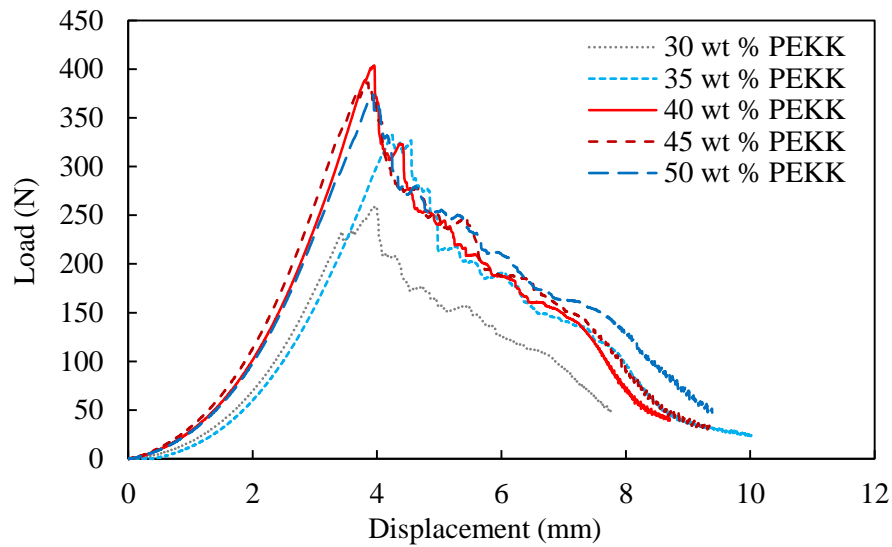
Figure 4-5. Load-displacement traces following quasi-static perforation tests on the GF/PEKK (4-ply) panels based on different weight fractions of PEKK.
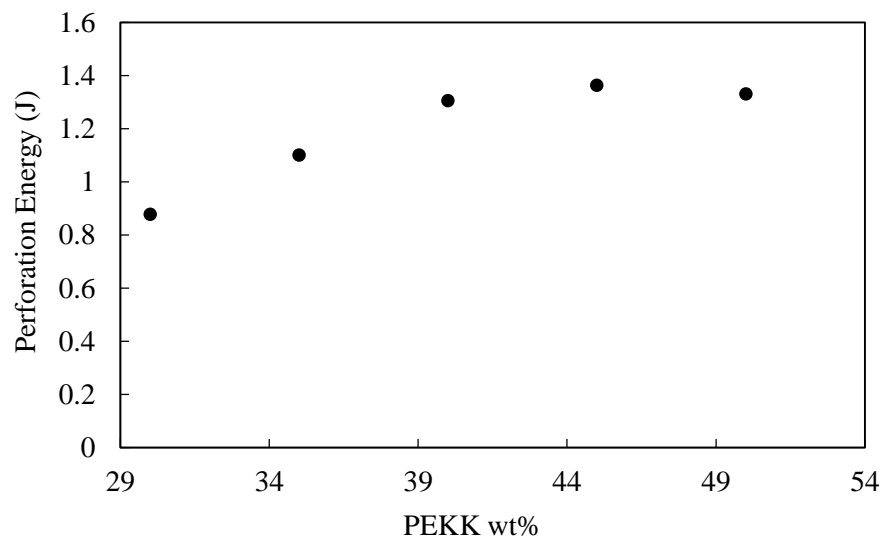
Figure 4-6. Perforation energies of the GF/PEKK (4-ply) composites based on different weight fractions of PEKK following quasi-static perforation tests.

Figure 4-7 shows the micrographs of laminates based on 30 % and 40% weight percentages of PEKK. An examination of the micrographs indicates that the amount of powder for the laminates with 30 wt. % of PEKK was not enough to provide good bonding between the resin and the fibres, leading to form resin-poor areas which act as weak points between the resin and the fibres, resulting in a lower peak force and energy absorption comparing with other panels with 40 % PEKK concentrations.
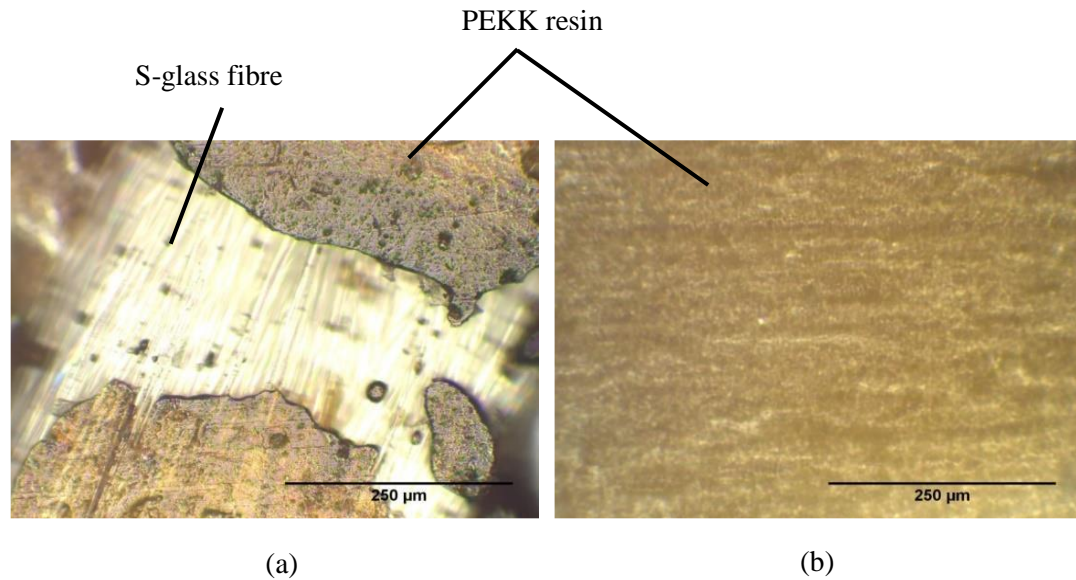
Figure 4-7. Micrographs of GF/PEKK laminates with 30 wt. % (a) and 40 wt. % (b) of PEKK resin at 250x magnification.

4.2.1.5 The effect of the thickness variation on the tensile properties of PEKK composites.

In order to assess the effect of specimen thickness on the tensile strength of GF/PEKK laminates, samples were manufactured with different thicknesses, i.e. 4, 8, 12 and 16-ply. The variation of tensile strength with specimen thickness is shown in Figure 4-8. The resulting experimental data show that the tensile strength of GF/PEKK panels is not significantly affected by the sample thickness, with the tensile strength being approximately 300 MPa, except for the 16-ply sample.

Figure 4-9 shows SEM images of a 4-ply GF/PEKK (60/40 wt. %), where it can be seen that the glass fibres are fully impregnated by the PEKK polymer. This point is emphasised when examining the high magnification image, where it is evident that the thermoplastic resin has flowed between the individual glass fibres to give a high-quality composite laminate.
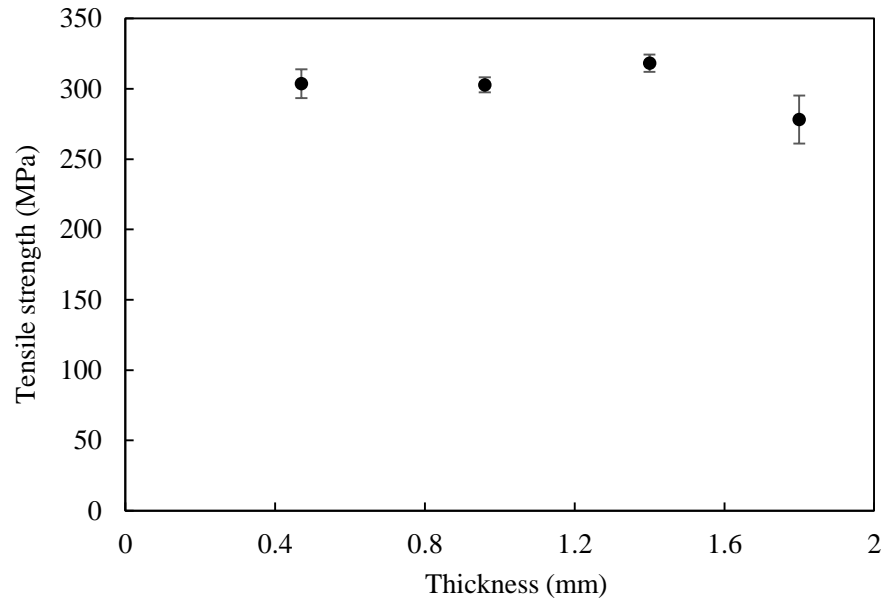
Figure 4-8. The variation of tensile strength with sample thickness for the GF/PEKK laminates.

(b)

(a)
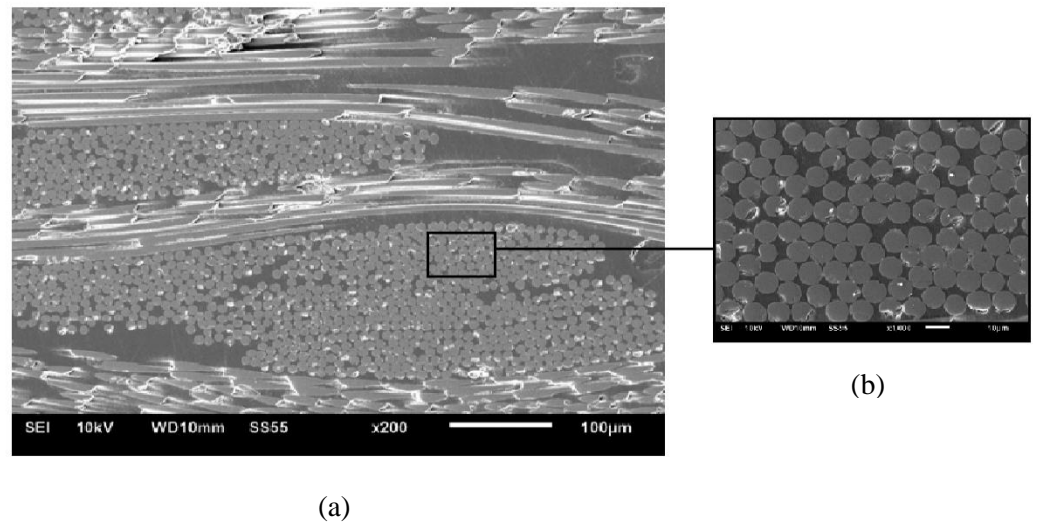
Figure 4-9. SEM images for the 4-ply GF/PEKK laminates at different magnifications.

4.3 Mechanical properties of the plain composites

The results of tensile, shear and flexural tests at room temperature as well as tensile tests at high temperature on the S-glass fibre reinforced PEKK samples (40 wt. % PEKK) are presented in this section. The data for these laminates under quasi-static and low velocity impact loadings are also given and discussed.

4.3.1 Flexural properties

Figure 4-10 shows load-displacement traces for three samples following flexural tests on the GF/PEKK laminate. From the figure, it is clear that the curves can be divided into three regions, these being a linear elastic region, a non-linear region up to peak force followed by a series of drops in the load until ultimate failure as shown in Figure 4-11. The average flexural strength and flexural modulus of the GF/PEKK laminates were found to be 172 MPa and 15 GPa, respectively.
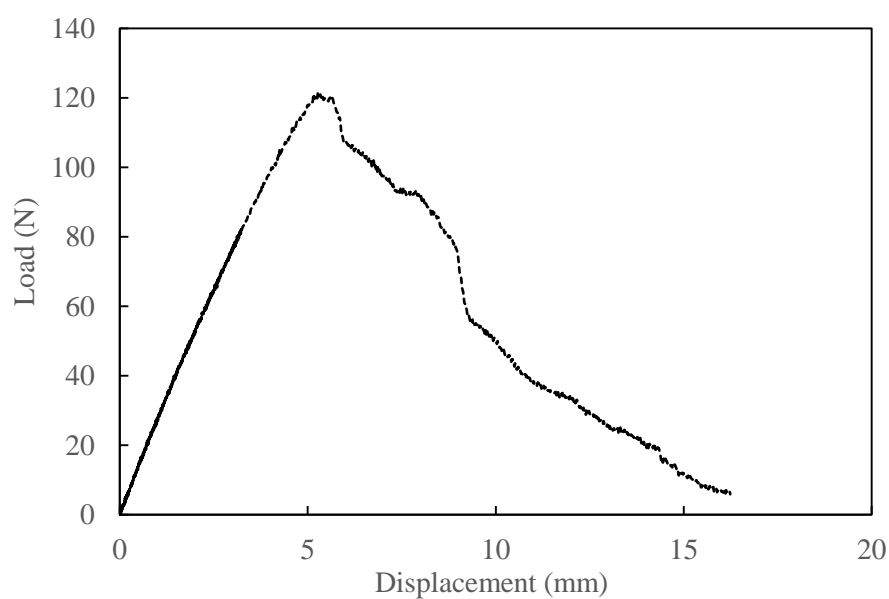
Figure 4-10. Typical load-displacement traces for the GF/PEKK samples following three-point bending tests.

Figure 4-11. Typical failure modes of the failed specimens under three-point tests.

4.3.2 Tensile properties

Load-displacement traces for the 4-ply GF/PEKK specimens following tensile tests are shown in Figure 4-12. From the figure, it can be observed that the composite laminates exhibit a roughly linear load-displacement curve up to the maximum value at which point the samples failed in a catastrophic manner across the sample width. The failure modes of the tested specimens are presented in Figure 4-13.
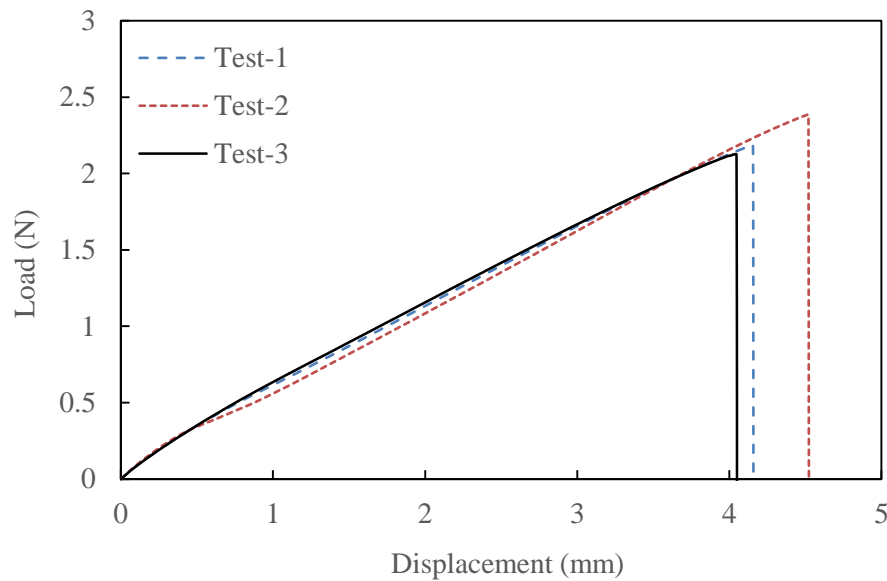
Figure 4-12. Quasi-static tensile load-displacement traces of 4-ply PEKK (40 wt. %).

Figure 4-13. Failure modes of the tested specimens.

The peak force values were used to calculate the tensile strength of the composite laminates and the modulus of elasticity was calculated from the initial linear part of the stress-strain trace of the GF/PEKK beams which is obtained using 25 mm extensometer as described in Section 3.3.2. The average values of tensile strength, modulus of elasticity were 304 MPa and 26 GPa, respectively. These values were later adopted in the finite element models.

4.3.3 Shear properties

The next part of this study focused on the shear properties of the GF/PEKK laminates. Here, the shear stress-strain traces are shown in Figure 4-14. Clearly, for the specimens investigated, a nonlinear response was observed for the shear stress-strain curves up to the maximum value, from which the shear strength can be calculated using Equation (3.5). Here, the shear strength and shear modulus for the glass fibre reinforced PEKK were obtained as 50.4 MPa and 2.6 GPa, respectively.
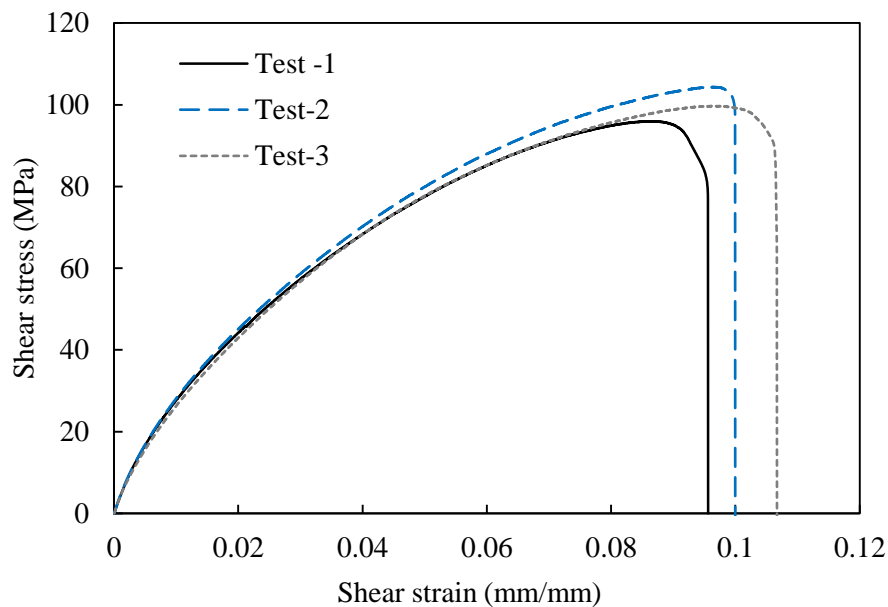
Figure 4-14. Typical in-plane shear stress-strain following a shear test on the GF/PEKK composite.

4.3.4 Quasi-static perforation response

The average load-displacement traces following quasi-static perforation tests of the GF/PEKK composites with various panel thicknesses are shown in Figure 4-15. It can be seen from the figure that the stiffness and the peak force values are increased with the number of plies of the samples (so thickness), as expected. The absorbed energy by the panels can be established by determining the areas under the load-displacement traces. The variation of the absorbed energy with the panel thickness is shown in Figure 4-16. From the figure, it is clear that the energy

required to perforate the targets increases with increasing the panel thickness, and it appears to be non-linear within the range of the thicknesses investigated here.

The quasi-static perforation response of the 4-, 8-, 12- and 16-ply GF/PEKK panels are compared with the corresponding results for glass fibre reinforced epoxy (GF/Epoxy) [164]. However, the sample thickness of GF/PEKK panels is slightly greater than those of GF/Epoxy panels. Therefore, the test results of both systems are normalised by the corresponded areal density to facilitate a clearer comparison, as shown in Figure 4-17. From the figure, it is clear that the specific perforation energy for both types of material increases in a similar pattern with increasing target thickness. It is also evident that the GF/PEKK laminates investigated show a perforation threshold up to 73% higher than that of the GF/Epoxy laminates, because of the higher peak force of the GF/PEKK composites, as shown in Figure 4-18. The higher stiffness of the GF/PEKK composites is due to the high modulus of the glass fibre (S-glass) which was used as a reinforcing material in this study. Moreover, using a thermoplastic resin (PEKK) as a matrix material increases the absorbed energy due to the improved ductility of this composite in comparison to the epoxy resin used.
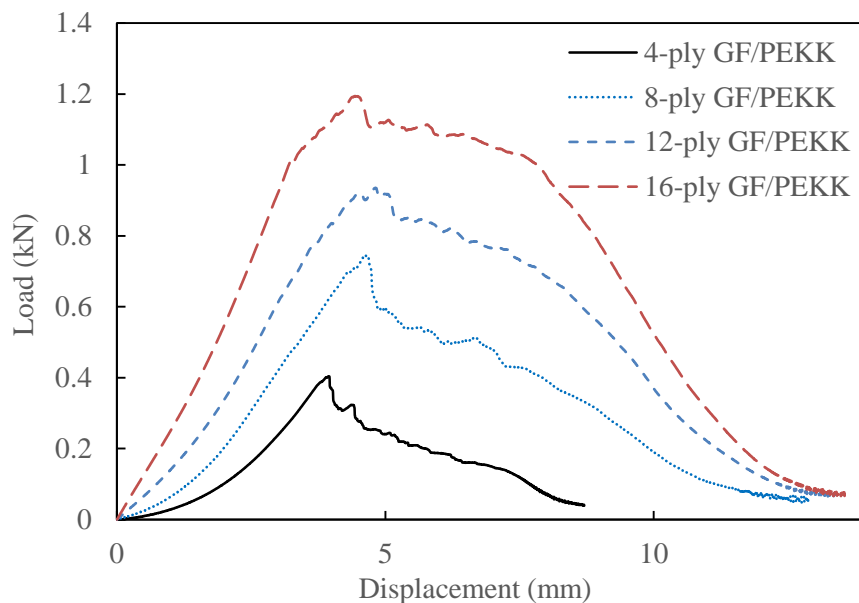
Figure 4-15. Load-displacement traces following quasi-static perforation tests on GF/PEKK laminates with differing thicknesses.
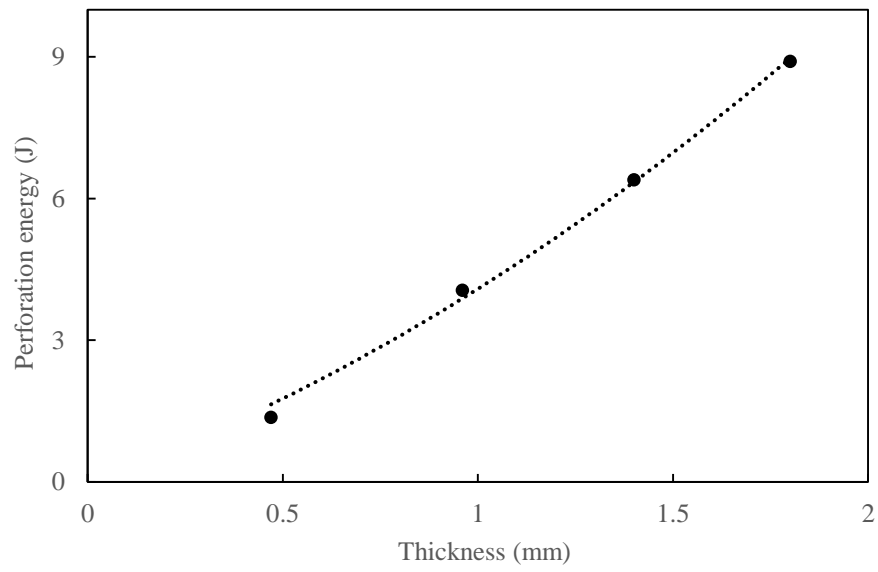
Figure 4-16. Perforation energy of the GF/PEKK composites following quasi-static loading.
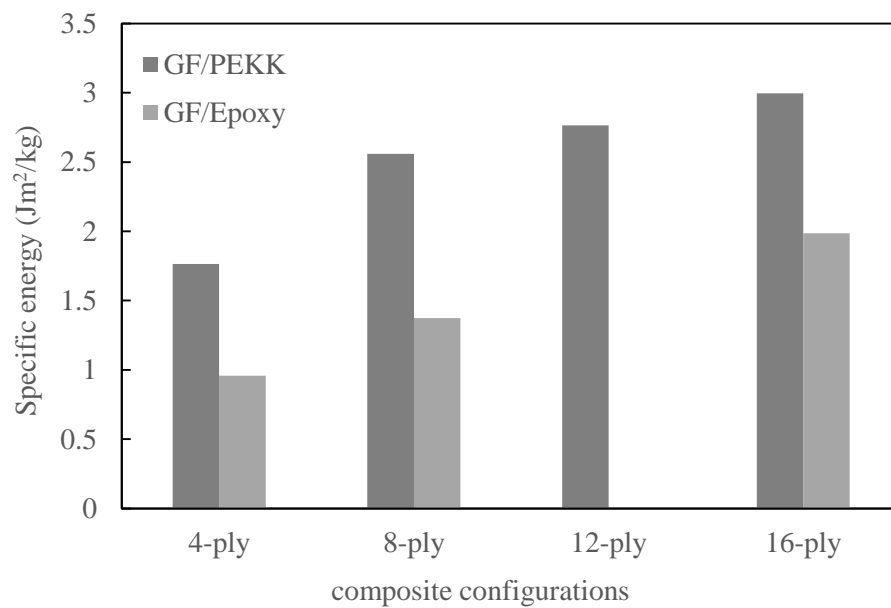
Figure 4-17. Comparison of the specific energy absorption of the GF/PEKK laminates with a GF/Epoxy [164].
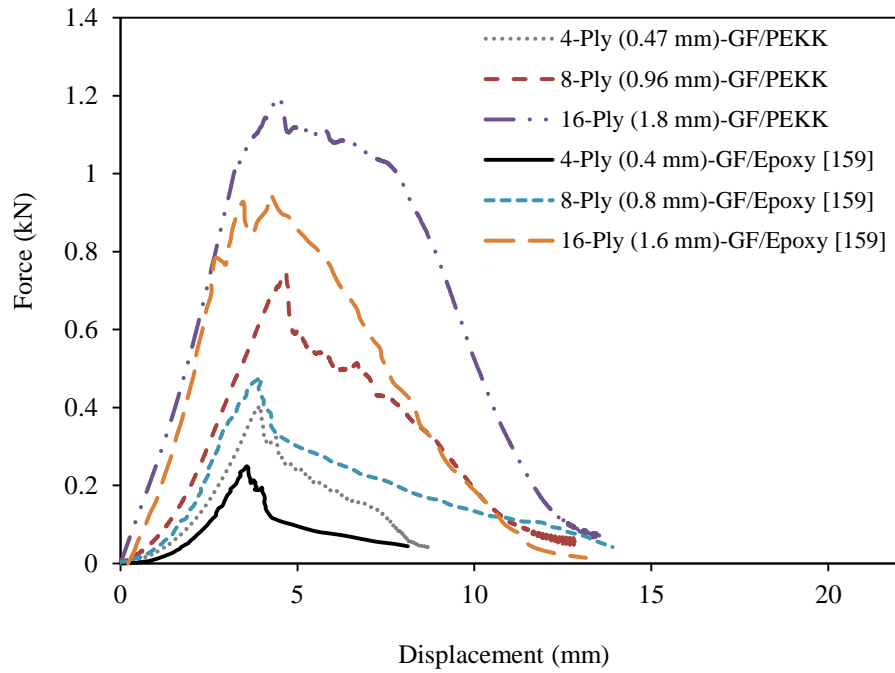
Figure 4-18. Comparison of the average load-displacement traces with published work on a GF/Epoxy following quasi-static perforation tests.

Figure 4-19 shows the failure modes of the front and the rear surfaces of the 4- and 16-ply composite panels following quasi-static perforation tests. Clearly, a similar failure pattern in the rear and the front surfaces were observed for the investigated specimens in which a cross-shaped fracture was formed on the rear surface of the panel, whereas a hole-shaped failure on the front surface of the laminates was created. The cross-shaped pattern fracture of the rear surface resulted from the tensile fracture. After that, these initial cracks propagated through the thickness of the panels, and therefore, facilitate the final phase of the passage of the indenter through the laminates, leading to formation the hole on the front surface of the laminates. It can also be noted from Figure 4-19 that the passage of the indenter in the thicker panels (16-ply) resulted in a more sever break in the centre of the panel.

Front surface   Rear surface
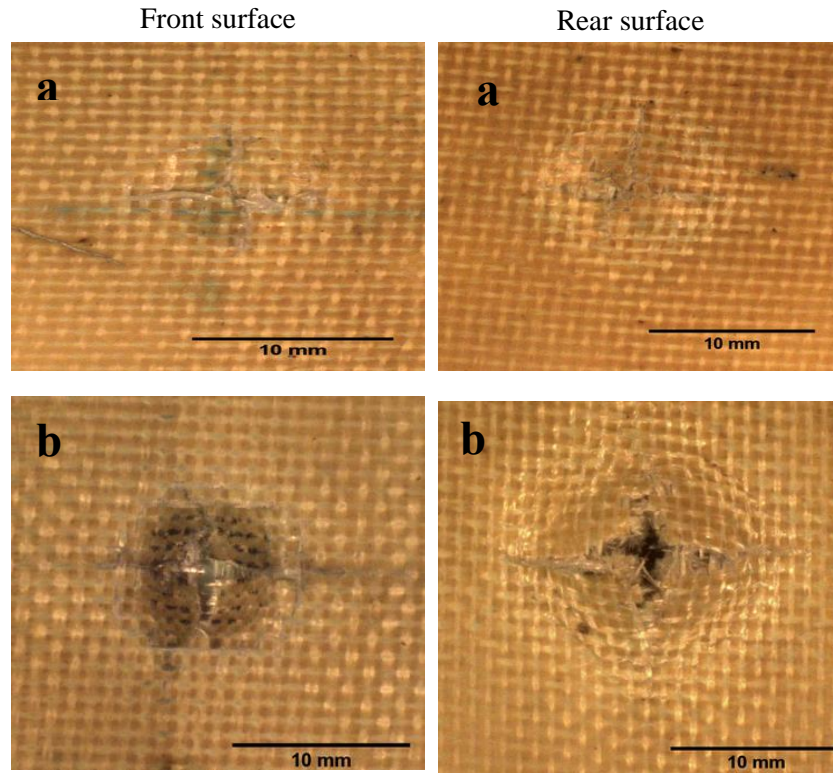
Figure 4-19. Photograph of the 4-ply (a), and 16-ply (b) GF/PEKK panels following quasi-static perforation tests using hemispherical indenter (10 mm diameter).

In order to highlight the failure mechanisms in the specimens tested under quasi-static perforation, failed GF/PEKK panels were cross-sectioned and polished using different grades of sand papers. Figure 4-20 shows the cross-sections of the 4-, 8-, 12- and 16-ply GF/PEKK panels following static perforation tests. Here, the micrographs were taken using a low magnification optical microscope (described in Section 3.5.1). Closer examination of the figure indicates that all panels show local deformations, as well as fracture on the composite plies at the centre of the impacted area, and the failure becomes more localised by increasing the panel thickness, including a combination of tensile and shear failure. It is interesting to note that these composites exhibit failure modes in the form of matrix cracking and fibre breakage, and with no significant delamination between the layers. This evidence suggests that a good bonding was formed between the plies of the laminates investigated.

(4-ply)

(8-Ply)

(12-Ply)

(16-Ply)

Figure 4-20. Cross-sections of GF/PEKK panels based on various thicknesses following quasi-static perforation tests.

4.3.5 High temperature tensile properties

The influence of temperature on the tensile response of GF/PEKK panels (4-ply) was studied by heating tensile specimens during the tests, with the test setup being described in Section 3.3.4. Figure 4-21 shows the variation of the tensile strength for the GF/PEKK samples with temperature. As expected, the tensile strength of the specimens decreases with the temperature. At a temperature of 250 ºC, the tensile strength has dropped by approximately 35% relative to

panels tested at room temperature. It is interesting to note that there was hardly any change in the tensile strength when the composite was heated to 100 ºC, compared to about 35 % reduction in tensile strength of GF/Epoxy [165] and about 33% of all polypropylene composites [142] at the same temperature. There was around a 10 % drop in tensile strength over the temperature range of 140 – 150 ºC for the panels investigated. This is not surprising, as this temperature range is very close to the resin glass transition temperature, 165 ºC, which causes softening of the resin matrix. Hence, the bonding strength between fibres and matrix is affected by the softening, i.e. it becomes weaker, leading to the reduction of the stiffness of the PEKK matrix and further reduction in the shear strength [142, 165]. Nevertheless, even at 250 ºC, the GF/PEKK still maintains a tensile strength of about 200 MPa. However, the GF/epoxy and GF/PP laminates lose their strength when the temperature exceeds 100 ºC. This evidence highlights the advantages of the materials investigated at high temperatures over the traditional composites such as epoxy-based fibre reinforced composites which are widely used in aerospace applications.
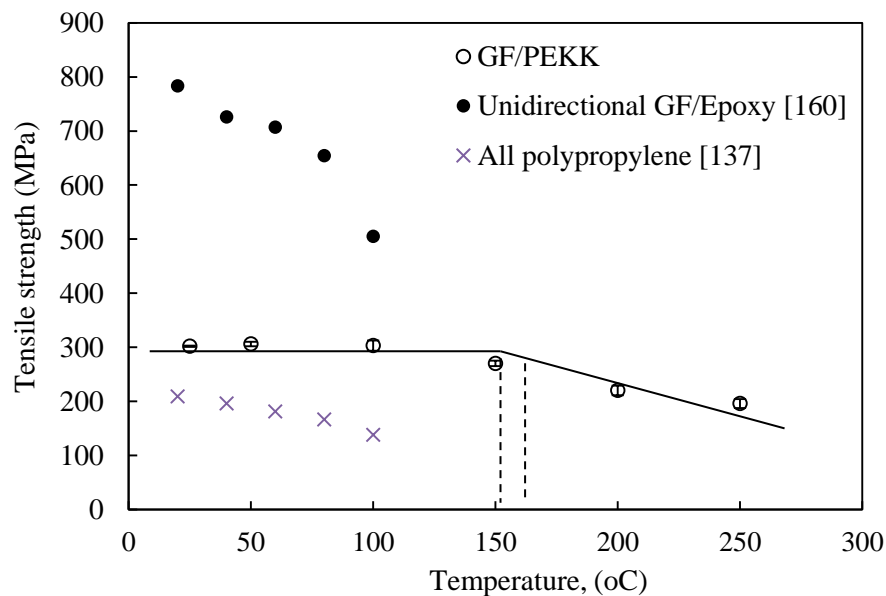
Figure 4-21. Tensile strength of the 4-ply GF/PEKK panels as a function of temperature. The data are compared with results from the published work.

4.3.6 Low velocity impact response

4.3.6.1 The effect of the target thickness on the impact response of the
GF/PEKK laminates

In order to investigate the influence of target thickness on the impact response of GF/PEKK laminates with 4-, 8-, 12- and 16-plies, were subjected to perforation impact tests. These laminates were impacted at various energies resulting in a full perforation. Details of the impact energies, sample sizes, impactor masses and velocities were described in Section 3.3.6.1. Figure 4-22 shows typical load-displacement traces for GF/PEKK panels in which three stages can be identified. Due to the clearance between the projectile and target, a non-uniform behaviour in the load-displace traces was observed in the first stage (I).

In the second stage (II), the force increases quickly with displacement up to the maximum value due to the full engagement (contact) of the projectile to the target. Clearly, the contact forces generated by impacting the thick targets are significantly greater than those by impacting the thin panels, due to the increased transverse stiffness. The peak force values for the 4-, 8-, 12- and 16-ply GF/PEKK composites are 495, 1049, 1711 and 1916 Newtons, respectively. Interestingly, the corresponding forces for these panels following the quasi-static perforation tests are 403, 746, 935, and 1194 Newtons, respectively. Clearly, the failed targets under dynamic loading exhibit a higher peak force than those following the quasi-static perforation tests, highlighting the rate-sensitivity of composites.

Finally, a significant on-going drop in the peak force was observed, associated with a cross-shaped fracture on the rear face of the specimens as the projectile started passing the targets. Moreover, a localised damage area occurred on the front face of the specimens, leading to localised fibre-resin splitting, as shown in Figure 4-23.
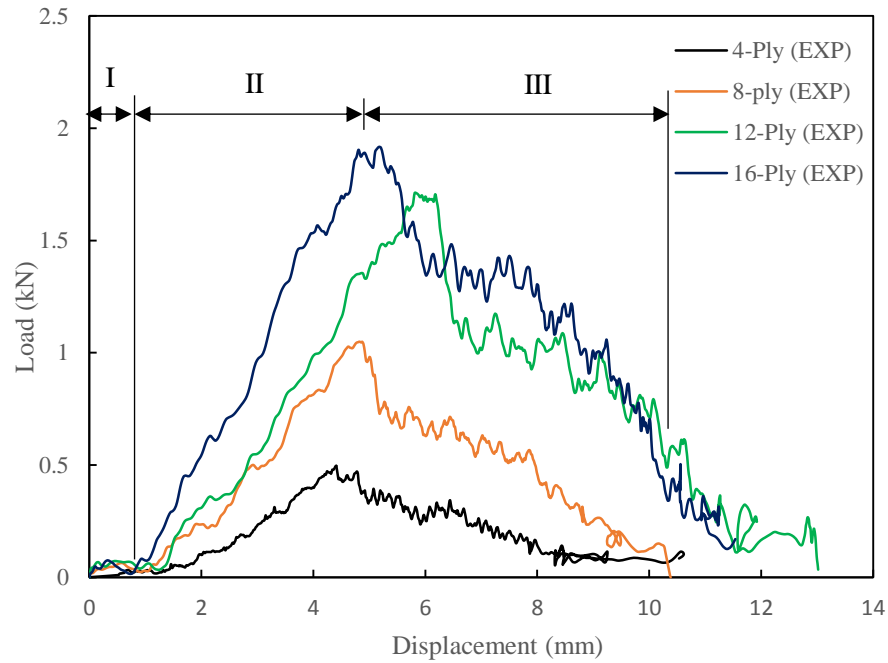
Figure 4-22. Load-displacement traces for the 4-, 8-, 12- and 16-Ply GF/PEKK
laminates subjected to low velocity impact loading.
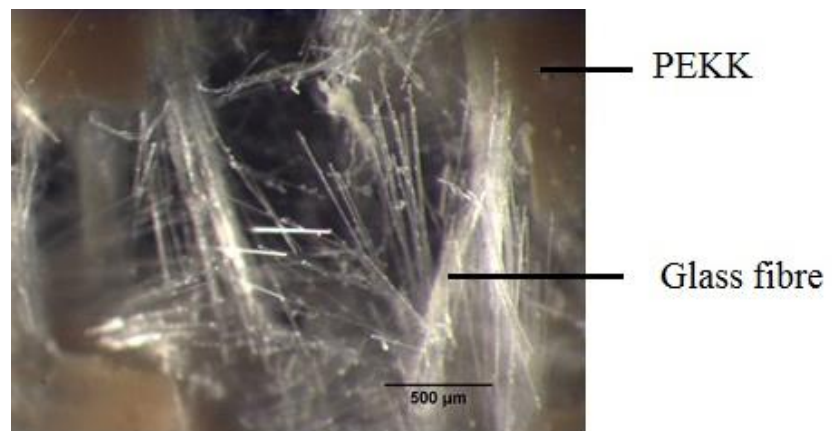
Figure 4-23. Fibre-resin splitting under the point of impact.

The energy required to perforate the composite panels was calculated using the area under the

load-displacement traces. The variation of perforation energy with target thickness for the

GF/PEKK laminates is shown in Figure 4-24. Here, it is evident that the perforation energy is

strongly dependent on target thickness, with the perforation energy increases rapidly with

increasing sample thicknesses, as expected. For example, the perforation energy of 4-ply

panels is 1.96 J, whereas that for the thickest specimens (16-ply) is 10.87 J. Similar variation

between the perforation energy and specimen thickness have been observed on GF/epoxy laminates following low velocity impact tests [124].
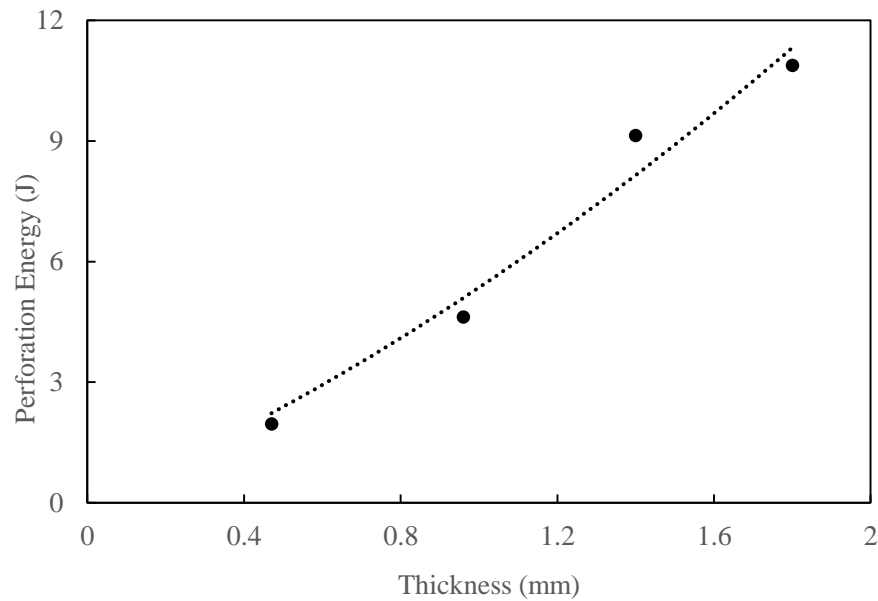
Figure 4-24. The variation of the perforation energy versus target thickness of GF/PEKK laminates following low velocity impact tests.

The failure of the specimens under impact tests was then characterised by examining the front and the rear surfaces. Figure 4-25 shows the failure modes of the front and the rear surfaces of the 4- and 16-ply composite panels following low velocity impact. It can be seen from the figure that the failure modes were similar to those observed earlier under quasi-static loading rates (Figure 4-19), in which a cross-shaped fracture in 0° and 90° directions and a hole were formed on the rear surface and the front surface, respectively. The damaged zones under dynamic loading were more severe than those tested quasi-statically. Clearly, the size of the damaged area at the centre point was relatively similar to the projectile size. Moreover, the damaged zone on the thick panel (i.e.16-ply) was more localised than that on the thin target (4-ply). This can be attributed to the higher stiffness of the thicker panels, leading to more localised deformation and damage.

The front

The rear
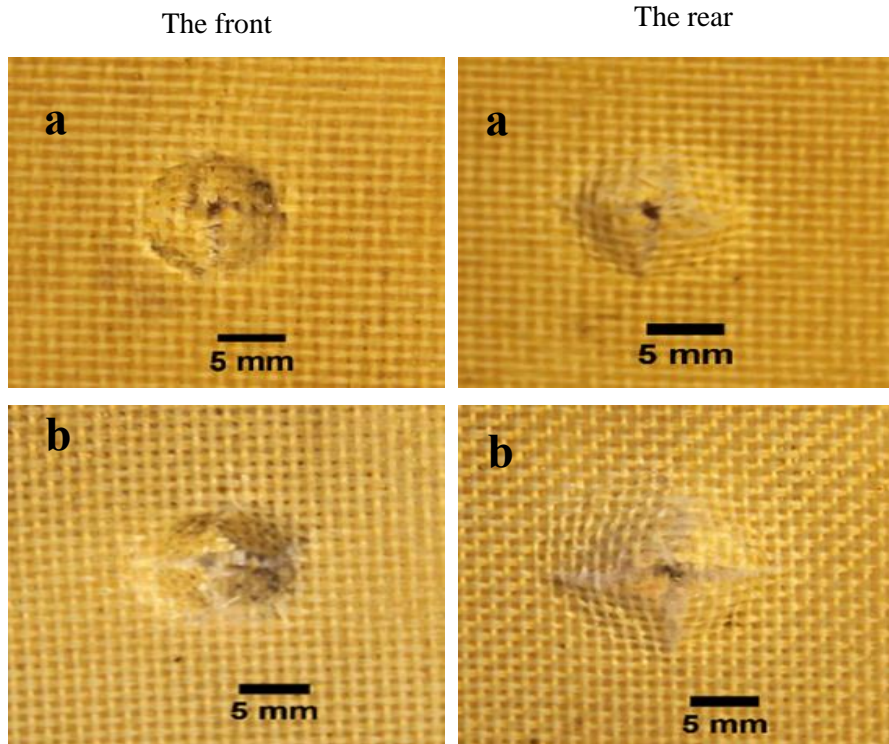
Figure 4-25. Comparison of front and rear faces for the 4-ply (a) and 16-ply (b) of GF/PEKK composites following impact perforation tests (see Table 3-3).

After impact, a number of specimens were sectioned and polished to investigate the failure mechanisms. The low magnification micrographs of the cross-sections of 4-, 8-, 12- and 16-ply GF/PEKK laminates subjected to impact perforation energies are shown in Figure 4-26. An examination of the cross-sections, around the impact location indicates that all specimens exhibit significant permanent deformation associated with matrix cracking in the highly deformed region under the projectile. As the target thickness is increased, the diameter of the perforation zone increases, resulting in a fracture structure with a frustum shape. Similar perforation zone shapes were observed in woven glass fibre reinforced epoxy by other researchers [164]. It is interesting to note that no significant delamination was observed in the targets after impact testing, suggesting that a little energy has been absorbed in this mechanism.

Figure 4-27 shows the absorbed energy following quasi-static and impact tests for the 4-, 8-, 12- and 16-ply GF/PEKK laminates. From the figure, it is clear that the impacted panels exhibit a higher level of energy absorption than those under quasi-static loading. The absorbed

105

energies for the 4-, 8-, 12- and 16-ply laminates under impact tests were 30, 12, 30, and 18%, higher than those obtained under quasi-static perforation, respectively. This can be attributed to the rate-sensitivity of the glass fibre composites. The influence of the dynamic loading on the maximum contact force for the investigated targets was assessed by comparing the peak forces of these panels under static perforation tests with the corresponded values following impact tests, with these data being shown in Figure 4-28. Again, the dynamic peak loads were higher than the corresponding quasi-static loads, highlighting the rate-sensitivity of the material, especially for the thick panels (16-ply).

(4-Ply)

(8-Ply)

(12-Ply)

(16-Ply)
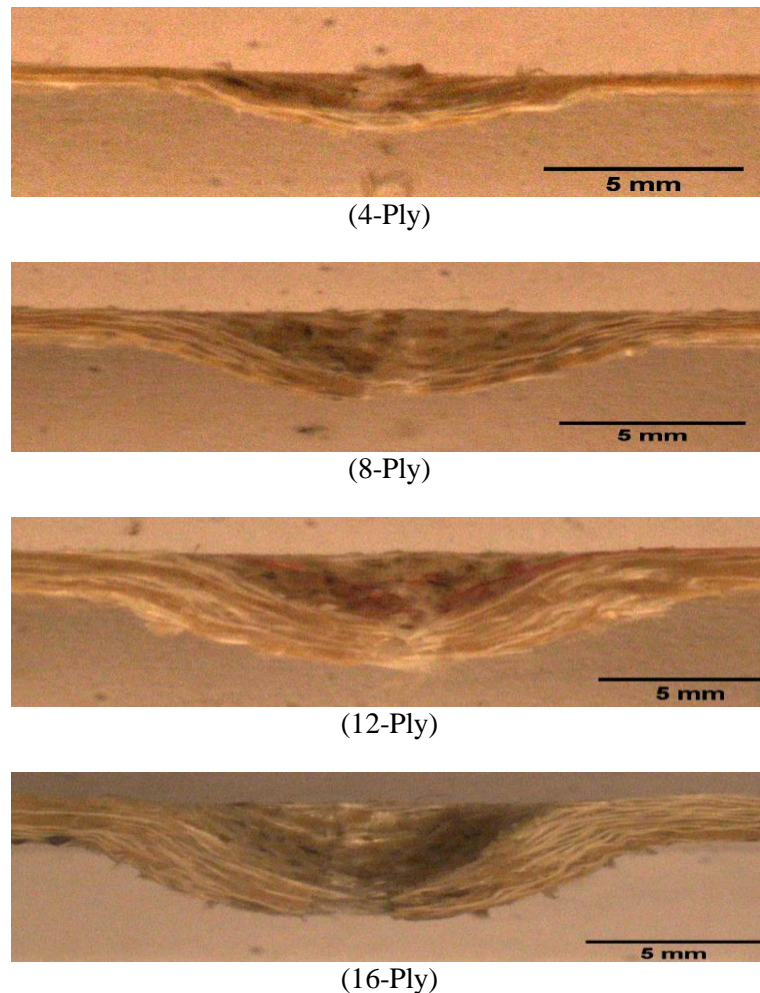
Figure 4-26. Comparison of cross-sections following impact perforation test on GF/PEKK laminates with various thicknesses.
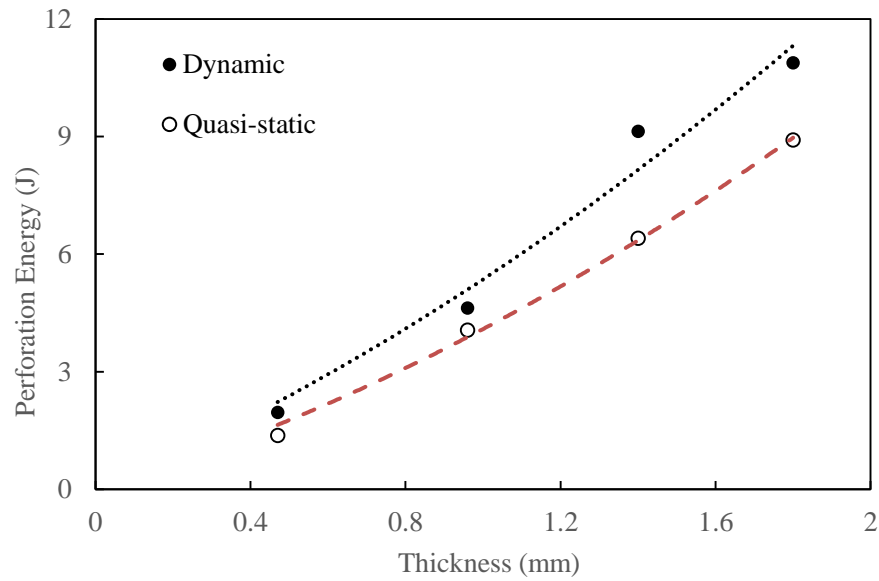
Figure 4-27. Variation of perforation energy with sample thickness for GF/PEKK panels following dynamic and quasi-static loading rates.
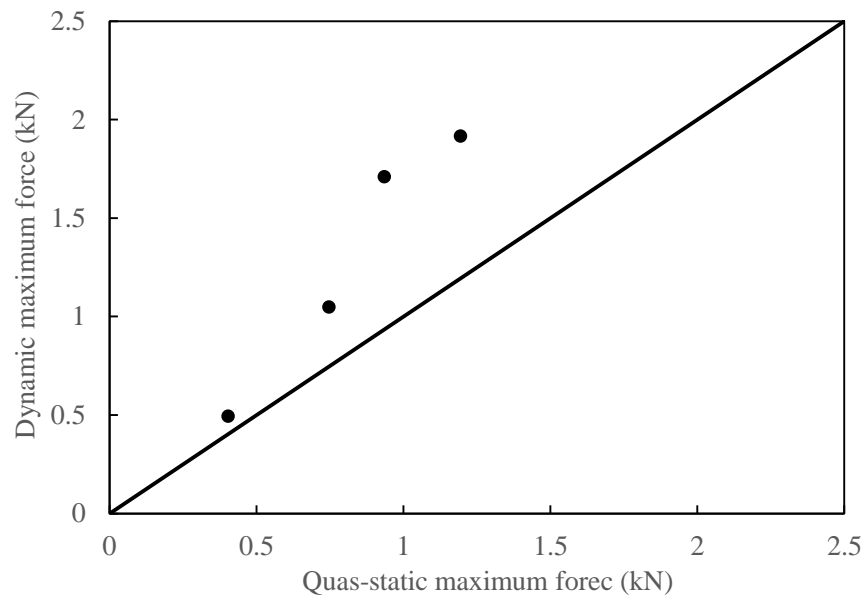
Figure 4-28. Comparison of dynamic peak force versus maximum static force for the GF/PEKK composite laminates.

4.3.6.2 The effect of the projectile diameter on the perforation response of GF/PEKK laminates

The response of GF/PEKK composites under low velocity impact is likely to be strongly dependent on the size and the shape of the projectile head. Therefore, GF/PEKK (8-ply) specimens (with dimensions of 100 mm x 100 mm) were clamped on a square fixture

(described in Section 3.3.5), and impacted by various projectile shapes and sizes. Here, the impact energies were selected to give a full perforation of the targets.

The influence of the projectile diameter on the response of GF/PEKK plain composites under low velocity impact was investigated by conducting impact tests on 8-ply panels. Four projectile diameters were used in this study, i.e. 5, 10, 15 and 20 mm. Figure 4-29 shows the load-displacement traces for the 8-ply composite panels subjected to impact tests with various projectile diameters. From the figure, it is clear that the maximum impact force and the associated displacement show a high dependency on the projectile size at which the peak force and the corresponding displacement increase with increasing projectile diameter and the highest peak value corresponded to the 20 mm diameter projectile. The peak force at the perforation threshold (the point at which the perforation damage is initiated) for the panels impacted by a 5 mm diameter projectile was 671 Newtons, compared to 1658 Newtons for those impacted with a 20 mm diameter projectile.

Closer examination to the figure indicates that the load-displacement traces show similar initial contact forces. As long as the contact area generated during the impact remains small, the contact force is expected to be independent on the diameter of the impactor head [166] in the very early stage of the impact. Clearly, the load-displacement traces for the panels impacted by a small projectile (5 mm diameter) were smoother than those impacted by the biggest indenter in this investigation, i.e. 20 mm diameter, reflecting the high level of impact energy by larger diameter size of the projectile.

Again, the area under the load-displacement traces was calculated to determine the energy required to perforate these composite laminates. The relationship between the perforation energy and the projectile diameter for the GF/PEKK panels is shown in Figure 4-30. From the figure, it is clear that the perforation energy increases with increasing the projectile diameter size.

The impacted specimens were then sectioned and polished to highlight the failure mechanisms in these panels. Figure 4-31 shows the cross-sections of the 8-ply GF/PEKK laminates following low velocity impact with various indenter diameters. It can be seen from the figure that laminates impacted by different projectile diameters show similar failure modes, in terms of fracture (the nature of this fracture was mentioned earlier in Section 4.3.6.1). However, the damage area increases as the projectile diameter size is increased. Interestingly, by taking the worst case in this investigation, in which GF/PEKK panels were impacted with projectile diameter of 20 mm (the largest diameter), delamination is not observed between the layers. Again, this evidence suggests a high binding strength between the resin and the fibres.
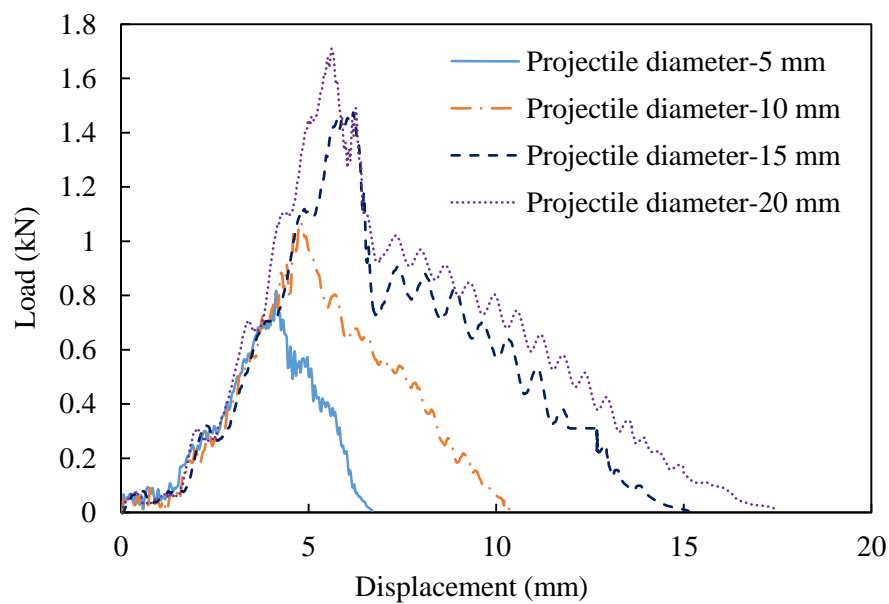
Figure 4-29. Load-displacement traces following impact tests on 8 ply laminates with various projectile diameter.
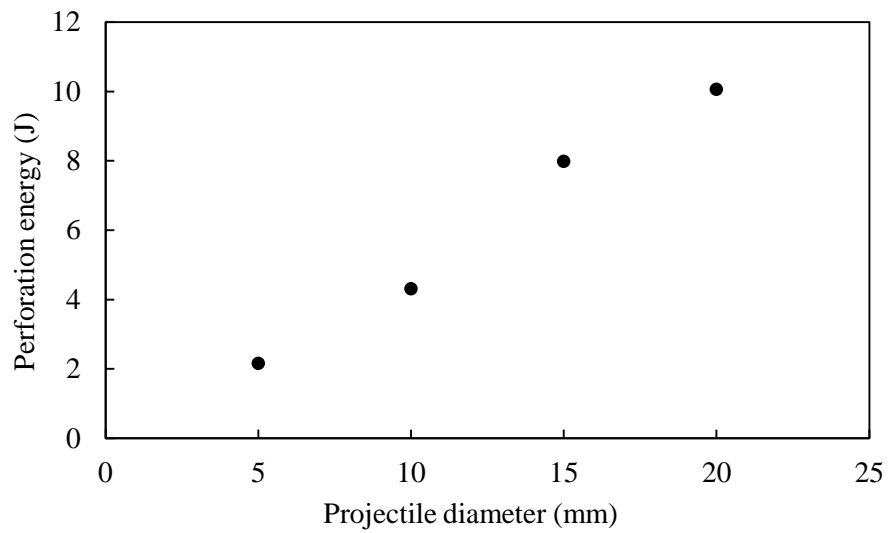
Figure 4-30. Variation of perforation energy with projectile diameter for 8-ply GF/PEKK panels impacted by projectile with diameters of 5, 10, 15 and 20 mm.

(a)

(b)

(c)

(d)
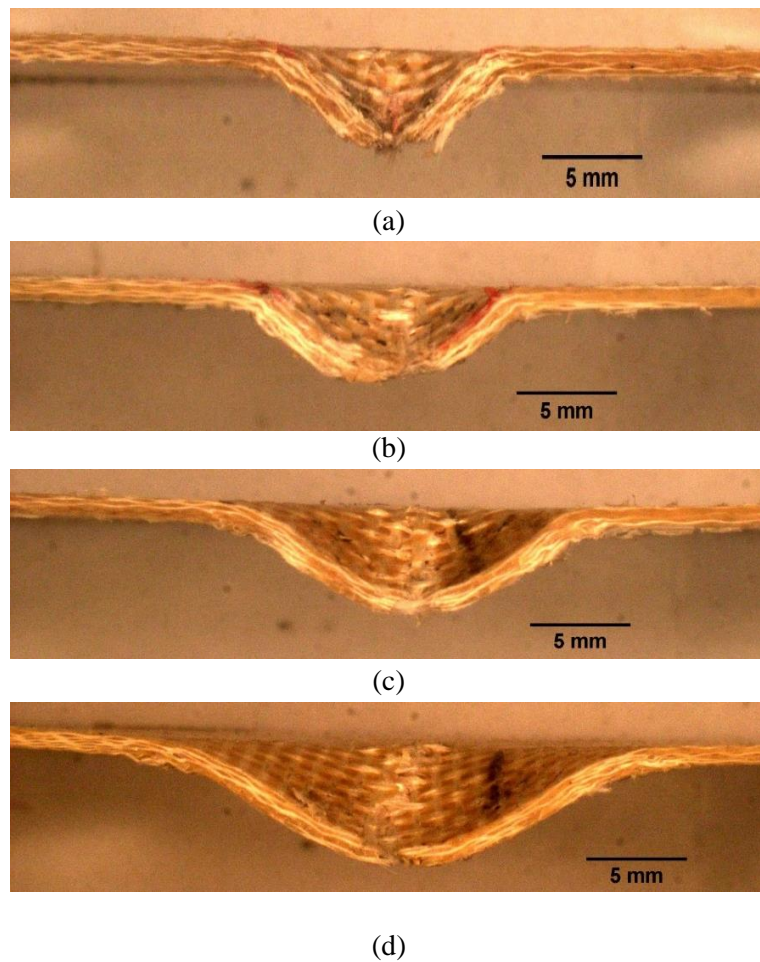
Figure 4-31. Comparison of cross-sections of GF/ PEKK (8-ply) impacted with hemispherical projectiles in diameters of (a) 5 mm, (b) 10 mm, (c) 15 mm and (d) 20 mm.

110

4.3.6.3 The effect of the projectile shape on the perforation response of GF/PEKK laminates

Here, three projectile shapes were used, these being hemispherical, partially flat and conical projectile shapes. These projectiles had a similar diameter of 10 mm to avoid the effect of impactor size (see Section 3.3.6.2). Figure 4-32 shows load-displacement traces for the 8-ply GF/PEKK laminates loaded by the hemispherical, conical, and partially flat impactors. It can be seen from the figure that panels impacted with a partially flat indenter show a higher peak load than those produced by the other projectile types investigated. This is due to the large contact area between the flat indenter and the target at which the resistance of the targets against the projectile perforation is increased, resulting in a high perforation force.

For example, the partially flat projectile generated on impact force of 2117 Newtons compared to 873 Newtons recorded by using the conical projectile. The lower peak force associated with the conical impactor is due to the high penetration capability against the targets by this sharp indenter but gradually, resulting in a high contact friction between the panel and the indenter and therefore, increasing the specimen-impactor contact duration. It can be also noted from the figure that the samples investigated in this study show similar initial load-displacement traces (stiffness) when loaded by various impactor shapes. This is due to aforementioned reason at which the contact force shows no dependency on the projectile radius at very early stage of impact when the contact area is much smaller than the panel total area.

The variation of the absorbed energy with different projectile shapes for the impacted 8-ply GF/PEKK panels is shown in Figure 4-33. From the figure, it is clear that energy required to perforate targets increases when the projectiles change from hemispherical to conical shapes and the highest absorbed energy corresponded to the partially flat projectile. As mentioned before, perforation energy values were measured from the area under the load-displacement curves and the largest area was produced by using a partial flat indenter.

A comparison of the failure modes for the panels of GF/PEKK (8-ply) impacted by various projectile shapes is shown in Figure 4-34. It is clear from the figure that localised damage in the specimen with a conical projectile was more severe than in those impacted by other projectile shapes. This is due to the high penetration capability of the sharp projectile against the target as mentioned previously. Again, for the range of the projectile shapes investigated, no significant delamination was observed between the plies within the composites.
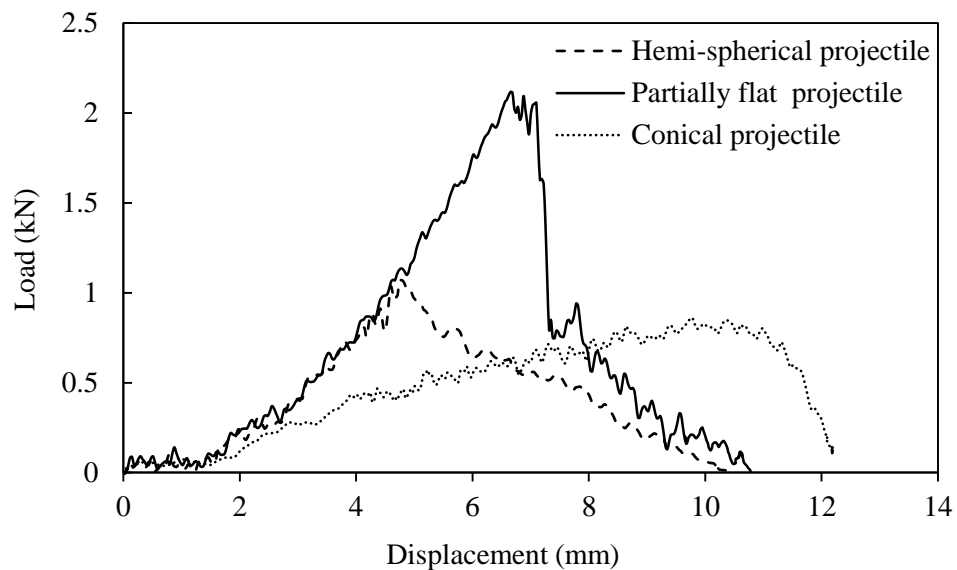
Figure 4-32. Load -displacement relationship for 8-ply panels impacted with projectiles with different shapes.
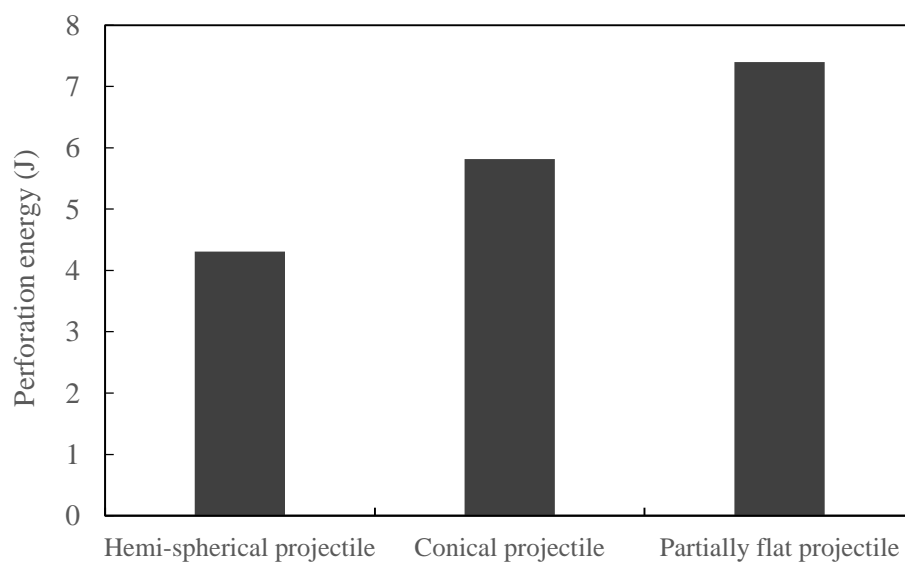
Figure 4-33. Variation of perforation energy with projectile head shape for 8-ply GF/PEKK panels following impact tests.

(a)

(b)

(c)
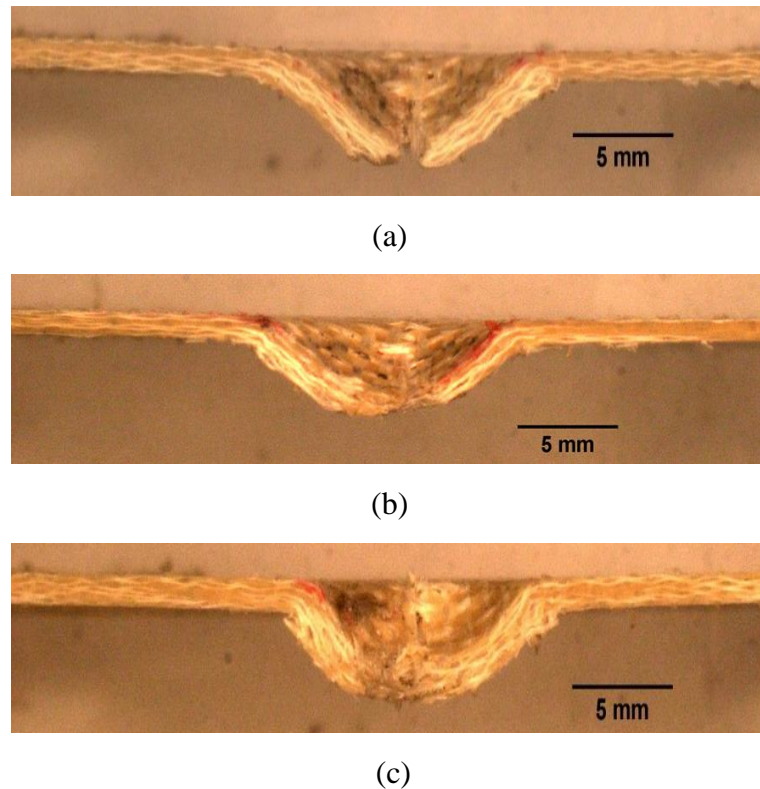
Figure 4-34. Comparison of cross-sections test of S-glass fibre reinforced PEKK (8-ply) impacted with (a) conical, (b) hemi-spherical, and (c) partially flat projectile shapes.

4.4 Mechanical properties of the fibre metal laminates

Two FML systems were investigated in this study, i.e. titanium-based FMLs and aluminium-based FMLs with various stacking configurations, as described in Sections 3.4.1.1 and 3.4.1.2, respectively. The response of these FMLs at quasi-static and dynamic loading rates is presented. Initially, attention was focused on the influence of the surface laser treatment of the titanium alloy on its tensile strength, as well as its bonding strength with the PEKK resin. The influence of varying the processing temperature of the aluminium alloy (2024-T3) on its residual strength was also evaluated in this section.

113

4.4.1 Effect of laser surface treatment on surface morphology of titanium alloy

The influence of laser treatment with various power parameters on creating a rough structure on the surface titanium alloy is shown in Table 4-1. It is clear that a relatively smooth surface with a roughness of 0.309 microns without a hierarchical structure was observed on the as-received specimens, compared to 1.72 microns to those treated with a laser fluence of 5.45 J/cm^2. During laser processing, the material's surface was altered by the laser through melting and evaporation, resulting in a significant change in the surface roughness. Effectively, the change in the surface roughness is due to the laser interaction with the material, which creates a microstructure with material removed, due to laser ablation and the re-deposition of the molten material by the thermal component of the nanosecond pulse [167]. Melting of the material creates a structure along the borders of the spot size, helping to increase the roughness of the material. Increasing the fluence on the laser increases the ablation rate and the amount of molten material in the surface.

Table 4-1. Mean roughness of titanium surface against laser fluence.

Laser fluence	Mean roughness (μm)
Untreated surface	0.309
4.09 J/cm^2	1.19
4.54 J/cm^2	1.43
5.00 J/cm^2	1.63
5.45 J/cm^2	1.72

4.4.2 Surface characterization of untreated and treated titanium alloy foils

SEM surface analysis was performed to characterise the surface texture of the pristine titanium foils after laser treatment with different power parameters. Figure 4-35 shows SEM images of the β-titanium alloy treated with various laser fluence. Here, same magnification of 1000x was employed to highlight the surface texture for the specimens tested. It is clear that different

rates of laser power create a different roughness value on the sample surface. A higher laser power generates a coarser texture on the sample surface compared to the received sample. As mentioned previously, with increasing the laser fluence, the material removal and the depth of the micro pits are increased.
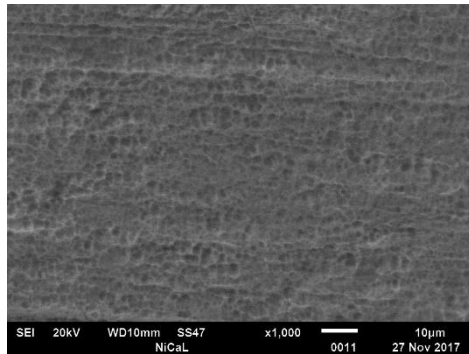
(a) Laser fluence = untreated
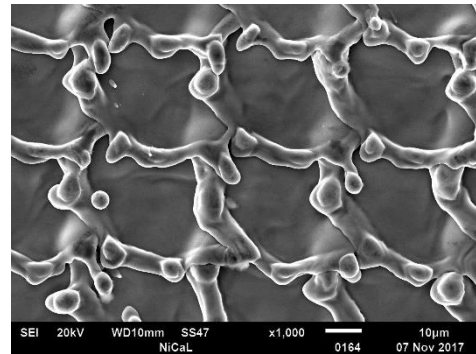
(b) Laser fluence = 4.09 J/cm^2
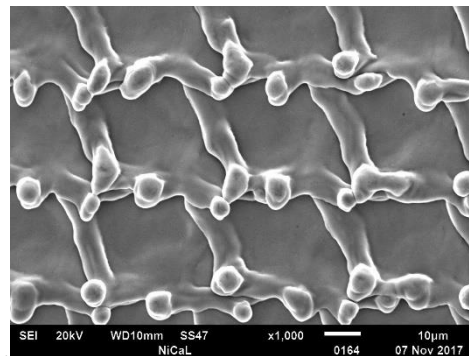
(c) Laser fluence = 4.54 J/cm^2
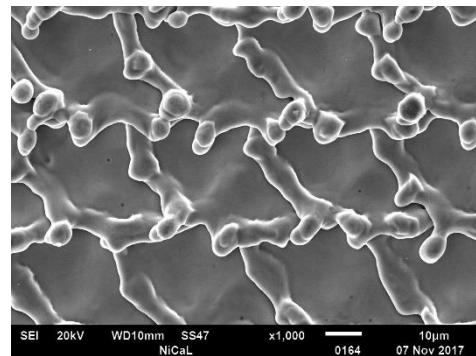
(d) Laser fluence = 5.00 J/cm^2
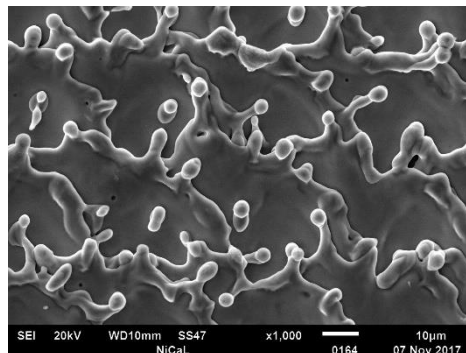
(e) Laser fluence = 5.45 J/cm^2

Figure 4-35.SEM images of titanium alloy surface treated with various laser fluence.

4.4.3 Effect of surface treatment on the tensile strength on the titanium foils

The next part of this study was to investigate the influence of the laser treatment parameters on the residual strength of the titanium alloy. Here, tensile tests were conducted on titanium (0.14 mm thick) foils treated with various levels of laser fluence, and these being 0, 4.09, 4.54, 5 and 5.45 J/cm^2. Here, zero value corresponds to the virgin specimens. Figure 4-36 shows the variation of tensile strength with the laser fluence parameters. An examination of this figure indicates that the tensile strength values vary with the laser influence in the range of 1122 MPa for the untreated specimens and 1069 MPa for those treated with a laser fluence of 5.45 J/cm^2. The reduction in the tensile strength could be attributed to the annealing process during laser treatment. The results also indicates that the pre-surface treatment on the titanium alloy has no significant effect on the tensile properties of these specimens. According to this observation the parameters of laser power were optimised based on bonding strength between the surface-modified titanium alloy and PEKK film.
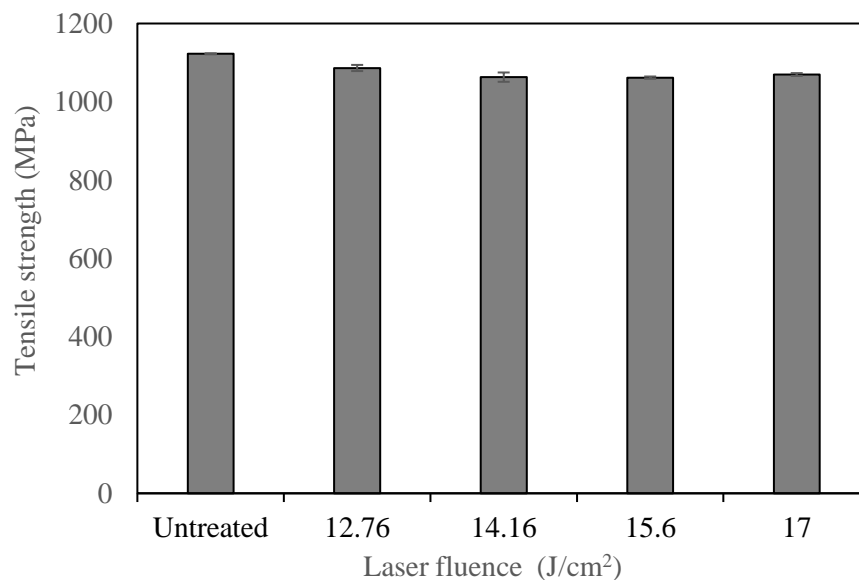
Figure 4-36. Laser power treatment versus tensile strength.

4.4.4 Effect of the laser fluence parameters on the metal-resin bonding strength

Figure 4-37 shows the values of shear strength of the pre-treated titanium foils by laser and PEKK film. The figure can be divided into two regions, i.e. a linear region (I) in which the bonding strength increase with increasing surface roughness of titanium. The maximum value corresponds to a surface roughness of 1.43 μm. This can be attributed to the formation of a microporous structure on the treated surface which filled with the resin, resulting in a good metal-resin bonding strength. In the second stage (II), there is no significant effect of laser power parameters on the bonding strength, resulting in very little difference in the bonding strength properties. Based on the above results, a laser fluence of 4.54 J/cm^2 is selected as the optimum parameter for a good bond strength between the titanium foils and the PEKK film. Therefore, this parameter was used to treat all the titanium foils investigated.

4.4.5 Tensile properties of the titanium alloy

The mechanical properties of the titanium alloy were determined by conducting a series of quasi-static uniaxial tensile tests. Titanium specimens, according to the ASTM recommendations (see Section 3.4.2.1), were removed from the titanium sheets. Here, the tensile specimens were loaded up to failure (fracture) and therefore, engineering stress-strain curves were obtained from the Instron machine. Figure 4-38 shows the stress-strain curves of three titanium alloy samples following tensile tests. It can be noted from the figure that titanium coupons exhibit an elastic behaviour up to the elastic limit (yield point) at which point the yield stress can be calculated. The elastic region of the stress-strain relationship was used to determine the modulus of elasticity (E) which is the gradient of the curve in the elastic stage. Then, the plastic stage started, with the specimens experiencing mild strain hardening up to failure. Nevertheless, engineering stress-strain values do not reflect the real behaviour of the titanium alloy under tension conditions because they do not include the effect of the cross-section area reduction. Therefore, the stress-strain curves are presented in terms of true stress-

strain before using it in the finite element models, which will be discussed in Chapter 5. The Young's modulus, yield strength and tensile strength of the titanium alloy are 100 GPa, 1000 MPa, 1122 MPa, respectively. The failure mode of the specimens tested is shown in Figure 4-39. It is clear for the figure that all specimens failed within the gauge length.
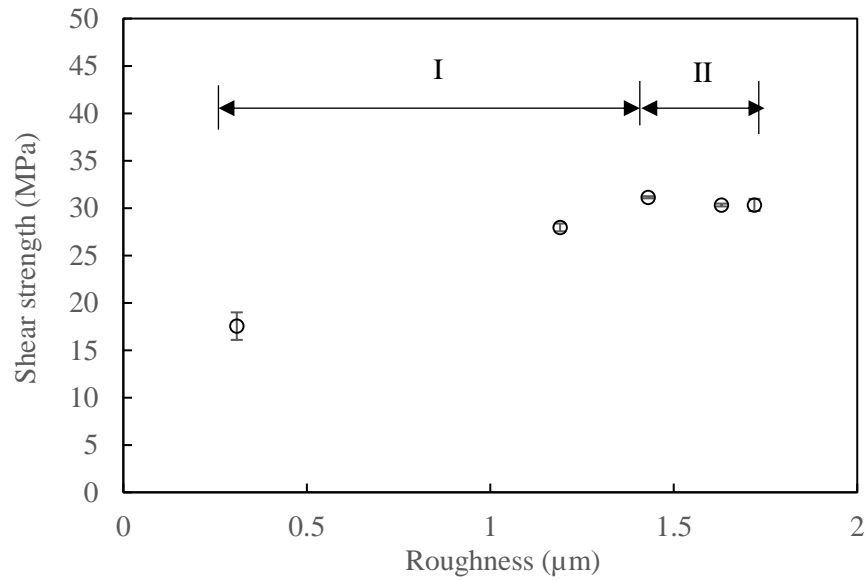
Figure 4-37. The variation of bonding strength with surface roughness using shear lap test (see Section 3.4.2.2).
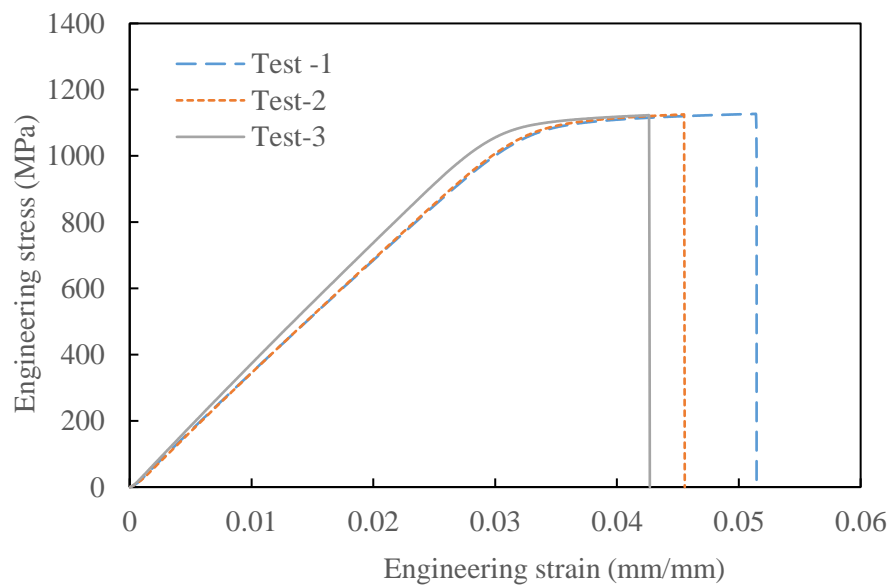
Figure 4-38. Engineering stress-strain relationship for the titanium alloy.

Figure 4-39. Typical failure mode in the titanium alloy specimens following tensile testing.

4.4.6 Quasi-static perforation of titanium based-FMLs

The perforation response of the titanium-based FMLs with different stacking configurations was evaluated by conducting a series of quasi-static perforation tests. The test details are described in Section (3.4.2.3). The load-displacement traces for the 2/1, 3/2, 4/3 and 5/4 fibre metal laminates following quasi-static perforation tests are shown in Figure 4-40. It can be seen from the figure that the traces of the investigated specimens exhibit similar trends in which the contact load increases up to a maximum value before the initiation of the damage, due to the tension-shear fracture initiated on the rear surface of the titanium alloy layer of the target. In the following stage, the damage evolution in the FMLs was continued as the target is penetrated by the indenter, resulting in a progressive drop in the contact force. It can also be noted from the figure that the higher thickness of FMLs produced the higher peak forces as well as higher stiffness values. For example, the FMLs based on 5/4 staking sequence show a peak force of 4490 N, which is almost three times that offered by the 2/1 FML.

By determining the area under the load-displacement trace, the energy absorbed by each laminate during the impact perforation process can be established. Figure 4-41 shows the variation of the energy absorbed as a function of target thickness. It is clear from the figure that the energy required to perforate these FML laminates increases with target thickness, with the same observation mentioned elsewhere [150]. The energy required to perforate the 5/4 FMLs is approximately three times higher than that required to perforate the 2/1 FMLs. The absorbed energies were then normalised by the areal density of the FMLs, to give the specific energy absorption (SEA). Figure 4-42 shows the effect of the target thickness on the specific

energy absorption of titanium-based FMLs. Clearly, the SEA values are varied in a range of

2.64 Jm^2/kg and 3.24 Jm^2/kg.
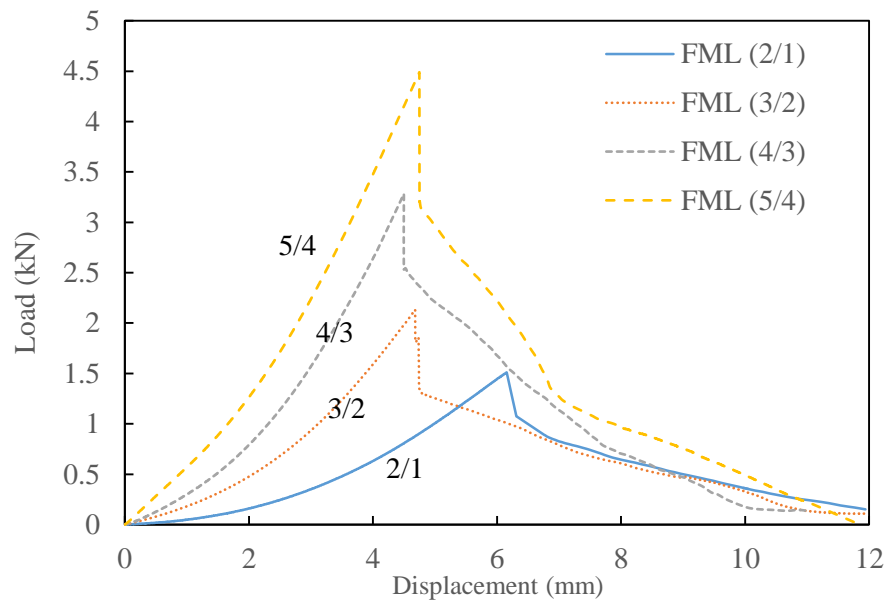
Figure 4-40. Load-displacement traces of FMLs laminates with different stacking configuration following quasi-static perforation tests.
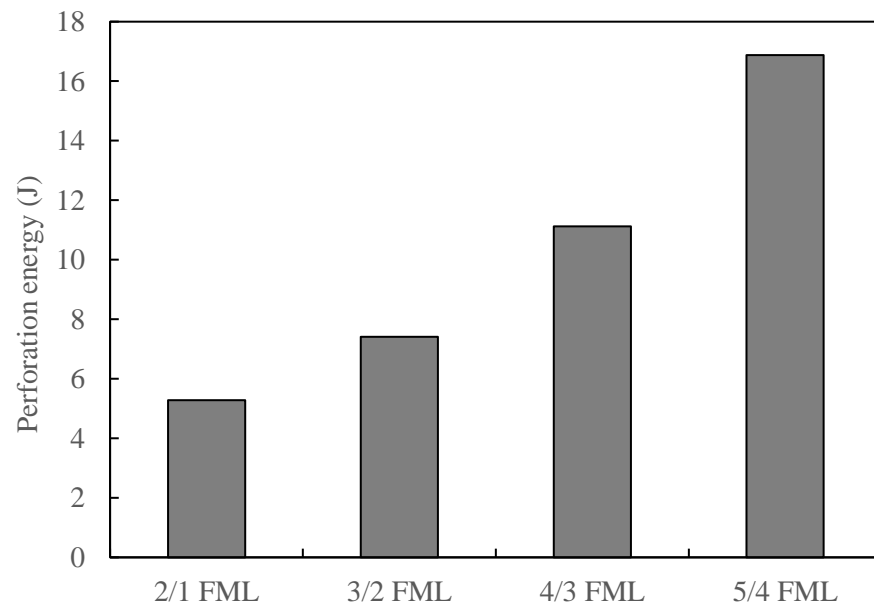
Figure 4-41. Variation of perforation energy with target thickness for 2/1, 3/2, 4/3 and 5/4 FMLs based on 2-ply composite cores.
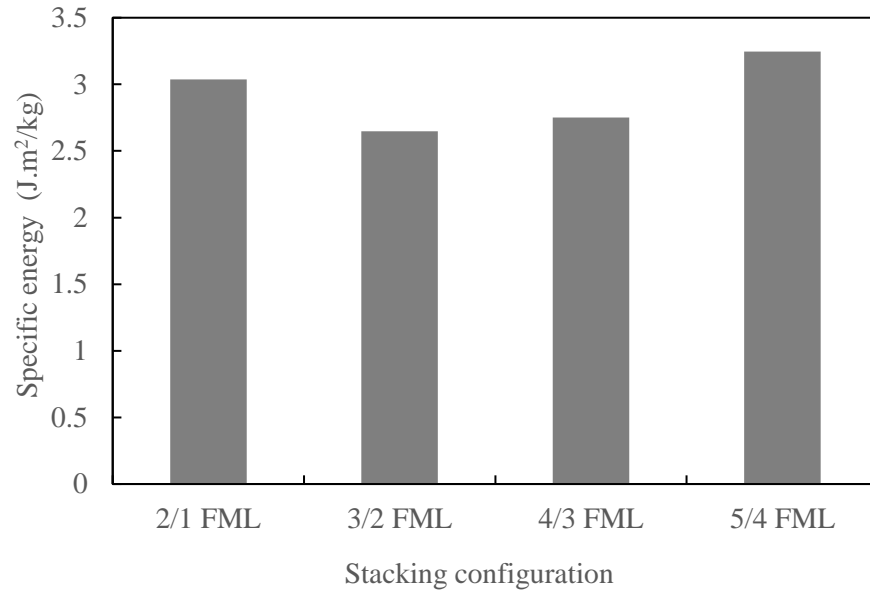
Figure 4-42. The values of the specific energy absorption versus target stacking configuration for the titanium based FMLs under static perforation tests.

The failure modes in the FMLs at quasi-static loading rate were highlighted by using low magnification optical microscopy. Figure 4-43 shows the cross-sections of 2/1, 3/2, 4/3 and 5/4 titanium-based FMLs subjected to quasi-static perforation testing. Here, all four laminates exhibit localised plastic deformations and fracture in the metal foils (titanium alloy) as well as fracture on the composite plies close to the perforation centre. Closer examination to the figure suggests that all the four laminated composites show significant delamination between the composite and metals plies (15-3-3-3-β titanium alloy).

Failure starts with a cross-shaped pattern resulting from the tensile fracture of the rear surface of the specimen (titanium layer). These cracks then propagated through the target thickness, enabling the indenter to finally perforate through the specimen, which leads to formation of a hole in the front face surface. Photographs of the failure modes on the front and rear surfaces of 2/1 FMLs and 5/4 FMLs are presented in Figure 4-44. It can be observed from the figure that there is a longitudinal crack in the rolling direction of the titanium alloy, highlighting the influence of the rolling direction on the failure process of these FMLs. The low perforation resistance of these FMLs can be attributed to the lack of plastic deformations in this type of titanium alloy.

2/1 FMLs
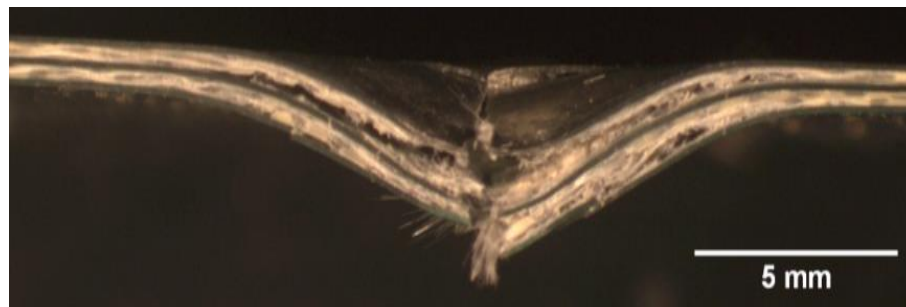
3/2 FMLs
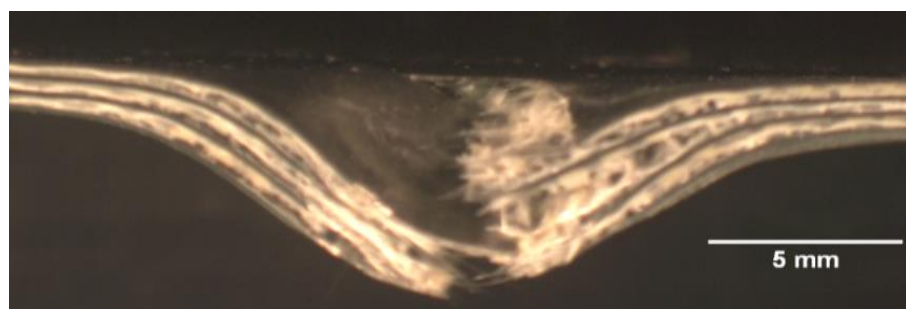
4/3 FMLs

5/4 FMLs

Figure 4-43. Comparison of cross-sections following quasi-static perforation tests on the titanium-based FMLs (2-ply composite core) with various stacking configurations.

Front surface   Rear surface

2/1 FMLs

5/4 FMLs
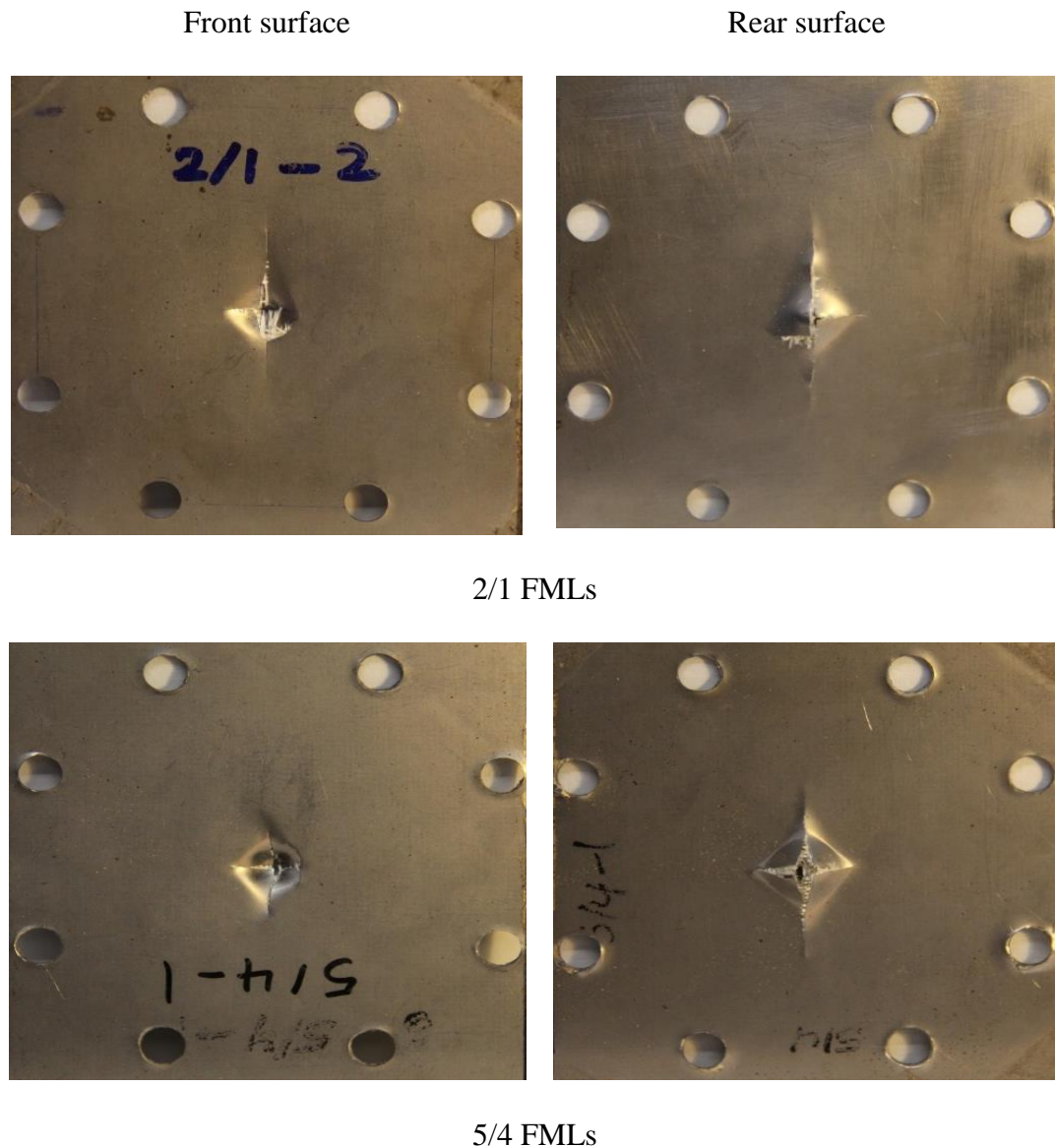
Figure 4-44. Photograph for the 2/1 and 5/4 titanium based FMLs stacked with 2-
ply composite core following quasi-static perforation tests.

4.4.7 Low velocity impact response of the titanium-based FMLs

4.4.7.1 Effect of stacking configurations on perforation resistance

In order to investigate the influence of the stacking configurations (i.e. total thickness) on the
impact perforation resistance, titanium-based FMLs with various stacking configurations were
subjected to low velocity impact. Details of the impact tests, in terms of impactor mass and
velocity, were given in Chapter 3 (Section 3.4.2.4).

Load-displacement traces for the 2/1, 3/2, 4/3 and 5/4 titanium-based FMLs under low velocity impact are shown in Figure 4-45. Here, all specimens show a similar behaviour in which the impact force increases to a maximum value before damage initiation (perforation threshold) occurs. The force then decreases rapidly after this point. Clearly, the traces are similar to those obtained under quasi-static perforation testing. However, the peak forces under dynamic loading were higher than the corresponding quasi-static ones. This can be attributed to the strain rate-sensitivity of these composites.
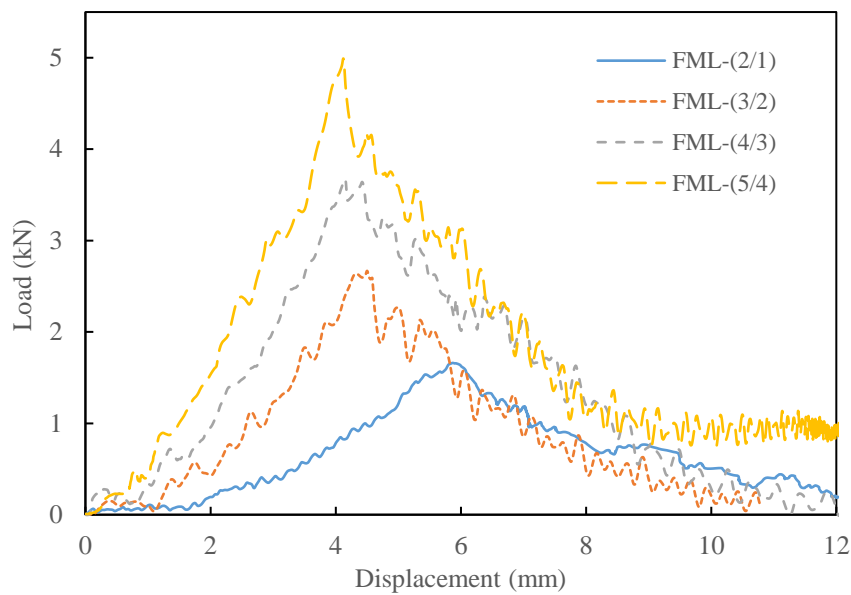
Figure 4-45. Load-displacement traces for the 2/1, 3/2, 4/3 and 5/4 FMLs following low velocity impact.

The failure mechanisms of the impacted panels were then investigated by taking cross-sections of a number of specimens transversely through the centre of the damaged area after impact. These sections were polished and examined using a low magnification optical microscope. The polished cross-sections for the titanium-based FMLs with various stacking configurations following low velocity impact tests are shown in Figure 4-46. The figure shows that, during perforation, fracture can be observed on the upper and the lower layers of titanium alloy as well as fracture in the composite core of these laminated structures. It is clear that all specimens exhibit extensive interfacial delamination associated with permanent deformation. The results indicate that a considerable amount of energy under impact loading are absorbed in this

124

mechanism. It is also worth mentioning that the failure processes in the dynamically-loaded panels is similar to the corresponding specimens following static testing as shown earlier in Figure 4-43.
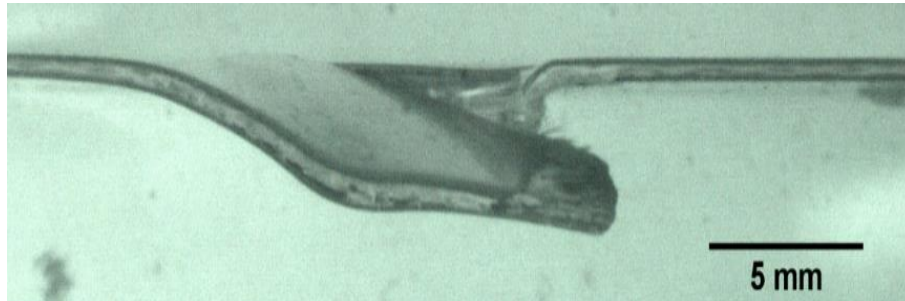
2/1 FMLs
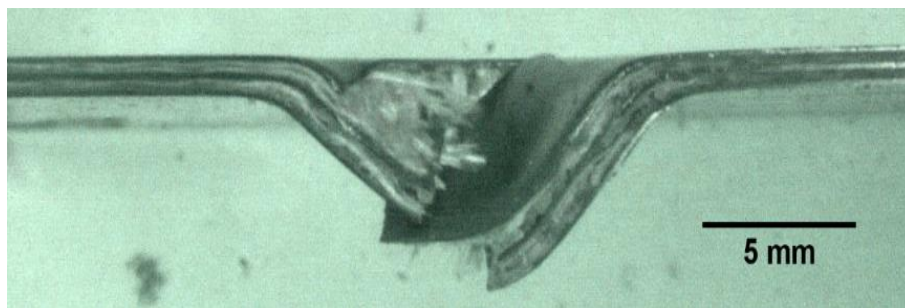
3/2 FMLs
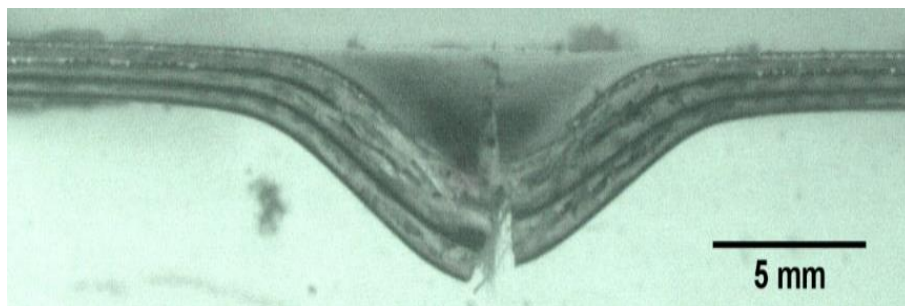
4/3 FMLs
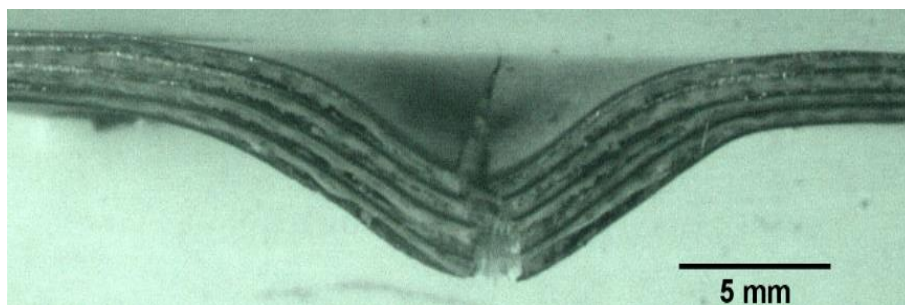
5/4 FMLs

Figure 4-46.Cross-sections following low velocity impact perforation of 2/1, 3/2, 4/3 and the 5/3 stacking configuration of the titanium based fibre metal laminates.

125

The fracture mechanisms of the titanium-based FMLs following low velocity impact tests were further investigated by examining the front and rear surfaces of the damaged panels. Figure 4-47 shows micrographs for the front and the back surfaces of the 2/1, 3/2, 4/3 and 5/4 FMLs. Clearly, at the perforation threshold, as a result of the projectile passing through the target, a hole with the same diameter as the steel impactor was formed on the front surface. It is also clear from the figure that perforation resulted in a longitudinal crack in the panels. This evidence suggests that these laminates have failed in a brittle mode with little plastic deformation which considered as the main failure mechanism that contributed to the low impact performance [144], resulting in a lower resistance to low velocity impact. It is interesting to note that the appearance of the dynamically-loaded specimens is similar to that observed under quasi-static loading rate. However, failure is more severe in the case of impact test but this could be attributed to the sensitivity of these laminates to the strain-rate.

Figure 4-48 shows the variation of the absorbed energy with the sample thickness for the titanium-based FMLs following low velocity impact testing. Once again, the energy required to perforate the targets increases with specimen thickness in a non-linear manner. For example, the absorbed energy by the FMLs with a stacking configuration of 2/1 was 6.5 J which is approximately one quarter that offered by the thickest panels (5/4 FMLs). The values of the absorbed energy were then normalised by the areal density of these laminates. The variation of the specific energy absorption as a function of specimen thickness is presented in Figure 4-49. From the figure, it is clear that the specific energy absorption for the panels investigated here fall into a narrow range between 3.56 Jm^2/kg for the 3/2 FMLs and 4.79 Jm^2/kg for the 4/3 FMLs. It is interesting to note that the scatter in the specific energy values is similar to those obtained under quasi-static tests for the range of the laminates investigated. However, the dynamic values were higher than those following quasi-static loading.

Front   Rear

2/1 FMLs

3/2 FMLs

4/3 FMLs
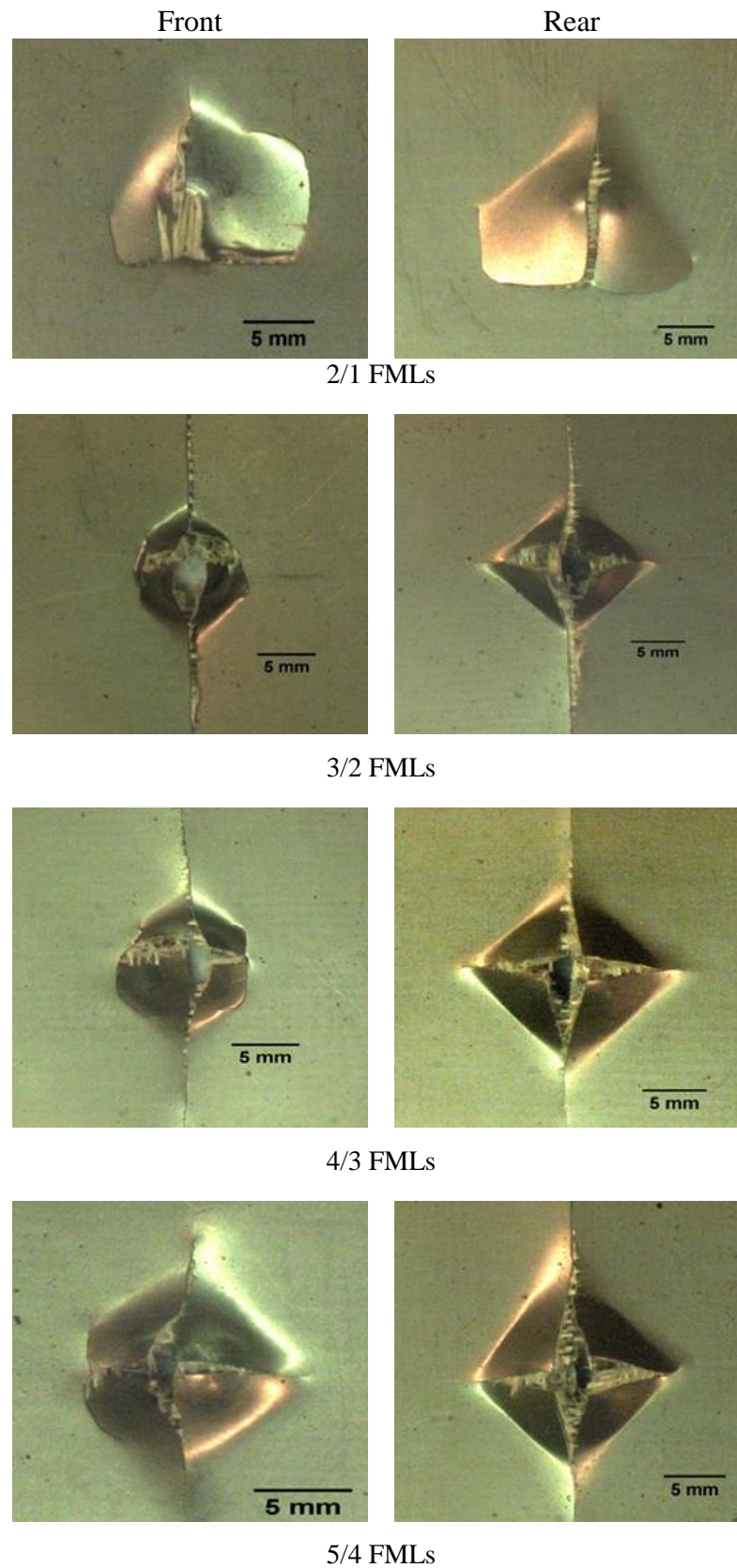
5/4 FMLs

Figure 4-47. Photographs of the front and rear surfaces of FMLs based on the titanium alloy following impact perforation testing.
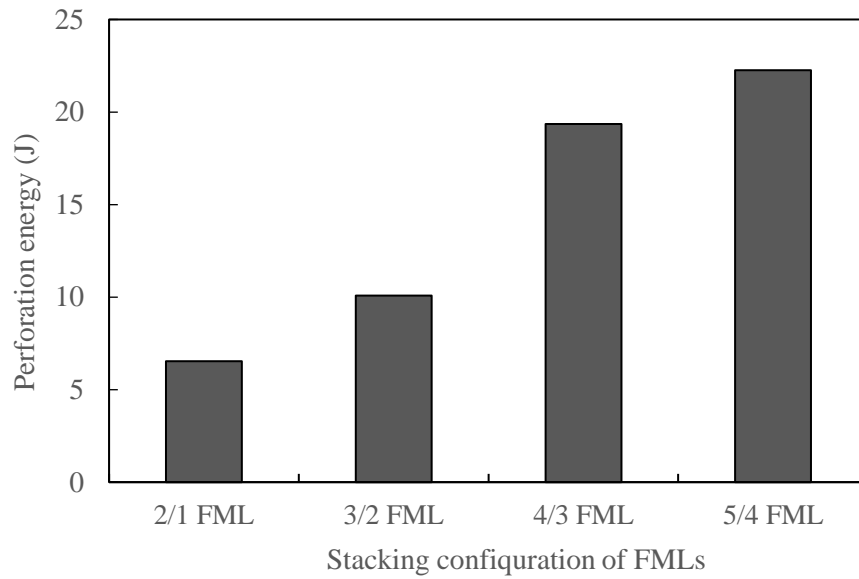
Figure 4-48. Variation of perforation energy with target thickness for 2/1, 3/2, 4/3 and 5/4 FMLs based on 2-ply composite cores following low velocity impact test.
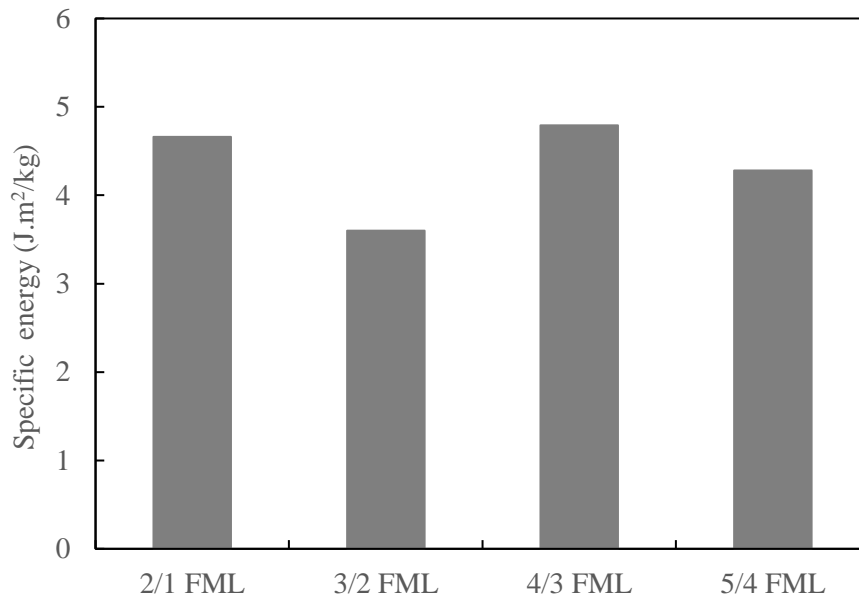
Figure 4-49. The variation in the specific absorbed energy as a function of the laminate thickness for the titanium based FMLs following low velocity impact tests.

The dynamic peak loads in Figure 4-45 were compared to the corresponding quasi-static values in Figure 4-40 to assess the rate-sensitivity of these laminates. Figure 4-50 shows the variation in the dynamic peak force with the quasi-static force for the titanium-based FMLs. As expected, the dynamic peak forces were higher than those under quasi-static loading for the laminates investigated. The dynamic values of absorbed energy were plotted against the

128

quasi-static values, as shown in Figure 4-51. Again, after impact, the FMLs exhibit a higher

energy absorption than those subjected to quasi-static perforation testing.
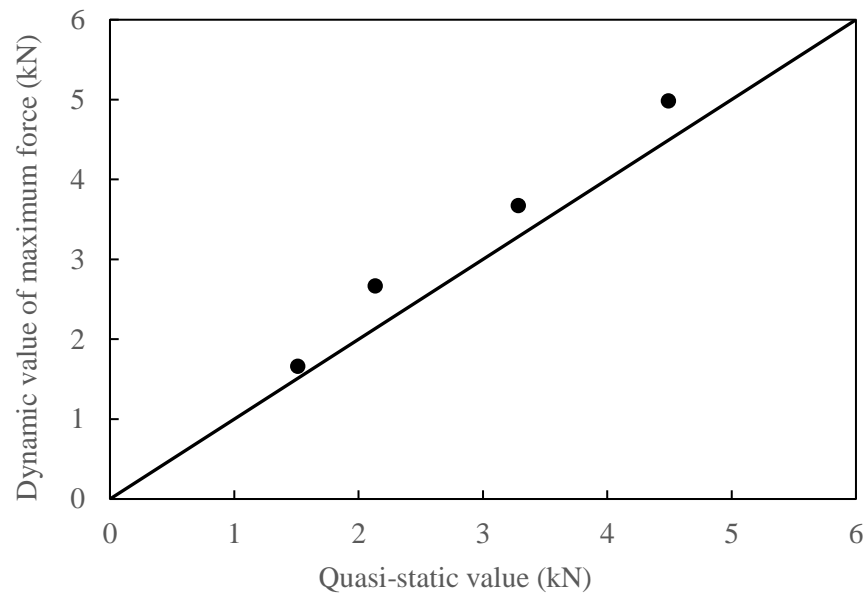
Figure 4-50. Variation on the maximum force following quasi-static and dynamic
loading for the 2/1, 3/2, 4/4, and 5/4 stacking configurations.
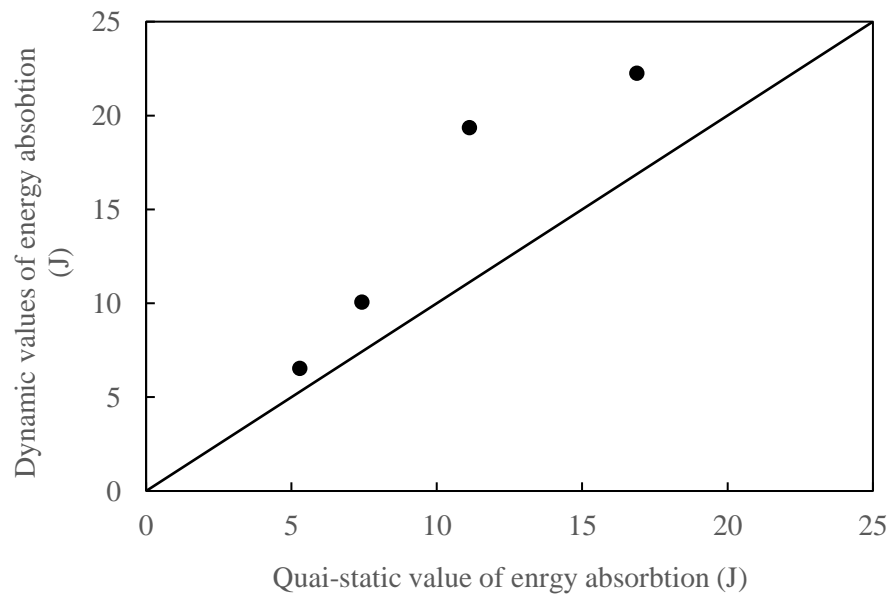
Figure 4-51. Variation on the perforation energy following quasi-static and dynamic
loading rates for the 2/1, 3/2, 4/4 and 5/4 stacking configurations of FMLs.

4.4.7.2 Effect of the composite thickness (core) on the perforation resistance of 2/1 FMLs

4.4.7.2.1 Density of the fibre metal laminates

Clearly, the density of the fibre metal laminates depends on the individual densities, as well as the relative proportion of the constitutive materials, i.e. the titanium alloy and the glass fibre reinforced PEKK (GF/PEKK). Here, the densities of all of the fibre metal laminates with different core thicknesses were calculated by weighing and measuring the dimensions of panels. The variation of density with composite core thickness for the 2/1 titanium-based fibre metal laminates is shown in Figure 4-52. From the figure, it is clear that the density decreases with increasing panel thickness, i.e. increasing core thickness. It is interesting to note that the FML configurations offer densities that are up to 35% lower than those offered by the titanium alloy.
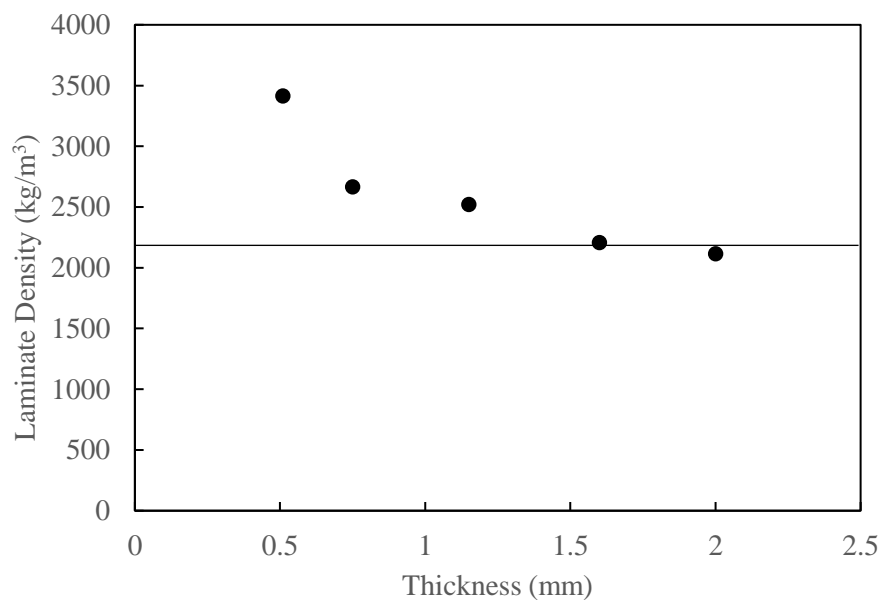
Figure 4-52. The variation of density against panel thickness for the 2/1 titanium based fibre metal laminates.

4.4.7.2.2 Impact response of the 2/1 titanium-based fibre metal laminates

This section investigates the impact response of the 2/1 titanium-based fibre metal laminates with various composite (core) thicknesses. Here, 2-, 4-, 8, 12- and 16-ply composite cores are stacked between two titanium foils. Here, the panels were impacted using the required energy to perforate the targets. The tests are detailed in Chapter 3 (Section 3.4.2.4). The load-displacement traces are presented in Figure 4-53. From the figure, it is clear that the stiffness and the maximum force of these hybrid composites show a high dependency on the thickness of the composite (core), with the impact force increasing rapidly with core thickness. Interestingly, all traces are highly oscillatory, due to the dynamic nature of the test.
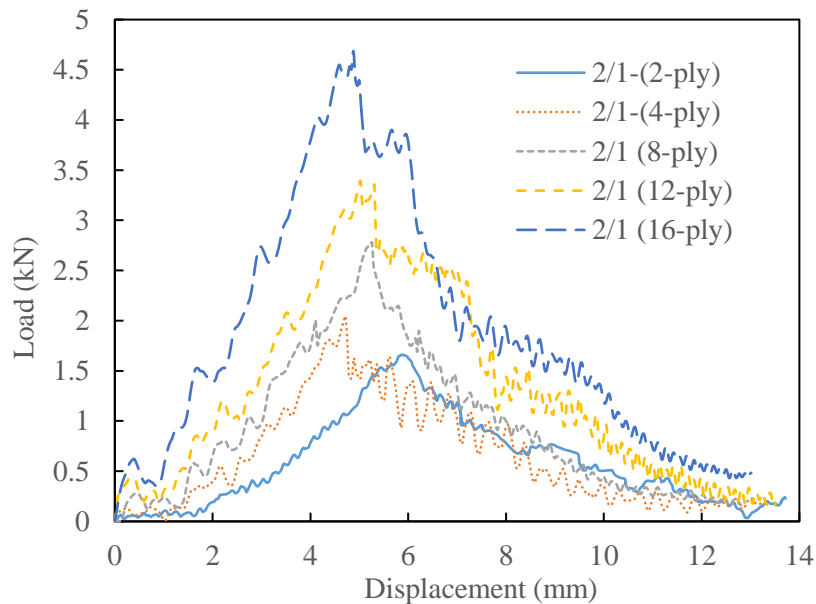
Figure 4-53. Load-displacement traces for FMLs (2/1) laminates based on 2-, 4- , 8-, 21- and 16-ply composite cores following low velocity impact testing.

4.4.7.2.3 Perforation resistance of the FMLs

The impact responses of the 2/1 fibre metal laminates with different core thicknesses was investigated by determining the perforation energies of all specimens studied in this work. Here, the areas under the load-displacement traces in Figure 4-53 were used to determine the perforation energies of the laminates. The variation of perforation energy with target thickness for the 2/1 FMLs following impact testing is shown in Figure 4-54. From the figure, it can be

seen that the perforation resistance of this type of FML increases with increasing panel thickness. For example, the perforation resistance of the 2/1 FMLs with a 16-ply core was three times higher than that based on a composite core of 2-ply.
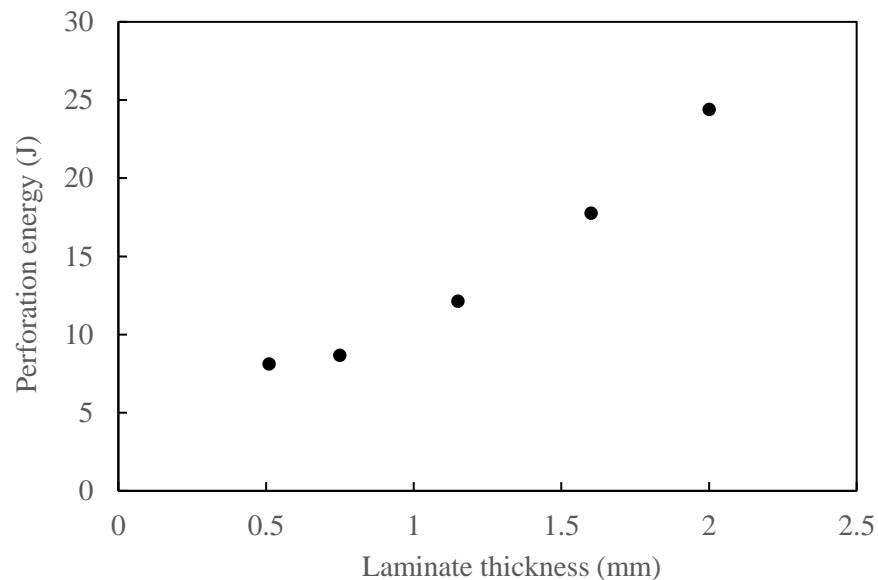
Figure 4-54. The variation of the perforation energy with the specimen thickness for 2/1 fibre metal laminates following low velocity impact tests.

Figure 4-55 compares the variation in the perforation energy with the GF/PEKK composite thickness for the GF/PEKK plain composites and titanium-based fibre metal laminates following low velocity impact testing. From the figure, it can be seen that the perforation energy of both systems increases with increasing target thickness. The superiority of FMLs is obvious, in which these hybrid composites showing a much higher perforation resistance than those offered by the plain composite with a range for the panels investigated. Moreover, the thickness of the FMLs is higher than that for the plain composites, resulting in a higher stiffness and impact force. It is worth mentioning that the increase rate of the perforation resistance of the FMLs with the core thickness is similar to that of the plain composite, except for cores above a 1.5 mm thickness, where the rate increases.

132
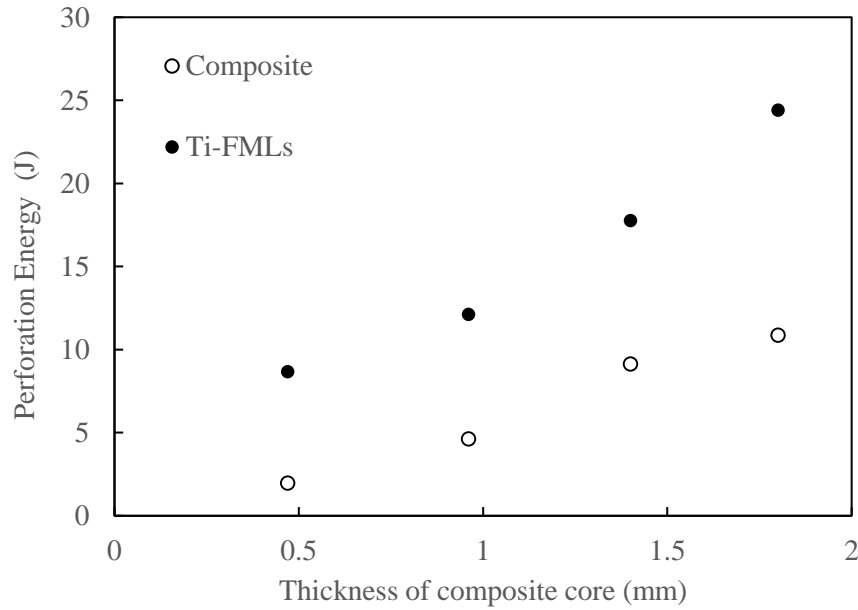
Figure 4-55. The variation of the perforation energy with the composite core thickness for the 2/1 FMLs. The perforation thresholds of the plain composite are included in the figure.

The absorbed energy was normalised by the areal density of the panels in order to facilitate a clearer comparison between the two laminate types. Figure 4-56 compares the data for the GF/PEKK composites and the FMLs in terms of specific energy absorption. From the figure, it is clear that the SEA values of the FMLs are higher than those offered by the plain composites. This highlights the superiority of these hybrid materials (FMLs) which offers a high perforation threshold.

Figure 4-57 shows polished cross-sections for the titanium-based FMLs based on 4-, 8-, 12- and 16-ply composites cores after impact testing. It is clear that delamination between the composite plies and lower titanium layers can be observed in all of the failed FMLs. It can also be noted that the severity of the delamination increases with increasing thickness of the composite core. This can be attributed to the composite stiffness, since the stiffer composite (1.8 mm thick) is difficult to deform in compared to the 0.14 mm thick titanium layer. Interestingly, no delamination was observed between the GF/PEKK plies.
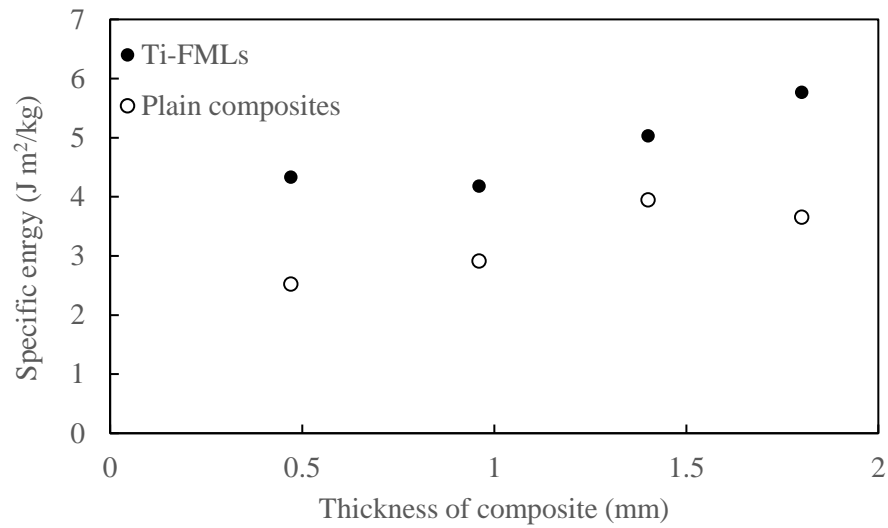
Figure 4-56. Variation of the specific perforation energy of the plain composites and the 2/1 (4-, 8-, 12- and 16-ply) titanium based FMLs following low velocity impact tests. The thickness of the FMLs refers to the thickness of the plain composites.
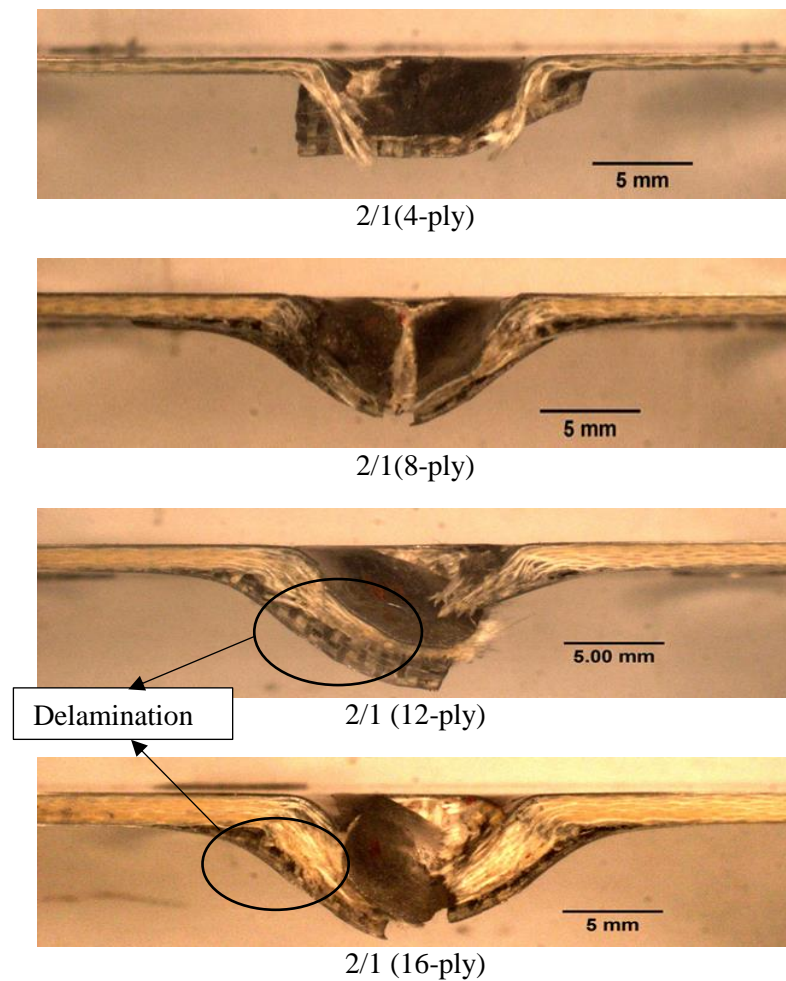
Figure 4-57. Cross-sections of the 2/1FMLs with various core thicknesses following low velocity impact testing (see Table 3-7).

4.4.8 Aluminium based –FMLs

A series of quasi-static and low velocity impact perforation tests were conducted on square fibre metal laminate plates based on aluminium alloy (2024-T3) and plain composite of S-glass fibre reinforced PEKK (GF/PEKK) composites to investigate their rate-sensitivity. The fabrication process of these FMLs was described previously in Section 3.4.1.2. Initially, this study focused on assessing the material properties of the aluminium alloy in tension (described in Section 3.4.2.1). This is followed by a series of perforation tests on 2/1, 3/2, 4/3 and 5/4 stacking configurations. The experimental results are presented and discussed here.

4.4.8.1 Tensile properties of the aluminium alloy

Uniaxial tensile tests were conducted on the aluminium alloy (2024-T3) to obtain its basic material properties, i.e. modulus of elasticity, yield strength, ultimate tensile strength. Figure 4-58 shows the engineering stress-strain relationships for the three aluminium alloy (2024-T3) samples following uniaxial tensile tests. It is clear from the figure that two regions can be distinguished, i.e. elastic and plastic regions. The modulus of elasticity, yield stress, and ultimate tensile strength were found to be 75 GPa, 320 MPa, and 458 MPa, respectively. The failure mode in the aluminium alloy coupons following quasi-static tensile tests were presented in Figure 4-59. Again, all samples failed within the gauge length.
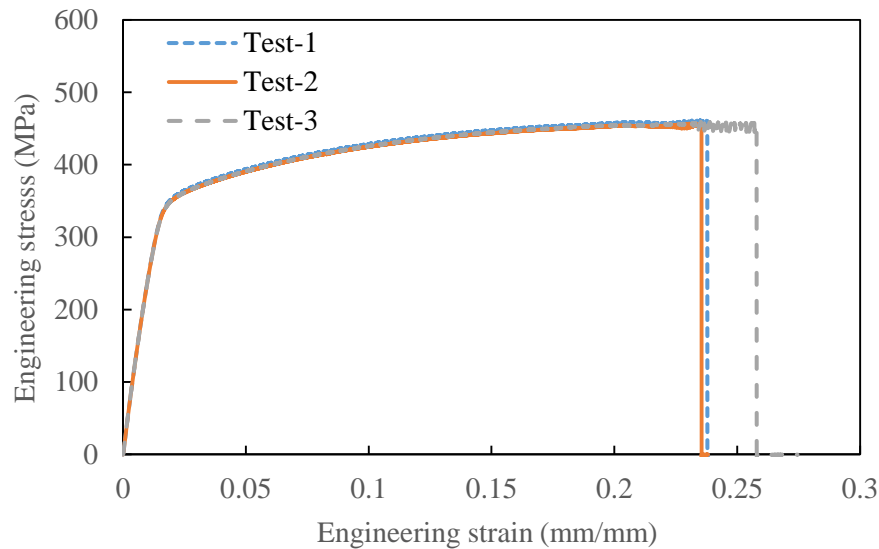
Figure 4-58.Engineering stress-strain curves for the aluminium alloy (2024-T3) following quasi-static tensile testing.
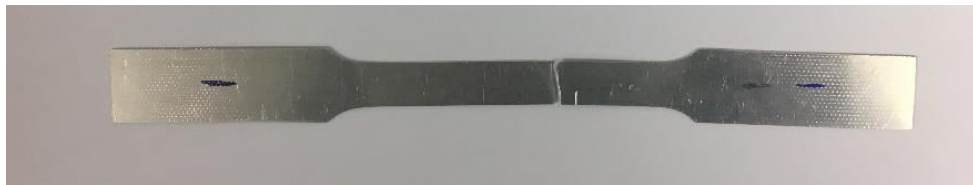
Figure 4-59. Failure mode in the aluminium coupons following tensile testing.

4.4.8.2 The influence of the processing cycle on the residual tensile strength of the aluminium alloy (2024-T3).

The influence of the manufacturing process on the residual tensile strength of the aluminium alloy (2024-T3) after a heating cycle was investigated. Here, aluminium sheets were heated to 330 °C before cooling down slowly inside the hot press. Figure 4-60 shows the effect of the processing temperature on the residual strength of aluminium alloy (2024-T3). From the figure, it can be seen that the modulus of elasticity of aluminium alloy is not affected by the high-temperature processing cycle. However, the tensile strength as well as the yield stress of the aluminium alloy drop, due to the temperature cycle. For example, the specimens heated to 330 °C resulted in a tensile strength of approximately 34% lower than the as-received ones. These kind of 2xxx alloys grade are heat-treatable by precipitation hardening, in which the

yield and the tensile strength increase with the time at a constant temperature (aging temperature) after rapidly cooling from the solution heat treatment temperature. Thus, the reason behind the drop in the yield and tensile strengths of the aluminium alloy investigated can be attributed to the over-aged manufacturing process, which leads to a significant coarsening of the precipitate within the alloy and lowers the yield strength (so tensile strength). The resulting stress-strain values after the heating cycle were used as material properties in the finite element modelling which will be described in Chapter 5.
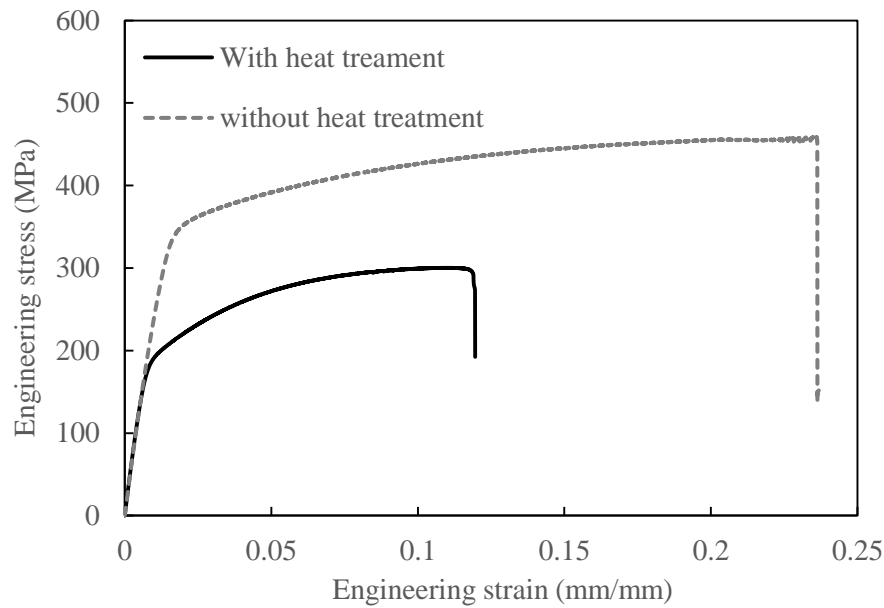
Figure 4-60. Comparison of the average engineering stress-strain traces for the as-received and heat treated aluminium alloys (2024-T3).

4.4.8.3 Quasi-static perforation of the 2024-T3 based-FMLs

The response of the aluminium-based FMLs with different stacking configurations following quasi-static perforation tests was investigated in this study. Figure 4-61 shows load-displacement traces for the 2/1, 3/2, 4/3 and 5/4 FMLs with a 4-ply (GF/PEKK) composite layer. From the figure, it can be seen that all FML specimens show a high stiffness during initial loading, due to membrane effects in these relatively thin metal sheets. Similar behaviour was observed by Zhou et al. [132] in their work on fibre metal laminates based on aluminium alloy 6061-T6 stacked with glass fibre reinforced composite.

It can also be noted that the load-displacement traces for the FMLs investigated exhibit two stages. In the first stage, the load increases monotonically with displacement as the indenter strikes the target. Once a tensile crack starts on the rear surface, and the indenter perforated the target, the force drops gradually during the second stage. Here, the stiffness of the FML plates increases with increasing thickness. Moreover, the thickest panels, i.e. 5/4 stacking configurations, exhibit the highest peak force, which is more than four times that offered by the thinnest plate (2/1-FMLs). It is interesting to note that the investigated FMLs show a proximately similar maximum displacement before damage initiation. This evidence suggests that damage initiation threshold of these laminates shows no dependency on the target thickness.

Again, the area under the load-displacement trace was used to determine the energy absorbed by the FMLs during the perforation process. The effect of panel thickness on energy absorption for the 2024-T3 based FMLs is presented in Figure 4-62. Clearly, as the stacking configuration (thickness) of the FMLs increases, the perforation energy increases. For example, the thickest specimens (5/4 FML) shows an energy absorption of 59 J compared to 14 J offered by the thinnest sample (2/1 FML).

The energy absorption values of these laminates were then normalised by the areal density to be presented in the terms of specific energy. The specific energy values were then compared to the corresponding data for FMLs based on the glass fibre reinforced epoxy and aluminium alloy (2024-O) [150], as shown in Figure 4-63. Clearly, the 2024-T3-based FMLs investigated in this study offered approximately doubled values of the specific energy absorption compared to data in Ref. [150]. This can be attributed to the superior properties of the constituent materials used in the fibre metal laminates. The perforation resistance is attributed to the superiority of the woven S-glass reinforced PEKK composites over the woven E-glass fibre reinforced epoxy (described in Section 4.3.4) and the stronger mechanical properties of aluminium alloy 2024-T3 over 2024-O grade, i.e. the tensile strength of 2024-T3 investigated is 300 MPa (see Section 4.4.8.2) compared to 186 MPa for 2024-O [150]. Figure 4-64 shows

the front and the rear views of the four FML configurations investigated in this study. An examination of the figure shows that all targets exhibit local plastic deformations on the aluminium alloy, as well as a fracture of the composite layers close to the perforation opening. The failure process in the specimens involves tensile fracture on the rear face of the specimens, resulting in a cross-shaped fracture pattern. As the indenter continues to push through the target, the cracks tended to propagate through the thickness of the laminate, leading to the formation of a hole in the front face.
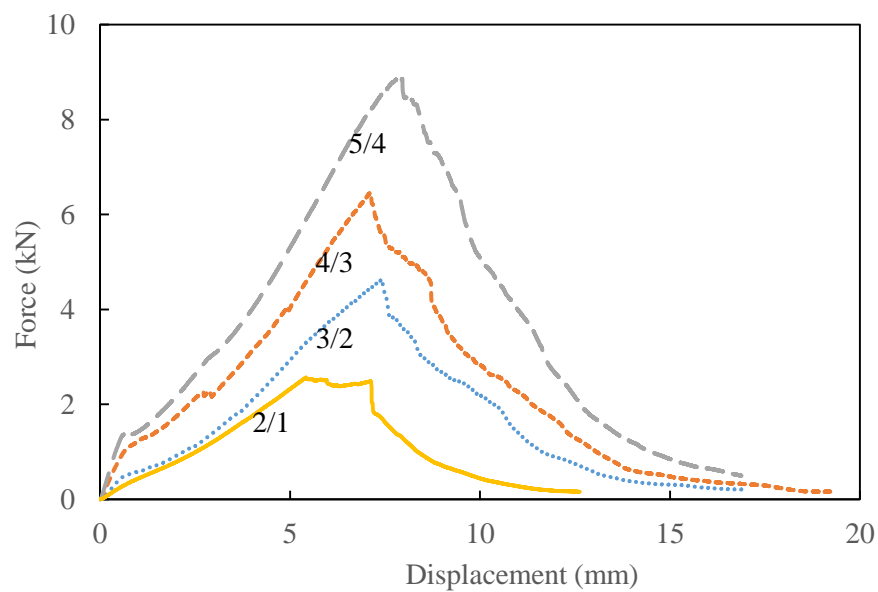
Figure 4-61. Load-displacement traces for the aluminium (2024-T3) based FMLs under quasi-static perforation tests.
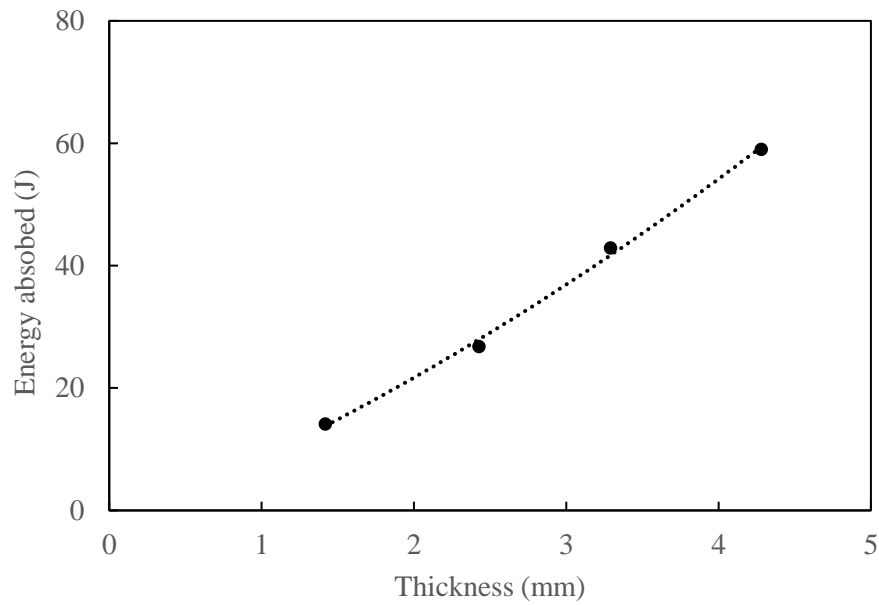
Figure 4-62. The variation of the absorbed energy with the FMLs thickness
following quasi-static perforation tests.
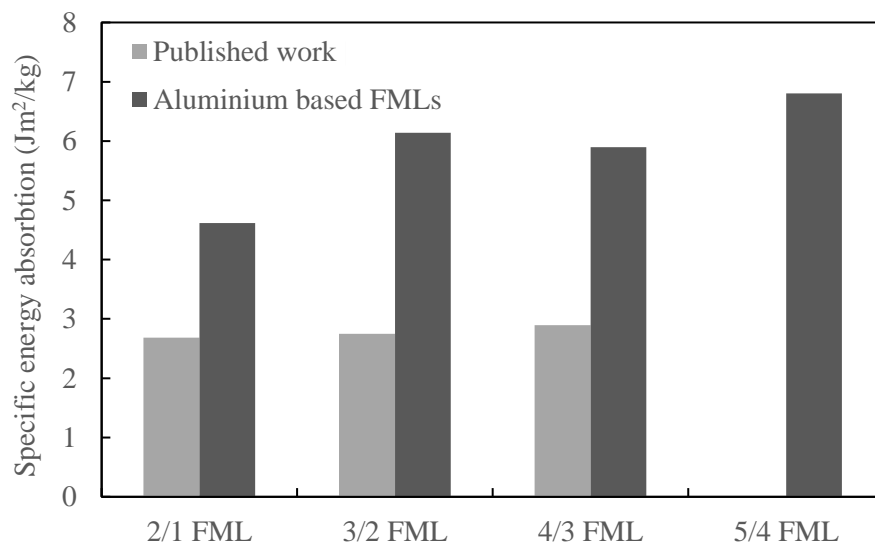
Figure 4-63. The specific energy absorption values following quasi-static perforation
tests of the investigated aluminium (2024-T3)-based FMLs and the FMLs of the
published work [150].

Front face   Rear face

2/1 FMLs
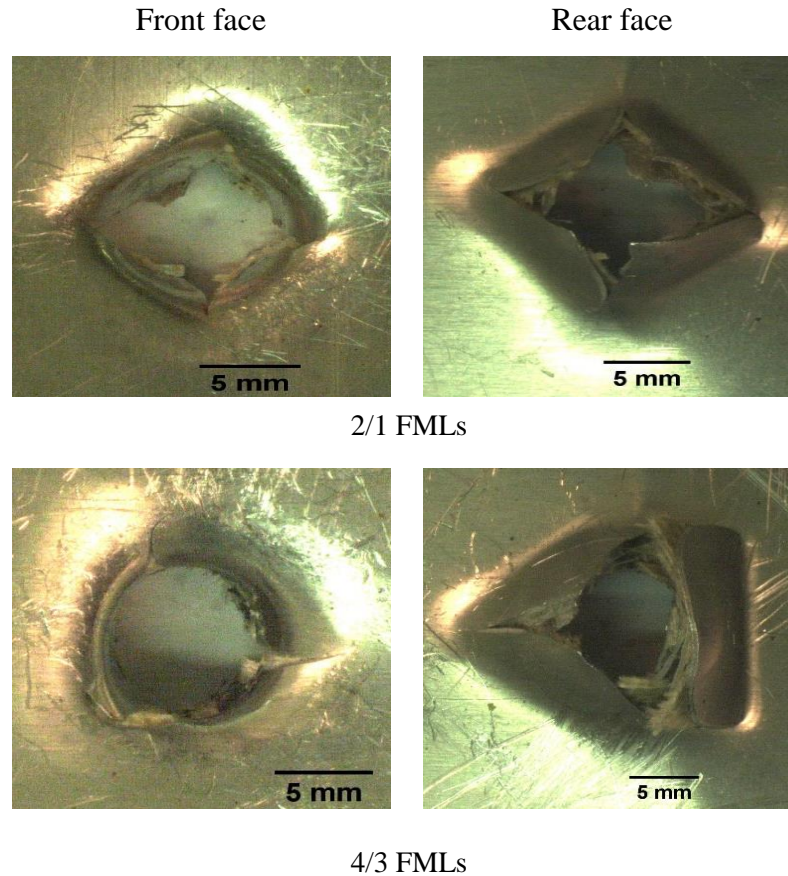
4/3 FMLs

Figure 4-64. Photographs of the front and rear surfaces of FMLs based on aluminium alloy 2024-T3 following quasi-static perforation testing for the 2/1 and 4/3 FMLs.

4.4.8.4 Low velocity impact response of FMLs with various stacking configurations

The effect of strain-rate on the perforation resistance for the aluminium-based fibre metal laminates was investigated. The load-displacement traces for the 2/1, 3/2, 4/3 and 5/4 2024-T3 based FMLs following low velocity impact testing are shown in Figure 4-65. Details of the impactor masses and the velocities were previously described in Section 3.4.2.4. It is clear that all of the specimens deformed in a similar fashion, in which the load-displacement curves exhibit two stages. The loads increase with increasing displacement (elastic region) in the first region. Here, the initial stiffness and the maximum force show a high dependency on the plate thickness. In the second region, due to the initiation of de-bonding (delamination) as well as the splitting of the composite and the aluminium alloys, a rapid drop in the impact force

141

occurred. It is interesting to note that all the FML laminates investigated exhibit an oscillatory response, due to the ringing effects in the load cell.

The variation of the energy absorbed as a function of specimen thickness for the aluminium-based FMLs is shown in Figure 4-66. It is clear from the figure that, for a given specimen thickness, the energy absorption increases with increasing the thickness of the laminates.

The influence of the strain-rate on the perforation resistance for the aluminium-based FMLs was investigated by comparing the quasi-static and the dynamic absorbed energies. Figure 4-67 summarises the quasi-static and impact perforation resistance of the aluminium-based FMLs. From the figure, it is clear that all samples tested, under impact loading, offer a higher level of energy absorption, with average values being 20 % higher than that obtained under quasi-static loading rate.
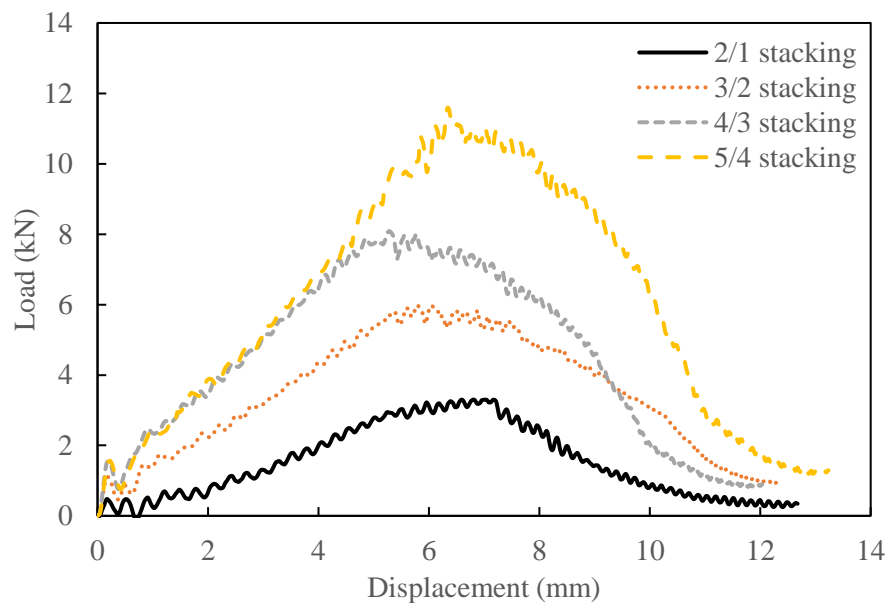
Figure 4-65. Load-displacement curves for the 2/1, 3/2, 4/3 and 5/4 aluminium based FMLs following low velocity impact tests.
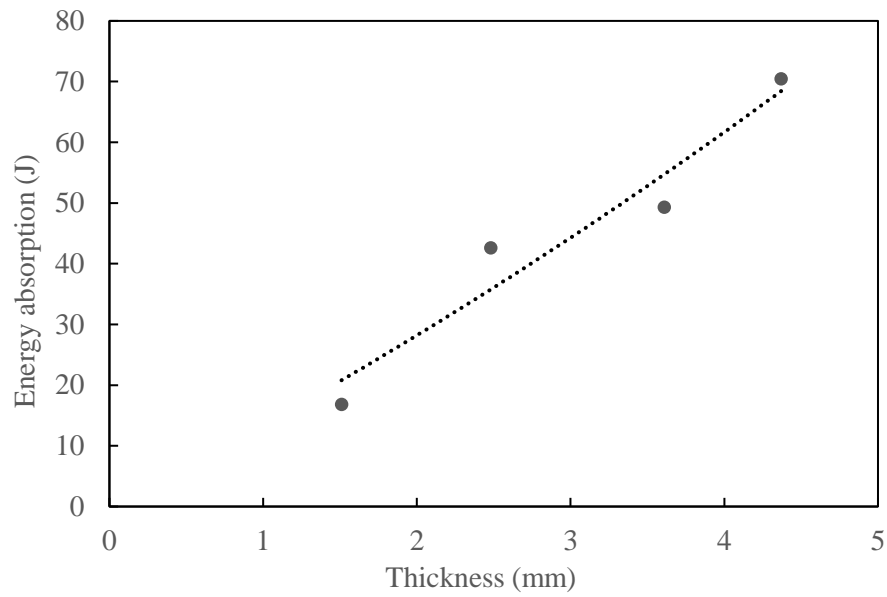
Figure 4-66. The influence of specimen thickness on the energy absorbing

characteristics of the aluminium based fibre metal laminates.
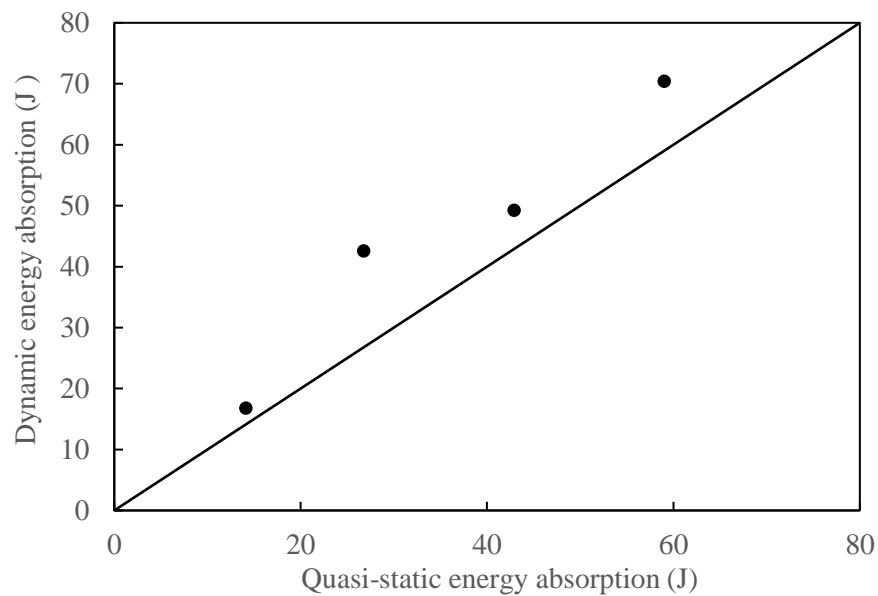
Figure 4-67. Comparison of the dynamic absorbed energy and quasi-static absorbed

energy for the 2/1, 3/2, 4/3 and 5/4 aluminium-based FMLs.

The front and rear surfaces of the FMLs investigated are shown in Figure 4-68. Clearly, the

appearance of the impacted panels is similar to the corresponding specimens tested under

quasi-static perforation.

143

Front face   Back face

2/1 FMLs

4/3 FMLs
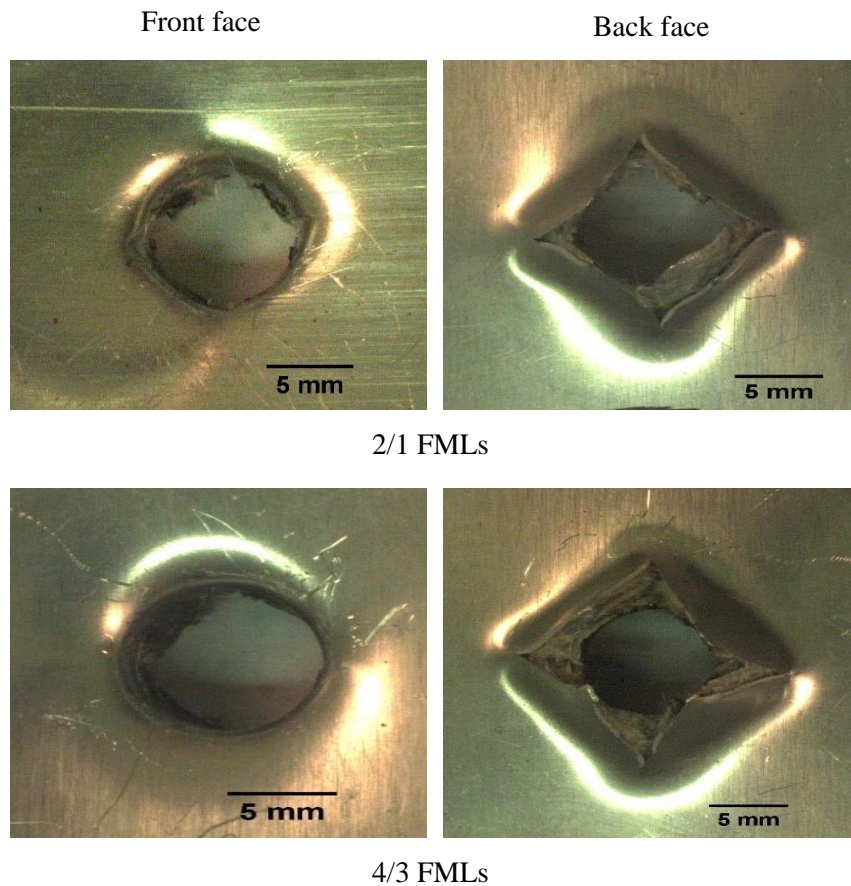
Figure 4-68. Photographs of the front and rear surfaces of FMLs based on aluminium alloy following impact perforation testing for 2/1 and 4/3 stacking configuration stacking configuration.

Figure 4-69 shows cross-sections of the impact-loaded FMLs. It is clear that the failure process involves fracture of the composite plies close to the impact zone, as well as local plastic deformations and fracture of the aluminium alloy. Closer examination of the figure suggests that the panels exhibit a substantial amount of delamination, along with some petalling of the rear surface of the aluminium alloy.
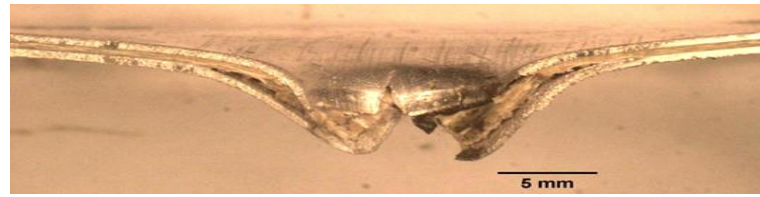
2/1 FMLs
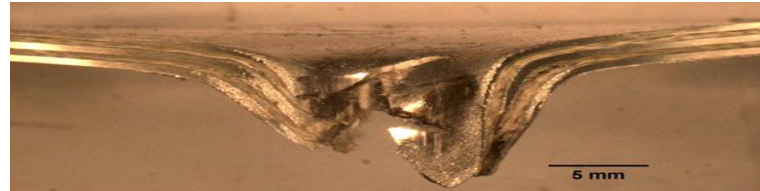
3/2 FMLs
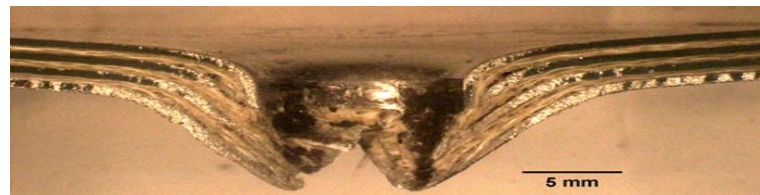
4/3 FMLs
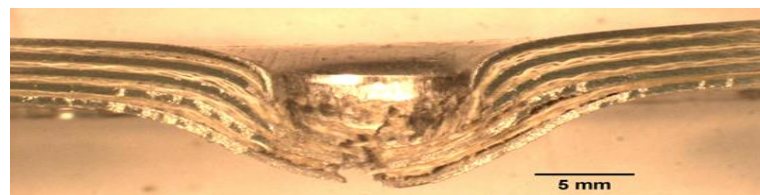
5/4 FMLs

Figure 4-69. Cross-sections following low velocity impact perforation of 2/1, 3/2, 4/3 and 5/3 stacking configuration of aluminium (2024-T3) based fibre metal laminates.

4.5 Comparisons between Ti- and Al- based FMLs

The perforation failure for the titanium-based and aluminium-based FMLs following quasi-static and low velocity impact perforation tests were compared. Here, a hemispherical indentor with a diameter of 10 mm was used to perforate specimens with dimensions of (100 mm x100 mm) for the both laminate systems. The thickness of the titanium sheets is less than that of the aluminium alloy. To improve clarity and facilitate comparisons, the perforation resistances of these plates were compared in terms of specific energy absorption by normalising the perforation energy of each system by its respective areal density. Moreover, the peak force of both the FML systems is normalised by the target thickness in terms of specific force.

4.5.1 Quasi-static perforation response of the FML systems

Figure 4-70 compares the specific energy absorption values of the aluminium- and titanium-based FMLs as a function of stacking configurations following quasi-static loading. From the figure, it can be noted that the specific energy absorption values for the aluminium-based FMLs are almost doubled those of the titanium-based FMLs. The specific energy absorption of the aluminium-based FMLs varied over a range of 4.6 $J.m^2.kg$ for the 2/1 FMLs and 6.8 $J.m^2.kg$ for the 5/4 FMLs compared to those offered by titanium-based FMLs of 3.03 $J.m^2.kg$ and 3.24 $J.m^2.kg$. It is apparent that the contribution of the aluminium alloy is significantly higher than those offered by the titanium. This evidence highlights the brittleness (low ductility) and relatively poor impact properties of the high strength titanium alloy-based FMLs, which was also observed by Cortes et al. [168].

A comparison of the maximum contact force for the two FML systems investigated following quasi-static perforation tests is shown in Figure 4-71. It is clear from the figure that titanium-based FMLs yielded higher peak forces than those offered by aluminium-based FMLs for all configurations investigated. The results suggest that the incorporation of the higher strength titanium (Ti-15-3-3-3) alloy into the composite effectively increases the stiffness of the FMLs, resulting in higher contact force at perforation threshold.
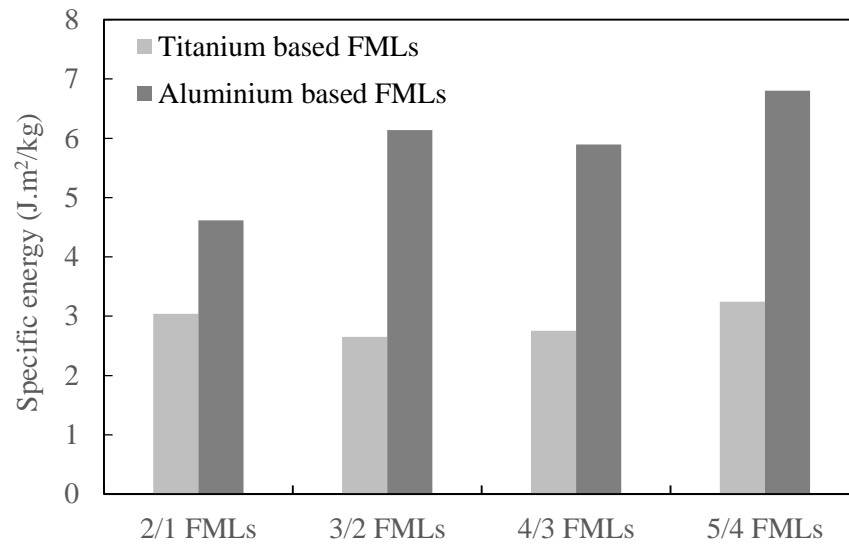
Figure 4-70. The variation of the specific energy absorption for the 2/1, 3/2, 4/3, and 5/4 titanium based and aluminium (2024-T3) based FMLs following quasi-static perforation tests.
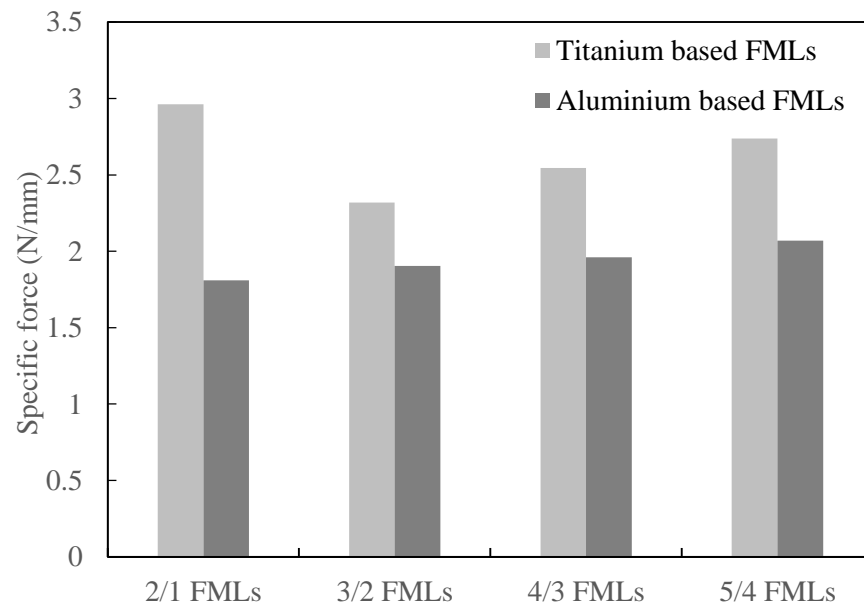
Figure 4-71. The comparison of the specific peak force for the 2/1, 3/2, 4/3, and 5/4 titanium based and aluminium (2024-T3) based fibre metal laminates following quasi-static perforation tests.

4.5.2 Low velocity impact response of the FMLs

Figure 4-72 shows the variation of the specific energy absorption (SEA) with target stacking configurations for the two FML systems following low velocity impact tests. From the figure,

it can be seen that the values of specific energy absorption of the aluminium-based FMLs are considerably higher than those for titanium-based FMLs, except for 2/1 FMLs. Clearly, the SEA value for the 2/1 aluminium-based FMLs falls in the same range as the titanium-based FMLs. This could be attributed to the low volume fraction of aluminium alloy, resulting in a lower perforation threshold. In the other hand, the thick plates, i.e. 3/2, 4/3, and 4/5 aluminium-based FMLs exhibit a higher energy absorption, highlighting the contribution of the aluminium alloy (higher volume fraction) in increasing the perforation resistance of these panels. It is apparent that the contribution of the aluminium alloy is significant, as mentioned before under quasi-static tests. It is also interesting to note that the variation of the perforation energy under dynamic loading rates for both the FML systems is less than that obtained following quasi-static rates.
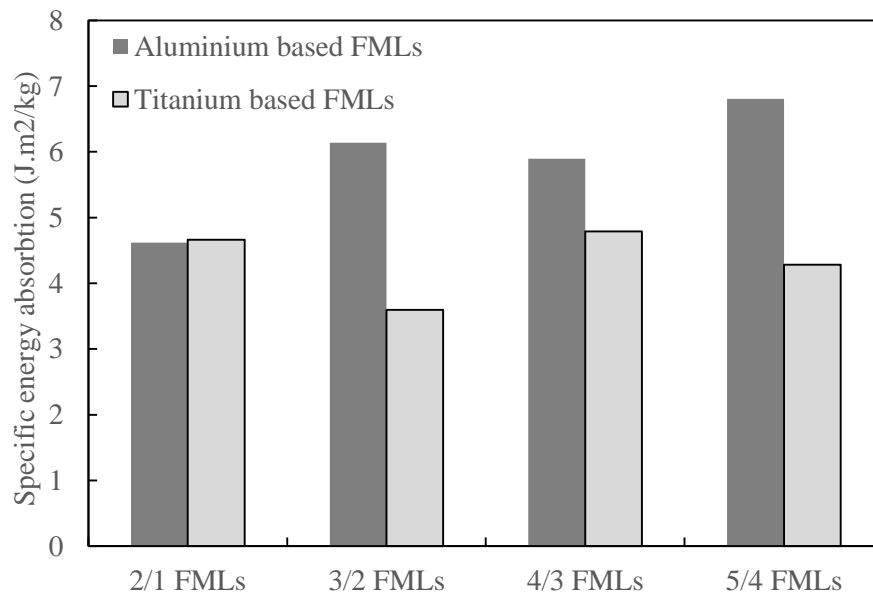
Figure 4-72. Summary of the specific energy absorption for the 2/1, 3/2, 4/3, and 5/4 titanium based and aluminium (2024-T3) based fibre metal laminates following low velocity impact tests.

Figure 4-73 compares the specific maximum force values for both FML systems as a function of the stacking configuration under impact testing. As expected, the values of the maximum impact force for the titanium-based FMLs are significantly higher than those offered by the

aluminium-based FMLs. This again highlights the low ductility (high stiffness) of the FMLs based on the high strength titanium alloy.
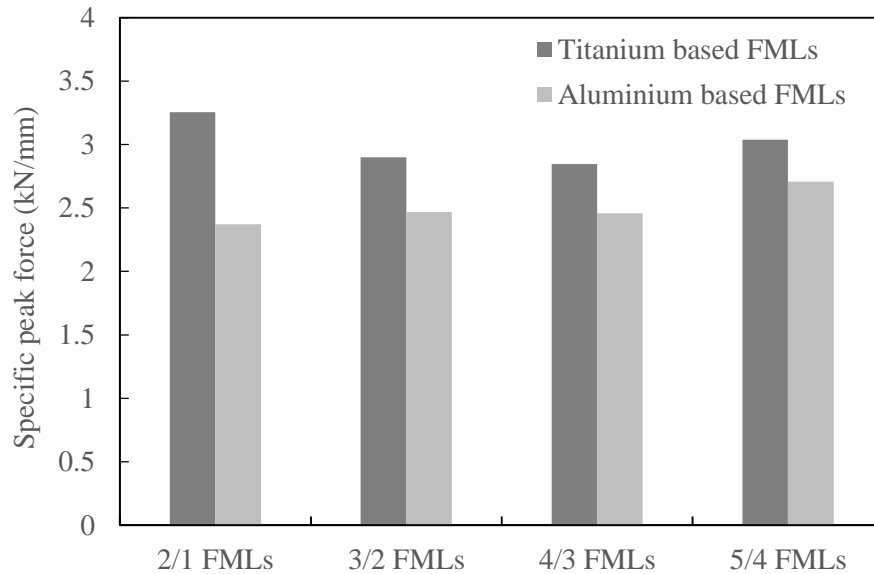
Figure 4-73. The variation of the specific peak force for the titanium and aluminium (2024-T3) based FMLs as a function of specimen stacking configurations following impact perforation tests.

4.6 Summary

Experimental investigations on plain GF/PEKK laminates were undertaken and the results are summarised in this chapter. Initially, the bonding strength between the S-glass fibre and the PEKK resin was evaluated. Subsequently, testing on these plain composites shows that the pre-treated fibres with a binder exhibit a higher bonding strength between the fibre and the resin powder than those obtained without fibre treatment. The properties of these composites at room and high temperature were also investigated. S-GF/PEKK composites offer a perforation threshold up to 73% higher than that of E-GF/Epoxy laminates. High temperature tensile tests on these composites showed that there is hardly any reduction in the tensile strength when the composite was heated to 100 ºC, whereas at a temperature of 250 ºC, the

tensile strength dropped by approximately 35%, relative to the panels tested at room temperature.

The GF/ PEKK laminates were then tested under quasi-static and dynamic loading rates to investigate their rate-sensitivity. The failed specimens after perforation testing were sectioned, polished before using a low magnification microscope to highlight the failure modes of these panels. The results show that, after testing, the targets failed in the form of a cross-shaped fracture on the rear face and a hole-shaped structure on the front surface. Furthermore, there was no obvious delamination between the plies under the all testing conditions. Therefore, this evidence suggests that delamination between the GF/PEKK prepregs is not significant.

The influence of the strain rate on the perforation resistance of titanium-based and aluminium-based FMLs with various stacking configurations was also investigated. Firstly, the results of tensile tests on surface pre-treated titanium alloys with different laser fluence parameters showed that there is no significant reduction in the residual tensile strength of the laser-treated specimens. For the metal-resin adhesion tests, a laser fluence of 4.54 J/cm^2 seems to be an optimum parameter in which a good bonding strength can be achieved. Tests on both FML systems, at quasi-static and dynamic loading rates, highlight the level of rate-sensitivity of these laminates. The results also showed that the specific energy absorption values of the aluminium-based FMLs were higher than those of titanium-based FMLs, highlighting the low ductility (high stiffness) of the FMLs based on high strength titanium alloy. The observation from samples following impact tests on titanium-based FMLs highlighted similar failure modes to those observed in the aluminium (2024-T3)-based FMLs. However, for the titanium based FMLs, a longitudinal split occurred in the titanium alloy, highlighting the influence of rolling direction of the titanium alloy on failure process in these fibre metal laminates. This evidence suggests that these laminates failed in a brittle mode with lower plastic deformations, resulting in lower resistance to the low velocity impact, in comparison to the aluminium-based FMLs.

5 Chapter 5: Numerical Modelling

5.1 Introduction

This chapter describes the theory and procedures employed for the numerical modelling used to model the response of the glass fibre reinforced PEKK (GF/PEKK) composites, titanium based-FMLs and aluminium based-FMLs under low velocity impact loading. In order to validate the finite element (FE) models, the predicted response of the laminates is compared to the corresponding experimental results. The validation processes of the FE models are included in this chapter.

Here, ABAQUS, a commercial finite element analysis code is employed to help understand the performance of laminates under dynamic loading. In ABAQUS, there are two analysis procedures which can be used in simulation, i.e. implicit and explicit tools. Although ABAQUS/implicit offers a solution for different linear and non-linear problems, explicit solution is adapted in this study because it is particularly well-suited to simulate dynamic events. Moreover, the severely non-linear behaviour such as contact can be handled effectively by using ABAQUS/explicit analysis.

The constitutive models used in the FE analysis are considered in this chapter. The geometrical details, i.e. element types and mesh size, loading and boundary conditions, interaction between the projectile and target as well as between laminates are also described.

5.2 Constitutive models of the GF/PEKK laminates

Details of the constitutive models for the S-glass fibre reinforced PEKK laminates, involving elastic behaviour, damage initiation and damage evaluation are described below. These constitutive models for the materials investigated are detailed in Abaqus manual [169].

5.2.1 Orthotropic elasticity

The elastic behaviour of the composite laminates can de described by defining the engineering constants, i.e. the moduli E_1, E_2, E_3, shear moduli G_{12}, G_{13}, and G_{23}, and the Poisson's ratios v_{12}, v_{13}, v_{23}. In this research, the woven glass fibre reinforced PEKK laminates were modelled

as an orthotropic elastic material prior to the onset of damage. Since the woven composite has fibres in $0°$ and $90°$, the material was assumed to have the same elastic modulus values within the plane along the two major axis directions.

5.2.2 Damage initiation

The elastic-brittle behaviour of the fibre reinforced composites can be modelled using the Hashin failure model [170] provided by ABAQUS. Damage initiation refers to the onset of the material degradation. The failure criteria consider more than one stress to evaluate the modes of the failure. Hashin's damage model assumes four different mechanisms of damage initiation, i.e. fibre tension, fibre compression, matrix tension and matrix compression.

The damage initiation criteria can be determined by using the components of the effective longitudinal $(\tilde{\sigma}_{11})$, transvers $(\tilde{\sigma}_{22})$ and shear stress tensor $(\tilde{\sigma}_{12})$ within the plane of the composites, which are expressed as [169]:

Fibre tension

$$F_f^t = \left(\frac{\tilde{\sigma}_{11}}{X_T}\right)^2 + \alpha \left(\frac{\tilde{\sigma}_{12}}{S_L}\right)^2, \ \tilde{\sigma}_{11} \geq 0 \qquad (5.1)$$

 Fibre compression

$$F_f^c = \left(\frac{\tilde{\sigma}_{11}}{X_C}\right)^2 \alpha, \ \tilde{\sigma}_{11} < 0 \qquad (5.2)$$

Matrix tension

$$F_m^t = \left(\frac{\tilde{\sigma}_{22}}{Y_T}\right)^2 + \left(\frac{\tilde{\sigma}_{12}}{S_L}\right)^2, \ \tilde{\sigma}_{22} \geq 0 \qquad (5.3)$$

Matrix compression

$$F_m^c = \left(\frac{\tilde{\sigma}_{22}}{2S_T}\right)^2 + \left[\left(\frac{Y_C}{2S_T}\right)^2 - 1\right]\frac{\tilde{\sigma}_{22}}{Y_C} + \left(\frac{\tilde{\sigma}_{12}}{S_L}\right)^2, \ \tilde{\sigma}_{22} < 0 \qquad (5.4)$$

where X_T, X_C are the tensile and compressive strengths in the longitudinal direction, Y_T, Y_C denote to the tensile and compressive strengths in the transverses direction, S_T, S_L are the longitudinal and transverse shear strengths.

5.2.3 Damage propagation

The damage model assumes that the material damage and failure resulted from the progressive degradation of the material stiffness. This type of damage occurs after the onset of the damage (damage initiation). Once a criterion of damage initiation is satisfied, more loading on the sample will lead to degradation of the material stiffness coefficients. The material stiffness degradation is monitored by damage variables which assume values of 0 for undamaged and 1 for fully damaged states. The damage variables, corresponded to a specific failure mode, are given by the following expression [169]:

$$d = \frac{\delta_{eq}^f \left(\delta_{eq} - \delta_{eq}^0 \right)}{\delta_{eq} \left(\delta_{eq}^f - \delta_{eq}^0 \right)} \tag{5.5}$$

where δ_{eq}^0 is the initial equivalent displacement at which the initiation criterion for a particular failure mode is met and δ_{eq}^f refers to the displacement at which the material is damaged.

Here, the numerical model introduces a linear damage evolution which is based on the fracture energies during the process of damage.

5.3 Constitutive models of the titanium and aluminium alloys

The analysis of the progressive failure of the titanium and aluminium alloys is necessary to predict their mechanical response under various loading conditions, while using appropriate constitutive models for these materials plays a crucial role. The constitutive models for modelling the titanium alloy (Ti-15-3-3-3-β) and the aluminium alloy (Al 2024-T3) used to manufacture the related FMLs are presented in this section. An isotropic elasto-plastic model, with strain hardening and rate-dependant, was employed to predict the behaviour of these

alloys. The elastic and the plastic behaviour as well as the failure criteria for these materials are detailed herein.

5.3.1 Elasto-plastic behaviour

An isotropic elasto-plasticity model, which is available in ABAQUS/Explicit, was used to model the behaviour of the titanium and aluminium layers based on their engineering stress-strain curves obtained experimentally through uniaxial tensile tests. The tensile test procedure of these alloys was presented in Chapter 3 (Section 3.4.2.1). The modulus of elasticity (E) and yield stress (σ_y) values for the titanium and aluminium alloys were taken from the experimental stress-strain curves, which were used as input data to define the elastic region up to the yield point of the alloys investigated. For the plastic region modelling, the stress-strain curves were modified to obtain proper material properties. Thus, the values associated with the engineering stress-strain curves were used in the FE models in terms of true stress-strain using the following formulas:

$$\sigma_{true} = \sigma_{eng} \left(1 + \varepsilon_{eng}\right) \qquad\qquad (5.6)$$

$$\varepsilon_{true} = \ln\left(1 + \varepsilon_{eng}\right) \qquad\qquad (5.7)$$

where σ_{eng} and ε_{eng} are the engineering stress and engineering strain, respectively.

Here, the behaviour of the plastic strain hardening was modelled based on the stress-strain relationship beyond the yield point. The effect of the strain rate on the stress-strain values was considered by using the dynamic increase factor that included in Johnson-Cook (DIF$_{JC}$) model as follows:

$$DIF_{JC} = 1 + C \ln \dot{\varepsilon}^* \qquad\qquad (5.8)$$

$$\dot{\varepsilon}^* = \dot{\varepsilon}/\dot{\varepsilon}_\circ \qquad\qquad (5.9)$$

where C is the strain rate constant, $\dot{\varepsilon}^*$ is the strain rate ratio, $\dot{\varepsilon}$ and $\dot{\varepsilon}_\circ$ are the current strain rate and the reference quasi-static strain rate, respectively. Here the values of the reference and

the strain rate constant were set to 0.001 s^{-1} and 0.069 for titanium alloy and [171] and 0.001

s^{-1} and 0.0083 for aluminium alloy [154], respectively.

5.3.2 Failure criteria

The damage initiation and damage evolution after the strain-hardening stage need to be

modelled. In this study, two damage mechanisms for ductile metals were used, i.e. ductile

damage model and shear damage model. The ductile fracture or ductile damage initiation

criterion is a phenomenological model for predicting the damage initiation due to nucleation,

growth and coalescence of voids. The model assumes that the equivalent plastic strain

associated with the initiation of damage, $\overline{\varepsilon}_D^{pl}$, is a function of strain-rate ($\dot{\overline{\varepsilon}}^{pl}$) and stress

triaxiality (η) [169]:

$$\overline{\varepsilon}_D^{pl} = f\left(\eta, \dot{\overline{\varepsilon}}^{pl}\right) \tag{5.10}$$

where $\dot{\overline{\varepsilon}}^{pl}$ is the equivalent plastic strain rate, $\eta = \dfrac{-p}{q}$ is the stress triaxiality, p and q are the

pressure stress and the Mises equivalent stress. Failure is assumed to occur if the following

condition is met

$$\omega_D = \int \frac{d\overline{\varepsilon}^{pl}}{\overline{\varepsilon}_D^{pl}(\eta, \dot{\overline{\varepsilon}}^{pl})} = 1 \tag{5.11}$$

Here, ω_D is a state variable that increases monotonically with plastic deformation.

For the shear damage model, fracture occurs due to the localisation of the shear band in ductile

metals and this model activates if the following condition is satisfied. The model assumes that

the shear damage initiation is expressed as a function of equivalent plastic strain ($\overline{\varepsilon}_s^{pl}$), strain

rate and shear stress ratio,

$$\omega_s = \int \frac{d\,\overline{\varepsilon}^{pl}}{\overline{\varepsilon}_s^{pl}(\theta_s, \dot{\overline{\varepsilon}}^{pl})} = 1 \tag{5.12}$$

157

where ω_s is the state variable that increases monotonically with plastic deformation and proportional to the incremental change in equivalent plastic strain ($\bar{\varepsilon}^{pl}$).

$$\theta_s = (q + k_s p)/\tau_{max} \qquad (5.13)$$

where θ_s is the shear stress ratio, k_s is the materials parameter and τ_{max} is the maximum shear stress.

Figure 5-1 shows the characteristic stress-strain behaviour of a ductile material undergoing damage. The degradation of the material strength is shown with two effects, i.e. yield stress softening and elasticity degradation. Here, the damage initiation is presented by the solid line after the onset of damage (Damage parameter (D) =0), whilst the material's response without damage is referred by the dashed line. The point of the damage initiation after the strain hardening state is presented in point B (phase A-B). During damage evolution (phase B-E), the capability of the load carrying reduces until complete failure.

A linear relationship between the effective plastic displacement (u^{pl}) and the damage variable was used to model damage evolution in this study. It is considered that the effective plastic displacement is a function of the mesh size and the equivalent plastic strain. When the damage initiation criterion is met, the effective plastic displacement can be defined as follows.

$$u^{pl} = L_c \, \dot{\bar{\varepsilon}}^{\,pl} \qquad (5.14)$$

Note that L_c is the characteristic element length, ($\dot{\bar{\varepsilon}}^{\,pl}$) is the equivalent plastic strain which can be calculated from the stress-strain curves of the material tested.
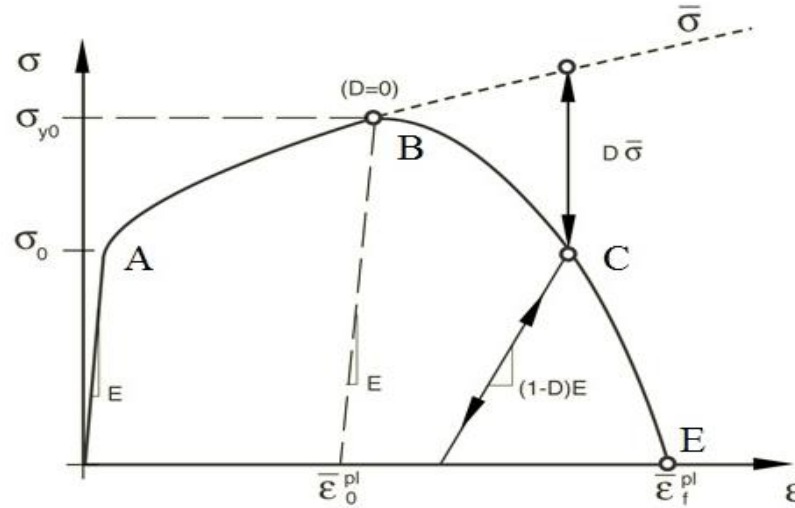
Figure 5-1. Stress-strain curve with progressive damage degradation [169].

5.4 Modelling of cohesive layers

Cohesive elements were used to model the adhesive layer (resin) between the adjacent layers. The cohesive element which defines traction-separation is available in ABAQUS [169]. In this study, a surface-based cohesive behaviour model was used to model the delamination between the composite and metal layers used, i.e. titanium and aluminium alloys. The advantage of this type of contact is that it allows traction-separation between the neighbouring layers without using cohesive elements [89]. Furthermore, surface-based cohesive offers the capability of modelling the damage same as cohesive elements. Moreover, a surface-based cohesive element is typically easier to define and allows simulation of a wide range of cohesive interactions, such as the interlaminar delamination and contact phenomena of composite laminate subjected to impact loads [172].

 The initial linear elastic behaviour followed by damage initiation and evolution was assumed in the traction-separation model. Prior to damage initiation, the elastic behaviour of the element can be written in terms of the elastic constitutive matrix that relates nominal stress to nominal strain as follow [169].

$$\hat{t} = \begin{Bmatrix} t_n \\ t_s \\ t_t \end{Bmatrix} = \begin{bmatrix} k_{nn} & 0 & 0 \\ 0 & k_{ss} & 0 \\ 0 & 0 & k_{tt} \end{bmatrix} \begin{Bmatrix} \delta_n \\ \delta_s \\ \delta_t \end{Bmatrix} = k \in \qquad (5.15)$$

where t_i are the nominal traction stress vectors, $\in$ is the nominal strain, k_{ii} are coefficients of the penalty stiffness and δ_i are the relative displacements.

Quadratic nominal stress criterion was used to predict the onset of the damage (i.e. damage initiation). The assumption of this criterion is that damage initiates when quadratic interaction function, involving the nominal stress ratios, reaches a value of unity, as presented below [169]:

$$\left\{ \frac{\langle t_n \rangle}{t_n^0} \right\}^2 + \left\{ \frac{\langle t_s \rangle}{t_s^0} \right\}^2 + \left\{ \frac{\langle t_t \rangle}{t_t^0} \right\}^2 = 1 \qquad (5.16)$$

where $\langle . \rangle$ is the Macaulay bracket, and t_n^0, t_s^0 and t_t^0 are the parameters of the interface strength.

The evolution of damage was defined based on the energy and the linear softening law, as shown in equation 5.17 [169].

$$\left\{ \frac{G_n}{G_n^c} \right\} + \left\{ \frac{G_s}{G_s^c} \right\} + \left\{ \frac{G_t}{G_t^c} \right\} = 1 \qquad (5.17)$$

where G_n, G_s, and G_t are the work done by the traction and its conjugate separation in the normal, first and second shear directions, G_n^c, G_s^c, and G_t^c are the fracture energies required to cause failure in the normal, first and second shear directions, respectively. Table 5-1 shows the parameters of cohesive based surface interaction used in this study.

Table 5-1. Material properties of the cohesive layer [78].

$k_{nn}=k_{ss}=k_{tt}$	t_n^0	t_s^0	t_t^0	G_{Ic}	G_{IIc}	G_{IIIc}
10^{14}	61	68.4	68.4	1564	2113	2113
N/m³	MPa	MPa	MPa	J/m²	J/m²	J/m²

5.5 Individual models for the composite laminates

In this investigation, FE models were developed to predict the response of the laminates investigated, i.e. glass fibre reinforced PEKK (GF/PEKK), aluminium-based FMLs, and titanium-based FMLs under low velocity impact. This section gives the details of the modelling undertaken in terms of geometry, loading and boundary conditions and mesh generation adapted for the various laminates.

5.5.1 Modelling of GF/PEKK laminates

5.5.1.1 Detailed model of the GF/PEKK laminates.

Prior to the onset of damage, the woven glass fibre reinforced PEKK laminates were modelled as an orthotropic elastic material with 2D Hashin's failure (described in Section 5.2). Table 5-2 shows the material properties of the laminates used in this study. An element removal procedure was employed to remove elements following matrix and fibre failure. Table 5-3 gives the damage initiation properties of the laminates investigated. The fracture energies values for the fibre tension (G_{ft}^F), fibre compression (G_{fc}^F), matrix tension (G_{mt}^F) and matrix compression (G_{mc}^F) failure modes with the combined effect of the fibre and the resin were based on previous work on glass fibre reinforced composites [150] and taken to be 50000, 60000, 50000 and 60000 J/m^2, respectively.

Table 5-2. Material properties for the GF/PEKK laminates used in this research.

Symbol	Value	Property
E_{11}	26 GPa	Young's modulus in longitudinal direction
E_{22}	26 GPa	Young's modulus in transverse direction
E_{33}	2.6 GPa	Young's modulus in thickness direction
G_{12}	2.6 GPa	In-plane shear modulus
G_{13}, G_{23}	2.6 GPa	Through-thickness shear modulus
v_{12}	0.15	In-plane Poisson's ratio
v_{13}, v_{23}	0.15	Through-thickness Poisson's ratio

Table 5-3. Strength data for the glass fibre reinforced PEKK laminates.

Symbol	Value (MPa)	Property
X_T	304	Longitudinal tensile strength
X_C	200	Longitudinal compressive strength
Y_T	304	Transverse tensile strength
Y_C	200	Transverse compressive strength
S_T	50.4	Transverse shear strength
S_L	50.4	Longitudinal shear strength

5.5.1.2 Geometries and boundary conditions

Table 5-4 shows the configurations, projectile sizes and shapes, as well as loading conditions for a fully-clamped 72 mm x 72 mm square GF/PEKK panels impacted at their centre. Due to the symmetric nature of these panels and to simplify the numerical analysis, half panel with appropriate boundary conditions was modelled as shown in Figure 5-2. This assumption substantially reduces the computational time and the associated cost. In this simulation, the targets were fully constrained on four edges. Therefore, the displacement, U, and the rotational displacement, UR, were set to zero. In contrast, the cylindrical projectile was modelled as a rigid body in comparison to the composite plates and the projectile was restrained against all degree of freedom, except for the vertical displacement (i.e. Ux=Uz=URx=URy=URz=0; Uy≠0). This boundary condition allows the projectile to move downwards at a specific velocity in order to progressively perforate the panel. A reference point was placed in the centre of the projectile surface to record the displacement of the target and the contact force was recorded through the contact pair between the targets and the projectile.

Table 5-4. Configurations, projectile mass and velocities of GF/PEKK plates modelled.

Configuration	Thickness (mm)	Geometry of the projectile	Projectile diameter (mm)	Projectile mass (kg)	Initial velocity (m/s)
4-ply	0.47	Hemisphere	10	1.37	2.4
8-ply	0.96	Hemisphere	10	1.37	3.4
12-ply	1.4	Hemisphere	10	1.37	4.0
16-ply	1.8	Hemisphere	10	1.37	4.6
8-ply	0.96	Hemisphere	5	3.02	4
8-ply	0.96	Hemisphere	10	3.02	4
8-ply	0.96	Hemisphere	15	3.19	4
8-ply	0.96	Hemisphere	20	3.22	4
8-ply	0.96	Partially-flat	10	3.02	4
8-ply	0.96	Conical	10	3.02	4
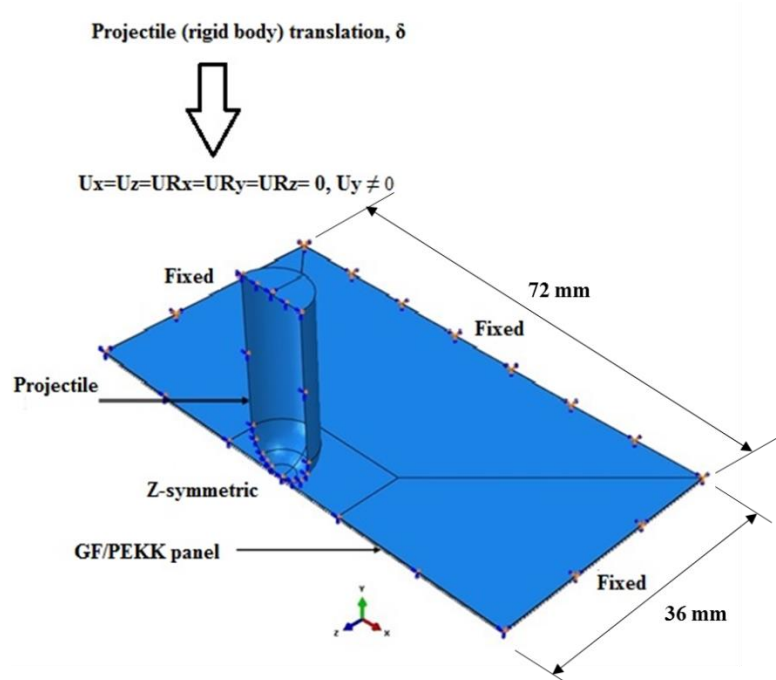
Figure 5-2.The assembly, loading and boundary conditions for the half-model of GF/PEKK plates.

5.5.1.3 Contact interactions

In finite element modelling, dealing with a various parts in contact is a critical process, and more attention should be taken to assign appropriate interaction properties to model the interaction. Here, two types of interactions were employed to model the contact between the surfaces, i.e. tie constrains and surface to surface contact formulations. It is worth mentioning that the cross-sections of the GF/PEKK laminates under the impact tests show that there is no significant delamination between the layers. Based on this observation, surface-based tie constrains was employed between the neighbouring layers of the plain composites (i.e. GF/PEKK), whereas surface to surface contact interaction was imposed between the projectile surface and the node set at the centre of the target for individual layer.

The penalty formulation was achieved using the classical isotropic Coulomb friction model. This model assumes no relative motion occurs if the equivalent frictional (τ_{eq}) stress is less than the critical stress as follows:

$$\tau_{eq} = \sqrt{\tau_1^2 + \tau_2^2} \qquad\qquad (5.18)$$

The critical stress is proportional to the contact pressure, ρ, and it can be defined as:

$$\tau_{crit} = \mu p \qquad\qquad (5.19)$$

where μ is the coefficient of friction and p is the contact pressure between the two surfaces.

The relationship of the contact pressure-overclosure that governs the surfaces motion can be specified in the property of the contact interaction.

In Abaqus, contact between surfaces can be defined using two types of contact pressure-overclosure relationships, i.e. hard and softened contact ones. Hard pressure-overclosure contact considers the most common pressure-overclosure relationship in which any contact pressure can be transmitted between the surfaces. If the contact pressure of surfaces in contact reduces to zero, the surfaces will separate. Softened contact relationships can prescribe the

relationship of the contact pressure and the clearance between the surfaces using a linear law, a piecewise linear (tabular) and exponential law.

The softened contact can be used with either the penalty or the kinematic constraint enforcement methods. With softened penalty contact, the contact collision is elastic except for the influence of contact damping and the time increment decreases with the contact stiffness increment. In contrast, with kinematic enforcement, the absorbed energy by the impact increases with increasing the contact stiffness, and the time increment is independent on the contact stiffness. In this FE model, penalty friction formulation between the contact surfaces with a friction coefficient of 0.15 and linear pressure-overclosure with contact stiffness of 0.5 MPa were selected to simulate the tangential and normal behaviours of the projectile-composites contact.

5.5.1.4 Element type

Eight-noded linear quadrilateral in-plane continuum shell elements with reduced integration and hourglass control (SC8R) were used to model GF/PEKK laminates. Many research outputs [150, 151, 155, 157] have shown that the using of SC8R as an element type is efficient to model the impact response of the laminated composite. The idea of using continuum shell elements to model the composites investigated is to use Hashin's damage criteria which are available in ABAQUS/Explicit finite element package. The projectile was modelled as a rigid body as it is made from a high strength steel with negligible deformation. The motion of all nodes and elements of the rigid body (i.e. projectile) is governed by the motion of a single reference point that has both translation and rotational degrees of freedom. Four-noded bilinear quadrilateral rigid elements (R3D4) were used to mesh the projectile.

5.5.1.5 Mesh sensitivity

Figure 5-3 shows the mesh generated in the composite laminates using the meshing tools of ABAQUS/CAE. It is known that the element size has a significant effect on the computational time. Too larger element leads to a lower CPU time and a higher stress, whereas a finer mesh

can use too much memory with a longer computational time. Therefore, a mesh-sensitivity study was conducted to optimise the mesh size at which a suitable balance between the accuracy of the model and the central processing unit (CPU) time can be achieved. This study was based on changing the element size of the shell element throughout the panel geometry. The variation of the maximum load and the CPU time as a function of the element size of the 4-ply GF/PEKK plates is shown in Figure 5-4. It is clear from the figure that the peak load shows a high dependency on the element size. In this simulation, a mesh size of 1.1 mm x 1.1 mm over a central area of 20 mm x 20 mm was selected to reduce CPU time. A similar mesh size was used to model the perforation response of the FMLs investigated under impact loading.
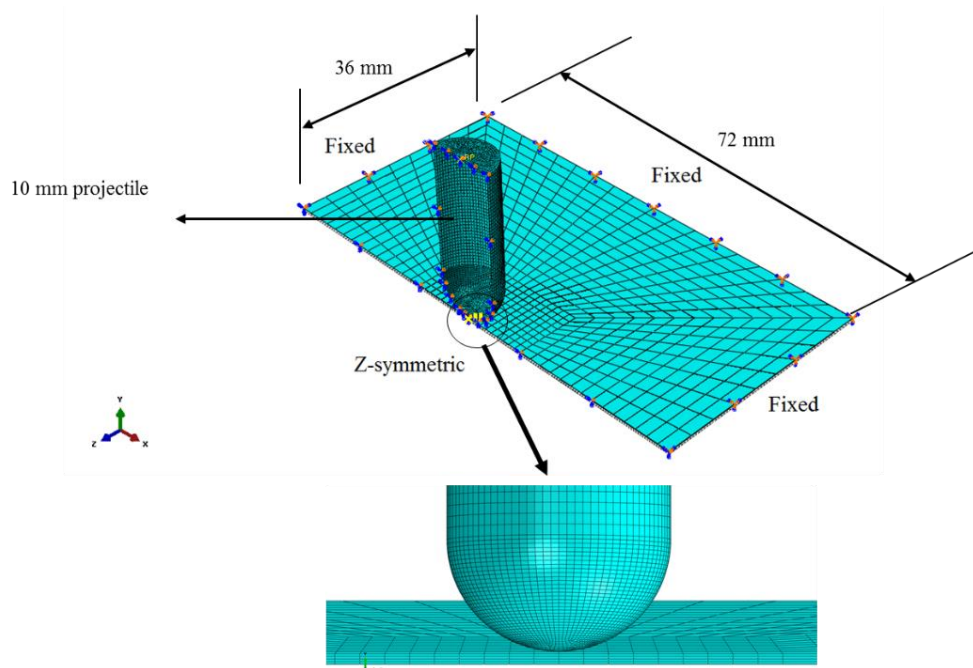
Figure 5-3. FE mesh for the composite laminates and the projectile.
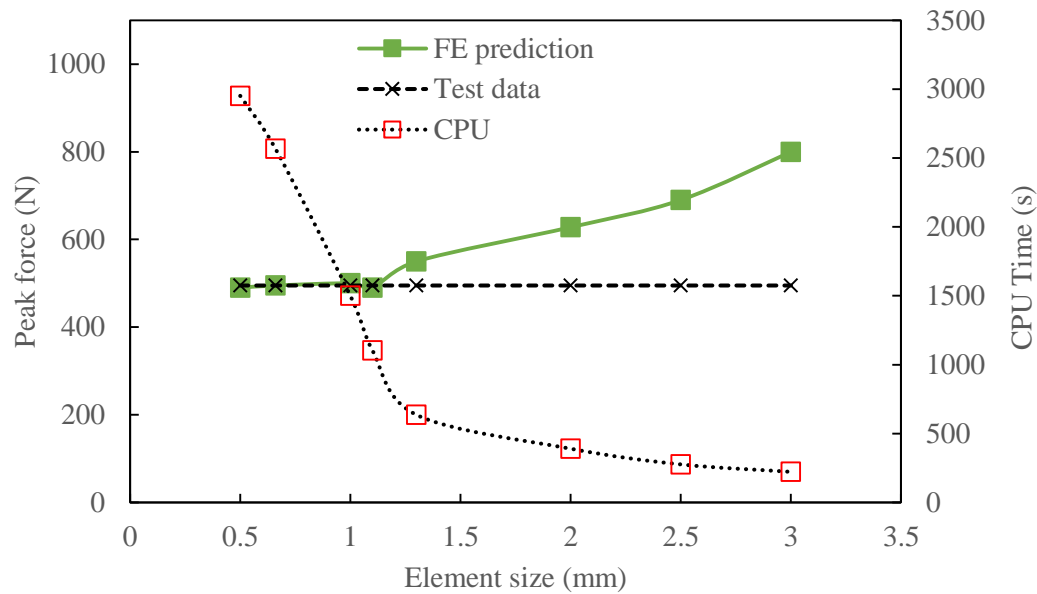
Figure 5-4. The peak force and CPU time against element size for the 4-ply GF/PEKK composites.

5.5.1.6 Process simulation output

The data output from the numerical simulation was specified by creating output requests at which many different variables for each step can be calculated by the Abaqus solver. The data output can be managed by the user so that the only required data for the analysis are produced. Here, the data output can be requested by two ways, i.e. history output and field output. The former are generated from spatially-distributed data over a portion or the whole model. This type of output describes the specimens at each requested interval. Here, stresses, strains, displacement, reaction force, contact, failure and status were requested for the whole model. In contrast, the history outputs can be generated from the whole or specific points in the model. The data output frequency depends on the interest of the users, and it can be very high if necessary. For the relevant direction, the contact forces and the displacement were requested in a history output in this simulation. The displacement was requested at the specific reference point of the projectile.

5.5.2 Modelling the impact response of the FMLs

The FE analyses on the titanium-based and aluminium-based FMLs were carried out to model their response under low velocity impact. Here, titanium layers, (GF/PEKK) composites, and PEKK (i.e. adhesive layers) were stacked together to produce titanium-based FMLs, whereas aluminium-based FMLs were made of aluminium layers, (GF/PEKK) composites, and PEKK layers. The GF/PEKK composites were modelled using an orthotropic elastic material with 2D Hashin's failure (described in Section 5.2). The titanium and aluminium alloys were modelled as isotropic elasto-plastic materials and the related damage criteria (described in Section 5.3). The elastic properties of the titanium and aluminium alloys are presented in Table 5-5.

The plastic response of these metallic materials (i.e. titanium and aluminium) was modelled using isotropic hardening. Table 5-6 shows the relationship between the flow stress and the plastic strain obtained experimentally from the stress-strain curves. Ductile and shear damage models, which are available in ABAQUS, were used to model the damage initiation of the titanium and aluminium layers. The failure strain obtained experimentally from the uniaxial tests was taken as the fracture strain at which the onset of the damage occurs. The ductile and shear damage properties for the aluminium alloys were taken from Hooputra et al. [173]. For modelling the titanium alloy, the ductile and shear damage parameters, i.e. stress triaxiality, shear stress ratio and strain rate were requested as output in a group of elements where the shear failure occurred using isotropic metal plasticity constitutive model. Again, the fracture strain is obtained from the true strain-stress curves resulted from uniaxial tensile tests. For these metallic layers investigated, once damage has initiated, an effective plastic displacement was adopted to model the damage evolution (described in Section 5.3.2). The cohesive layers on both FML systems were simulated using cohesive elements based on nominal stress and energy conjunction defined in terms of traction-separation (described in Section 5.4).

Table 5-5. Summary of the elastic properties of the titanium and aluminium alloys
undertaken in this study.

Material	Density (kg/m^3)	Young's modulus (GPa)	Poisson's ratio
Titanium alloy (Ti-15-3-3-3-β)	4760	100	0.33
Aluminium alloy (Al 2024-T3)	2780	75	0.33

Table 5-6. Summary of the plasticity properties of the titanium and aluminium alloys
investigated.

Titanium alloy (Ti-15-3-3-3-β)		Aluminium alloy (Al 2024-T3)	
Plastic strain	Yield stress (MPa)	Plastic strain	Yield stress (MPa)
0	1000	0	178
0.0304	1015	0.011	200
0.0311	1030	0.019	225
0.0318	1045	0.033	257
0.0326	1060	0.042	275
0.0333	1070	0.051	289
0.0341	1080	0.059	300
0.0367	1100	0.077	317
0.0394	1110	0.088	325
0.0438	1120	0.095	329
0.0454	1122	0.108	334

5.5.2.1 Geometries, contact, mesh and boundary conditions

Table 5-7 and Table 5-8 show the configurations, geometries, projectile masses and velocities
for the aluminium-based and titanium-based FMLs modelled in this research, respectively. A
plate size of 72 mm x 72 mm with fully-fixed edges as boundary conditions was considered in
the simulations. Again, only one half of the specimen was modelled, due to geometric and

loading symmetries. The specimen geometry and boundary conditions were similar to those applied to model GF/PEKK panels (described previously). The initial velocity was applied to the projectile in a vertical direction (normal to the target) as the only degree of freedom.

Eight-noded continuum shell elements (SC8R) along with Hashin-2D criteria (described in Section 5.5.1.4) were applied to model the plain composite laminates (i.e. GF/PEKK) in FMLs. Eight-noded solid brick elements (C3D8R) with reduced integration and hourglass control were used to mesh the titanium and aluminium layers. The interaction between the layers in the FMLs was defined as a general contact interaction, and surface-to-surface (contact pair) interaction between the projectile surface and the node set at the target centre of each layer.

The interfaces between the titanium layer and the composites layer in titanium-based FMLs and between the aluminium layer and composites in aluminium-based FMLs were modelled using eight-noded 3D cohesive elements (COH3D8). The properties of the contact interactions between the composite plies, composites and the projectile (Proj-GF/PEKK), titanium and composite layers (Ti-GF/PEKK), aluminium and composite layers (Al-GF/PEKK), projectile and titanium layers (Proj-Ti) and between the projectile and aluminium layers (Proj-Al) are shown in Table 5-9.

Table 5-7.Summary of the stacking configurations, geometry, projectile mass and velocity of the aluminium-based FMLs modelled in this research.

Configurations	Thickness (mm)	Projectile mass (kg)	Initial velocity (m/s)
2/1 (4-ply)	1.51	3.56	4
3/2 (4-ply)	2.48	5.57	4
4/3 (4-ply)	3.61	8.34	4
5/4 (4-ply)	4.37	9.80	4

Table 5-8. Summary of the stacking configurations, geometry, projectile mass and velocity of the titanium-based FMLs modelled in this research

Configurations	Thickness (mm)	Projectile mass (kg)	Initial velocity (m/s)
2/1 (2-ply)	0.51	1.48	3.6
3/2 (2-ply)	0.92	2.67	3.6
4/3 (2-ply)	1.29	3.84	3.6
5/4 (2-ply)	1.64	4.97	3.6
2/1 (4-ply)	0.75	1.43	3.6
2/1 (8-ply)	1.15	1.43	4
2/1 (12-ply)	1.6	1.43	4.4
2/1 (16-ply)	2	1.43	4.7

Table 5-9. The contact interaction properties used in the FE models.

Interaction	Contact algorithms	Mechanical constrain formulation	Friction formulation	Contact stiffness (MPa)	Pressure - overclosure
GF/PEKK	Tie-based constrains	-	-		-
Proj- GF/PEKK	Contact pair	Kinematic	Penalty	0.5	linear
Ti-GF/PEKK	General contact	Penalty	Penalty	10000	linear
Al-GF/PEKK	General contact	Penalty	Penalty	10000	linear
Proj-Ti	Contact pair	Kinematic	Penalty	1	linear
Proj-Al	Contact pair	Kinematic	Penalty	1	linear

5.6 Results from the finite element simulations

The simulation results of the GF/PEKK composites, titanium-based FMLs and aluminium-based FMLs subjected to low velocity impact are presented in this section. The FE results are then compared with the corresponding results obtained experimentally (presented in Chapter 4). Initially, the simulations were focused on the GF/PEKK plain composite. The FE models were then developed to model the perforation response of the FMLs investigated.

5.6.1 Simulation of GF/PEKK composites under impact loading

5.6.1.1 The effect of panel thickness

FE models were developed to predict the perforation response of the GF/PEKK composites based on various thicknesses or ply number, i.e. 4-, 8-, 12- and 16-ply under low velocity impact loading. The reliability of the FE models was examined by comparing the predicted results with the corresponding experimental data in terms of load-displacement traces and failure modes. For the FE models, the adopted geometric, boundary and loading conditions were similar to those used experimentally. Figure 5-5 shows a comparison between the load-displacement traces obtained from the FE models and the corresponding experimental data. It can be seen that, for the range of target thicknesses considered, good agreement was observed between the numerical simulations and experimental results.

The predicted initial stiffness shows a good correlation with experimental data. Also, the displacement at peak forces correlates well with the corresponding experimental results. Interestingly, at the perforation stage, the predicted load-displacement traces exhibit the similar trends to those produced experimentally, i.e. perforation resistance reduces as the projectile perforates the targets. The predicted peak loads of the 4-, 8-, 12- and 16- ply GF/PEKK were 489, 1021, 1771 and 1942 Newtons, respectively and the corresponding experimental values were 495, 1049, 1711 and 1916 Newtons. The correlation between the predicted and measured peak loads is shown in Figure 5-6. Clearly, the predicted values are in a high agreement with the measured ones with largest error of 3.5%.

The predicted perforation energy values for the laminates investigated were then compared to the corresponding experimental values to further assess the accuracy of the FE models, and these data are presented in Figure 5-7. Clearly, the FE model shows good agreement with the experimental values for the thin (i.e. 4-ply) and thick (i.e. 16-ply) panels. The largest error between the data sets was approximately 8 %. The good agreement shown in Figure 5-6 and

Figure 5-7 supports the conclusion that the FE models are capable to capture the response of

GF/PEKK laminates under low velocity impact.

(a) 4 -Ply GF/PEKK laminates   (b) 8 -Ply GF/PEKK laminates

(c) 12 -Ply GF/PEKK laminates   (d) 16 -Ply GF/PEKK laminates
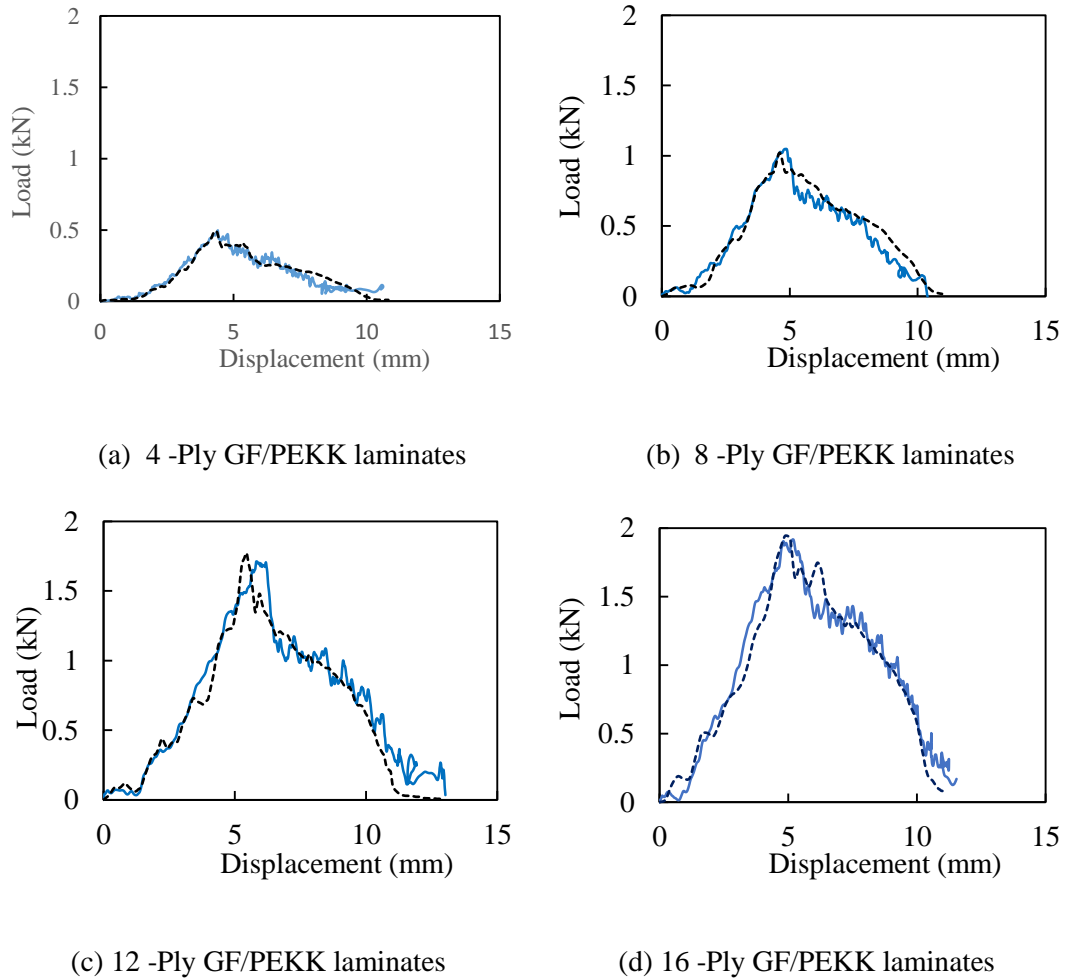
Figure 5-5. Numerical and measured load-displacement traces for the GF/PEKK
plates impacted with a 10 mm hemispherical projectile with mass of 1.37 kg and
velocity of 2.4 m/s (a), 3.4 m/s (b), 4 m/s (c), and 4.6 m/s (d). The solids lines
correspond to experimental traces and the dashed line to numerical predictions.
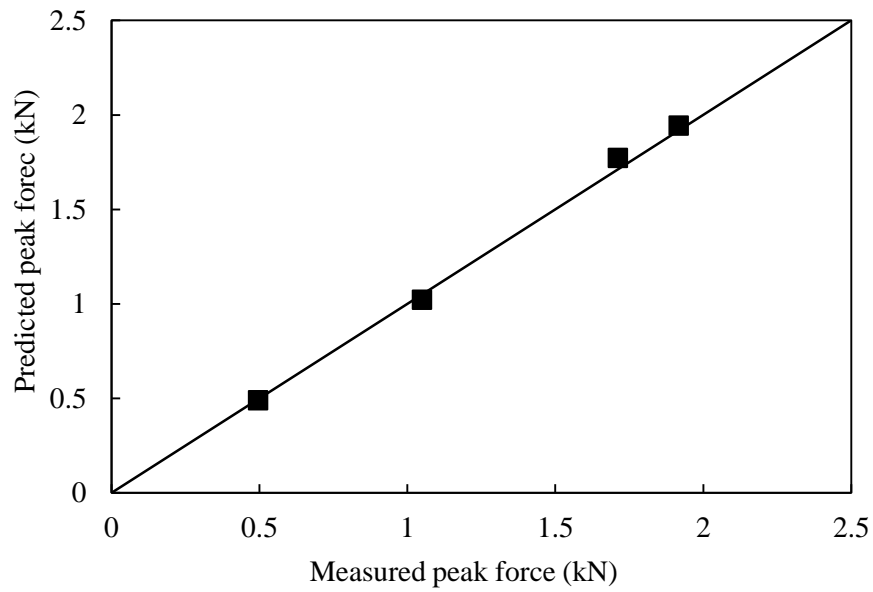
Figure 5-6. Comparison of the predicted and measured peak forces of the 4-, 8-, 12- and 16-ply GF/PEKK under perforation impact.
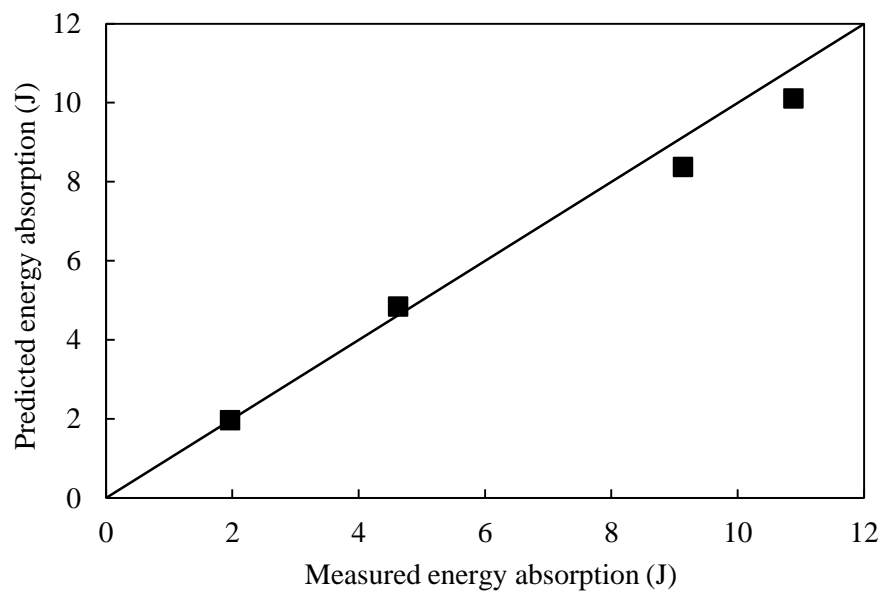
Figure 5-7. Comparison of the predicted and measured perforation energies for the 4-, 8-, 12- and 16-ply GF/PEKK under perforation impact.

Figure 5-8 shows a comparison of the experimental and predicted rear surfaces of perforated 4-ply of GF/PEKK composites following impact. Here, the experimental failure mode was captured after removing the projectile from the damaged panel, whereas the predicted cross-

section was taken without unloading the panel (i.e. removing the projectile). From the figure, the fibre fractures in the 0 and 90 directions at the plate centre can be observed in the predicted and the experimental data. Clearly, the FE simulation shows a good degree of agreement with the experimental damage pattern, in terms of the local deformation at the target centre and the cross-cracks on the rear surface of the panel. This evidence suggests that the FE model captures the failure modes in the perforated GF/PEKK composite successfully. Similar failure modes were observed in the 8-, 12- and 16-ply GF/PEKK panels following low velocity impact tests. It is encouraging to note that the FE model predicts the perforation impact of the laminates investigated and the main features of impact event were successfully captured by the numerical model.
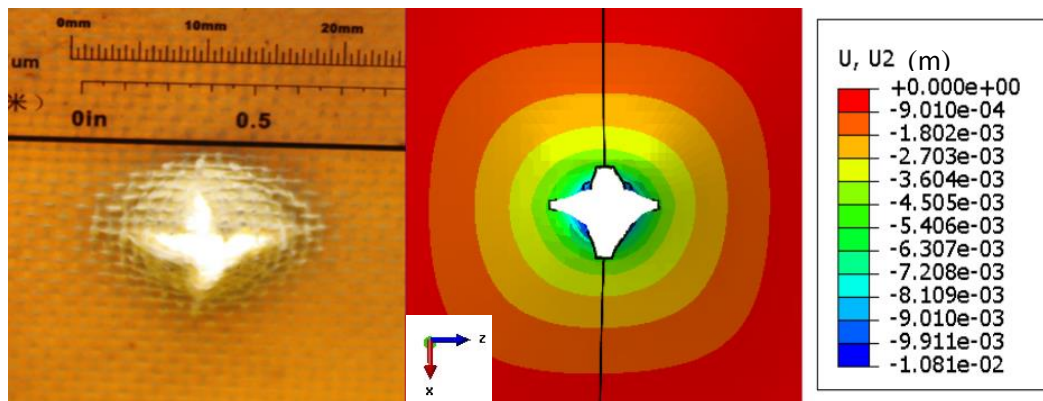
Figure 5-8. Comparison of the predicted and experimental failure modes of the 4-ply GF/PEKK panels under impact tests.

5.6.1.2 The effect of projectile diameter

In this investigation, the impact response of 8-ply laminates impacted by projectiles with diameters in 5, 10, 15 and 20 mm was investigated both experimentally and numerically. The predicted load-displacement traces were then compared to the corresponding experimental curves, as shown in Figure 5-9. The dashed lines represent the predicted results. It is clear from the figure that the prediction of the numerical models are in a good degree of correlation with the values measured experimentally for the panels investigated. As expected, the peak force increases with projectile diameter. For example, the panel impacted by a 20 mm indenter

results in a much higher impact force of 1710 N than the value of 815 N resulted from impact by a 5 mm projectile. This is due to the larger volume of sheared material in the panel impacted by the large diameter projectile.

(a) Projectile diameter = 5 mm   (b) Projectile diameter = 10 mm

(c) Projectile diameter = 15 mm   (d) Projectile diameter = 20 mm
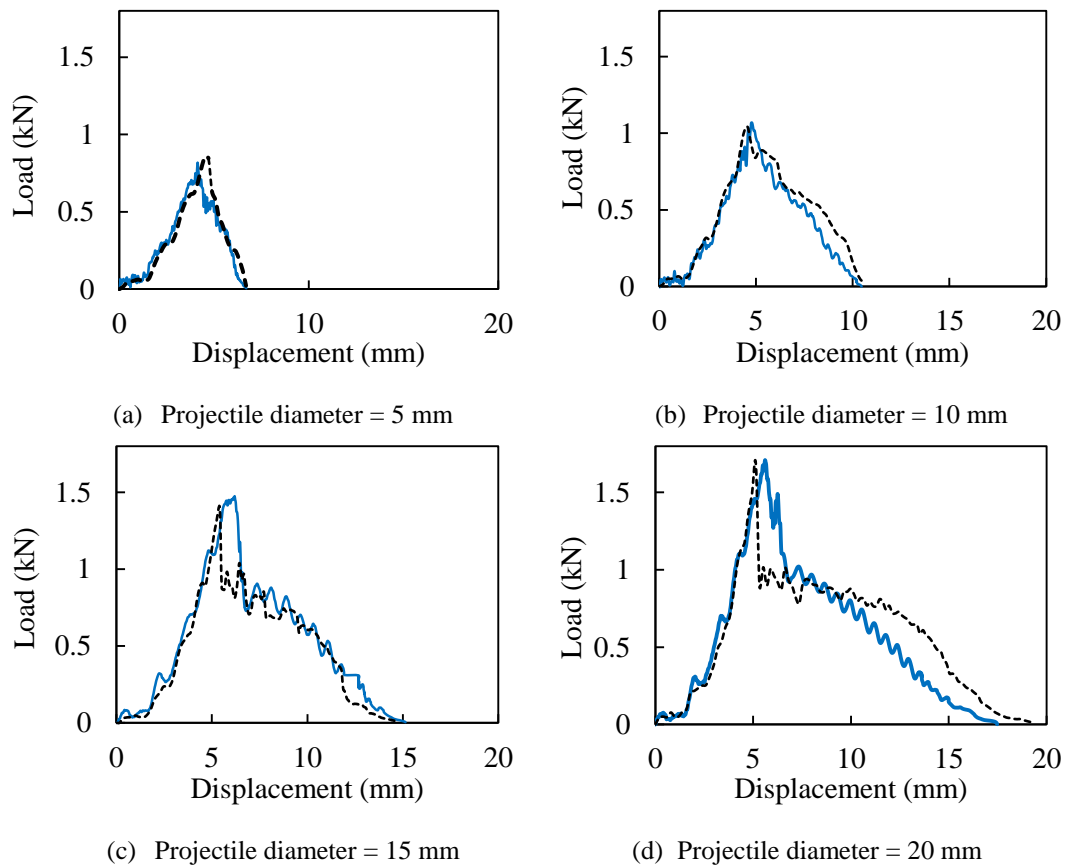
Figure 5-9. Load-displacement traces for 8-ply GF/PEKK laminates impacted by various projectile diameters. The solids lines correspond to experimental traces and the dashed line to numerical predictions.

The influence of the projectile diameter on the perforation energy of the 8-ply GF/PEKK laminates is shown in Figure 5-10. The solid line represents the prediction of the FE analysis. Clearly, the perforation energy increases rapidly with increasing the projectile diameter in a non-linear pattern. Good agreement between the predicted and measured data is obtained and the FE output suggests that the absorbed energy increases with projectile diameter in a parabolic relationship. The results of Figure 5-9 and Figure 5-10 support the conclusion that

the FE models developed are capable to accurately predict the perforation response of GF/PEKK laminates investigated under various loading conditions.
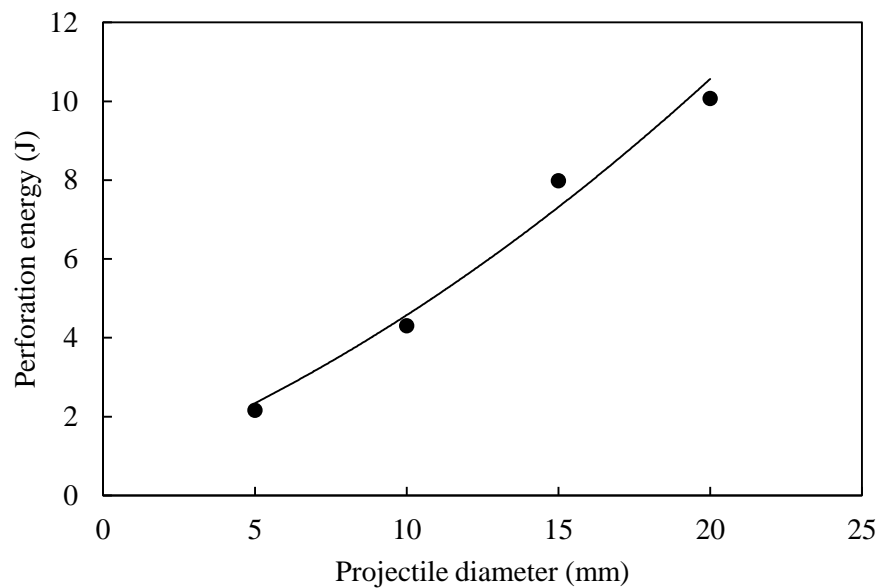
Figure 5-10. Variation of the perforation energy with projectile diameter for 8-ply GF/PEKK panels impacted by various projectile diameters: 5; 10; 15 and 20 mm. The solid line represents the prediction of the FE analysis.

5.6.1.3 The effect of projectile shape

The influence of varying projectile shape on the impact response of the GF/PEKK panels is investigated. Figure 5-11 compares the predicted and experimental load-displacement traces of 8-ply GF/PEKK panels resulted from impact by partially flat and conical projectiles, where a good agreement between the predicted and measured traces is apparent. Interestingly, the simulated results capture the experimental features from the beginning to the full perforation stages.

Figure 5-12 shows the variation of the perforation resistance of GF/PEKK laminates with projectile shape. It can be seen that the highest perforation resistance was offered by panels impacted with a partially flat indenter. Again, a good agreement between the measured and predicted data was obtained over the range of the projectile shapes investigated.

In conclusion, the finite element models (FEMs), developed to predict the perforation response of the glass fibre reinforced PEKK (GF/PEKK) laminates under various impact loadings, show good correlation with the data obtained experimentally. This evidence indicates that the simulations can be used to predict the perforation resistance of the fibre metal laminates, i.e. titanium-based and aluminium-based FMLs under low velocity impact.

(a)   (b)
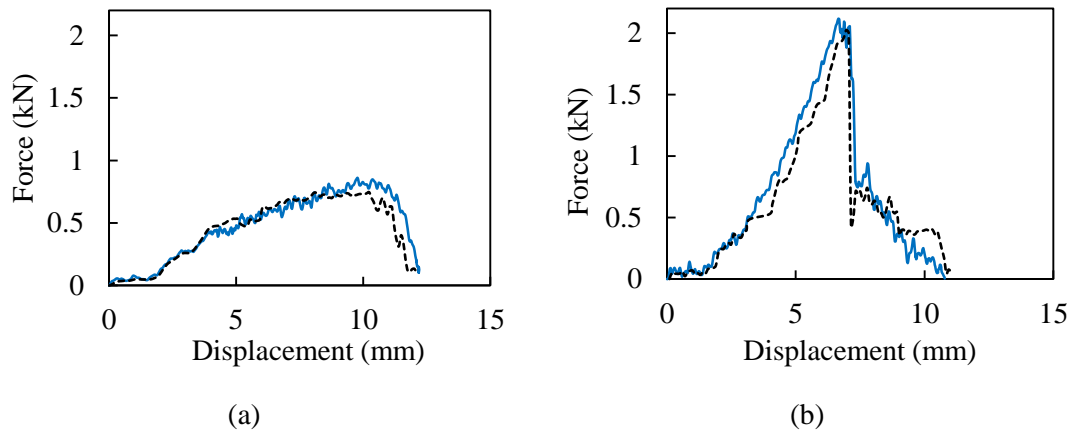
Figure 5-11. Predicted and experimental load-displacement traces of 8-ply GF/PEKK panels impacted with different projectile shapes: (a) conical; (b) partially-flat. The solids lines correspond to experimental traces and the dashed line to numerical predictions.
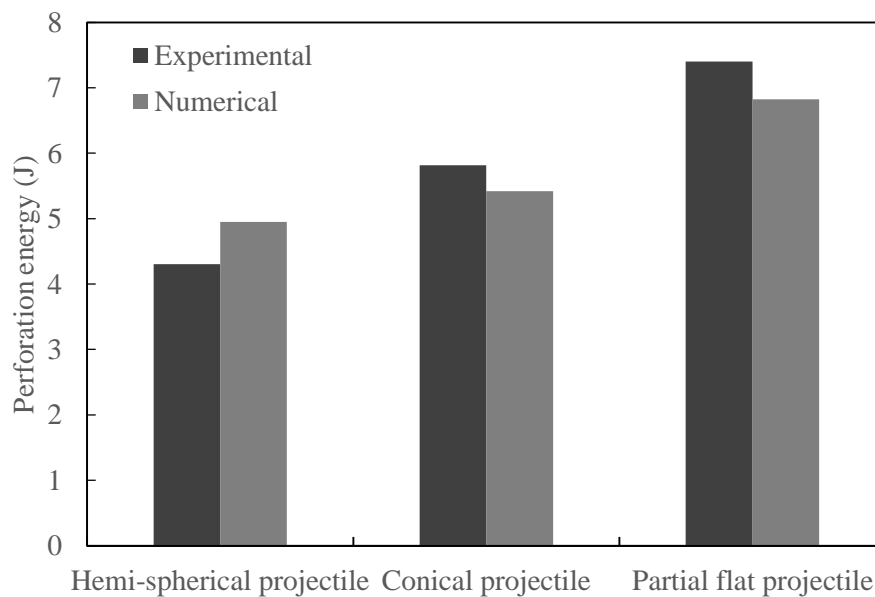
Figure 5-12. Variation of the perforation energy with projectile head shapes of 8-ply GF/PEKK panels.

5.6.2   Simulation of FMLs subjected to impact loading

In this study, the structural behaviour of the fibre metal laminates under perforation impact was predicted by FE analysis. The material constitutive models and the failure criteria for the composite, titanium, aluminium and adhesive layers are detailed in Sections 5.2, 5.3 and 5.4, respectively. Here, the FMLs were based on various stacking configurations ranging from a simple 2/1 lay-up to 5/4 stacking configurations. The outcome results of the numerical models are then compared to those obtained experimentally in terms of load-displacement and failure modes. The modelling results of these impact tests on these FMLs are discussed below.

5.6.2.1 Simulation of titanium-based FMLs

5.6.2.1.1   The effect of core thickness on perforation resistance

Figure 5-13 shows the predicted load-displacement traces of the 2/1 FMLs based on 4-, 8-, 12- and 16-ply GF/PEKK composite cores under impact tests. Closer examination of the figure indicates that the overall features of the experimental load-displacement traces are simulated reasonably well. This level of agreement includes the initial stiffness, peak load, and the subsequent damage behaviour. Interestingly, the trend of the predicted load-displacement traces after the peak load is similar to those obtained experimentally. It is also worth mentioning that the initial stiffness values obtained by the FE analysis are slightly over-estimated. This can be attributed to the perfect contact assumed between the projectile and targets. The predicted perforation energies of the 2/1 FMLs based on 4-ply, 8-ply, 12-ply and 16-ply GF/PEKK composite cores were 9.5, 13.5, 20 and 24 Joules, respectively. Relative to the experimental energy absorption values of 8.6, 12.1, 17.7 and 24.3 Joules, the differences between the predicted and measured values were 9.7, 11.3, 12.6 and 1.63 %, respectively.

Figure 5-14 compares the numerical and experimental failure modes of the FMLs investigated under impact tests. Clearly, the failure modes predicted by the simulations correlate reasonably well with the experimental observations. Also, the FE models are capable to capture the delamination between the titanium and composite layers. Again, the images of the failure

modes obtained experimentally were captured after removing the projectile, resulting in significant recovery in deformation. In contrast, the predicted failure images were taken while the projectiles were still in the targets. Since the number of plies in the composite layer was only the difference in the FMLs, the experimental failure modes for these four FMLs were similar. Although the crack pattern of the 2/1 FMLs based on 4-ply GF/PEKK composite cores was not well predicted, the delamination between the layers were successfully simulated. Interestingly, the crack patterns in the FMLs investigated were predicted reasonably well by the models developed.

(a) 4-ply composite core   (b) 8-ply composite core

(c) 12-ply composite core   (d) 16-ply composite core
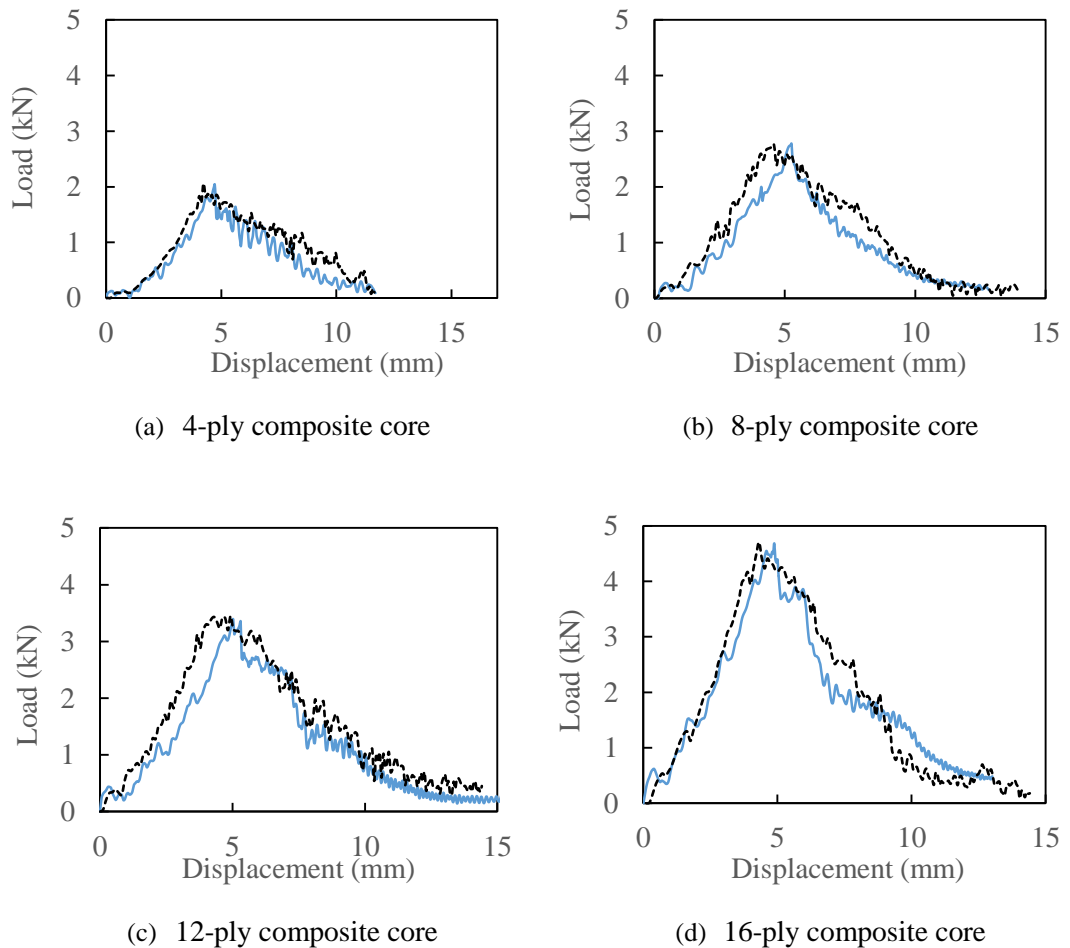
Figure 5-13. Load-displacement traces for the 2/1 FMLs with different composite cores following low velocity impact. The solids lines correspond to experimental traces and the dashed line to numerical predictions.
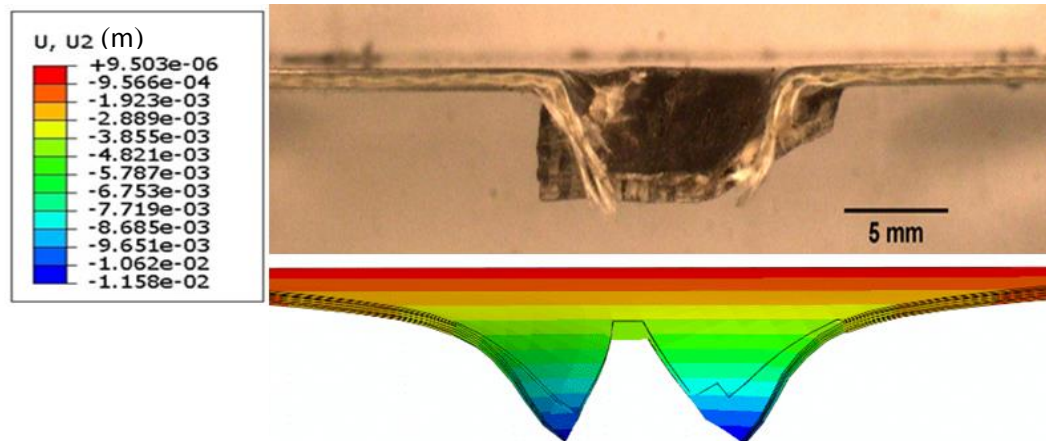
(a) 2/1 FMLs (4-ply) composite.
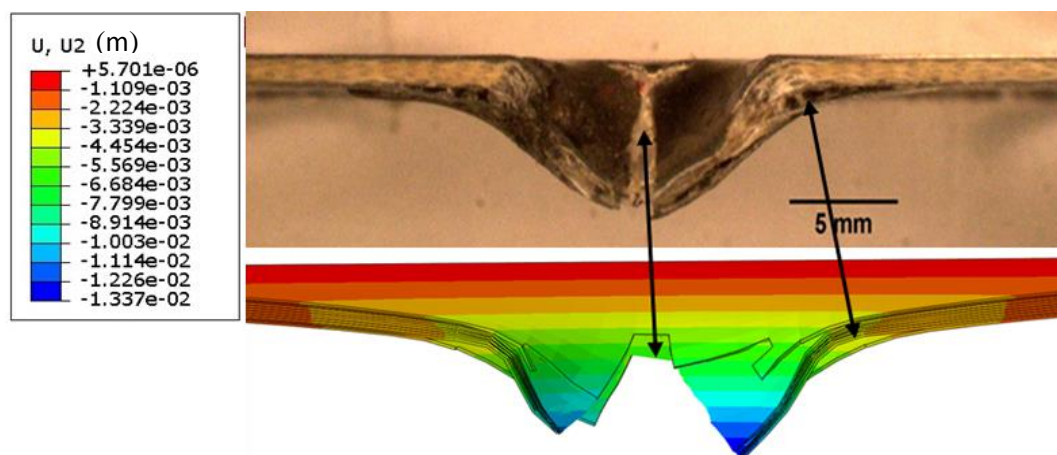
(b) 2/1 FMLs (8-ply) composite.
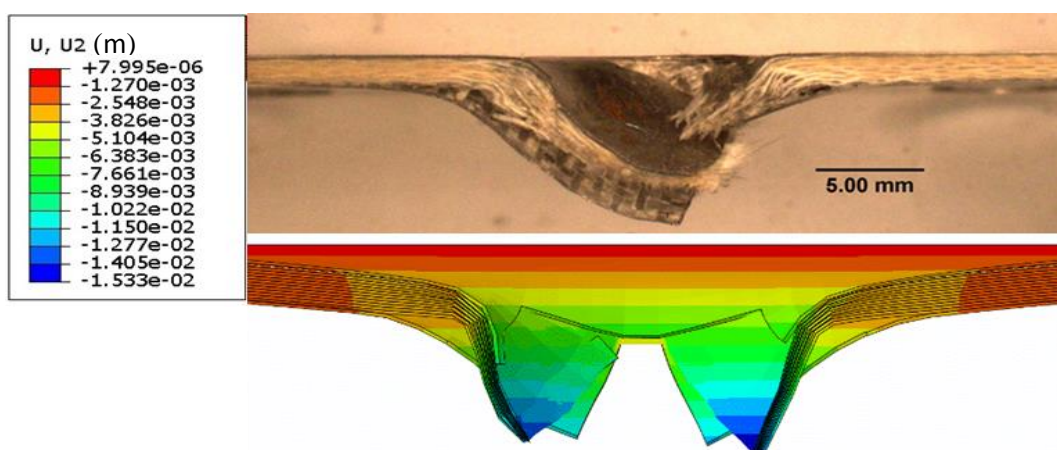
(c) 2/1 FMLs (12-ply) composite.
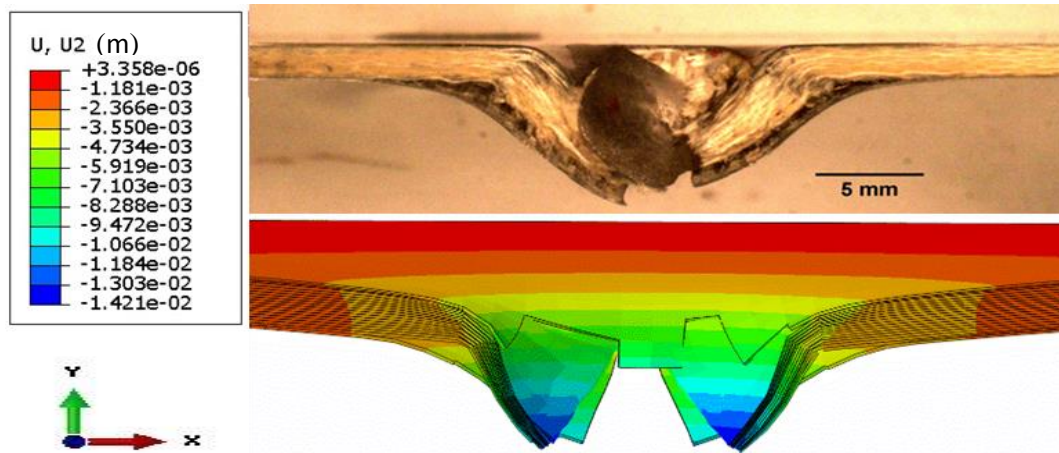
(d) 2/1 FMLs (16-ply) composite.

Figure 5-14. Comparison between the experimental and numerical simulations of the failed 2/1 FMLs stacked with various composite cores under impact loading.

5.6.2.1.2 The effect of the stacking configurations on the perforation resistance

In order to broaden the validation, the finite element models were used to predict the perforation resistance of the titanium-based FMLs with various stacking configurations under impact loading. Four stacking configurations were employed in this study, which were 2/1, 3/2, 4/3 and 5/4 titanium FMLs based on 2-ply GF/PEKK composite cores. Details about the stacking configurations investigated are described previously in Chapter 3. Figure 5-15 shows the numerical and measured load-displacement traces of the panels used under impact by a hemispherical projectile (10 mm diameter). It should be noted that the numerical results show good agreement with experimental data. During impact loading, the predicted and the measured traces show an oscillatory response due to the dynamic nature of the tests.

Again, the FE models yields slightly an over-estimated values of stiffness compared to the corresponding experimental values due to the perfect contact between the projectile and targets assumed in the model. The peak loads of the 2/1, 3/2, 4/3 and 5/4 FMLs are 1689, 2540, 3602 and 5001 Newtons, respectively, in comparison to the measured values of 1660, 2667, 3671 and 4983 Newtons. The discrepancies between these values are only of 1.7, 4.7, 1.9 and 0.4 %, respectively.

Clearly, the perforation stage of the impact event at which impact force decreases after reaching the peak load, as the projectile continues passing through the target, was accurately captured by the finite element models. The numerical values of the displacement at peak load are 5.51, 4.24, 4.23 and 4.01 mm with relatively small discrepancies of 6.0, 5.7, 1.9 and 2.5 % relative to the corresponding experiment values of 5.86, 4.50, 4.15 and 4.12 mm, respectively. It is worth pointing out that the FE models appear to succeed in predicting the trend of the displacement at peak loads, when the displacement decreases with the panel thickness. The differences between the predicted perforation energies and the associated experimental data are 9.5, 19, 3.9 and 12.2 %, respectively.
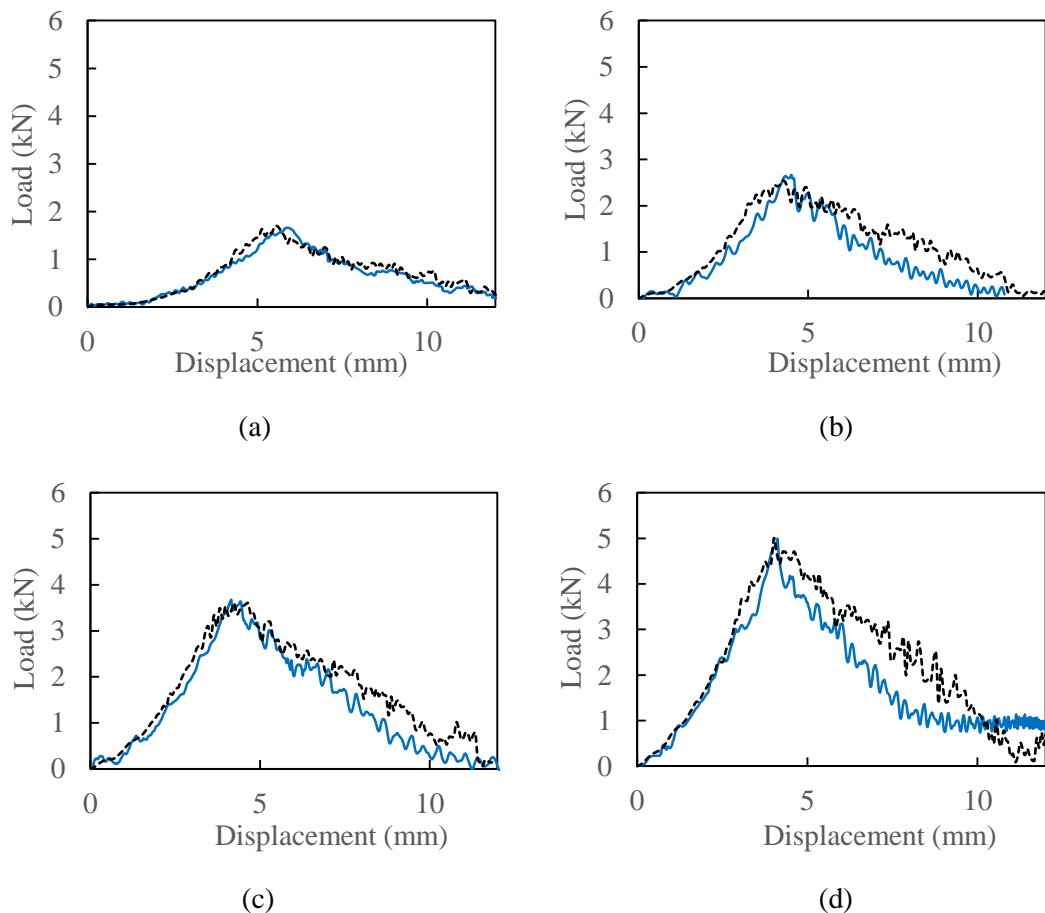
Figure 5-15. Load-displacement traces: (a) 2/1; (b) 3/2; (c) 4/3; (d); 5/4 titanium FMLs based on 2-ply GF/PEKK cores subjected to impact loading. The solids lines correspond to experimental traces and the dashed line to numerical predictions.

Figure 5-16 shows the comparisons between the predicted and experimental failure modes of FMLs under impact perforation tests. It can be seen that the predicted rear surface profile is similar in appearance to those recorded in impact tests. The main features of the experimental failure modes (i.e. the cross-fracture in the rear surfaces) are reasonably captured on the FML panels investigated. Although the failure modes in the 2/1 FMLs were not well predicted, the failure modes were successfully simulated in the three FML panels, i.e. 3/2, 4/3 and 5/4 FMLs.

Figure 5-17 compares the predicted and experimental cross-sections of the titanium-based FMLs investigated. Clearly, the FE models are capable to predict the basic features of the failure modes obtained experimentally, in terms of local deformations in the centre of the plate, delamination between the adjacent layers, interlaminar damage and the cross fractures at the rear surface for all the FMLs investigated. An examination of the figures indicates that the cross fractures in the FE models are slightly greater than that in the experimental tests. As mentioned before, the image of the FE modes were captured while the projectile still inside the targets and however, the photos for the experimental failure modes were taken while the project was removed from the plates, giving a significant recovery of the deformation.
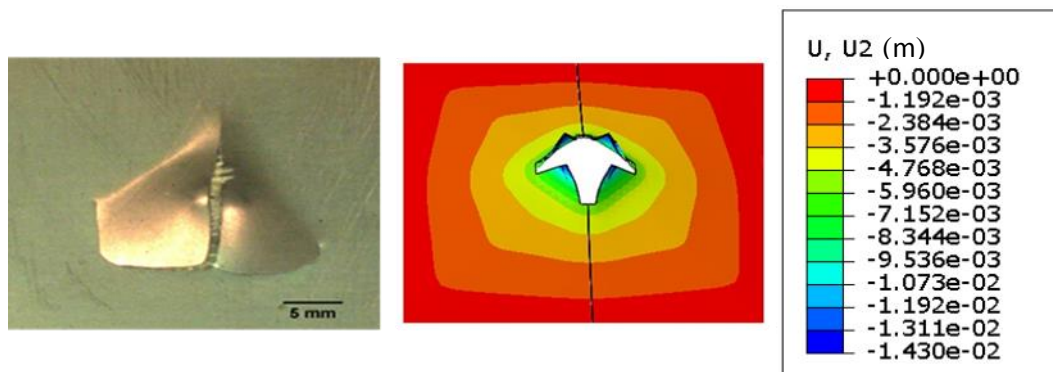
(a)
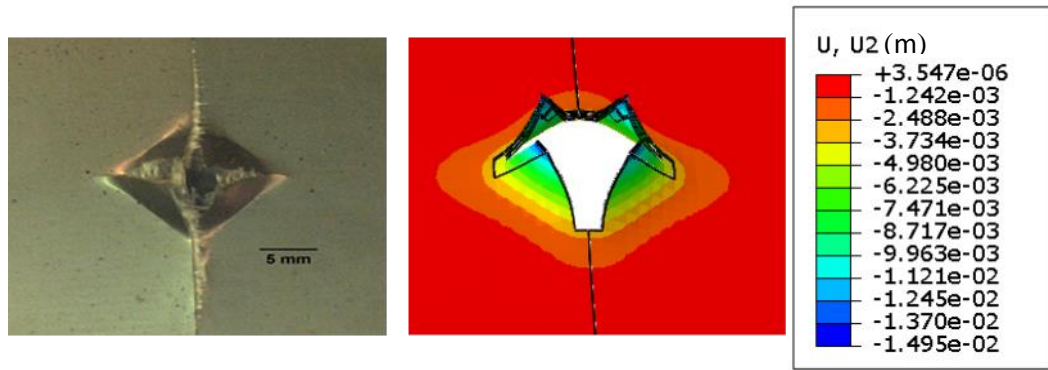
(b)
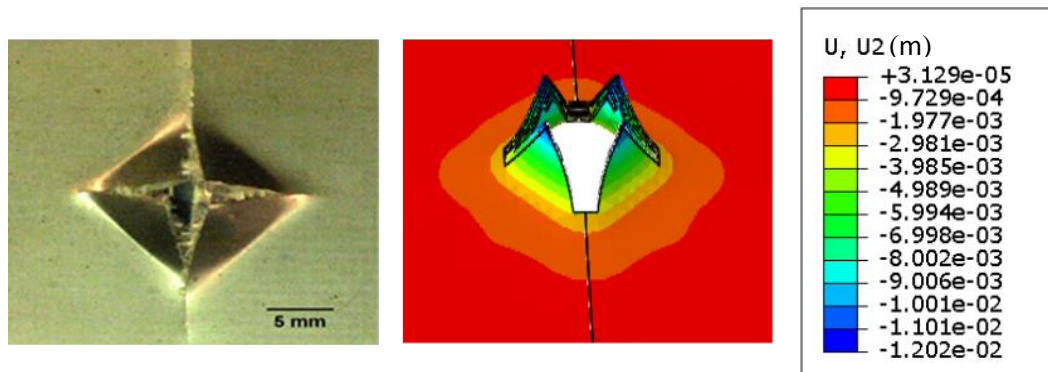
(c)
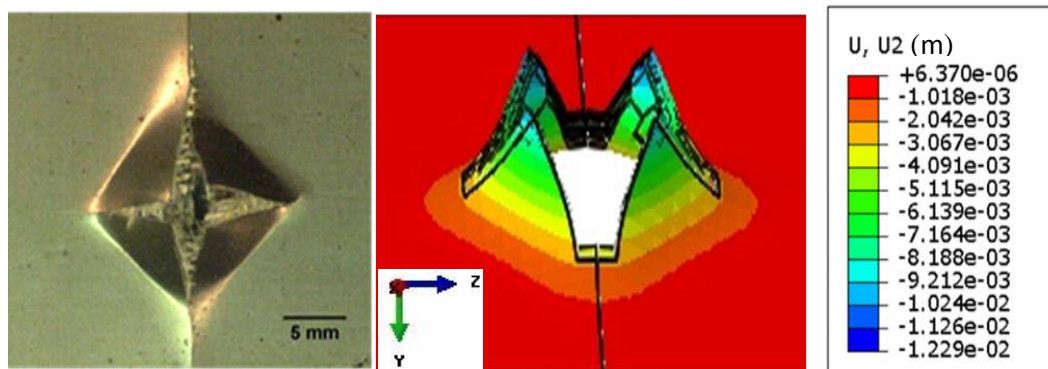
(d)

Figure 5-16. Failure modes in: (a) 2/1; (b) 3/2; (c); 4/3; (d) 5/4 titanium FMLs based on 2-ply GF/PEKK cores.

(a) 2/1 FML

(b) 3/2 FML

(c) 4/3 FML

(d) 5/4 FML
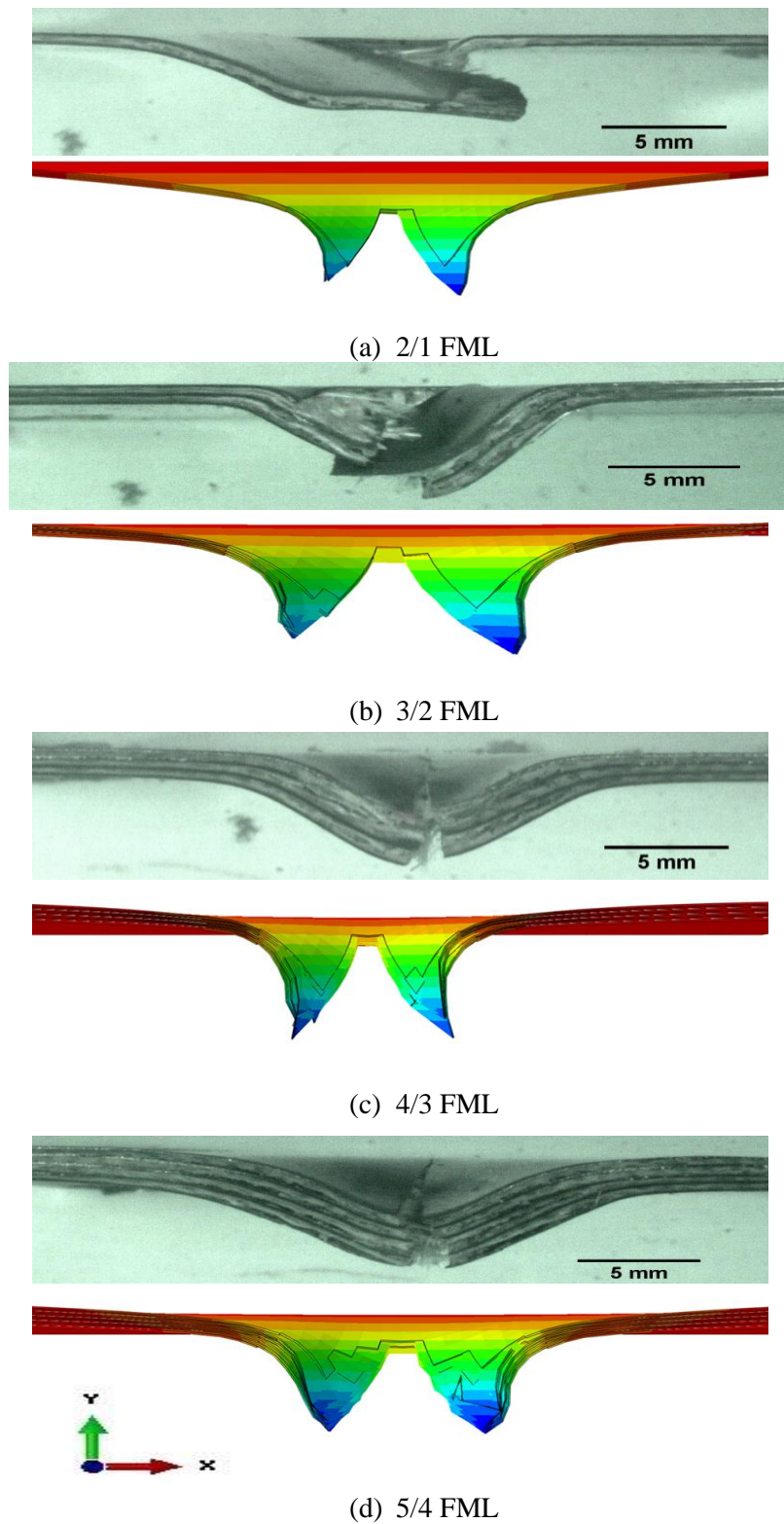
Figure 5-17. Comparison of the experimental and numerical simulations of the failed titanium-based FMLs with 2-ply composite cores.

5.6.2.2 Simulation of aluminium-based FMLs

Finite element models were also developed to simulate the structural behaviour of the aluminium-based FML plates with various stacking configurations under impact perforation loading. The results of the finite element models were then compared to the corresponding experimental results in terms of load-displacement, energy absorption and failure modes. Figure 5-18 shows comparisons of the predicted and measured load-displacement traces of 2/1, 3/2, 4/3 and 5/4 FML plates based on 2024-T3 (0.5 mm thick) with a 4-ply (GF/PEKK) composite layer subjected to impact loading. It can be seen that the trend in the predicted load-displacement traces are well correlated with those obtained under impact tests, i.e. the impact force increases to peak values with increasing the displacement before dropping rapidly when projectile perforates the targets. The FE models are also capable to predict the dependency of the peak load on the target thickness, i.e. the peak load increases with thickness.

Again, the predicted initial stiffness values of the FMLs investigated are slightly higher than the corresponded experimental ones due to the perfect contact assumed between the projectile and targets. The numerical peak loads of the 2/1, 3/2, 4/3 and 5/4 FMLs are 3309, 6329, 8081 and 11719 Newtons, respectively, which are only 0.28, 5.60, 9.50 and 1.08%, respectively, higher than those obtained experimentally.

The predicted values of energy absorption of the FMLs investigated can be established by determining the areas under the load-displacement traces, and these values were compared to the experimental results, in Figure 5-19. Clearly, the predicted values of energy absorption are in a good agreement with those obtained from impact tests. The energy absorption values from the numerical simulations for the 2/1, 3/2, 4.3 and 5/4 FMLs are 20.1, 38.1, 54.3 and 82.5 Joules, respectively, in comparison to the corresponding measured values of 18.9, 36.8, 57.3 and 78.9 Joules, respectively.

The failure modes predicted on the rear surfaces of 2/1 and 4/3 aluminium-based FMLs are compared with the corresponding experimental failure modes, as shown in Figure 5-20. It can

be seen that the failure modes in terms of deformation as well as specimen's fracture are successfully predicted by the finite element models. Clearly, the numerical simulations also show a cross-fracture at the central region of the target, which is similar to that of specimens perforated experimentally.
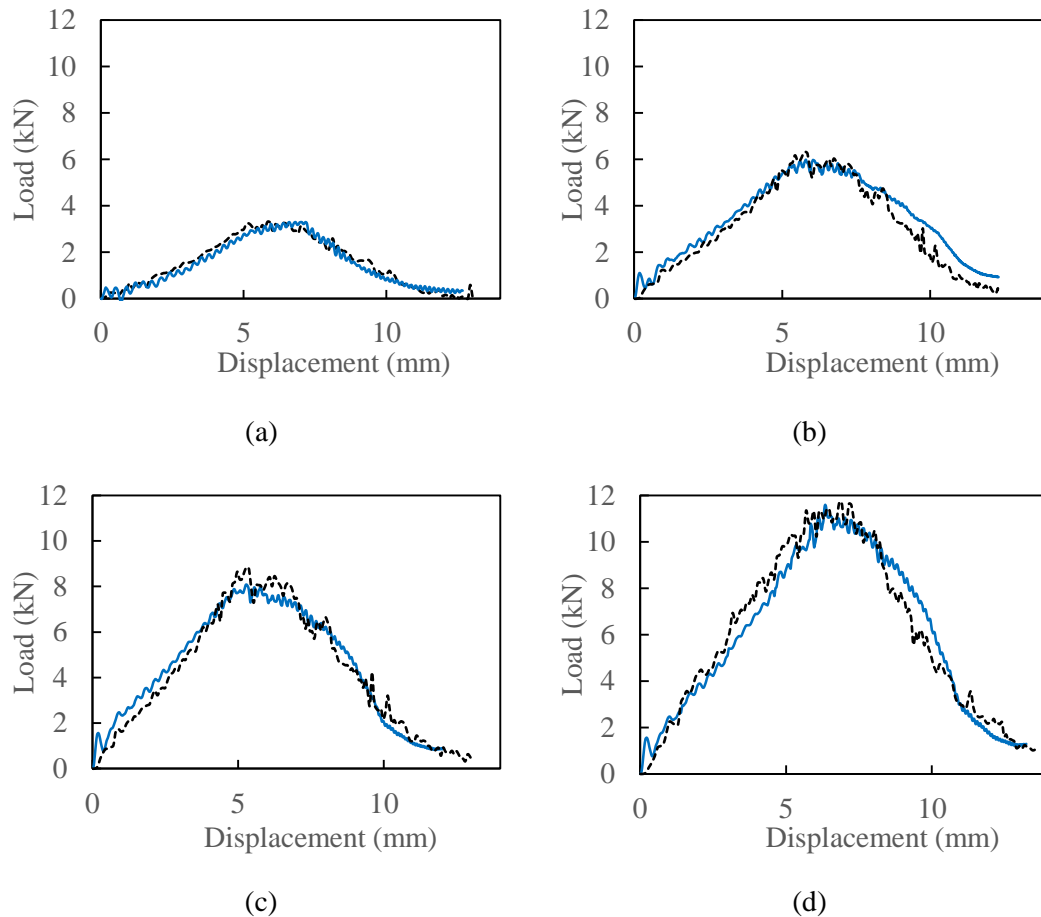
Figure 5-18. Load-displacement traces for (a) 2/1; (b) 3/2; (c) 4/3; (d) 5/4 aluminium (2024-T3) based FMLs subjected to low velocity impact loading. The solids lines correspond to experimental traces and the dashed lines to numerical predictions.
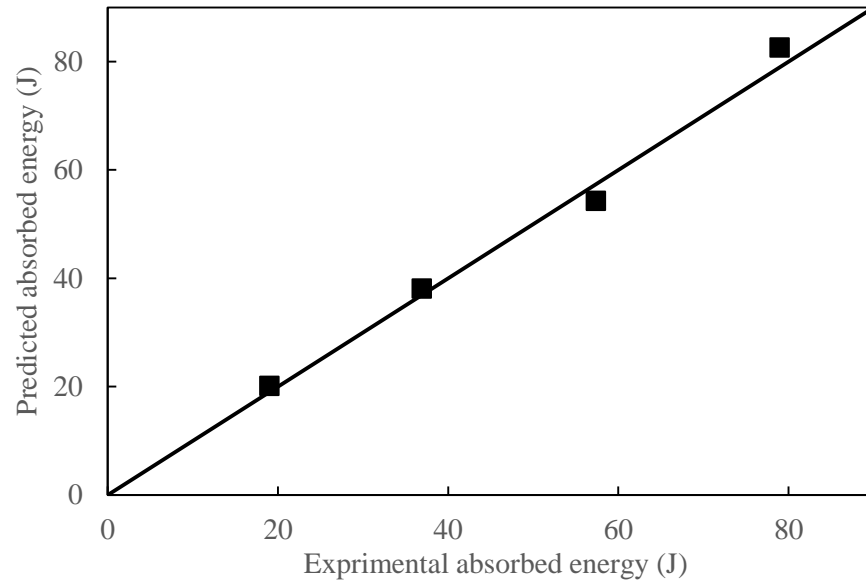
Figure 5-19. Comparison of the predicted and measured perforation energies of the 2/1, 3/2, 4/3, and 5/4 aluminium FMLs based on 4-ply GF/PEKK cores under impact perforation tests.

(a)

(b)
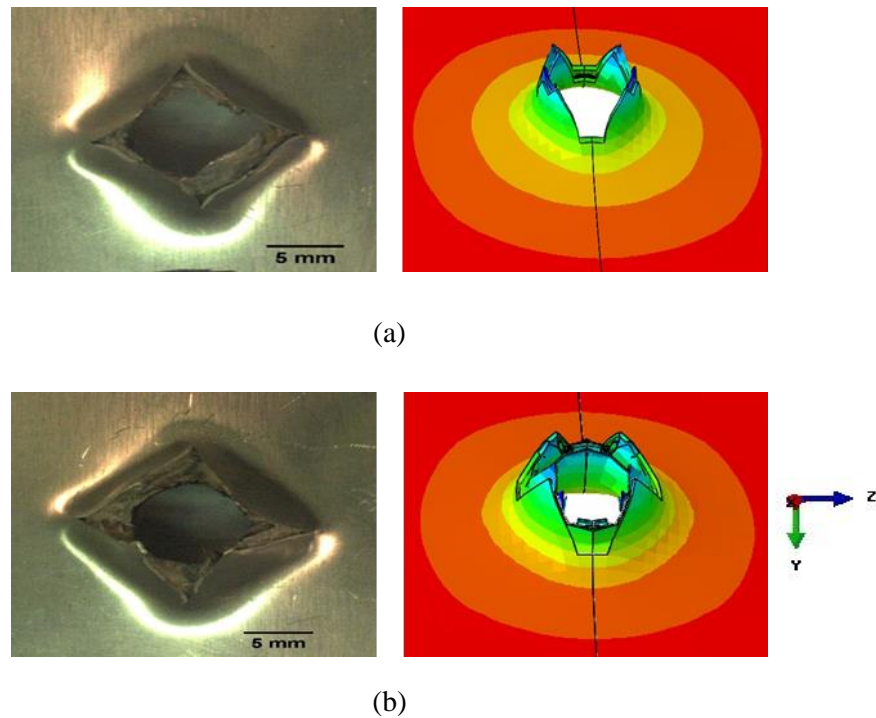
Figure 5-20. Failure modes in the 2/1 (a) and 4/3 (b) aluminium-based FMLs with a 4-ply composite core subjected to perforation impact.

The experimental and predicted cross-section failure modes of the FML plates investigated subjected to impact perforation are shown in Figure 5-21 . It can be noted that the basic features of the failure modes under impact testing for all the FMLs investigated were accurately predicted in terms of cross-crack on the rear surface, local deformation in the specimen's centre and delamination between the layers.

(a) 2/1 FML

(b) 3/2 FML

(c) 4/3 FML

190
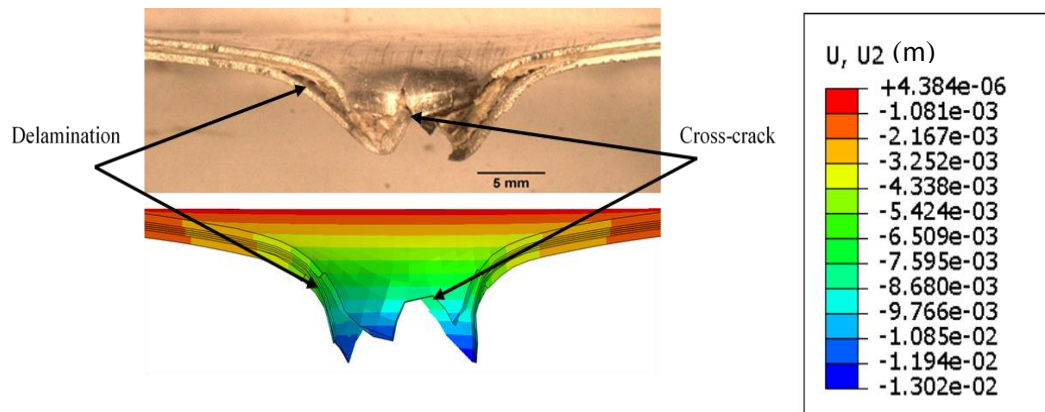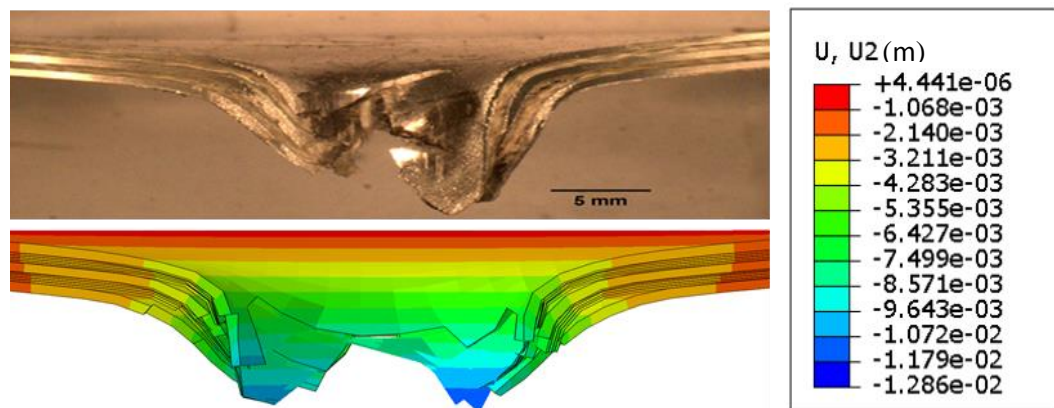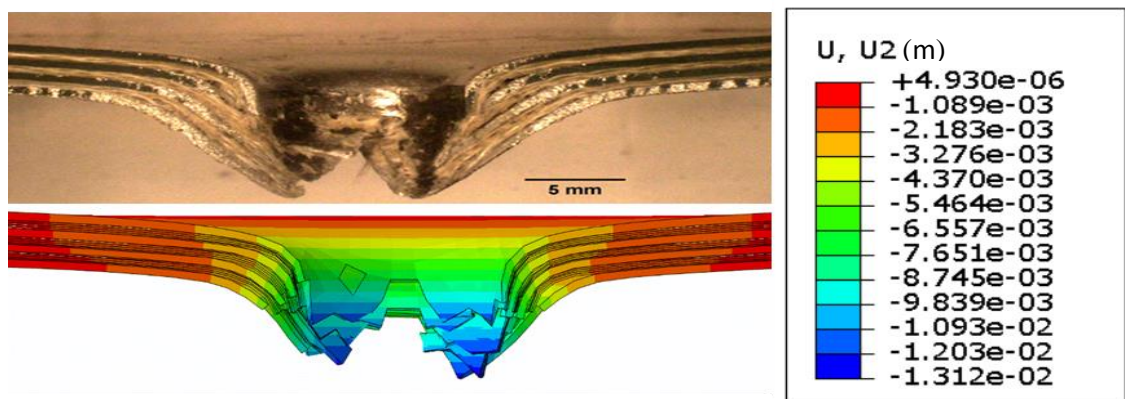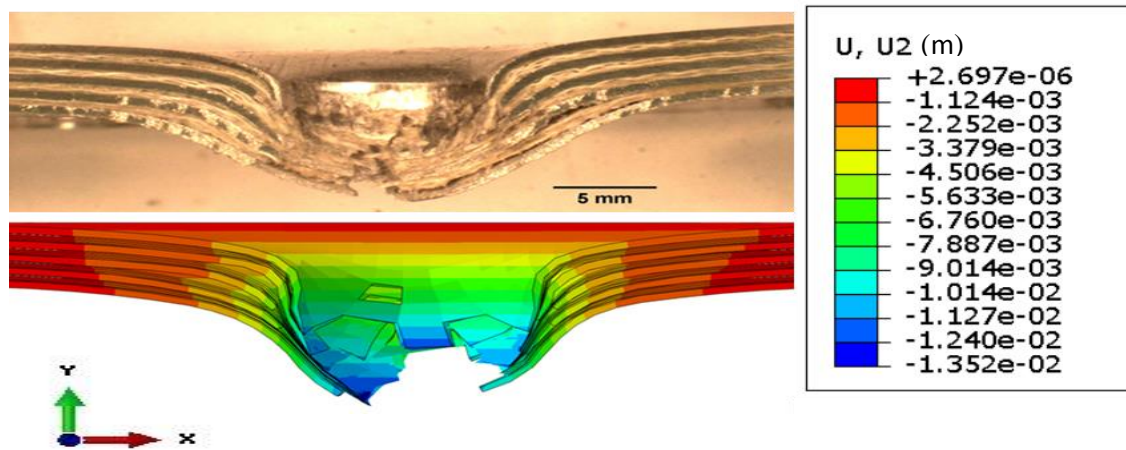
(e) 5/4 FML

Figure 5-21. Experimental and numerical cross-sections of the failed aluminium-based FMLs subjected to low velocity impact.

5.7 Parametric studies

Initially, the reliability of the proposed FE models to predict the perforation response of the FMLs investigated under low velocity impact loadings was verified. The developed FE models were then used to explore the structural behaviour of the fibre metal laminates investigated with extended variation of parameters. Although the experimental investigations are important and reliable for research, they are costly, time-consuming and sometimes hard to conduct. Comparably, many engineering investigations with a wide range of parameters can be carried out using numerical analyses which is more affordable. Initially, the validation of the FE models was assessed through comparison with the corresponding results of the experimental work. The results showed that the proposed simulations are capable of predicting the dynamic response of the laminates investigated with a high degree of success.

This section presents the findings of the parametric studies conducted on the FMLs, i.e. 2/1 titanium FMLs based on 2-ply composite cores and 2/1 aluminium FMLs based on 4-ply composite cores under impact with a variety of loading conditions. Therefore, a wide range of parameters were considered, i.e. projectile striking angle, impact locations, projectile's

geometry and velocity. The outcomes of the FE models are presented in terms of load-displacement traces, energy absorption and failure modes.

5.7.1   Effect of angle of obliquity

In real life applications, the aforementioned direct central impacts rarely occurred. Alternatively, composite structures are more frequently loaded at some obliquity. The response of the composite structures under this type of loading condition is difficult to investigate experimentally, especially using a drop-weight impact rig. In oblique impact tests, the impactor produces a horizontal force component which drives the projectile against one of the vertical columns used to guide the projectile. The main advantage of using the validated model is that the response of the composite structures under these more complex conditions can be predicted with a reasonable confidence. Four numerical impact simulations with different striking angles, i.e. 60°, 70°, 80° and 90°, on the 2/1 titanium-based and aluminium-based FMLs were undertaken. The load-displacement traces generated by the finite element analysis are shown in Figure 5-22 and Figure 5-23. Here, the impact angle refers to the angle between the target axis and the projectile. It can be seen from the figures that all traces show similar stiffness values, with the force increasing up to maximum values in a roughly linear fashion after the initial plateau stage. The forces then reduce to the lowest values (i.e. depending on the friction between the projectile and targets) when the projectile fully perforates the targets.

It can be also noted that increasing the striking angle of the impactor for the titanium-based FMLs leads to increasing displacement values at peak load and decreasing maximum load, maximum displacement as well as the corresponding energy absorption, as shown in Table 5-10. This evidence suggests that the energy absorption capacity of the targets investigated under impacts with obliquity between 70° and 60° is better than those impacted at 90° (i.e. normal impact). The increase in the perforation energy can be attributed to the fact that, at an off-axis angle, a larger material volume should be fractured when the projectile passes through the target. However, for a given striking angle, aluminium-based FMLs did

not show any significant dependency on obliquity as shown in Table 5-11. Figure 5-24 and Figure 5-25 compare the cross-sections predicted by the numerical analysis of the FMLs investigated subjected to impact by a 10 mm hemispherical projectile at different striking angles. From the figures, it can be noted that as the angle of obliquity decreases, the cross-shaped fracture occurred further away from the centre of the target.
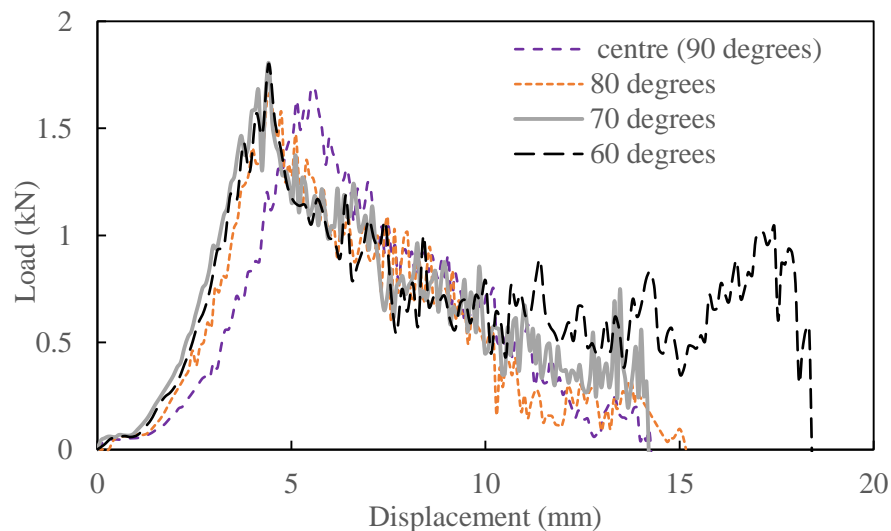
Figure 5-22. Predicted load-displacement traces for titanium-based FMLs under impact with various striking angles. The impactor mass and velocity were 1.48 kg and 4 m/s, respectively.
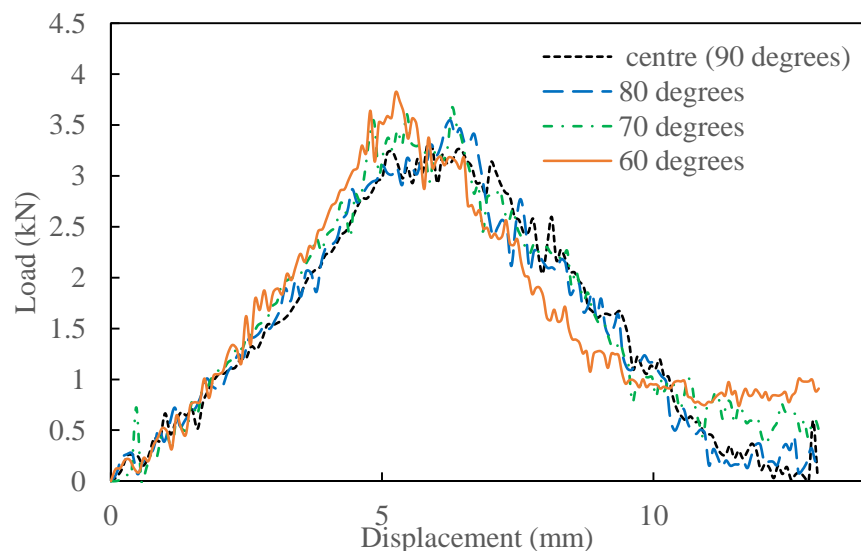
Figure 5-23.Predicted load-displacement traces for aluminium-based FMLs under impact with various striking angles. The impactor mass and velocity were 3.56 kg and 4 m/s, respectively.

Table 5-10. Summary of results for 2/1 titanium-based FMLs impacted at different angles.

Striking angle (degrees)	Peak force (N)	Displacement at peak force (mm)	Maximum displacement (mm)	Energy absorption (J)
60	1801	4.41	18.4	13.08
70	1804	4.41	14.2	9.87
80	1666	4.46	15.1	8.69
90	1689	5.51	14.3	8.7

Table 5-11.Summary of results for 2/1 aluminium-based FMLs impacted at different angles.

Striking angle (degrees)	Peak force (N)	Displacement at peak force (mm)	Maximum displacement (mm)	Energy absorption (J)
60	3822	5.77	13	21.3
70	3669	6.28	13	23.4
80	3545	6.26	13	20.0
90	3309	5.83	13	20.1

(a) 80°

(b) 70°
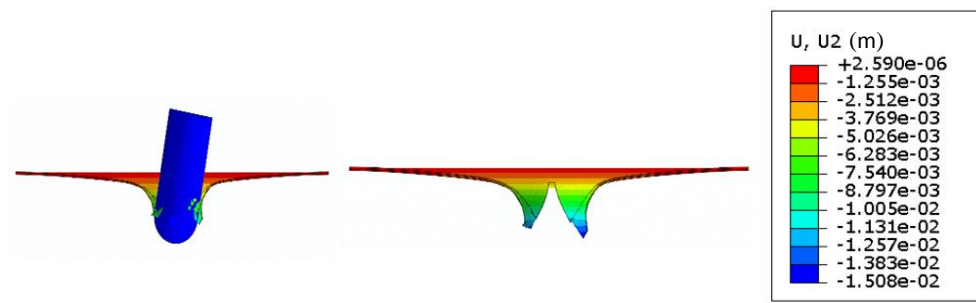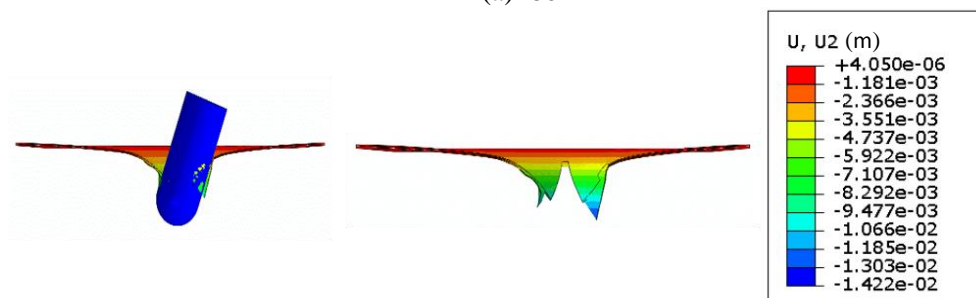
(c) 60°
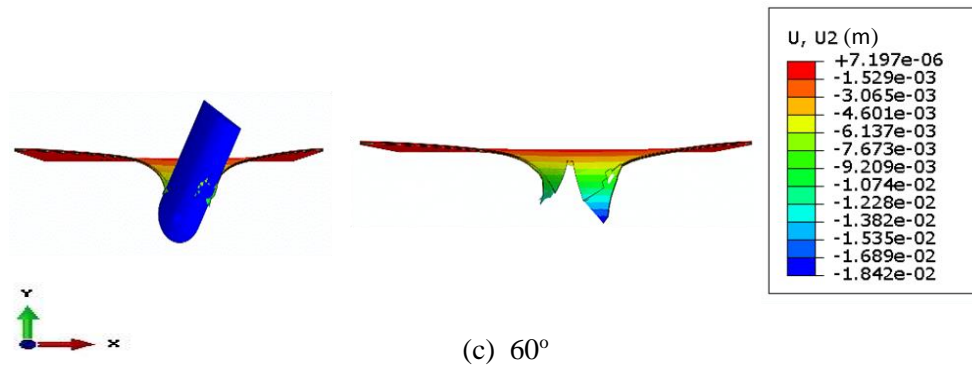
Figure 5-24. Cross-sections of 2/1 titanium-based FMLs impacted by a 10 mm hemispherical projectile at different striking angles.

(a) 80°

(b) 70°

(c) 60°
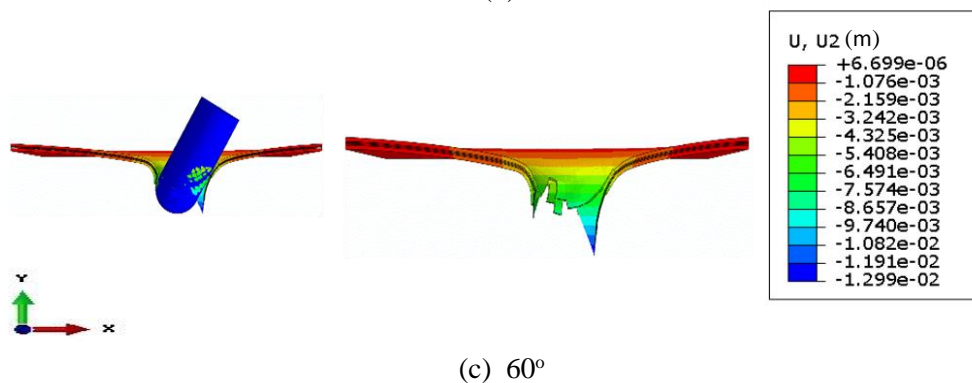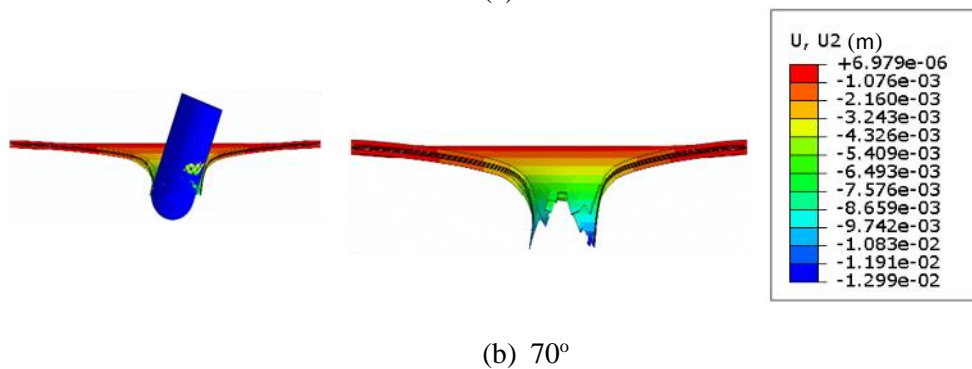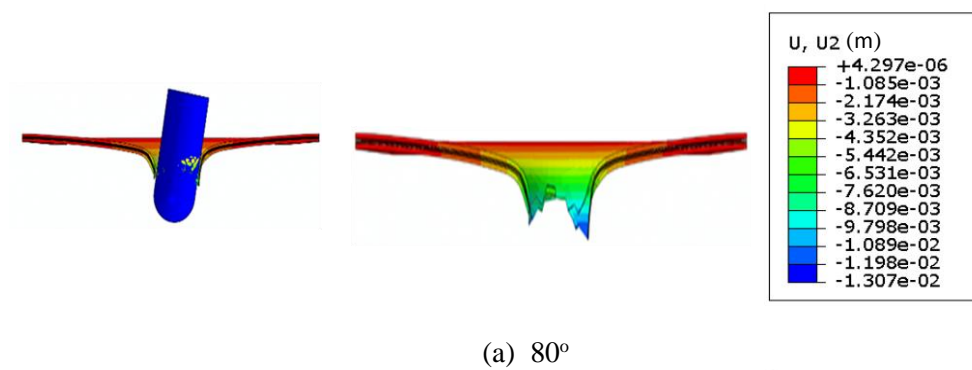
Figure 5-25.Cross-sections of 2/1 aluminium-based FMLs impacted by a 10 mm hemispherical projectile at different striking angles.

5.7.2 Effect of impactor mass and velocity

Initially, an impactor with a mass of 1.48 kg and velocity of 4 m/s was used to generate an impact energy of 11.8 J on the 2/1 titanium FMLs based on 2-ply composite cores. In contrast, another impactor with a mass of 3.56 kg and velocity of 4 m/s was used to produce a constant energy of 28.4 J on the 2/1 aluminium FMLs based on 4-ply composite cores. Clearly, the impact energy generated is directly related to the mass and the initial velocity of the impactor according to the following formula;

$$E = \frac{1}{2} M V_e{}^2 \qquad\qquad\qquad (5.1)$$

where M and V_e are the impactor mass and velocity, respectively.

Here, the effect of changing the impactor velocity and the mass to generate a similar impact energy used was investigated. Three numerical tests with different velocities and masses on each FML system were conducted. Figure 5-26 shows the load-displacement traces of the FMLs investigated subjected to impact with a 10 mm hemispherical projectile with different velocities. The values of the peak load, maximum displacement and the corresponding energy are presented in Table 5-12 and Table 5-13. The numerical results show that increasing the impactor velocity and decreasing the impactor mass lead to increase the peak forces for the fibre metal laminates investigated. This evidence suggests that, for the range of velocities investigated, both FML systems show a better perforation resistance under high velocity impact. The reason can be attributed to the effect of the strain-rate (i.e. high impact velocity) at which the strength of the material increases.
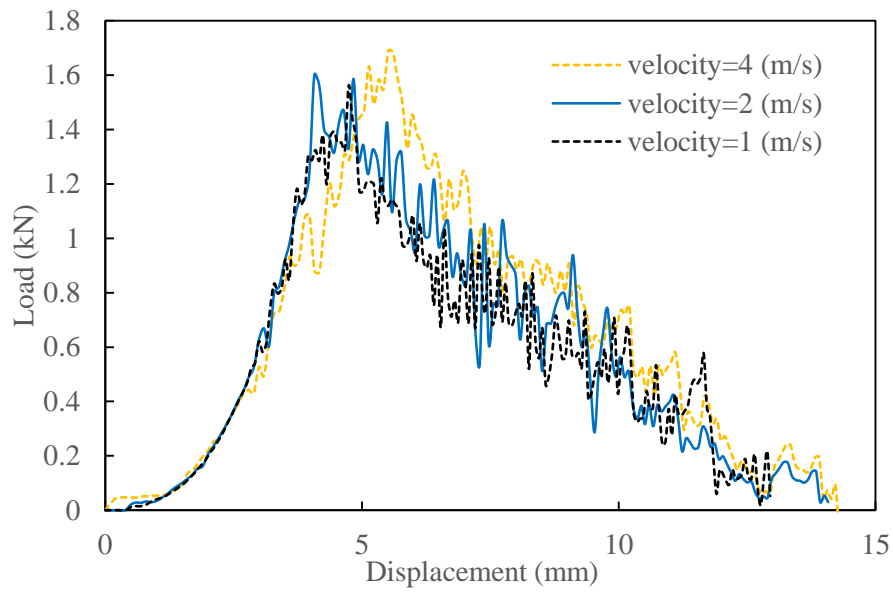
(a)
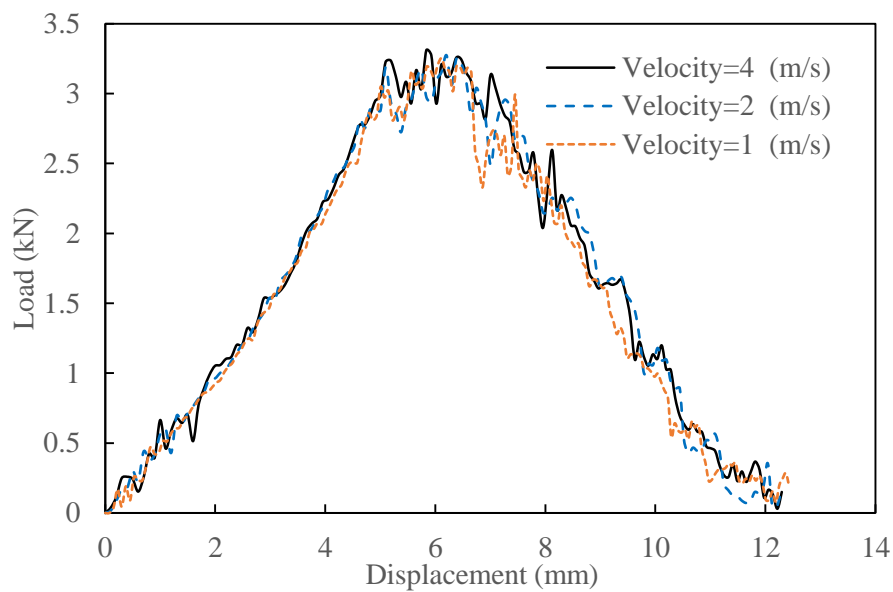
(b)

Figure 5-26. Load-displacement traces for 2/1 titanium-based FMLs (a), and 2/1 aluminium-based FMLs (b) impacted by a hemispherical indenter at different velocities.

Table 5-12. Details and results of 2/1 titanium-based FMLs impacted with different masses and velocities.

Impactor mass (kg)	Impact energy (J)	Velocity (m/s)	Peak force (N)	Maximum displacement (mm)	Energy absorption (J)
1.48	11.84	4	1689	14.3	8.7
5.94	11.84	2	1600	14.0	7.4
23.68	11.84	1	1561	13.9	7.5

Table 5-13. Details and results of 2/1 aluminium-based FMLs impacted with different masses and velocities.

Impactor mass (kg)	Impact energy (J)	Velocity (m/s)	Peak force (N)	Maximum displacement (mm)	Energy absorption (J)
3.56	28.48	4	3309	13.0	20.1
14.24	28.48	2	3273	14.0	20.0
56.96	28.48	1	3251	13.4	18.7

5.7.3 Effect of the projectile size

It has been shown in this study that the projectile geometry has a significant effect on the perforation resistance of the plain GF/PEKK composites. Hence, it will be beneficial to employ the validated FE models to predict the perforation response of the dynamically-loaded FMLs under different projectile diameters. This section considers the influence of projectile size on the impact response of 2/1 titanium FMLs based on 2-ply composite cores and 2/1 aluminium FMLs based on 4-ply composite cores. Four hemi-spherical projectiles with diameters of 5, 10, 15 and 20 mm were employed in this study. Figure 5-27 shows the predicted load-displacement traces by the FE models of laminates investigated under impact loading. It can be seen that the impacted specimens show a similar initial stiffness which is also observed on GF/PEKK laminates under impact with various projectile sizes. It can also be noted that the specimens show similar trends, i.e. the load increases with displacement up to maximum value before dropping when the projectile starts to perforate the targets.
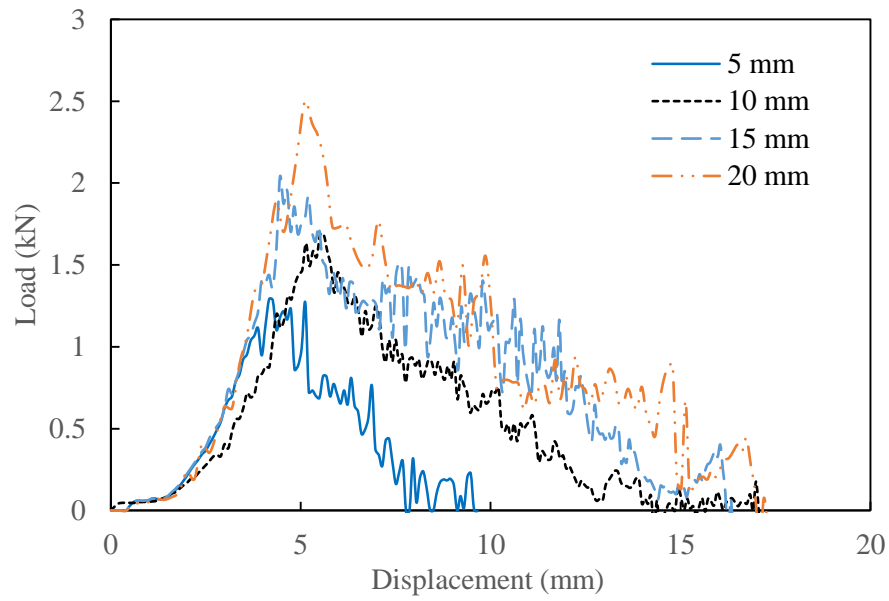
(a) 2/1 titanium (0.51 mm thick) FMLs based on 2-ply composite cores
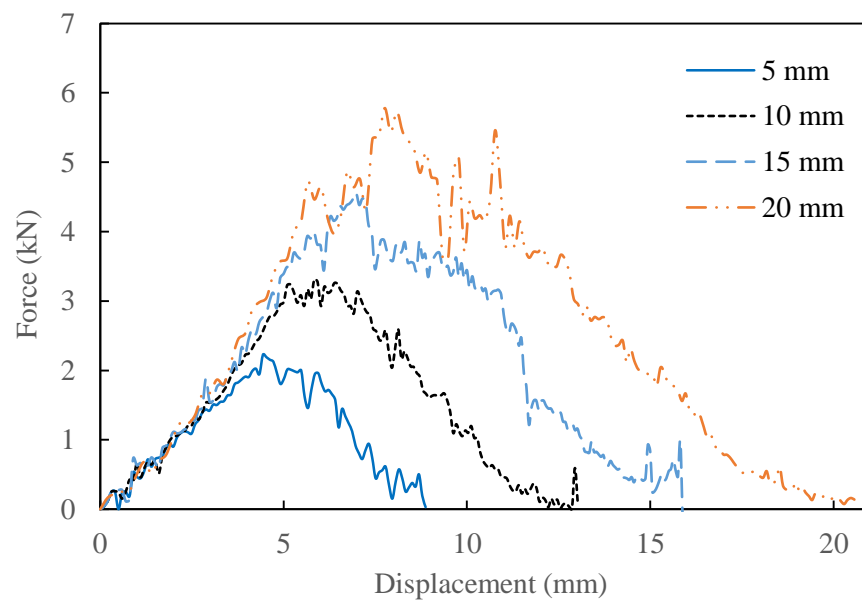
(b) 2/1 aluminium (1.51 mm thick) FMLs based on 4-ply composite cores

Figure 5-27. Load-displacement traces of the FMLs investigated subjected to impact loading with various hemispherical projectile diameters.

The variation of the peak force and energy absorption with the projectile diameter of both FML systems is shown in Figure 5-28. It is clear that with increasing the projectile diameter, the peak force and energy absorption increase. The peak forces for titanium-based (0.51 mm thick) and aluminium-based (1.51 mm thick) FMLs impacted with a 20 mm projectile diameter are 2500 and 5779 Newtons, respectively. Relative to the corresponding results of those impacted with a 5 mm projectile of 1291 and 2227 Newtons, they are 48 and 61 % higher, respectively. The energy absorption values of the titanium-based and aluminium-based FMLs impacted with a 20 mm projectile diameter were 61 and 71 %, respectively, higher than the corresponding values obtained using a 5 mm projectile diameter, due to a larger contact area.

Figure 5-29 and Figure 5-30 show the cross-sections of the FMLs predicted by the FE analyses. Closer examination to the figures indicates that the panels show local plastic deformation and fracture at the centre of the impacted area, including a combination of tensile and shear failure. As expected, the increasing of the projectile diameter leads to increase the damaged area. Delamination can be clearly observed between the metal sheets (i.e. titanium and aluminium alloys) and the GF/PEKK layers. The delamination becomes more sever with increasing projectile diameter. The reason can be attributed to impact time effect, that is, a larger projectile i.e. 20 mm diameter would take more time to perforate the specimen , which cause more damage as well as more delamination between the layers.
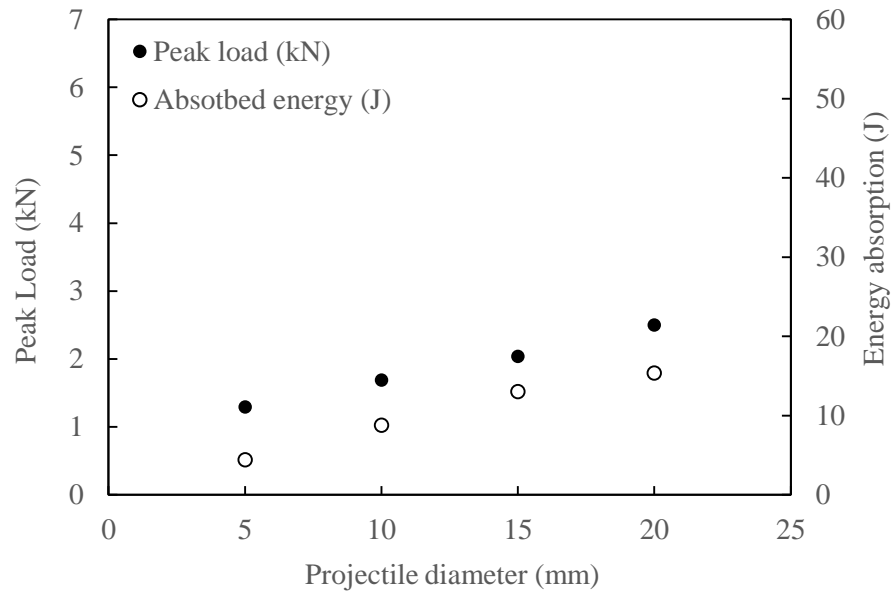
(a)
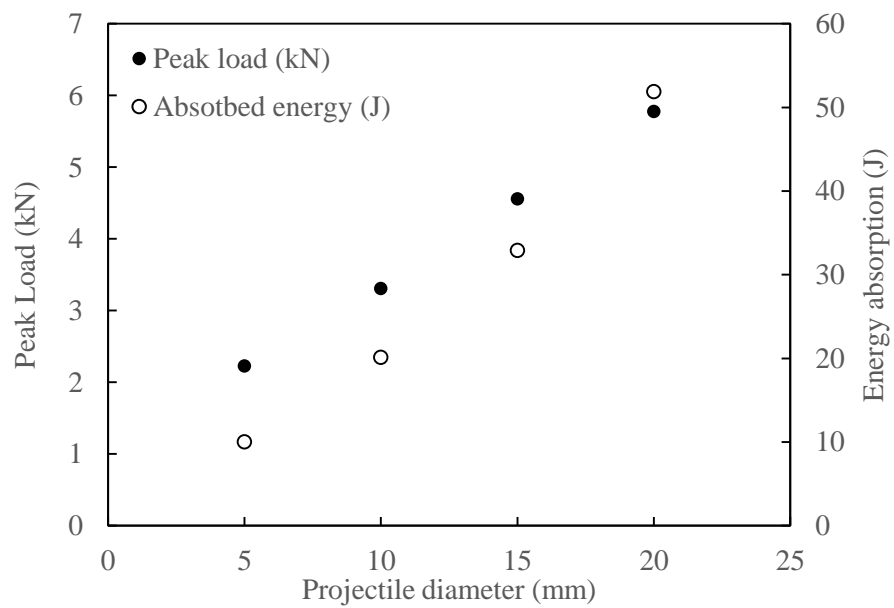
(b)

Figure 5-28. Variation of the peak load and perforation energy with projectile
diameter for 2/1 titanium-based FMLs (a) and aluminium-based FMLs (b).
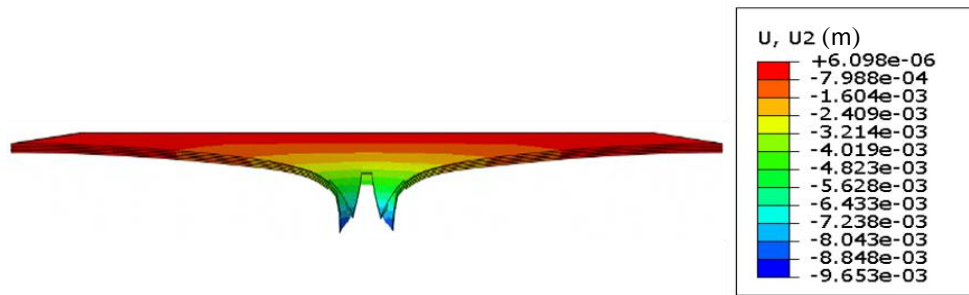
(a)
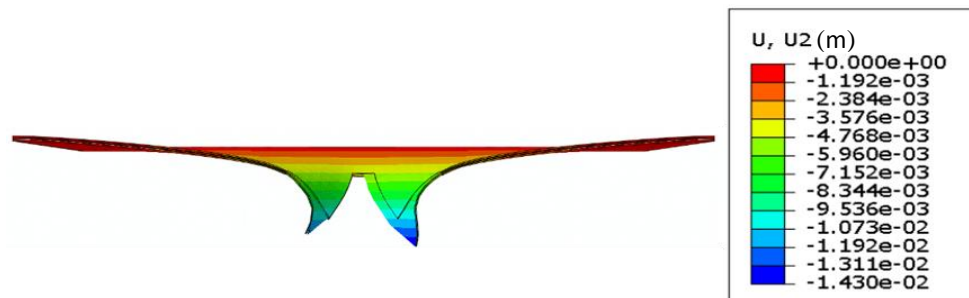
(b)
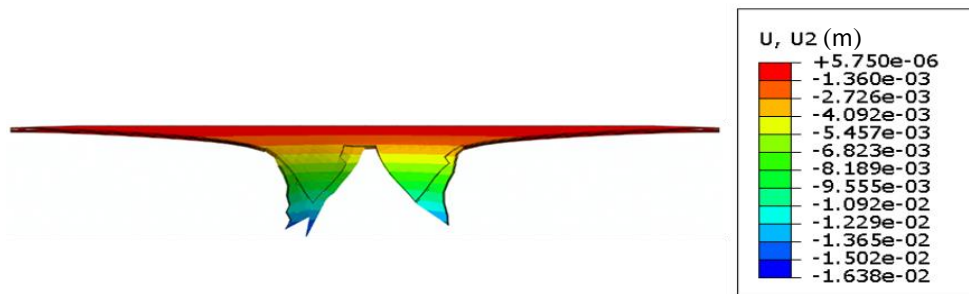
(c)
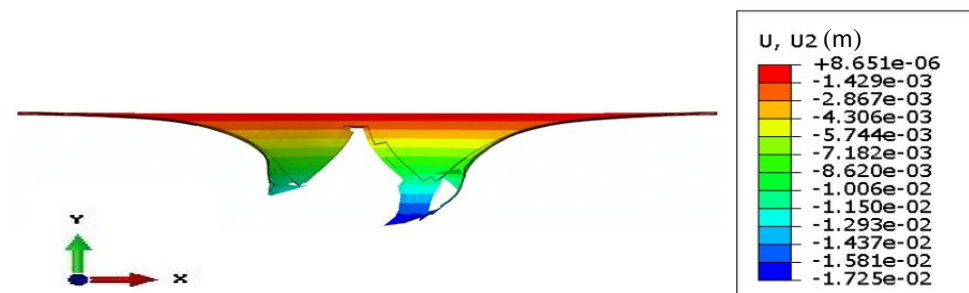
(d)

Figure 5-29. Predicted cross -sections of the 2/1 titanium-based FMLs impacted with different projectile diameters: (a) 5 mm; (b) 10 mm; (c) 15 mm; (d) 20 mm.

(a)

(b)

(c)

(d)
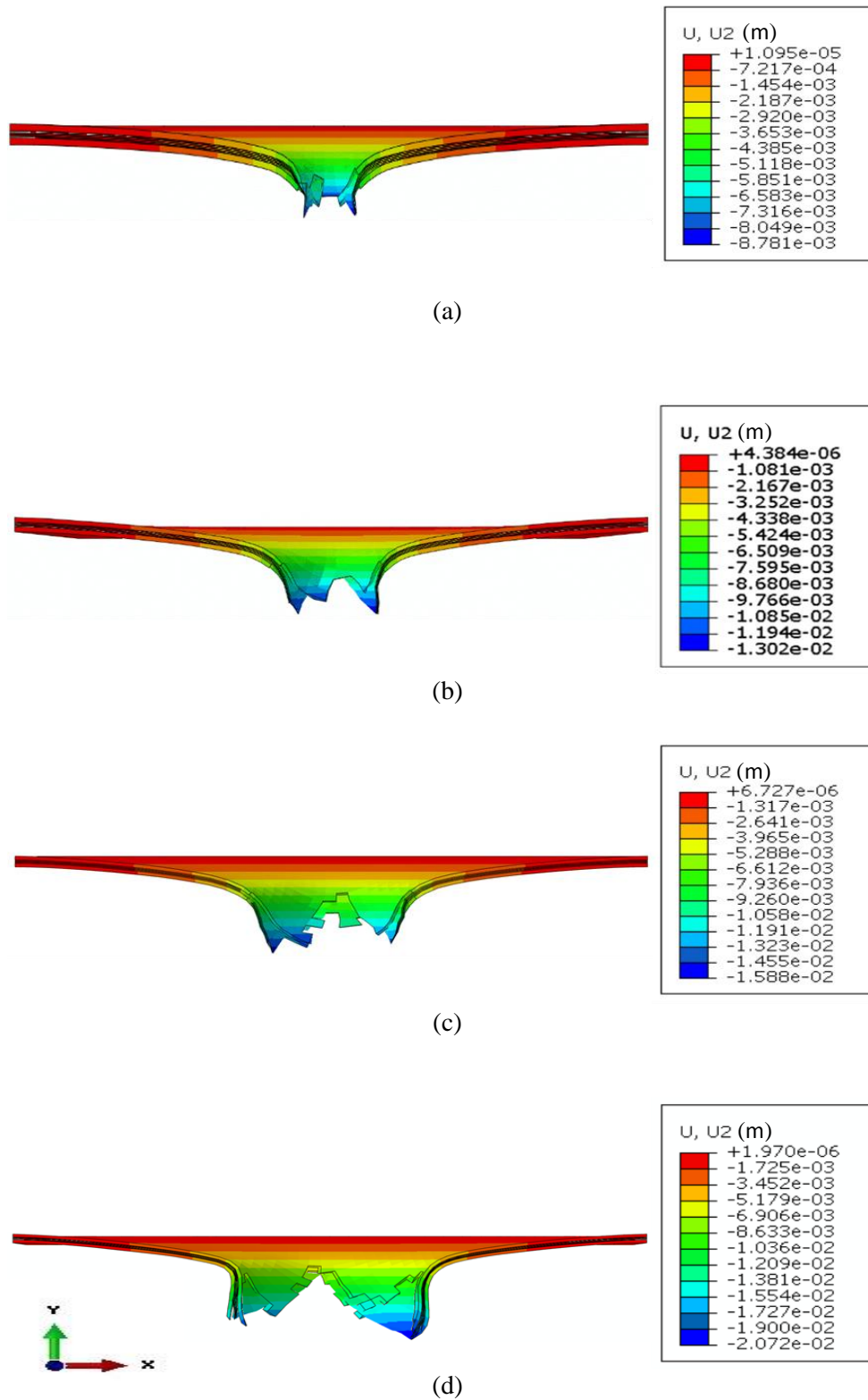
Figure 5-30. Numerical cross-sections failure modes of the 2/1 aluminium-based FMLs impacted with various projectile diameters: (a) 5 mm; (b) 10 mm; (c) 15 mm; (d) 20 mm.

5.7.4 Effect of impact location

In the practice, during routine maintenance and service conditions, composite structures may be exposed to impact at different locations, i.e. near or on the edge of the composite structure. Limited research work has been conducted to investigate the impact response of composite structures under various locations. Breen et al. [174] considered the effect of central and near-edge impacts on the residual strength of carbon fibre reinforced plastic laminates. Their results showed that near edge impacts caused a greater reduction in the residual compressive strength than those under central impacts. This evidence suggests that the commonly-adopted test scenario in which panels subjected to impact at central location may yield a non-conservative damage outlook. This may have a great importance in the aerospace industry, where impact loading on composite aircraft structures rarely occur at mid-bay locations, i.e. structures based on thin skins connected to stringers, spars and ribs. Therefore, considerations should be given to more realistic loading conditions.

The validated FE models were employed to investigate the influence of the impact locations on the perforation response of the FMLs. The targets were impacted at different locations, i.e. 10, 20 and 30 mm off-centre. Figure 5-31 shows the predicted load-displacement traces for these laminates at different impact locations. It can be seen that off-setting the impact location serves to increase the effective slope of the traces, highlighting the increased stiffness associated with such loading conditions [175].

Figure 5-32 shows the variation of the peak load and energy absorption of the fibre metal laminates investigated with the striking positions. An examination of the figure indicates that off-setting the impact location from the centre has no a significant effect on the peak load. This may be due to the size of the specimens with a fully fixed boundary condition in which there is not a great scope to significantly change the positions of the impact within the relatively small target, i.e. 72 mm x 72 mm. From the figure, it can also be noted that the perforation energies of the both systems are higher at the centre of the target, decreasing to what appears to be a constant value as the boundary condition is approached. Interestingly, the

perforation energy values at 30 off-centre impact location of the titanium-, and aluminium-based FMLs are approximately 20 and 18 %, respectively, lower than those obtained under central impact indicating that off-centre impacts are more serious than the commonly-investigated central impact scenario.
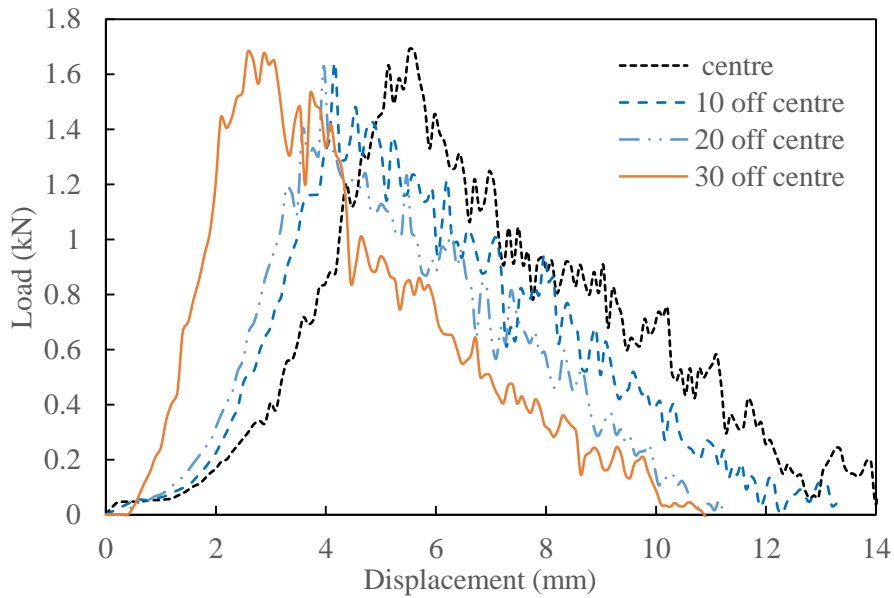
(a)
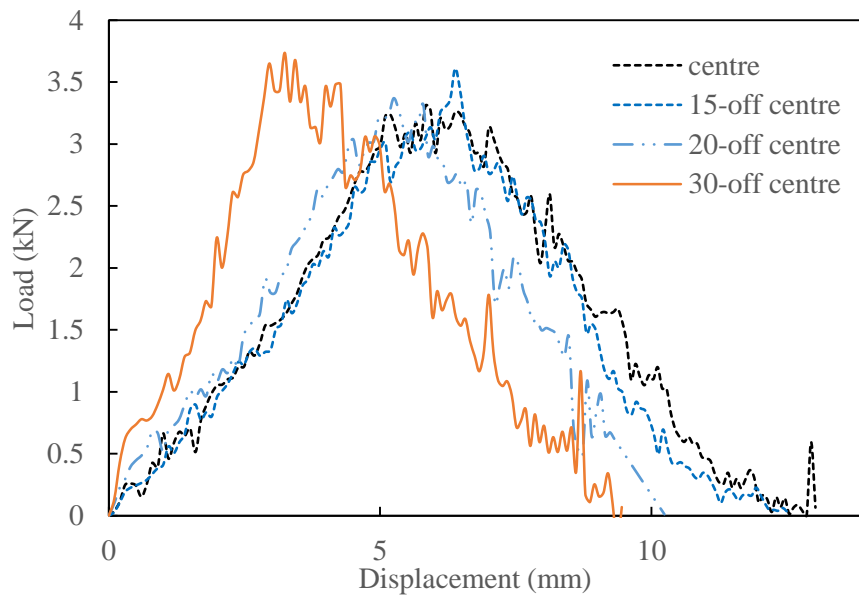
(b)

Figure 5-31. Load-displacement traces for the 2/1 titanium-based FML (a) and 2/1 aluminium-based FML (b) following impact tests with a hemispherical projectile (10 mm diameter) at different impact locations.
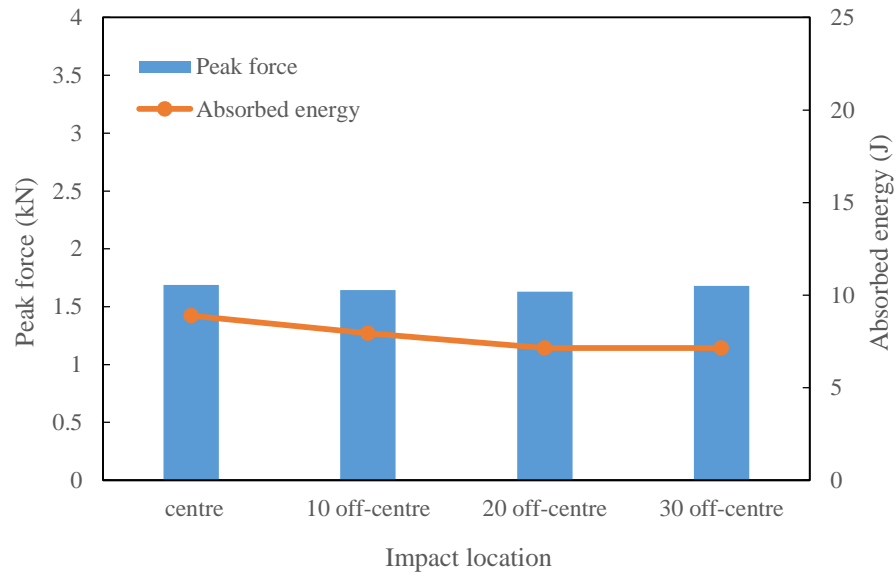
(a)
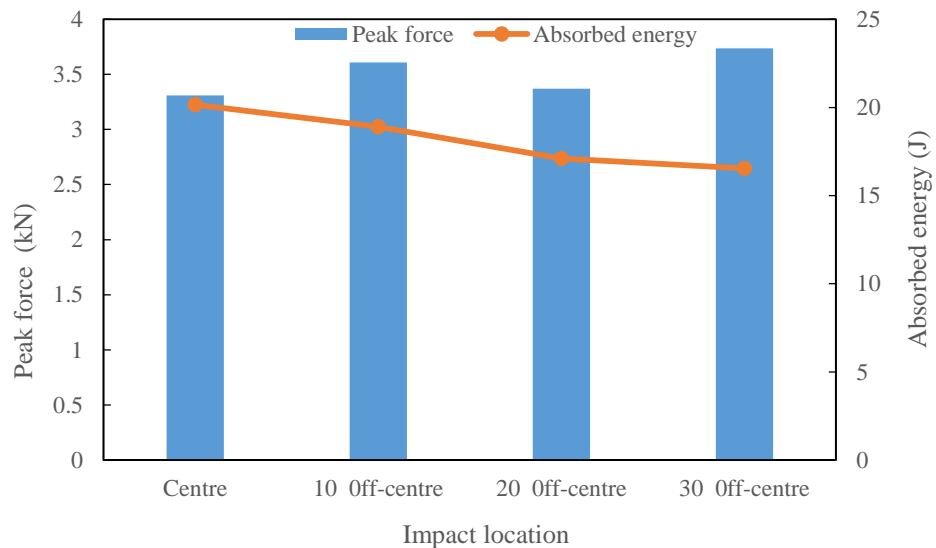
(b)

Figure 5-32. Variation of the peak force and the absorbed energy with the impact
location for the 2/1 titanium-based (a) and 2/1 aluminium-based (b) FMLs impacted
with a hemispherical projectile (10 mm). The bar charts are the peak forces and the
line is the energy absorption.

Figure 5-33 and Figure 5-34 show the simulated cross-sections for the FMLs subjected to off-
centre perforation impact. An examination of the fracture zones indicates that off-setting the
impact location from the centre to the boundary condition leads to produce sever damage and
significant delamination, especially for the aluminium-based FMLs.

(a)

(b)

(c)
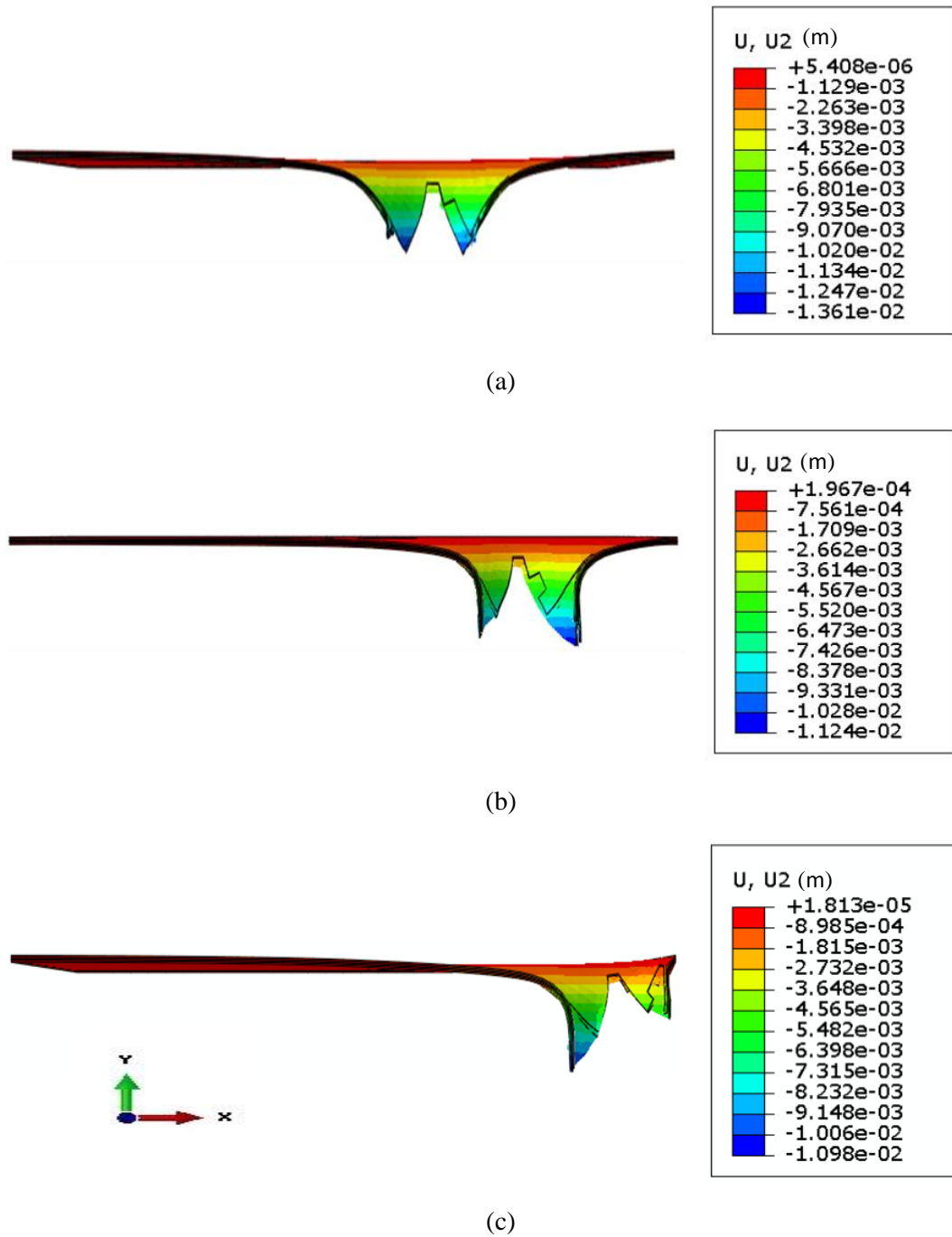
Figure 5-33. Numerical cross -sections of the 2/1 titanium-based FMLs impacted with a hemispherical projectile (10 mm diameter) at different locations of 10 mm off- centre (a) 20 mm off-centre (b) 30 mm off-centre (c).

(a)

(b)

(c)
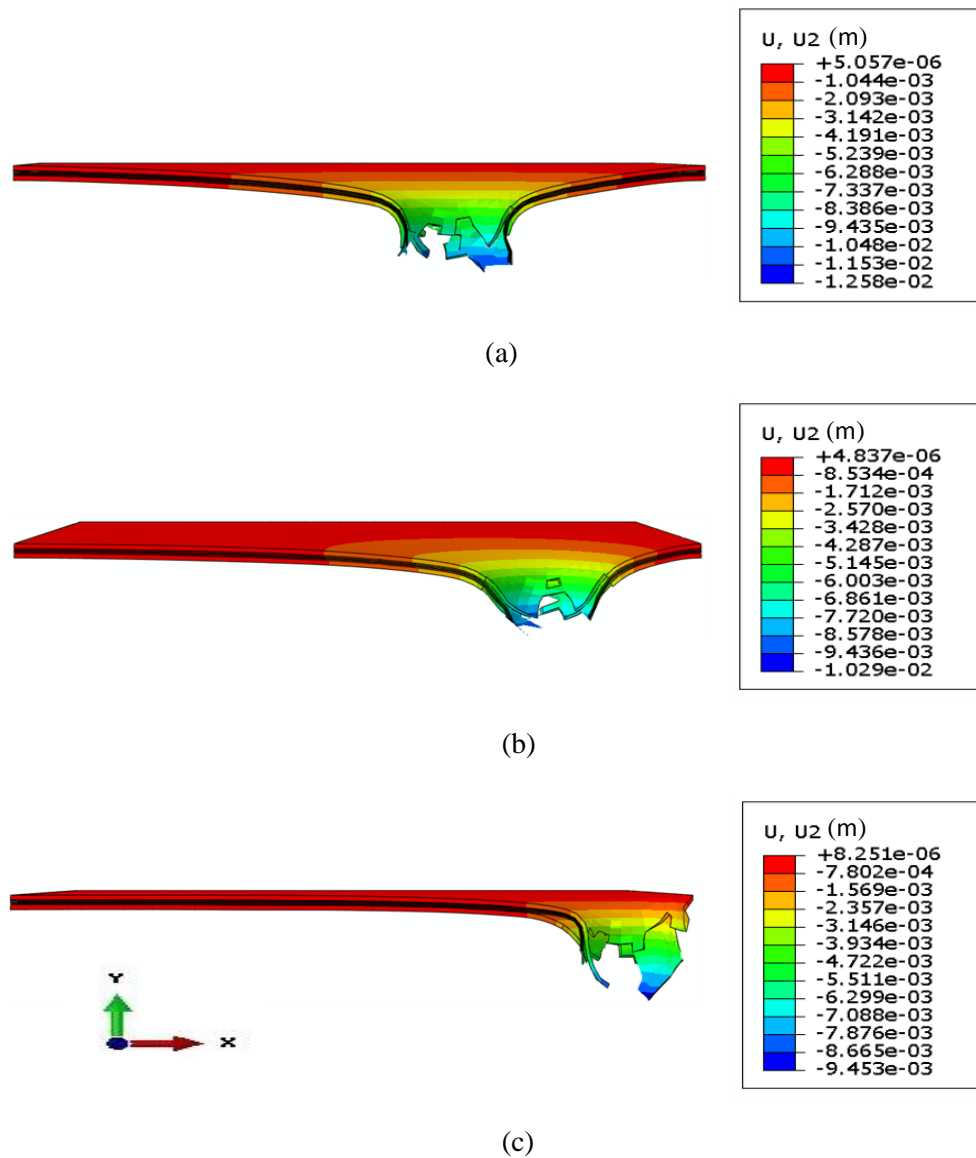
Figure 5-34. Numerical cross-sections of the 2/1 aluminium-based FMLs impacted with a hemispherical projectile (10 mm diameter) at different locations of 10 mm off- centre (a) 20 mm off-centre (b) 30 mm off-centre (c).

5.8 Summary

This chapter presents the finite element modelling to understand the structural behaviour of laminates investigated under impact loading. An explicit dynamic solver, Abaqus/Explicit was used to predict the perforation resistance of GF/PEKK composites, titanium- and aluminium-based FMLs. Here, woven glass fibre reinforced PEKK laminates were modelled as an

orthotropic elastic material up to the onset of failure, followed with Hashin failure criteria. Titanium and aluminium alloys were modelled as elasto-plastic materials with ductile damage and shear damage failure criteria. In these simulations, the effect of the target thickness and projectile geometry were considered. The numerical results by FE models corresponding to low velocity impact were then validated against the corresponding results obtained experimentally. The results were presented in terms of load-displacement, energy absorption and failure modes. The essential deformation features of the panels were captured by the FE model is with good correlation with the experimental results.

For the FMLs, however, the FE simulations give a slight overestimation of the stiffness values relative to the corresponding experimental results. In general, the FE models yielded accurate predictions of the load-displacement traces and the associated perforation threshold energy. The validated FE models were further used to for parametric studies. Therefore, the validated FE models were then exploited to explore the structural behaviour of the fibre metal laminates investigated with extended variation of parameters that were not undertaken in the experimental work. Thus, the influence of varying the impact obliquity, projectile geometries, impact velocities and impact locations on impact response was investigated. It was found that the energy absorption of the FMLs investigated under impacts with obliquity is better than those subjected to normal impact (i.e. 90º). Both FML systems show a higher perforation resistance under impact at high velocity due to the effect of the strain-rate at which the strength of the material increases. It is also noted that with increasing the projectile diameter, the peak force as well as energy absorption of the FML investigated increase. Furthermore, off-setting the impact location from the centre to the boundary condition leads to a high severity of damage with significant delamination for the laminates investigated.

6 Chapter 6: Conclusions and Future Work

6.1 Conclusions

Based on the main findings of the current study, the following conclusions can be drawn:

- Specimens based on pre-treated fibres with adhesive exhibit higher bonding strength than those obtained without fibre treatment.

- The high temperature tensile tests of GF/PEKK composites have shown that there is no obvious reduction in its tensile strength under the heating up to 100 °C, whereas, at a temperature of 250 °C, a significant reduction in the tensile strength by approximately 35% relative to panels tested at room temperature was observed.

- The maximum perforation force and tensile strength were corresponding to a PEKK weight percentage of 40 %, when such a percentage was varied between 30% to 50%.

- The GF/PEKK laminates offer a perforation threshold up to two times of the GF/Epoxy laminates.

- For the GF/PEKK laminates, the energy can be absorbed in the form of fibre fracture and matrix cracking. The delamination between the layers was not significant in these laminates for the stacking configurations investigated.

- The absorbed energy of the GF/PEKK targets increased with the projectile size, resulting in a higher perforation resistance.

- The experimental results of the panels impacted with various projectile shapes have shown that the higher perforation energy required to perforate the targets was belong to those impacted with a partially-flatted projectile.

- A reduction of around 35% in both the tensile strength and the yield strength of the aluminium alloy was produced due to the processing temperature cycle.

- The laser fluence of 4.54 J/cm^2 seems an optimum parameter in which a good bonding strength between titanium foils and PEKK film was achieved.

- A comparison of the quasi-static and dynamic perforation responses of the FMLs has shown the strain rate sensitivity of these laminates at which the perforation energy increases when the loading rate changes from quasi-static to dynamic.

- The failure modes of the FMLs were similar under both test conditions.

- The perforation resistance of the FMLs investigated increases with the total thickness and the composite core thickness.

- It has been concluded that the titanium-based FML with 2/1 stacking configuration can offer densities around 35 % lower than that offered by just the titanium alloy, easing the high-density issue of the high temperature alloys.

- A comparison of the quasi-static and impact responses for the FMLs investigated has shown that the contribution of the aluminium alloy in energy absorption is significantly higher than that offered by the titanium alloy, highlighting the low ductility and poor impact properties of the high strength titanium alloy.

- The titanium-based FMLs exhibit higher impact force than that of their aluminium-based counterparts. The results indicate that incorporation of the titanium alloy increases the stiffness of the resulted FMLs.

- Finite element methods have been successfully developed to simulate the perforation response of the GF/PEKK laminates and the related FMLs impacted with projectiles in different sizes and shapes. The deformed shapes have also been captured with reasonable accuracy.

6.2 The proposed future work

The following recommendations are proposed for the future work based on the results of the current study:

- It would be valuable to conduct more manufacturing processes by changing the impregnation technique or the binder type in order to improve the properties of high-performance composites investigated.

- To study the effects of incorporating various nanomaterials in these thermoplastic prepregs on fire resistance, mechanical and interfacial properties with alloys, especially in relation to high temperature fibre metal laminates.

- It would be worth to undertake more experimental investigations on the plain composite and the related FMLs under blast and high velocity impact loadings.

- In ABAQUS, the existed code for Hashin's failure can only be used with 2D elements, i.e. shell or continuum shell elements. Therefore, it would be valuable to implement Hashin's failure criteria using 3D elements to improve the accuracy of the finite element solutions through the thickness direction.

- It would be interesting to develop new sandwich structures using these high-performance composites materials as skins.

- The high-temperature properties are the principal demand for the new generation of aircraft. High-performance thermoplastic polymers will be the best candidates for these requirements. Therefore, more investigations with aluminium alloys are needed to improve their high-temperature properties to retain their mechanical properties at high processing temperatures required for these polymers.

- The response of such composites under combined high-temperature and impact loading is worth investigating as it is the case most happened in the practice.

References:

[1]   C. Soutis, "Fibre reinforced composites in aircraft construction," *Prog. Aerosp. Sci.*, vol. 41, pp. 143–151, 2005.

[2]   R. Jain and L. Lee, *Fiber reinforced polymer (FRP) composites for infrastructure applications*. 2012.

[3]   G. Tsigkourakos, H. Ullah, F. Vartzopoulos, I. A. Ashcroft, and V. V Silberschmidt, "Dynamic loading of fibre-reinforced laminates : Experiments and simulations," pp. 24–28, 2012.

[4]   P. K. Mallick, *Fibre-reinforced composites materials, manufacturing and design*, Third Edi. Taylor & Francis Group, LLC, 2007.

[5]   D. H. J. A. Lukaszewicz, C. Ward, and K. D. Potter, "The engineering aspects of automated prepreg layup: History, present and future," *Compos. Part B Eng.*, vol. 43, pp. 997–1009, 2012.

[6]   J. Tomblin, "Overview of composite material trends in aviation manufacturing," *Natl. Inst. Aviat. Res.*, 2006.

[7]   R. Martin and D. Evans, "Reducing costs in aircraft: The metals affordability initiative consortium," *Jom*, vol. 52, pp. 24–28, 2000.

[8]   R. Stewart, "Thermoplastic composites - Recyclable and fast to process," *Reinf. Plast.*, 2011.

[9]   A. Gilliot, "From carbon fibre to carbon-fibre-reinforced thermoplastics," *JEC Composites Magazine*, pp. 60–62, Mar-2012.

[10]   M. H. Salek, "Effect of processing parameters on the mechanical properties of carbon/PEKK thermoplastic composite materials," Master diss., Concordia University, Canada, 2005.

[11]   B. Choi, O. Diestel, and P. Offermann, "Commingled CF / PEEK hybrid yarns for use in textile reinforced high performance rotors," *12th Int. Conf. Compos. Mater. (ICCM), Paris*, pp. 796–806, 1999.

[12]   N. S. Taylor, S. B. Jones, and M. Weld, "The feasibility of welding thermoplastic composite materials," *Constr. Build. Mater.*, vol. 3, pp. 213–219, 1989.

[13]   J. Heth, "From art to science: A prepreg overview," *High-Performance Composites*, vol. 8. pp. 32–36, 2000.

[14]   K. J. Ahn and J. C. Seferis, "Prepreg processing science and engineering," *Polym. Eng. Sci.*, vol. 33, pp. 1177–1188, 1993.

[15]   J. H. Hodgkin, G. P. Simon, and R. J. Varley, "Thermoplastic toughening of epoxy eesins: a critical review," *Polym. Adv. Technol.*, vol. 9, pp. 3–10, 1998.

[16]   M. G. Bader, "Selection of composite materials and manufacturing routes for cost-effective performance," *Compos. Part A Appl. Sci. Manuf.*, vol. 33, pp. 913–934, 2002.

[17]   V. Babrauskas and R. D. Peacock, "Heat release rate: The single most important variable in fire hazard," *Fire Safety Journal*, vol. 18. pp. 255–272, 1992.

[18]   G. T. Linteris and I. P. Rafferty, "Flame size, heat release, and smoke points in materials flammability," *Fire Saf. J.*, vol. 43, pp. 442–450, 2008.

[19]   A. P. Mouritz, Z. Mathys, and A. G. Gibson, "Heat release of polymer composites in fire," *Compos. Part A Appl. Sci. Manuf.*, vol. 37, pp. 1040–1054, 2006.

[20]   P. Olivier, J. P. Cottu, and B. Ferret, "Effects of cure cycle pressure and voids on some mechanical properties of carbon/epoxy laminates," *Composites*, vol. 26, pp. 509–515, 1995.

[21]   A. Vlot, "Impact loading on fibre metal laminates," *Int. J. Impact Eng.*, vol. 18, pp. 291–307, 1996.

[22]   A. J. Herrod-Taylor, "The crystallisation of poly (aryl ether etherketone) (PEEK) and its carbon fibre composites," *MSc thesis, Univ. Birmingham, UK*, 2011.

[23]   I. Y. Chang and J. K. Lees, "Recent development in thermoplastic composites: A review of matrix systems and processing methods," *J. Thermoplast. Compos. Mater.*, vol. 1, pp. 277–296, 1988.

[24]   U. K. Vaidya and K. K. Chawla, "Processing of fibre reinforced thermoplastic composites," *Int. Mater. Rev.*, vol. 53, pp. 185–218, 2008.

[25]   T. Hartness, "Thermoplastic powder technology for advanced composite systems," *J. Thermoplast. Compos. Mater.*, vol. 1, pp. 210–220, 1988.

[26]   M. Oxley, "The Effect of low velocity impact damage on the performance of a woven CFRP," University of Sheffield, 1991.

[27]   A. Malhotra, F. J. Guild, and M. J. Pavier, "Edge impact to composite laminates: Experiments and simulations," *J. Mater. Sci.*, vol. 43, pp. 6661–6667, 2008.

[28]   W. J. Cantwell and J. Morton, "The impact resistance of composite materials — a review," *Composites*, vol. 22, pp. 347–362, 1991.

[29]   Daniel and Ishai, *Engineering mechanics of composite materials*, Second Edi. Oxford University Press, 2006.

[30]   W. Callister and D. Rethwisch, *Materials science and engineering: an introduction*, Seventh Ed. USA: John Wiley & Sons, Inc., 2007.

[31]   S. Dolati, A. Fereidoon, and A. R. Sabet, "Experimental investigation into glass fiber/epoxy composite laminates subjected to single and repeated high-velocity impacts of ice," *Iran. Polym. J.*, vol. 23, pp. 477–486, 2014.

[32]   D. D. L. Chung, *Composite materials, science and applications*, Second Edi. Springer-Verlag London Limited, 2010.

[33] Y. Yang, R. Boom, B. Irion, D. J. van Heerden, P. Kuiper, and H. de Wit, "Recycling of composite materials," *Chem. Eng. Process. Process Intensif.*, vol. 51, pp. 53–68, 2012.

[34] A. K. Kaw and F. Group, *Mechanics of composite materials*, Second Edi. Taylor & Francis Group, LLC, 2006.

[35] S. Rana and R. Fangueiro, *Fibrous and textile materials for composite applications*. Springer Science+Business Media Singapore, 2016.

[36] J. Wang, G. Yang, F. Zhang, Y. Xiong, and Q. Xiong, "The preparation and mechanical properties of carbon/carbon (C/C) composite and carbon fiber reinforced silicon carbide (Cf/SiC) composite joint by partial transient liquid phase (PTLP) diffusion bonding process," *Vacuum*, vol. 158, pp. 113–116, 2018.

[37] M. Patel, V. Singh, S. Singh, and V. V. Bhanu Prasad, "Micro-structural evolution during diffusion bonding of C-SiC/C-SiC composite using Ti interlayer," *Mater. Charact.*, vol. 135, pp. 71–75, 2018.

[38] K. B. Armstrong, W. Cole, and G. Bevan, *Care and repair of advanced composites*. USA: SAE International, 2005.

[39] J. Sloan, "In-house prepregging: Cost/benefit calculus," *Gardner Business Media, Inc.*, 2013. .

[40] Frederic Neil Cogswell, *Thermoplastic aromatic polymer composites, a study of the structure, processing and properties of carbon fibre reinforced polyetheretherketone and related materials*. Butterworth-Heinemann Ltd, 1992.

[41] A. Zaki, *Thermoplastic – Composite materials*. Croatia: InTech, 2012.

[42] G. Pritchard, *Developments in reinforced plastics-4*. London and New York: Elsevier Applied Science publishers, 1984.

[43]   H. E. N. Bersee, "Composite aerospace manufacturing processes," *Encycl. Aerosp. Eng.*, pp. 1–16, 2010.

[44]   M. U. Ocheje, B. P. Charron, A. Nyayachavadi, and S. Rondeau-Gagné, "Stretchable electronics: Recent progress in the preparation of stretchable and self-healing semiconducting conjugated polymers," *Flex. Print. Electron.*, vol. 2, 2017.

[45]   S. Beland, *High performance resins thermoplastic and their composites*. Ottawa, Canada: National Research Council of Canada, 1990.

[46]   J. Gorto, "Characterization of thermosets part 19: Heat deflection temperature (HDT) -2," 2017. [Online]. Available: https://polymerinnovationblog.com/characterization-thermosets-part-19-heat-deflection-temperature-hdt-2/.

[47]   P. P. Parlevliet and C. Weimer, "Thermoplastic high performance composites : environmental requirements on future helicopter airframes," *ICCM-18. 21 - 26 Aug 2011, . Jeju Int. Conv. Center, Jeju Island, South Korea.*

[48]   M. Chanda and S. K. Roy, *Plastics technology handbook*. Taylor & Francis Group, LLC, 2006.

[49]   R. Sengupta, S. Chakraborty, S. Bandyopadhyay, S. Dasgupta, R. Mukhopadhyay, K. Auddy, and a S. Deuri, "A short review on rubber / clay nnocomposites with emphasis on mechanical properties," *Engineering*, vol. 47, pp. 21–25, 2007.

[50]   G. da Cunha Vasconcelos, R. L. Mazur, E. C. Botelho, M. C. Rezende, and M. L. Costa, "Evaluation of crystallization kinetics of poly (ether-ketone- ketone) and poly (ether-ether- ketone) by DSC," *J. Aerosp. Technol. Manag.*, vol. 2, pp. 155–162, 2010.

[51]   P. A. S. T. E. Attwood, P. C. Dawson, J. L. Freeman, L. R. J. Hoy, J. B. Rose, "Synthesis and properties of polyaryletherketones," *Polymer,* vol. 22, pp. 1096–1103, 1980.

[52] Y. S. Chun and R. A. Weiss, "Thermal behavior of poly(ether ketone ketone)/thermoplastic polyimide blends," *J. Appl. Polym. Sci.*, vol. 94, pp. 1227–1235, 2004.

[53] T. Sinmazçelik, E. Avcu, M. Ö. Bora, and O. Çoban, "A review: Fibre metal laminates, background, bonding types and applied test methods," *Mater. Des.*, vol. 32, pp. 3671–3685, 2011.

[54] P.-Y. B. Jar, R. Mulone, P. Davies, and H.-H. Kausch, "A study of the effect of forming temperature on the mechanical behaviour of carbon-fibre/peek composites," *Compos. Sci. Technol.*, vol. 46, pp. 7–19, 1993.

[55] H. Wang and T. Vu-Khanh, "Damage extension in carbon fiber/PEEK crossply laminates under low veIocity impact," *Compos. Mater.*, vol. 28, pp. 684–707, 1994.

[56] B. Vieille, V. M. Casado, and C. Bouvet, "About the impact behavior of woven-ply carbon fiber-reinforced thermoplastic- and thermosetting-composites: A comparative study," *Compos. Struct.*, vol. 101, pp. 9–21, 2013.

[57] M. N. Ghasemi Nejhad and A. Parvizi-Majidi, "Impact behaviour and damage tolerance of woven carbon fibre-reinforced thermoplastic composites," *Composites*, vol. 21, pp. 155–168, 1990.

[58] J. P. Davim and R. Cardoso, "Effect of the reinforcement (carbon or glass fibres) on friction and wear behaviour of the PEEK against steel surface at long dry sliding," *Wear*, vol. 266, pp. 795–799, 2009.

[59] T. Choupin, B. Fayolle, G. Régnier, C. Paris, J. Cinquin, and B. Brulé, "Isothermal crystallization kinetic modeling of poly(etherketoneketone) (PEKK) copolymer," *Polym. (United Kingdom)*, vol. 111, pp. 73–82, 2017.

[60] L. Q. Cortes, N. Causse, E. Dantras, A. Lonjon, and C. Lacabanne, "Morphology and dynamical mechanical properties of poly ether ketone ketone (PEKK) with meta phenyl

links," *J. Appl. Polym. Sci.*, vol. 133, pp. 1–10, 2016.

[61]   W. Wang, J. M. Schultz, and B. S. Hsiao, "Dynamic study of crystallization- and melting-induced phase separation in PEEK/PEKK blends," *Macromolecules*, vol. 30, pp. 4544–4550, 1997.

[62]   G. Reyes and U. Sharma, "Modeling and damage repair of woven thermoplastic composites subjected to low velocity impact," *Compos. Struct.*, vol. 92, pp. 523–531, 2010.

[63]   F. C. Campbell, *Manufacturing processes for advanced composites*. Oxford, UK: Elsevier Advanced Technology., 2004.

[64]   L. J. . Agarwal, B. D., and Broutman, *Analysis and performance of fiber composites*, Third Edi. John Wiley & Sons, Inc., 2006.

[65]   K. E. Goodman and A. C. Loos, "Thermoplastic prepreg manufacture," *J. Thermoplast. Compos. Mater.*, vol. 3, pp. 34–40, 1990.

[66]   R. Marissen, L. T. Van Der Drift, and J. Sterk, "Technology for rapid impregnation of fibre bundles with a molten thermoplastic polymer," *Compos. Sci. Technol.*, vol. 60, pp. 2029–2034, 2000.

[67]   R. Ali, S. Iannace, and L. Nicolais, "Effects of processing conditions on the impregnation of glass fibre mat in extrusion/calendering and film stacking operations," *Compos. Sci. Technol.*, vol. 63, pp. 2217–2222, 2003.

[68]   A. Texier, R. M. Davis, K. R. Lyon, A. Gungor, J. E. McGrath, H. Marand, and J. S. Riffle, "Fabrication of PEEK/carbon fibre composites by aqueous suspension prepregging," *Polym. ,* vol. 34, pp. 896–906, 1993.

[69]   L. B. Nohara, M. L. Costa, M. A. Alves, M. F. K. Takahashi, E. L. Nohara, and M. C. Rezende, "Processing of high performance composites based on PEKK by aqueous

suspension prepregging," *Mater. Res.*, vol. 13, pp. 245–252, 2010.

[70]   S. R. Iyer and L. T. Drzal, "Manufacture of powder-impregnated thermoplastic composites," *J. Thermoplast. Compos. Mater.*, vol. 3, pp. 325–355, 1990.

[71]   R. V. Price, "Production of impregnated roving," vol. US Patents, 1973.

[72]   N. Chand, S. Kreuzberger, and G. Hinrichsen, "Influence of processin conditions on the tensile properties of unidirectional UHMWPE fibre/LDPE fiber composites," *Composites*, vol. 25, pp. 878–880, 1994.

[73]   J. Muzzy, B. Varughese, V. Thammongkol, and W. Tincher, "Electrostatic prepregging of thermoplastic matrices," *SAMPE J.*, vol. 25, pp. 15–21, 1989.

[74]   D. D. Edie and G. C. Lickfield, "Thermoplastic coating of carbon fibers," *Annu. Rep.*, 1991.

[75]   A. L. OGDEN, M. W. HYER, G. L. WILKES, and A. C. LOOS, "Development of an alternative thermoplastic powder prepregging technique," *J. Thermoplast. Compos. Mater.*, vol. 5, pp. 14–31, 1992.

[76]   B. Vieille, V. M. Casado, and C. Bouvet, "About the impact behavior of woven-ply carbon fiber-reinforced thermoplastic- and thermosetting-composites: A comparative study," *Compos. Struct.*, vol. 101, pp. 9–21, 2013.

[77]   R. L. Mazur, G. M. Candido, M. C. Rezende, and E. C. Botelho, "Accelerated aging effects on carbon fiber PEKK composites manufactured by hot compression molding," *J. Thermoplast. Compos. Mater.*, vol. 29, pp. 1429–1442, 2016.

[78]   W. Tan and B. G. Falzon, "Modelling the nonlinear behaviour and fracture process of AS4/PEKK thermoplastic composite under shear loading," *Compos. Sci. Technol.*, vol. 126, pp. 60–77, 2016.

[79]   I. Baran, L. L. Warnet, and R. Akkerman, "Assessment of failure and cohesive zone

length in co-consolidated hybrid C/PEKK butt joint," *Eng. Struct.*, vol. 168, pp. 420–430, 2018.

[80] Y. Su, M. de Rooij, W. Grouve, and R. Akkerman, "The effect of titanium surface treatment on the interfacial strength of titanium – Thermoplastic composite joints," *Int. J. Adhes. Adhes.*, vol. 72, pp. 98–108, 2017.

[81] R. A. Bucher and J. A. Hinkley, "Fiber / matrix adhesion in graphite / PEKK composites," *J. Thermoplast. Compos. Mater.*, vol. 5, pp. 2–13, 1992.

[82] C. T. Sun, I. Chung, and I. Y. Chang, "Modeling of elastic-plastic behavior of LDF and continuous fiber reinforced AS-4/PEKK composites," *Compos. Sci. Technol.*, vol. 43, pp. 339–345, 1992.

[83] W. Wang, Y. Takao, and T. Matsubara, "Galvanic corrosion-resistant carbon fiber metal laminates," *ICCM 16*, pp. 1–10, 2007.

[84] A. Asundi and A. Y. N. Choi, "Fiber metal laminates: An advanced material for future aircraft," *J. Mater. Process. Technol.*, vol. 63, pp. 384–394, 1997.

[85] L. B. Vogelesang and A. Vlot, "Development of fibre metal laminates for advanced aerospace structures," *J. Mater. Process. Technol.*, vol. 103, pp. 1–5, 2000.

[86] A. Vlot, "Low-velocity impact loading on fibre reinforced aluminium laminates (ARALL and GLARE) and other aircraft sheet materials." Delft University of Technology, 1993.

[87] F. D. Morinière, R. C. Alderliesten, and R. Benedictus, "Modelling of impact damage and dynamics in fibre-metal laminates - A review," *Int. J. Impact Eng.*, vol. 67, pp. 27–38, 2014.

[88] P. Cortés and W. J. Cantwell, "Fracture properties of a fiber-metal laminates based on magnesium alloy," *J. Mater. Sci.*, vol. 39, pp. 1081–1083, 2004.

[89]   A. P. Sharma, S. H. Khan, and V. Parameswaran, "Experimental and numerical investigation on the uni-axial tensile response and failure of fiber metal laminates," *Compos. Part B Eng.*, vol. 125, pp. 259–274, 2017.

[90]   P. Cortes and W. J. Cantwell, "The tensile and fatigue properties of carbon fiber-reinforced PEEK-Titanium fiber-metal laminates," *J. Reinf. Plast. Compos.*, vol. 23, pp. 1615–1623, 2004.

[91]   P. Cortés and W. J. Cantwell, "The prediction of tensile failure in titanium-based thermoplastic fibre-metal laminates," *Compos. Sci. Technol.*, vol. 66, pp. 2306–2316, 2006.

[92]   A. VLOT and J. W. GUNNINK, *Fibre metal laminates an introduction*. Delft: Springer-Science+Business Media, B,V, 2001.

[93]   M. Kawai and A. Hachinohe, "Two-stress level fatigue of unidirectional fiber-metal hybrid composite: GLARE 2," *Int. J. Fatigue*, vol. 24, pp. 567–580, 2002.

[94]   A. Akbari, "Adiabatic shear banding in Titanium 15-3-3-3 alloy," Master diss., Tampere University of Technology, Finland, 2013.

[95]   C. Leyen and M. Peters, *Titanium and titanium alloys, fundamentals and applications.* WILEY-VCH Verlag GmbH & Co. KGaA, Weinheim, 2003.

[96]   Z. N. Ismarrubie, A. Ali, T. Satake, and M. Sugano, "Influence of microstructures on fatigue damage mechanisms in Ti-15-3 alloy," *Mater. Des.*, vol. 32, pp. 1456–1461, 2011.

[97]   Z. Huda, N. I. Taib, and T. Zaharinie, "Characterization of 2024-T3: An aerospace aluminum alloy," *Mater. Chem. Phys.*, vol. 113, pp. 515–517, 2009.

[98]   D. Zhu and W. J. van Ooij, "Corrosion protection of AA 2024-T3 by bis-[3-(triethoxysilyl) propyl]tetrasulfide in neutral sodium chloride solution. Part 1:

Corrosion of AA 2024-T3," *Corros. Sci.*, vol. 45, pp. 2163–2175, 2003.

[99] R. B. Loftin, "Aerospace applications of virtual environment technology.," *Comput. Graph. (ACM).*, vol. 30, pp. 33–35, 1996.

[100] A. Warren, "Developments and challenges for aluminum-A boeing perspective," *Mater. Forum*, vol. 28, pp. 24–31, 2004.

[101] N. E. Prasad and V. V Kutumbarao, *Aerospace materials and material technologies*. Springer Science+Business Media Singapore, 2017.

[102] C. Atas, B. M. Icten, and M. Küçük, "Thickness effect on repeated impact response of woven fabric composite plates," *Compos. Part B Eng.*, vol. 49, pp. 80–85, 2013.

[103] D. Kreculj and B. Rašuo, "Review of impact damages modelling in laminated composite aircraft structures," *Teh. Vjesn.*, vol. 3, pp. 485–495, 2013.

[104] E. Sevkat, B. Liaw, F. Delale, and B. B. Raju, "Effect of repeated impacts on the response of plain-woven hybrid composites," *Compos. Part B Eng.*, vol. 41, pp. 403–413, 2010.

[105] M. S. Found and I. C. Howard, "Single and multiple impact behaviour of a CFRP laminate," *Compos. Struct.*, vol. 32, pp. 159–163, 1995.

[106] S.-X. Wang, L.-Z. Wu, and L. Ma, "Low-velocity impact and residual tensile strength analysis to carbon fiber composite laminates," *Mater. Des.*, vol. 31, pp. 118–125, 2010.

[107] G. Sala, "Post-impact behaviour of aerospace composites for high-temperature applications: experiments and simulations," *Compos. Part B Eng.*, vol. 28, pp. 651–665, 1997.

[108] G. Perillo, N. P. N. Vedvik, and A. A. T. Echtermeyer, "Numerical analyses of low velocity impacts on composite. Advanced modelling techniques.," *SIMULIA Community Conf.*, pp. 1–16, 2012.

[109] B. Sadasivam and P. K. Mallick, "Impact damage resistance of random fiber reinforced automotive composites," *J. Thermoplast. Compos. Mater.*, vol. 15, pp. 181–191, 2002.

[110] W. J. Cantwell and J. Morton, "The impact resistance of composite materials - a review," *Composites*, vol. 22, pp. 347–362, 1991.

[111] T. Gómez-del Río, R. Zaera, E. Barbero, and C. Navarro, "Damage in CFRPs due to low velocity impact at low temperature," *Compos. Part B Eng.*, vol. 36, pp. 41–50, 2005.

[112] V. Tita, J. de Carvalho, and D. Vandepitte, "Failure analysis of low velocity impact on thin composite laminates: Experimental and numerical approaches," *Compos. Struct.*, vol. 83, pp. 413–428, 2008.

[113] C. Lopes, Z. Gürdal, P. P. Camanho, Maimí, and E. V González, "Simulation of low-velocity impact damage on composite laminates," *50th AIAA/ASME/ASCE/AHS/ASC Struct. Struct. Dyn. Mater. Conf.*, 2009.

[114] G. P. Zhao and C. D. Cho, "Damage initiation and propagation in composite shells subjected to impact," *Compos. Struct.*, vol. 78, pp. 91–100, 2007.

[115] W. Cantwell, "Geometrical effects in the low velocity impact response of GFRP," *Compos. Sci. Technol.*, vol. 67, pp. 1900–1908, 2007.

[116] P. N. B. Reis, J. a M. Ferreira, P. Santos, M. O. W. Richardson, and J. B. Santos, "Impact response of Kevlar composites with filled epoxy matrix," *Compos. Struct.*, vol. 94, pp. 3520–3528, 2012.

[117] Y. Zhang, P. Zhu, and X. Lai, "Finite element analysis of low-velocity impact damage in composite laminated plates," *Mater. Des.*, vol. 27, pp. 513–519, 2006.

[118] G. A. O. Davies and X. Zhang, "Impact damage prediction in carbon composite structures," *Int. J. Impact Eng.*, vol. 16, pp. 149–170, 1995.

[119] F. J. Yang and W. J. Cantwell, "Impact damage initiation in composite materials," *Compos. Sci. Technol.*, vol. 70, pp. 336–342, 2010.

[120] T. Mitrevski, I. H. Marshall, R. Thomson, R. Jones, and B. Whittingham, "The effect of impactor shape on the impact response of composite laminates," *Compos. Struct.*, vol. 67, pp. 139–148, 2005.

[121] H. Y. Choi and F.-K. Chang, "A Model for predicting damage in graphite/epoxy laminated composites resulting from low-velocity point impact," *J. Compos. Mater.*, vol. 26, pp. 2134–2169, 1992.

[122] P. Kumar and B. Rai, "Delaminations of barely visible impact damage in CFRP laminates," *Compos. Struct.*, vol. 23, pp. 313–318, 1993.

[123] J. Lopez-Puente, R. Zaera, and C. Navarro, "The effect of low temperatures on the intermediate and high velocity impact response of CFRPs," *Compos. Part B-Engineering*, vol. 33, pp. 559–566, 2002.

[124] J. Fan, Z. Guan, and W. J. Cantwell, "Modeling perforation in glass fiber reinforced composites subjected to low velocity impact loading," *Polym. Compos.*, vol. 16, pp. 1380–1388, 2011.

[125] T. Ishikawa, S. Sugimoto, M. Matsushima, and Y. Hayashi, "Some experimental findings in compression-after-impact (CAI) tests of CF/PEEK (APC-2) and conventional CF/epoxy flat plates," *Compos. Sci. Technol.*, vol. 55, pp. 349–363, 1995.

[126] P. Davies, "Thermoplastic composite cylinders for underwater applications," *J. Thermoplast. Compos. Mater.*, vol. 18, pp. 417–443, 2005.

[127] G. Bibo, D. Leicy, P. J. Hogg, and M. Kemp, "High-temperature damage tolerance of carbon fibre-reinforced plastics. Part 1: Impact characteristics," *Composites*, vol. 25, pp. 414–424, 1994.

[128] G. A. Bibo, P. J. Hogg, and M. Kemp, "High-temperature damage tolerance of carbon fibre-reinforced plastics:. 2. Post-impact compression characteristics," *Composites*, vol. 26, pp. 91–102, 1995.

[129] B. P. Jang, C. T. Huang, C. Y. Hsieh, W. Kowbel, and B. Z. Jang, "Repeated impact failure of continuous fiber reinforced thermoplastic and thermoset composites," *J. Compos. Mater.*, vol. 25, pp. 1171–1203, 1991.

[130] H. Morita, A. K. Hamamoto, and T. Hiroyuki, "Characterization of impact damage resistance of CF, PEEK and CF, toughened epoxy laminates under low and high velocity impact tests," *Journal of the Society of Materials Science, Japan*, vol. 44. pp. 423–427, 1995.

[131] J. Morton and E. W. Godwin, "Impact response of tough carbon fibre composites," *Compos. Struct.*, vol. 13, pp. 1–19, 1989.

[132] J. Zhou, Z. W. Guan, and W. J. Cantwell, "The influence of strain-rate on the perforation resistance of fiber metal laminates," *Compos. Struct.*, vol. 125, pp. 247–255, 2015.

[133] G. R. Rajkumar, M. Krishna, H. N. N. Murthy, S. C. Sharma, and K. R. V. Mahesh, "Experimental investigation of low-velocity repeated impacts on glass fiber metal composites," *J. Mater. Eng. Perform.*, vol. 21, pp. 1485–1490, 2012.

[134] X. Li, X. Zhang, H. Zhang, J. Yang, A. B. Nia, and G. B. Chai, "Mechanical behaviors of Ti/CFRP/Ti laminates with different surface treatments of titanium sheets," *Compos. Struct.*, vol. 163, pp. 21–31, 2017.

[135] S. Bernhardt, M. Ramulu, and a. S. Kobayashi, "Low-velocity impact response characterization of a hybrid titanium composite laminate," *J. Eng. Mater. Technol.*, vol. 129, p. 220, 2007.

[136] G. R. Rajkumar, M. Krishna, H. N. Narasimha Murthy, S. C. Sharma, and K. R. Vishnu

Mahesh, "Investigation of repeated low velocity impact behaviour of GFRP/aluminium and CFRP/aluminium laminates," *Int. J. Soft Comput. Eng*, vol. 1, pp. 50–58, 2012.

[137] F. D. Morinière, R. C. Alderliesten, M. Y. Tooski, and R. Benedictus, "Damage evolution in GLARE fibre-metal laminate under repeated low-velocity impact tests," *Cent. Eur. J. Eng.*, vol. 2, pp. 603–611, 2012.

[138] G. Caprino, G. Spataro, and S. Del Luongo, "Low-velocity impact behaviour of fibreglass-aluminium laminates," *Compos. Part A Appl. Sci. Manuf.*, vol. 35, pp. 605–616, 2004.

[139] G. Wu, J. M. Yang, and H. T. Hahn, "The impact properties and damage tolerance and of bi-directionally reinforced fiber metal laminates," *J. Mater. Sci.*, vol. 42, pp. 948–957, 2007.

[140] J. Fan, W. Cantwell, and Z. Guan, "The low-velocity impact response of fiber-metal laminates," *J. Reinf. Plast. Compos.*, vol. 30, pp. 26–35, 2011.

[141] G. Simeoli, D. Acierno, C. Meola, L. Sorrentino, S. Iannace, and P. Russo, "The role of interface strength on the low velocity impact behaviour of PP/glass fibre laminates," *Compos. Part B Eng.*, vol. 62, pp. 88–96, 2014.

[142] B. Alcock, N. O. Cabrera, N. M. Barkoula, C. T. Reynolds, L. E. Govaert, and T. Peijs, "The effect of temperature and strain rate on the mechanical properties of highly oriented polypropylene tapes and all-polypropylene composites," *Compos. Sci. Technol.*, vol. 67, pp. 2061–2070, 2007.

[143] S. D. Bartus and U. K. Vaidya, "Performance of long fiber reinforced thermoplastics subjected to transverse intermediate velocity blunt object impact," *Compos. Struct.*, vol. 67, pp. 263–277, 2005.

[144] G. V Reyes and W. J. Cantwell, "The mechanical properties of fibre -metal laminates based on glass fibre reinforced polypropylene," vol. 60, pp. 2–6, 2000.

[145] N. M. Barkoula, B. Alcock, N. O. Cabrera, and T. Peijs, "Fatigue properties of highly oriented polypropylene tapes and all-polypropylene composites," *Polym. Polym. Compos.*, vol. 16, pp. 101–113, 2008.

[146] P. Cortes and W. J. Cantwell, "The impact properties of high-temperature fiber metal laminates," *J. Compos. Mater.*, vol. 41, pp. 613–632, 2006.

[147] W.-S. Lee, C.-H. La, and & S.-T. Chi, "Simulation of perforation behaviour of carbon fiber reinforced 6061-T6 aluminum metal matrix composite by a tungsten projectile," *Struct. under Shock Impact VI*, pp. 185–194, 2000.

[148] Z. W. Guan, W. J. Cantwell, and R. Abdullah, "Numerical modeling of the impact response of fiber–metal laminates," *Polym. Compos.*, pp. 603–609, 2009.

[149] G. H. Payeganeh, F. Ashenai Ghasemi, and K. Malekzadeh, "Dynamic response of fiber-metal laminates (FMLs) subjected to low-velocity impact," *Thin-Walled Struct.*, vol. 48, pp. 62–70, 2010.

[150] J. Fan, Z. W. Guan, and W. J. Cantwell, "Numerical modelling of perforation failure in fibre metal laminates subjected to low velocity impact loading," *Compos. Struct.*, vol. 93, pp. 2430–2436, 2011.

[151] H. Nakatani, T. Kosaka, K. Osaka, and Y. Sawada, "Damage characterization of titanium/GFRP hybrid laminates subjected to low-velocity impact," *Compos. Part A Appl. Sci. Manuf.*, vol. 42, pp. 772–781, 2011.

[152] E. Sitnikova, Z. W. Guan, G. K. Schleyer, and W. J. Cantwell, "Modelling of perforation failure in fibre metal laminates subjected to high impulsive blast loading," *Int. J. Solids Struct.*, vol. 51, pp. 3135–3146, 2014.

[153] T. P. Vo, Z. W. Guan, W. J. Cantwell, and G. K. Schleyer, "Low-impulse blast behaviour of fibre-metal laminates," *Compos. Struct.*, vol. 94, pp. 954–965, 2012.

[154] T. P. Vo, Z. W. Guan, W. J. Cantwell, and G. K. Schleyer, "Modelling of the low-impulse blast behaviour of fibre-metal laminates based on different aluminium alloys," *Compos. Part B Eng.*, vol. 44, pp. 141–151, 2013.

[155] J. Zhou, Z. W. Guan, and W. J. Cantwell, "The perforation resistance of sandwich structures subjected to Low velocity projectile impact loading," *Aeronaut. J.*, vol. 116, pp. 1247–1262, 2012.

[156] H. Seo, J. Hundley, H. T. Hahn, and J.-M. Yang, "Numerical simulation of glass-fiber-reinforced aluminum laminates with diverse impact damage," *AIAA J.*, vol. 48, pp. 676–687, 2010.

[157] S. H. Song, Y. S. Byun, T. W. Ku, W. J. Song, J. Kim, and B. S. Kang, "Experimental and numerical investigation on impact performance of carbon reinforced aluminum laminates," *J. Mater. Sci. Technol.*, vol. 26, pp. 327–332, 2010.

[158] ASTM D7264/D7264M-15, "Standard test method for flexural properties of polymer matrix composite materials," *Annu. B. ASTM Stand.*, pp. 1–10, 2015.

[159] ASTM D3039/D3039M-14, "Standard test method for tensile properties of polymer matrix composite materials," *Annu. B. ASTM Stand.*, pp. 1–13, 2014.

[160] EN ISO14129, "Determination of the in-plane shear stress/shear strain response, including the in-plane shear modulus and strength, by the +/- 45 tension test method," *Eur. Comm. Stand.*, 1998.

[161] ASTM E8/E8M − 16a, "Standard test methods for tension testing of metallic materials," pp. 1–27, 2016.

[162] P. Verleysen, I. De Baere, and J. Degrieck, "Pre-fatigue influence on quasi-static tensile properties of Ti-6Al-4V in thin-sheet form," *EDP Sci.*, vol. 6, pp. 3–9, 2010.

[163] J. Haubrich, K. Schulze, and J. Hausmann, "Laser treatments of titanium surfaces in

different atmospheres for improved adhesion properties," *Euro Hybrid Mater. Struct.*, pp. 13–16, 2014.

[164] J. Fan, W. Cantwell, and Z. Guan, "The low-velocity impact response of fiber-metal laminates," *J. Reinf. Plast. Compos.*, vol. 30, pp. 26–35, 2011.

[165] M. Aktas and R. Karakuzu, "Determination of mechanical properties of glass-epoxy composites in high temperatures," *Polym. Compos.*, vol. 30, pp. 1438–1441, 2009.

[166] D. Whisler and H. Kim, "Effect of impactor radius on low-velocity impact damage of glass/epoxy composites," *J. Compos. Mater.*, vol. 46, pp. 3137–3149, 2012.

[167] V. D. Ta, A. Dunn, T. J. Wasley, J. Li, R. W. Kay, J. Stringer, P. J. Smith, E. Esenturk, C. Connaughton, and J. D. Shephard, "Laser textured superhydrophobic surfaces and their applications for homogeneous spot deposition," *Appl. Surf. Sci.*, vol. 365, pp. 153–159, 2016.

[168] P. Cortes and W. J. Cantwell, "The impact Properties of High-temperature Fiber-Metal Laminates," *J. Compos. Mater.*, vol. 41, pp. 613–632, 2006.

[169] Dassault Systèmes Simulia, "Abaqus CAE User's Manual," *Abaqus 6.12*, 2012.

[170] Z. Hashin, "Failure criteria for unidirectional fibre composites," *J. Appl. Mech.*, vol. 47, pp. 329–334, 1980.

[171] M. Hokka, T. Leemet, A. Shrot, M. Baeker, and V. T. Kuokkala, "Characterization and numerical modeling of high strain rate mechanical behavior of Ti-15-3 alloy for machining simulations," *Mater. Sci. Eng. A*, vol. 550, pp. 350–357, 2012.

[172] J. Zhang and X. Zhang, "Simulating low-velocity impact induced delamination in composites by a quasi-static load model with surface-based cohesive contact," *Compos. Struct.*, vol. 125, pp. 51–57, 2015.

[173] H. Hooputra, H. Gese, H. Dell, and H. Werner, "A comprehensive failure model for

crashworthiness simulation of aluminium extrusions," *Int. J. Crashworthiness*, vol. 9, pp. 449–463, 2004.

[174] C. Breen, F. Guild, and M. Pavier, "Impact damage to thick carbon fibre reinforced plastic composite laminates," *J. Mater. Sci.*, vol. 41, pp. 6718–6724, 2006.

[175] N. Nassir, Z. W. Guan, R. S. Birch, and W. J. Cantwell, "Damage initiation in composite materials under off-centre impact loading," *Polym. Test.*, vol. 69, pp. 456–461, 2018.